Multi-Electron Reduction of Small Molecules by Triiron Reaction Sites

Multi-Electron Reduction of Small Molecules by Triiron Reaction Sites

A dissertation presented

by

Tamara Michelle Powers

to

The Department of Chemistry and Chemical Biology

in partial fulfillment of the requirements
for the degree of
Doctor of Philosophy
in the subject of
Chemistry

Harvard University
Cambridge, Massachusetts

June 2013

Dissertation Advisor: Professor Theodore A. Betley Tamara Michelle Powers

Multi-Electron Reduction of Small Molecules by Triiron Reaction Sites

Abstract

The observation that multi-electron activation of small molecule substrates occurs at polynuclear reaction sites, common to both metalloenzymes and heterogeneous catalysts, has led to the articulation of the polynuclear hypothesis – the idea that the expanded redox reservoir afforded by M–M interactions in polynuclear systems stabilizes multiple oxidation states and facilitates multi-electron transformations. Currently, examples of synthetic clusters that test the viability of polynuclear reaction sites towards effecting multi-electron activation of small molecule substrates are lacking.

To test the polynuclear hypothesis, we targeted a system that embodies design elements common to metaloenzyme cofactors: polynuclear reaction sites that feature high-spin, coordinatively unsaturated metal centers. Metallation of $^{tbs}LH_6$ [$^{tbs}LH_6$ = 1,3,5-C_6H_9(NHC_6H_4-*o*-$NHSiMe_2{}^tBu)_3$] yields high-spin trinuclear Fe^{II} complex (^{tbs}L)Fe_3(THF). The filled anti-bonding orbitals in high-spin cluster (^{tbs}L)Fe_3(THF) renders ligand reorganization facile, which allows for a range of metal–substrate binding modes. The polynuclear site within the (^{tbs}L)Fe_3(THF) cluster cooperatively binds anionic donors and allows $2e^-$ reduction of substrates including inorganic azide and hydrazines, yielding μ^3-nitrido and μ^3-imido products, respectively. The $4e^-$ reductive N=N bond cleavage of azobenzene is also achieved in the presence of (^{tbs}L)Fe_3(THF) to yield Fe_3 *bis*-imido complex (^{tbs}L)Fe_3(μ^3-NPh)(μ^2-NPh), which has been structurally characterized. Cyclic voltammograms of a series of selected Fe_3 imido and nitrido clusters suggest that oxidation states up to (Fe^{IV})(Fe^{III})$_2$ are electrochemically accessible.

Addition of neutral π-acidic molecules including *tert*-butylisonitrile (^{t}BuNC) and carbon monoxode (CO) to trinuclear cluster (^{tbs}L)Fe$_3$(THF) led to the formation of a new series of coordination compounds, where binding to a single metal center is favored over cooperative substrate binding. Coordinated substrates are activated toward further reactivity, highlighted by the reductive coupling of isonitriles by (^{tbs}L)Fe$_3$(μ^1-CN^{t}Bu)$_3$ in the presence of phenylsilane.

Finally, efforts to synthesize of a family of mixed Fe–Mn clusters that differ by single metal-site substitutions are presented. Substitutionally homogeneous (^{tbs}L)Fe$_2$Mn(THF) cluster is accessed from binuclear complex (^{tbs}LH$_2$)Fe$_2$. Attempts to synthesize similar Mn$_2$Fe clusters results in isolation of a mixture of heterotrinuclear species. In conjunction with NMR, EPR, Mössbauer, and X-ray fluorescence spectroscopies, anomalous scattering measurements were critical for the unambiguous assignment of the metal substitution products that were synthesized.

Table of Contents

for David

Acknowledgements

I first and foremost must thank my advisor, Ted. Ted has been an all around amazing advisor. I first would like to thank Ted for his never-ending patience and guidance, as I continue to learn what it takes to be an independent scientist. Ted has taught me to strive to be creative in my work and to be my own harshest critic. The hours spent listening to and giving practice talks, group meetings, and subgroups are some of the most valuable experiences during my graduate career. Ted is an inspiring teacher both in the classroom as well as in the laboratory setting, and working in his lab reminded me why I love science. While Ted demands the best, he never once gave me grief about leaving a couple hours early once a week to go horseback riding. Something so simple deeply affected my graduate experience and I feel extremely fortunate to have found an advisor who understands work/life balance, while pushing his students to excellence.

I would like to thank my committee members, Roy Gordon and Dick Holm, for their support, guidance, and input throughout my degree. I admire both of them and look forward to working with Roy in the future as I continue my scientific career a Postdoc.

I owe a great deal of thanks to all those who contributed directly or indirectly to the work in this thesis. Thank you to Emily and Kin, for building the foundation of the polynuclear subgroup. The work that they accomplished in such a short period of time is nothing but extraordinary. I also want to thank Alison, both for her scientific contributions as well as for taking me under her wing and supporting me through many, many failed experiments. Alison's hard work and dedication inspired me to push through the toughest times of my graduate career. I had the opportunity to work with two very talented undergraduates, Annie Baldwin and Nina Gu, both of whom made significant contributions to the synthesis and characterization of bimetallic trinuclear clusters. I remember how busy it was to be an undergraduate student and I

want to thank them both for their hard work and dedication to research. I would also like to thank Shao, who has gone above and beyond his duties as manager of the X-ray facility, spending hundreds of hours helping me with challenging structures and taking the time to teach me crystallography.

Thank you to all past and current Betley group members for your support and scientific input. Thanks to Libby, Graham, Austin, Matt, Dave Harris, Alison, and Raúl for their helpful discussions. Thanks to my classmates, Libby, Graham, and Austin for their friendship and support. The day we joined Ted's group we went out for a glass of beer at the Queen's Head. We raised our glasses and toasted, pronouncing that the coolest people from our class had joined the Betley group. I still think we were right, and I am so happy and privileged to have shared this journey with them. Finally, I want to extend a special thanks to Libby for being an awesome office-mate, lab-mate, hood-mate, colleague, and most importantly friend. I will miss our graduate school years together, but have no doubt that our friendship will last a lifetime.

On a personal note, I would like to thank my undergraduate advisor, Claude Yoder. I cannot say enough about Dr. Yoder; he is a true inspiration and an exemplary professor. I have greatly appreciated his continuing support throughout my graduate career. Thank you to my family, including my parents and my in-laws, for their continuous support and encouragement. Mom and Dad, thank you for always believing in me and letting me follow my dreams. Finally, I must thank my best friend, my colleague, and my husband, David. Without you, I would not have written a thesis. Thank you for believing in me when I could not believe in myself. Your dedication and pure love for science has not only inspired me to work hard, but also to live my life to its fullest.

List of Schemes

List of Figures

List of Tables

List of Chemical Abbreviations

ACN	acetonitrile
Ad	adamantyl
Ala	alanine
Ar	aryl
ATP	adenosine triphosphate
ADP	adenosine diphosphate
Bu	butyl
Cp	cyclopentadienyl
DHA	9,10-dihydroanthracene
Et	ethyl
Fc	ferrocene
Fc^+	ferrocenium
Gln	glutamine
Gly	glycine
His	histidine
Ile	isoleucine
Me	methyl
Mes	mesityl or 2,4,6-trimethylphenyl
Ph	phenyl
^{n}Pr	*n*-propyl
py	pyridine
tba	tetrabutylammonium
$^{tbs}L^{6-}$	$1,3,5\text{-}C_6H_9(NC_6H_4\text{-}o\text{-}NSiMe_2{}^{t}Bu)_3{}^{6-}$
tbs	*tert*-butyldimethylsilyl
^{t}Bu	*tert*-butyl
TEMPOH	1-hydroxy-2,2,6,6-tetramethyl-piperidine
THF	tetrahydrofuran
OTf	triflate
Val	valine

List of Acronyms, Symbols, and Units

^{13}C	carbon-13
^{1}H or H^{+}	proton
^{2}H	deuterium
^{15}N	nitrogen-15
^{57}Fe	iron-57
^{95}Mo	molybdenum-95
A	alternating
Å	angstrom, 10^{-10} meters
atm	atmospheres
avg	average
br	broad
CW	continuous wave
D	distil
d	doublet in NMR
d_n	deuterated (*n* is the number of protons where ^{2}H replaces ^{1}H)
E_o	reduction potential, measured in volts
$E_{1/2}$	half cell potential, measured in millivolts
e^-	electron
EELS	electron energy loss spectroscopy
E_n	*n*th state in the Lowe-Thorneley model, where *n* = number of electrons/protons
ENDOR	electron-nuclear double resonance
EPR	electron paramagnetic resonance
ESEEM	electron spin echo envelope modulation
eV	electron volts
f'	real anomalous scattering term
f"	imaginary anomalous scattering term
FT	Fischer-Tropsch
g	grams
GCMS	gas chromatography/mass spectrometry
h	hours
H	nitrogenase intermediate **H**, E_7 in Lowe-Thorneley kinetic model
I	nitrogenase intermediate **I**, E_8 in Lowe-Thorneley kinetic model
IR	infrared spectroscopy
K	kelvin
kcal	kilocalories, 10^3 calories
lp	lone pair
LT	Lowe-Thorneley kinetic model
M	molar (moles per liter) or metal
m	multiplet in NMR
mg	milligrams
MHz	megahertz, 10^6 Hertz or 10^6 s^{-1}
min	minutes
mL	milliliter, 10^{-3} liters
mmol	millimole, 10^{-3} moles
MO	molecular orbital
mol	moles
mV	millivolt, 10^{-3} volts
nm	nanometer, 10^{-9} meters
NMR	nuclear magnetic resonance

o-	*ortho*- position on an aryl ring, indicating a 1,2 relationship
OCP	open circuit potential
P_i	inorganic phosphate
ppm	parts per million
q	quartet in NMR
RT	room temperature
s	singlet in NMR or second
S	spin
SHE	standard hydrogen electrode
t	triplet in NMR
T	temperature
UV-vis	ultraviolet-visible absorption spectroscopy
V	volt
XRF	X-ray fluorescence spectroscopy
Γ	gamma, width at half maximum for ^{57}Fe Mössbauer in mm/s
δ	delta, chemical shift in ppm
δ	delta, isomer shift for ^{57}Fe Mössbauer in mm/s
$\lvert \Delta E_Q \rvert$	quadrupole splitting for ^{57}Fe Mössbauer in mm/s
η^n	eta, hapticity, or the number (n) of contiguous atoms in a ligand bound to a metal
λ	lambda, wavelength in nm
μ_B	Bohr magneton, 9.274×10^{-21} erg/G
μ_{eff}	mu effective, effective magnetic moment in Bohr magnetons
μ^n	mu, the number, n, of metal atoms to which a bridging ligand is bound
ν	frequency

Chapter 1. The Polynuclear Hypothesis

1-1. Introduction

Activation and functionalization of small molecules is desirable, both in terms of harnessing the energy stored in the chemical bonds of molecules such as CH_4, as well as utilization of the atomic constituents in molecules including N_2, CO, and CO_2 as synthons for more complex molecules. For example, the Fischer-Tropsch (FT) process catalyzes the production of petroleum substitutes by combination of CO and H_2 over a metal surface catalyst (Eq. 1.1).[1]

$$(2n + 1)\,H_2 + n\,CO \xrightarrow{[M]} C_nH_{(2n+2)} + n\,H_2O \qquad \text{(Eq. 1.1)}$$

The FT process, which operates at temperatures ranging from 200–350 ^oC and pressures of 20–45 Bar,[1] yields a range of alkane products, some of which are undesirable including gaseous hydrocarbons (CH_4 and C_2H_4) and long-chain hydrocarbons (waxes).[2] The development of homogeneous catalysts that facilitate activation of small molecules has been an area of significant research and, in particular, catalysts based on first row transition metals are viewed as attractive targets because of their earth abundance and low cost. However, progress in developing homogeneous catalysts featuring first row transition metals, whose chemistries are dominated by $1e^-$ pathways, has been limited due to the fact that small molecule activation requires the control of multi-electron processes (Table 1.1).

Nature frequently utilizes bi- and polynuclear metalloenzyme cofactors that feature close (ca. < 3 Å) M–M contacts to achieve a variety of enzymatic reactions, including both electron transfer as well as catalytic reduction and oxidation of small molecule substrates, at ambient temperature and pressure. Table 1.2 shows examples of metalloenzyme cofactors, composed of a

1. Khodakov, A. Y.; Chu, W.; Fongarland, P. *Chem. Rev.* **2007**, *107*, 1692-1744.
2. Schulz, H. *App. Cat. A* **1999**, *186*, 3-12.

Table 1.1. Desirable small molecule activation reactions

Transformation	e^- equivalents
$N_2 + 6H^+ \rightarrow 2NH_3$	$6e^-$
$2H_2O \rightarrow 2H_2 + O_2$	$4e^-$
$CO_2 + 2H^+ \rightarrow CO + H_2O$	$2e^-$
$CO + 4H^+ \rightarrow CH_3OH$	$4e^-$
$CO_2 + 6H^+ \rightarrow CH_3OH + H_2O$	$6e^-$
$CH_4 + O_2 + 2H^+ \rightarrow CH_3OH + H_2O$	$2e^-$

variety of earth abundant transition metals. For example, iron-sulfur proteins, including 2-, 3-, and 4-iron ferredoxins, contain iron-sulfur clusters, which mediate electron transfer.[3,4] Iron-sulfur clusters also are utilized to transfer electrons within enzymes, providing electron equivalents for reduction or accepting electrons during oxidation of substrates. Nitrogenase, nature's N_2 fixation machinery, features a [4Fe–4S] cluster that shuttles electrons to the polynuclear FeMo, FeV, or Fe-only cofactor, where N_2 is reduced to ammonia.[5,6,7] The Cu_z site in nitrous oxide reductase contains a Cu_4S center that reduces N_2O to N_2 and H_2O.[8,9,10] Oxidizing metalloenzymes include the Mn_4CaO_4 cluster in the oxygen-evolving complex in Photosystem II[11,12,13,14] and the Cu- and Fe-containing binuclear centers in particulate (pMMO)[15] and soluble (sMMO)[16] methane monooxygenase.

3. Rao, P. V.; Holm, R. H. *Chem. Rev.* **2004**, *104*, 527-560, and references therein.
4. Lippard, S. J.; Berg, J. M. *Principles of Bioinorganic Chemistry*, 1st ed.; University Science Books: Mill Valley, 1994.
5. Peters, J. W.; Stowell, M. H. B.; Soltis, S. M.; Finnegan, M. G.; Johnson, M. K.; Rees, D. C. *Biochemistry* **1997**, *36*, 1181-1187.
6. Mayer, S. M.; Lawson, D. M.; Gormal, C. A.; Roe, S. M.; Smith, B. E. *J. Mol. Biol.* **1999**, *292*, 871-891.
7. Einsle, O.; Tezcan, F. A.; Andrade, S.; A.; Schmid, B.; Yoshida, M.; Howard, J. B.; Rees, D. C. *Science* **2002**, *297*, 1696-1700.
8. Brown, K.; Djnovic-Carugo, K.; Haltia, T.; Cabrito, I.; Saraste, M.; Moura, J. J. G.; Moura, I.; Tegoni, M.; Cambillau, C. *J. Biol. Chem.* **2000**, *275*, 41133-41136.
9. Brown, K.; Tegonia, M.; Prudêncio, M.; Pereira, A. S.; Besson, S.; Moura, J. J.; Moura, I.; Cambillau, C. *Nat. Struct. Biol.* **2000**, *7*, 191-195.
10. Chen, P.; George, S. D.; Cabrito, I.; Antholine, W. E.; Moura, J. G.; Moura, I.; Hedman, B.; Hodgson, K.; Solomon, E. I. *J. Am. Chem. Soc.* **2002**, *124*, 744-745.
11. Nugent, J. H. A.; Rich, A. M.; Evans, M. C. W. *Biochim. Biophys. Acta, Bioenerg.* **2001**, *1503*, 138-146.
12. Ferreira, K. N.; Iverson, T. M.; Maghlaoui, K.; Barber, J.; Iwata, S. *Science* **2004**, *303*, 1831-1838.
13. Iwata, S.; Barber, J. *Curr. Opin. Struct. Biol.* **2004**, *14*, 447-453.
14. Barber, J. *Philos. Trans. R. Soc. London Ser. A* **2007**, *365*, 1007-1023.

Table 1.2. Structure and electronic properties of selected polynuclear cofactors in metalloenzymes

Protein (*function*)	Cluster		Oxidation State	Formal valence
2-Iron ferredoxin (*electron transfer*)	Fe_2S_2	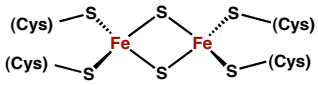	Oxidized Reduced	$2Fe^{III}$ $1Fe^{III}$, $1Fe^{II}$
3-Iron ferredoxin (*electron transfer*)	Fe_3S_4	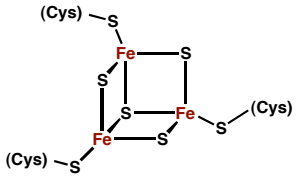	Oxidized Reduced	$3Fe^{III}$ $2Fe^{III}$, $1Fe^{II}$
4-Iron ferredoxin (*electron transfer*)	Fe_4S_4	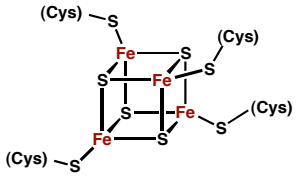	Oxidized Intermediate Reduced	$3Fe^{III}$, $1Fe^{II}$ $2Fe^{III}$, $2Fe^{II}$ $1Fe^{III}$, $3Fe^{II}$
Cu_Z center Nitrous oxide reductase (*reductant*)	Cu_4S	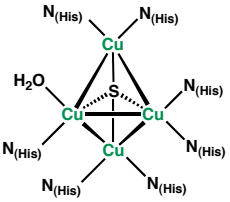	Reduced	$3Cu^{I}$, $1Cu^{II}$
Nitrogenase (*reductant*)	MFe_7S_9C	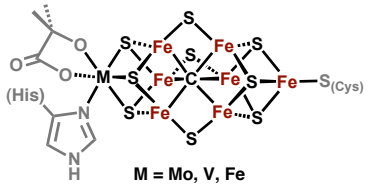 M = Mo, V, Fe	As-isolated (FeMoco)	$1Mo^{III}$, $6Fe^{III}$, $1Fe^{II}$
OEC photosystem II (*oxidant*)	Mn_4CaO_4	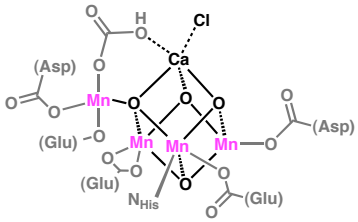	Reduced	$3Mn^{III}$, $1Mn^{IV}$
sMMO (*oxidant*)	Fe_2	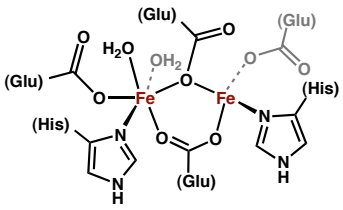	Reduced	$2Fe^{II}$

15. Balasubramanian, R.; Rosenzweig, A. C. *Acc. Chem. Res.* **2007**, *40*, 573-580, and references therein.
16. Baik, M.-H.; Newcomb, M.; Friesner, R. A.; Lippard, S. J. *Chem. Rev.* **2003**, *103*, 2385-2419, and references therein.

With the exception of carbonyl/cyanide supported Fe-only hydrogenases,[17,18,19] nearly all of the metalloenzymes featuring bi- and polynuclear sites operate with open-shell electronic configurations, a result of 3*d* metal centers and weak-field ligand environments composed of amino acid residues and σ- and π-donor ligands such as S^{2-}, N^{3-}, and O^{2-} (Table 1.2). While it is hypothesized that nature uses synergistic interactions between high-spin metal centers in polynuclear metalloenzyme cofactors to activate small molecules, the role M–M interactions play in facilitating redox events is frequently not well understood.[20]

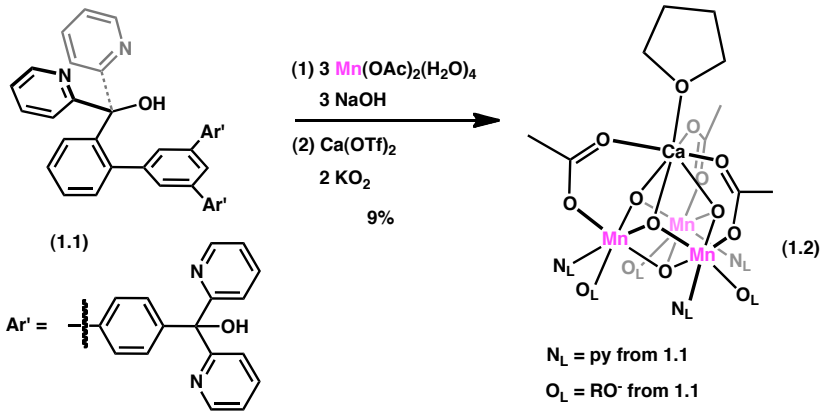

Figure 1.1. Synthetic structural model of the Mn_3CaO_4 center of the OEC in Photosystem II.

Synthetic model clusters of the polynuclear cofactors in metalloenzymes have been targeted both to gain a better understanding of the role individual metal centers play within the assembly, as well as to develop biologically inspired synthetic catalysts. However, synthetic structural models frequently do not exhibit reactivity native to the metalloenzyme. For example, Kanady *et al.* have published the synthesis of a synthetic model of the Mn_3CaO_4 center of the OEC in Photosystem II, supported by a polynucleating ligand platform comprised of a 1,3,5-

17. Peters, J. W.; Lanzilotta, W. N.; Lemon, B. J.; Seefeldt, L. C. *Science* **1998**, *282*, 1853-1858.
18. Nicolet, Y.; Lemon, B. J.; Fontecilla-Camps, J. C.; Peters, J. W. *Trends Biochem. Sci.* **2000**, *25*, 138-143.
19. De Lacey, A. L.; Fernández, V. M. *Chem. Rev.* **2007**, *107*, 4304-4330.
20. Holm, R. H.; Kennepohl, P.; Solomon, E. I. *Chem. Rev.* **1996**, *96*, 2239-2314.

triarylbenzene backbone, six pyridine, and three alcohol groups (**1.1**) (Figure 1.1).[21] Metallation of **1.1** with 3 equivalents of Mn(II) acetate in the presence of base, followed by oxidation of with KO_2 (serving both as an oxidant and O-atom source) in the presence of $Ca(OTf)_2$ results in formation of the $Mn^{IV}_3CaO_4$ cluster (**1.2**) (Figure 1.1). While this cluster structurally resembles a portion of the Mn–O cluster of Photosystem II and features three uncoupled high spin Mn^{IV} centers ($S = 3/2$),[22] it lacks the fourth 'dangling' Mn atom and does not exhibit reactivity inherent to the native metalloenzyme.

1-2. The polynuclear hypothesis

The observation that multi-electron activation of small molecule substrates occurs at polynuclear reaction sites, common to both metalloenzymes and heterogeneous catalysts, has led to the articulation of the polynuclear hypothesis – the idea that the expanded redox reservoir afforded by M–M interactions in polynuclear systems stabilizes multiple oxidation states and facilitates multi-electron transformations. For example, N_2 reduction occurs biologically by the nitrogenase enzymes, which contain FeMo, FeV, or Fe-only polynuclear cofactors,[5,6,7] and abiologically by the high temperature, high pressure combination of hydrogen and nitrogen in the Haber Bosch process, which uses a solid-state Fe-based catalyst.[23] Currently, examples of synthetic clusters that test the viability of polynuclear reaction sites towards effecting multi-electron activation of small molecule substrates are lacking. In the following sections, the reduction of N_2 by biological and abiological systems will be discussed, with focus on polynuclear Fe containing species.

---

21. Kanady, J. S.; Tsui, E. Y.; Day, M. W.; Agapie, T. *Science* **2011**, *333*, 733-736.
22. Kanady, J. S.; Mendoxa-Cortes, J. L.; Tsui, E. Y.; Nielsen, R. J.; Goddard, III, W. A.; Agapie, T. *J. Am. Chem. Soc.* **2013**, *135*, 1073-1082.
23. Smil, V. *Enriching the Earth: Fritz Haber, Carl Bosch, and the Transformation of the World Food Production*, MIT Press: Cambridge, 2001.

1-3. N_2 reduction

Reduction of N_2 to ammonia, a key chemical step in the global biogeochemical nitrogen cycle,[23] requires the transfer of six electrons and six protons. N_2 is an inert, non-polar diatomic molecule with a high triple-bond dissociation energy (225 kcal/mol).[24] While the N–N triple bond dissociation energy is in line with that observed for the C–C triple bond in acetylene (230 kcal/mol),[25] N_2 is more challenging to reduce compared to its isoelectronic counterpart.[26] Therefore, the inertness of N_2 is not solely a result of the N–N triple bond strength. In fact, the key difference between reduction of N_2 and acetylene lies in the first of the three bond dissociation energies. The dissociation energy of the first N–N bond (>100 kcal/mol) accounts for almost half of the total triple bond energy and is nearly double that for the first C–C bond dissociation energy (53 kcal/mol) for acetylene.[26,27]

The high bond dissociation energy associated with cleaving the first N–N bond in N_2 is reflected in the high reduction potential (E_o). Addition of one electron, accompanied by proton transfer would require a strong reducing agent to overcome the large, negative E_o value (Figure 1.2).[27] However, transferring multiple electron/proton equivalents simultaneously circumvents the high overpotential incurred by single electron/proton transfer pathways. For example, reduction of N_2 to hydrazine (coupled transfer of $4e^-$ and $4H^+$) or ammonia (coupled transfer of $6e^-$ and $6H^+$) in aqueous solution exhibits lower redox potentials of –0.36 V and +0.55 V respectively (Figure 1.2).[27] The inertness of N_2 necessitates the use of a catalyst that is either capable of weakening the N–N triple bond and stabilizing intermediates along the reduction pathway, or that could provide access to an alternative reduction pathway.

---

24. Vedeneyev, V. I.; Gurvich, L. V.; Kondrat'yev, V. N.; Medvedev, V. A.; Frankevich, Ye. L. *Bond Energies, Ionization Potentials and Electron Affinities*, St. Martin's Press: New York, 1962.
25. Blanksby, S. J.; Ellison, G. B. *Acc. Chem. Res.* **2003**, *36*, 255-263.
26. Bazhenova, T. A.; Shilov, A. E. *Coord. Chem. Rev.* **1995**, *144*, 69-145.
27. Shilov, A. E. *Russ. Chem. Bull., Int. Ed.* **2003**, *52*, 2555-2562.

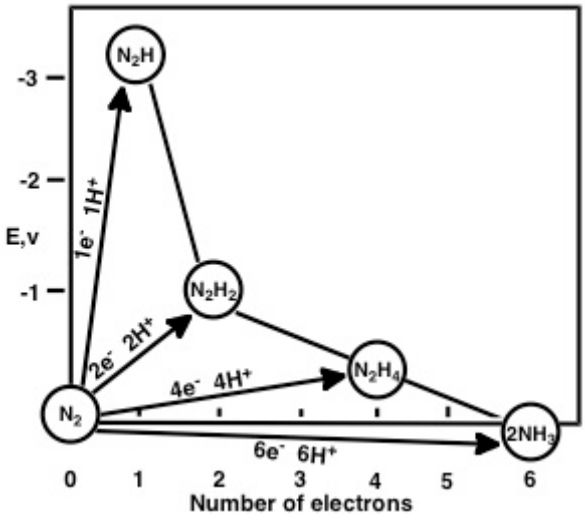

Figure 1.2. Redox potential dependence on the number of electrons/proton equivalents transferred to N_2 in water, referenced to SHE. Reprinted from *Coord. Chem. Rev.*, Vol. 144, Bazhenova, T.A., Shilov, A. E., "Nitrogen Fixation in solution," 69-145, **1995**, with permission from Elsevier.

1-4. Biological N_2 reduction

There are three known nitrogenase enzymes, referred to as Fe-only, FeV-, and FeMo-nitrogenases,[28,29,30] which catalyze the conversion of dinitrogen to ammonia (Equation 1.2).[31,32]

$$N_2 + 8e^- + 16MgATP + 8H^+ \rightarrow 2NH_3 + H_2 + 16MgADP + 16P_i \quad \text{(Eq. 1.2)}$$

The three nitrogenase enzymes differ in metal composition at the cofactor (Table 1.2, *vide supra*). Metal substitution from Fe-only nitrogenase to FeMo- and FeV-based nitrogenases results in significant changes in reactivity.[28,30,33,34] While all three nitrogenases display structurally similar cofactors, they exhibit markedly different catalytic activity (at ambient temperature and pressure, FeMoco has a higher activity toward dinitrogen relative to FeVco and Fe-only nitrogenase[32]) and chemoselectivity (mixed-metal FeMo and FeV cofactors engage

28. Burgess, B. K.; Lowe, D. J. *Chem. Rev.* **1996**, *96*, 2983-3012.
29. Eady, R. R. *Coord. Chem. Rev.* **2003**, *237*, 23-30.
30. Howard, J. B.; Rees, D. C. *Chem. Rev.* **1996**, *96*, 2965-2982.
31. Simpson, F. B.; Burris, R. H. *Science*, **1984**, *224*, 1095-1097.
32. Eady, R. R. *Chem. Rev.* **1996**, *96*, 3013-3030.
33. Dos Santos, P. C.; Igarashi, R. Y.; Lee, J.-I.; Hoffman, B. M.; Seefeldt, L. C.; Dean, D. R. *Acc. Chem. Res.* **2005**, *38*, 208-214.
34. Hoffman, B. M.; Lukoyanov, D.; Dean, D. R.; Seefeldt, L. C. *Acc. Chem. Res.* **2009**, *42*, 609-619.

alternative substrates including CO and ethylene,[35] while Fe-only nitrogenase does not). In this section, the structure of the FeMoco containing nitrogenase and the two proposed mechanisms of N_2 activation will be discussed.

1-4-1. Nitrogenase structure

The most commonly studied form of nitrogenase contains the FeMoco active site and is comprised of two component proteins, the Fe protein (component II or dinitrogenase reductase) and the MoFe protein (component I or dinitrogenase).[28] The Fe protein contains a [4Fe–4S] cluster, which serves as a reductant, transfering electrons one at a time to the MoFe protein.[36,37] Electron transfer from the Fe protein is linked to the hydrolysis of 2MgATP to 2MgADP[36,37] (Eq. 2, *vide supra*) and results in dissociation of the Fe protein from the MoFe protein (Figure 1.3).[38]

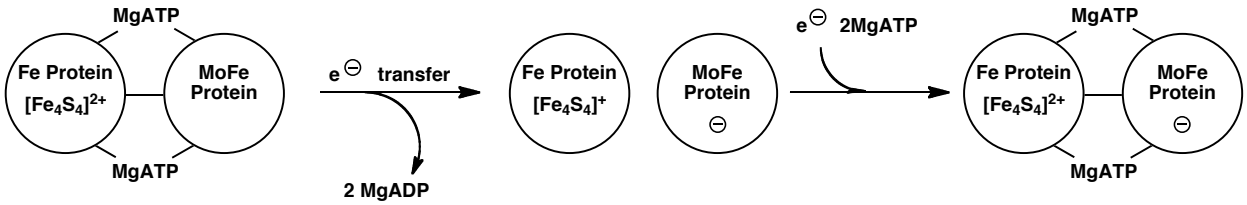

Figure 1.3. Electron transfer from the [4Fe–4S] cluster in the Fe protein to the MoFe protein is linked to the hydrolysis of 2MgATP units. Upon electron transfer, the two component proteins dissociate. Reduction of the [4Fe–4S] cluster and addition of two new MgATP units results in re-association of the Fe and MoFe proteins. The oxidation state of the [4Fe–4S] cluster during electron transfer is still under debate.[39]

Upon dissociation, the Fe protein is reduced to its original oxidation state and the MgADP nucleotides are replaced with MgATP. Eight consecutive association/dissociation events are required to fully reduce N_2 to ammonia. The MoFe protein contains the cofactor known as

35. Hu, Y.; Lee, C. C.; Ribbe, M. W. *Dalton Trans.* **2012,** *41*, 1118-1127.
36. Seefeldt, L. C.; Dean, D. R. *Acc. Chem. Res.* **1997**, *30*, 260-266.
37. Howard, J. B.; Rees, D. C. *Annu. Rev. Biochem.* **1994**, *63*, 235-264.
38. Hageman, R. V.; Burris, R. H. *Proc. Natl. Acad. Sci. USA* **1978**, *75*, 2699-2702.
39. Mitra, D.; George, S. J.; Guo, Y.; Kamali, S.; Keable, S.; Peters, J. W.; Pelmenschikov, V.; Case, D. A.; Cramer, S. P. *J. Am. Chem. Soc.* **2013**, *135*, 2530-2543.

FeMoco,[40,41] where substrate binding and activation occurs, as well as the P-cluster [8Fe–7S], which facilitates electron transfer from the Fe protein to the FeMoco.[42]

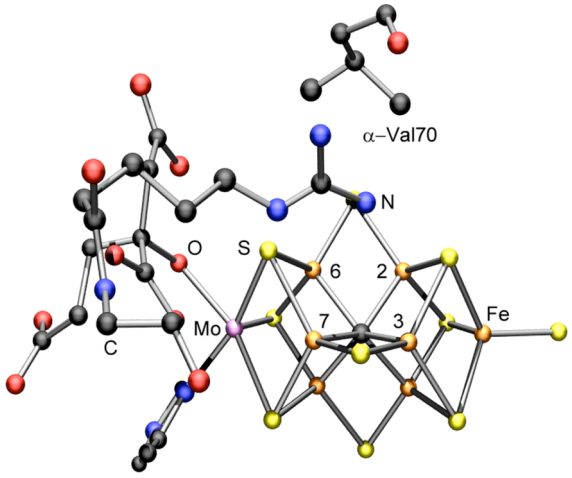

Figure 1.4. Nitrogenase FeMo-cofactor from Spatzal *et al.*[50] (Mo pink, Fe orange, C black, N blue, O red, S yellow) where the α-Val70 residue and Fe(2367) tetrairon face are illustrated.

The X-ray crystal structure of the MoFe containing nitrogenase has been refined as separate protein components[7,43,44,45,46,47] and as the entire enzyme.[48,49] Low resolution data (between 2.8 and 1.6 Å) of the FeMoco was consistent with composition [Mo:7Fe:9S]:homocitrate, which is bound to the protein by two protein residue side chains that are coordinated to Fe and Mo sites located on opposite sides of the cluster.[43,44,45,46,47] In 2002, the MoFe protein was solved at 1.16 Å, which revealed a central ligand X, hypothesized to be N, O, or C (heavier atoms such as S were ruled out by comparing respective resolution dependent

40. Shah, V. K.; Brill, W. J. *Proc. Natl. Acad. Sci. USA* **1977**, *74*, 3249-3253.
41. Hawkes, T. R.; McLean, P. A.; Smith, B. E. *Biochem. J.* **1984**, *217*, 317-321.
42. Chan, J. M.; Christiansen, J.; Dean, D. R.; Seefeldt, L .C. *Biochemistry* **1999**, *38*, 5779-5785.
43. Kim, J.; Rees, D. C. *Nature* **1992**, *360*, 553-560.
44. Chan, M. K.; Kim, J.; Rees, D. C. *Science* **1993**, *260*, 792-794.
45. Jang, S. B.; Seefeldt, L. C.; Peters, J. W. *Biochemistry* **2000**, *39*, 14745-14752.
46. Sorlie, M; Christiansen, J.; Lemon, B. J.; Peters, J. W.; Dean, D. R.; Hales, B. J. *Biochemisry* **2001**, *40*, 1540-1549.
47. Mayer, S. M.; Lawson, D. M.; Gormal, C. A.; Roe, S. M.; Smith, B. E. *J. Mol. Biol.* **1999**, *292*, 871-891.
48. Schindelin, H.; Kisker, C.; Schlessman, J. L.; Howard, J. B.; Rees, D. C. *Nature*, **1997**, *387*, 370-376.
49. Chiu, H.-J.; Peters, J. W.; Lanzilotta, W. N.; Ryle, M. J.; Seefeldt, L. C.; Howard, J. B.; Rees, D. C. *Biochemistry* **2001**, *40*, 641-650.

electron density profiles as well as Fe–X bond metrics[7]) in the FeMo-cofactor. More recently, the X-ray crystal structure of the MoFe protein was solved at 1.0 Å, which confirmed the identity of X as C (Figure 1.4).[50] The X-ray emission spectrum of the FeMoco of nitrogenase also supported the identity of the interstitial atom as C.[51]

1-4-2. Mechanistic hypotheses for N_2 reduction by nitrogenase

While X-ray crystallography provided structural information of the N_2 reduction enzyme, the crystal structure does not explain how N_2 binds and is activated by the FeMoco of nitrogenase. The precise sequence of chemical steps in N_2 fixation by nitrogenase remains elusive and has inspired a great deal of mechanistic investigation, as well as motivated the synthesis of model complexes that catalytically reduce N_2 to ammonia. The results of these studies have led to two hypotheses regarding how N_2 binds and is activated at the FeMoco of nitrogenase: (1) substrate uptake and reduction occurs at a single metal center;[52] or (2) a polynuclear iron face of the cluster mediates all requisite reaction chemistry.[53]

Kinetic studies of the enzyme during N_2 activation led to the formulation of the Lowe-Thorneley (LT) kinetic model for nitrogenase function (Figure 1.5),[28,55,54] which is described in terms of eight states E_n, where n is equal to the number of electrons (and protons) that accumulate within the MoFe protein during turnover (n = 1 – 8). Each electron transfer from the Fe protein to the MoFe protein involves a nucleotide-dependent association and dissociation of the two proteins and is the rate-limiting step of substrate reduction. Several complicating factors have hindered progress towards understanding how N_2 interacts with the active site of the

50. Spatzal, T.; Aksoyoglu, M.; Zhang, L.; Andrade, S. L. A.; Schleicher, E.; Weber, S.; Rees, D. C.; Einsle, O. *Science* **2011**, *334*, 940.
51. Lancaster, K. M.; Roemelt, M.; Ettenhuber, P.; Hu, Y.; Ribbe, M. W.; Neese, F.; Bergmann, U.; DeBeer, S. *Science* **2011**, *334*, 974-977.
52. Pickett, C. J. *J. Biol. Inorg. Chem.* **1996**, *1*, 601–606.
53. Seefeldt, L. C.; Dance, I. G.; Dean, D. R. *Biochemistry* **2004**, *43*, 1401-1409.
54. Wilson, P. E.; Nyborg, A. C.; Watt, G. D. *Biophys. Chem.* **2001**, *91*, 281-304.

enzyme.[53] For example, N_2 does not bind to the resting state of the native protein. Instead, N_2 engages with the FeMoco only under "turnover" conditions, when three or more proton and electron equivalents have accumulated within the MoFe protein (Figure 1.5).[55] While the FeMoco has an EPR signal in the absence of substrate, the signature disappears during turnover resulting in EPR-silent states.[56,57]

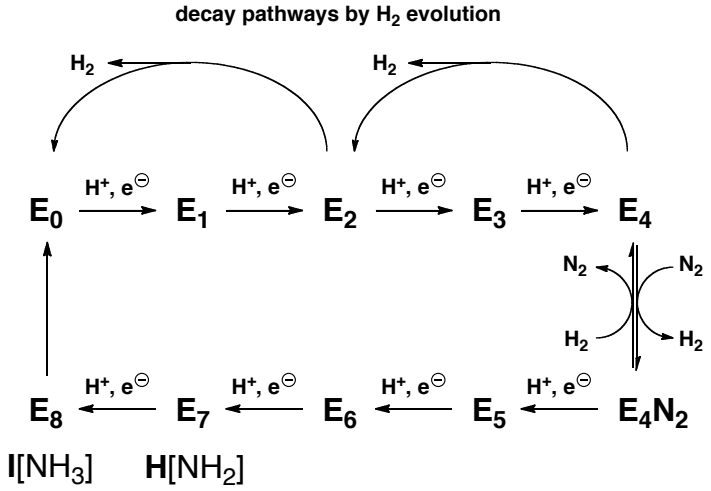

Figure 1.5. A simplified depiction of the Lowe-Thorneley (LT) kinetic model for N_2 fixation by nitrogenase.[34] Highlighted above: (1) eight concerted H^+/e^- transfer steps traversing eight E_n states, (2) possible decay pathways by H_2 evolution, (3) N_2 binding and H_2 generation at the E_4 state, and (4) freeze-trapped intermediates **I** and **H** isolated during hydrazine and diazene reduction by the mutated enzyme (*vide infra*).

Two proposed mechanistic pathways for N_2 fixation by the MoFe protein have emerged: distal (**D**, more commonly known as the Chatt mechanism) and alternating (**A**) pathways (Figure 1.6). The **D** pathway, proposed to occur at the Mo center of FeMoco,[58] results in hydrogenation of a single N of N_2 to liberate one equivalent of NH_3 prior to hydrogenation of the second N center. In the **A** pathway, suggested to involve one or more Fe centers of the FeMoco,[59] the two

55. Thorneley, R. N. F.; Lowe, D. J. Kinetics and mechanisms of the nitrogenase enzyme system. In *Molybdenum Enzymes*; Spiro, T. G., Ed.; Wiley: New York, 1985; p 221-284.
56. Zimmerman, R.; Münick, E.; Brill, W. J.; Shah, V. K.; Henzl, M. T.; Rawlings, J.; Orme-Johnson, W. H. *Biochim. Biophys. Acta* **1978**, *537*, 185-207.
57. Benton, P. M. C.; Laryukhin, M.; Mayer, S. M.; Hoffman, B. M.; Dean, D. R.; Seefeldt, L. C. *Biochemistry* **2003**, *42*, 9102-9109.
58. Kastner, J.; Biochi, P. E. *J. Am. Chem. Soc.* **2007**, *129*, 2998-3006.
59. Hinnemann, B.; Norskov, J. K. *Top. Catal.* **2005**, *38*, 955-962.

N's are protonated in an alternating fashion. As a result two proposed intermediates include diazine and hydrazine-bound states in the **A** pathway. Mechanistic evidence for N_2 reduction by nitrogenase has come from reaction studies with non-native nitrogenase substrates and inhibitors, as well as investigations with residue modified nitrogenases.

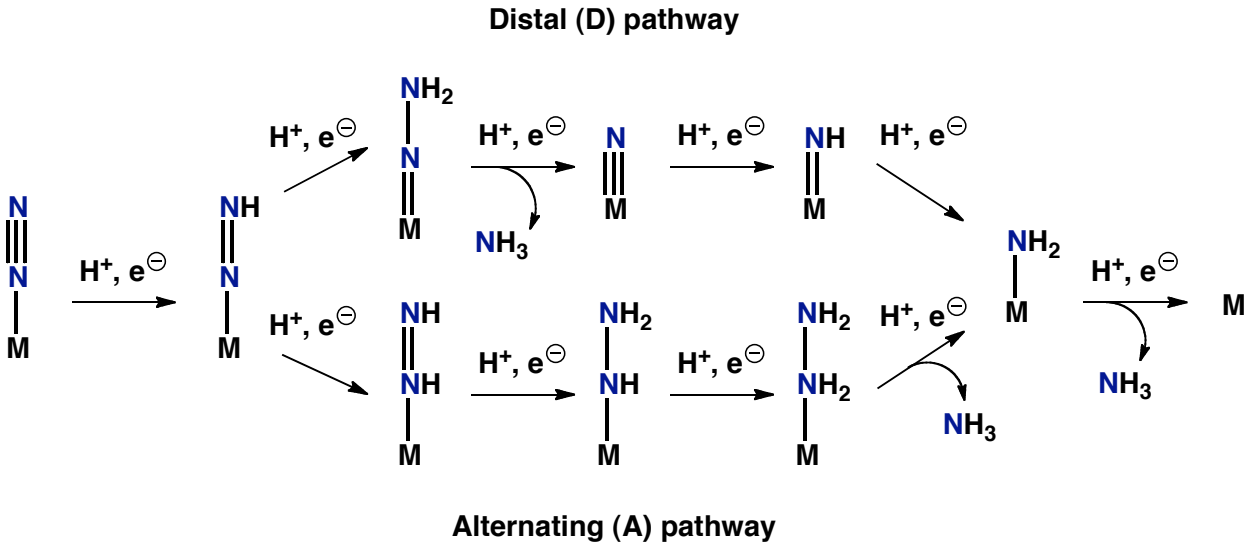

Figure 1.6. Two proposed mechanistic pathways for N_2 reduction by nitrogenase: distal (**D**) pathway and alternating (**A**) pathway.

1-4-3. The Mo hypothesis

The hypothesis that the Mo center in nitrogenase plays a significant role in substrate binding and activation was formulated based in part on the discovery of synthetic inorganic N_2-fixing Mo complexes including work from Pickett,[52,60] Coucouvanis,[61,62] Shrock,[63,64] and Cummins.[65,66,67] In the FeMoco of nitrogenase, the Mo center is coordinatively saturated in the resting state. Therefore, for Mo to serve as the site for binding and activation of N_2, one or more

60. Pickett, C. J. & Talarmin, J. Electrosynthesis of ammonia. *Nature* **1985**, *317*, 652–653.
61. Demadis, K. D.; Malinkak, S. M.; Coucouvanis, D. *Inorg. Chem.* **1995**, *35*, 4038-4046.
62. Malinak, S. M.; Coucouvanis, D. *Prog. Inorg. Chem.* **2001**, *49*, 599-662.
63. Yandulov, D. V.; Schrock, R. R. *Science* **2003**, *301*, 76–78.
64. Schrock, R. R. *Chem. Commun.* **2003**, 2389-2391.
65. Laplaza, C. E.; Cummins, C. C. *Science*, **1995**, *268*, 861-863.
66. Laplaza, C. E.; Johnson, M. J. A.; Peters, J. C.; Odom, A. L.; Kim, E.; Cummins, C. C.; George, G. N.; Pickering, I. J. *J. Am. Chem. Soc.* **1996**, *118,* 8623-8638.
67. Curley, J. J.; Cook, T. R.; Reece, S. Y.; Müller, P.; Cummins, C. *J. Am. Chem. Soc.* **2008**, *130,* 9394-9405.

of the ligands bound to Mo in the resting state of the protein must dissociate. Ligand modification at the Mo center has been shown to have a significant impact on the reactivity toward N_2 binding and/or reduction[68,69,70] as well as chemoselectivity[71] of the FeMo cofactor. For example, substitution of the (*R*)-homocitrate bound to Mo in the FeMoco with citrate alters the catalytic properties of the enzyme.[68] While non-native substrates of nitrogenase including proton and acetylene reduction is enhanced by this ligand substitution, the level of N_2 reduction by the mutated enzyme is significantly lower relative to the wild-type.

1-4-4. The Fe hypothesis

Alternatively, N_2 could bind to the central Fe atom(s) of the FeMoco of nitrogenase. While previous research efforts have focused on structural iron-sulfur cluster models of the nitrogenase cofactor,[72,73,74,75,76,77] support for Fe atom involvement in N_2-fixation by nitrogenase has emerged mainly from studies with substrates or inhibitors of the nitrogenase enzyme, as well as investigation of residue modified nitrogenases.

Freeze-trapping the MoFe protein during turnover in the presence of CO, an inhibitor to N_2 reduction,[78] results in a new EPR signal.[79] ENDOR spectroscopy of ^{13}CO- and ^{57}Fe-labeled FeMoco was found to be consistent with CO binding end-on to the Fe atom(s) in the

68. Mayer, S. M.; Cormal, C. A.; Smith, B. E.; Lawson, D. M. *J. Biol. Chem.* **2002**, *120*, 10613-10621.
69. Imperial, J.; Hoover, T. R.; Madden, M. S.; Ludden, P. W.; Shah, V. K. *Biochemistry*, **1989**, *28*, 7796-7799.
70. Scott, D. J.; Dean, D. R.; Newton, W. E. *J. Biol. Chem.* **1992**, *267*, 20002-20010.
71. Gronberg, K. L. C.; Gormal, C. A.; Durrant, M. C.; Smith, B. E.; Henderson. R. A. *J. Am. Chem. Soc.* **1998**, *120*, 10613-10621.
72. Coucouvanis, D. *Acc. Chem. Res.* **1981**, *14*, 201-209.
73. Müller, A.; Diemann, E.; Jostes, R.; Bögge, H. *Angew. Chem., Int. Ed. Engl.* **1981**, *20*, 934-955.
74. Coucouvanis, D. *Acc. Chem. Res.* **1991**, *24*, 1-8.
75. Bienert, H.; Holm, R. H.; Münck, E. *Science* **1997**, *277*, 653-659.
76. Malinak, S. M.; Coucouvanis, D. *Prog. Inorg. Chem.* **2001**, *49*, 592.
77. Lee, S. C.; Holm, R. H. *Chem. Rev.* **2004**, *104*, 1135–1158.
78. Hwang, J. C.; Chen, C. H.; Burris, R. H. *Biochim. Biophys. Acta* **1973**, *292*, 256-270.
79. Davis, L. C.; Henzl, M. T.; Burris, R. H.; Orme-Johnson, W. H. *Biochemistry* **1979**, *18*, 4860-4869.

cofactor,[80,81] suggesting that CO inhibits N_2 reduction by occupying one or more of the substrate binding sites. Analogous experiments were conducted on freeze-trapped states of the MoFe protein during turnover in the presence of acetylene[82,83] and CS_2.[84] Based on EPR and ENDOR spectroscopy, those non-native substrates were also hypothesized to bind via C to one or more Fe atoms within the FeMoco. While these initial reports indicated that inhibitors and alternative substrates coordinate to Fe centers within the FeMoco, it was not clear how these results were related to the wild type N_2 reduction activity.

More recently, studies involving modification of the protein residue α-70^{Val} near the FeMoco has suggested that one of the [4Fe–4S] faces serves as the site of substrate binding. While nitrogenase can reduce alternative small molecule substrates featuring triple bonds (i.e. reduction of acetylene to ethylene), larger alkynes are poor substrates because they have greater difficulty reaching the active site of the MoFe protein.[85] However, substitution of the α-70^{Val} residue, which sits above the Fe2, Fe3, Fe6, Fe7 face of the FeMoco (Figure 1.4, *vide supra*), for smaller amino acids such as alanine (Ala) or glycine (Gly) side chains leads to mutant nitrogenase enzymes that are capable of reducing larger alkynes including propyne, propargyl alcohol, and 1-butyne.[86] Binding of propargyl alcohol inhibits reduction of both N_2 and protons and exhibits a freeze-trapped intermediate that is EPR active.[87] ENDOR spectroscopy of isotopically substituted (^{13}C, $^{1,2}H$) freeze-trapped propargyl alcohol bound to the FeMoco lead to

80. Lee, H. I.; Cameron, L. M.; Hales, B. J.; Hoffman, B. M. *J. Am. Chem. Soc.* **1997**, *119*, 10121-10126.
81. Christie, P. D.; Lee, H. I.; Cameron, L. M.; Hales, B. J. *J. Am. Chem. Soc.* **1996**, *118*, 8707-8709.
82. Lee, H. I.; Sorlie, M.; Christiansen, J.; Song, R.; Dean, D. R.; Hales, B. J.; Hoffman, B. M. *J. Am. Chem. Soc.* **2000**, *122*, 5582-5587.
83. Sorle, M.; Christiansen, J.; Dean, D. R.; Hales, B. J. *J. Am. Chem. Soc.* **1999**, *121*, 9457-9458.
84. Ryle, M. J.; Lee, H. I.; Seefeldt, L. C.; Hoffman, B. M. *Biochemistry* **2000**, *39*, 1114-1119.
85. Burgess, B. J. Substrate reactions of nitrogenase. In *Metal ions in biology: molybdenum enzymes*; Spiro, T. G. Ed.; John Wiley and Sons: New York, 1985; p 161-220.
86. Mayer, S. M.; Niehaus, W. G.; Dean, D. R. *J. Chem. Soc., Dalton Trans.* **2002**, 802-807.
87. Benton, P. M. C.; Laryukhin, M.; Mayer, S. M.; Hoffman, B. M.; Dean, D. R.; Seefeldt, L. C. *Biochemistry* **2003**, *42*, 9102-9109.

the first description of a trapped nitrogenase reduction intermediate, where the alkene product is proposed to bind side-on to a single Fe ion at a [4Fe–4S] face of the FeMoco (Figure 1.7).[88]

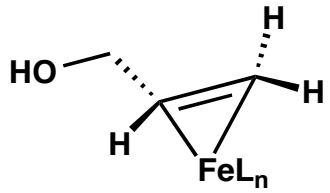

Figure 1.7. During reduction of propargyl alcohol by the α-70^{Ala} mutated MoFe protein, an allyl alcohol bound intermediate was freeze trapped. It was hypothesized that H-bonding between the –OH group and the α-195^{His} residue stabilized the intermediate. The specific Fe center (FeL_n) in the FeMoco that is coordinated to substrate is unknown.

Substitution of the valine α-70 side chain for larger amino acids such as isoleucine (Ile) significantly diminishes the ability of nitrogenase to reduce both N_2 and acetylene relative to the wild-type MoFe protein, while maintaining normal proton reduction activity.[89] This result suggests that both N_2 and acetylene may need to access the same [4Fe–4S] face during substrate reduction.

Studies on substrate activation by α-70^{Ala}/α-195^{Gln} mutated MoFe protein has shed light on several proposed intermediates during N_2 reduction. For example, while hydrazine (an intermediate evoked in the **A** pathway) is a poor substrate for the wild-type MoFe protein,[28,90,91] substitution of the valine α-70 residue for a smaller side chain such as alanine improves the ability of the MoFe protein to reduce N_2H_4 to yield ammonia.[89] Mutagenisis of a second residue (α-196^{His} to α-196^{Gln}, located near the same [4Fe–4S] face as α-70^{Val}) limits the delivery of protons during substrate reduction, thereby enabling the trapping of intermediates (intermediates

88. Lee, H.-I.; Igarashi, R. Y.; Laryukhin, M.; Doan, P. E.; Dos Santos, P. C.; Dean, D. R.; Seefeldt, L. C.; Hoffman, B. M. *J. Am. Chem. Soc.* **2004**, *126*, 9563-9569.
89. Barney, B. M.; Igarashi, R. Y.; Dos Santos, P. C.; Dean, D. R.; Seefeldt, L. C. *J. Biol. Chem.* **2004**, *279*, 53621-53624.
90. Thorneley, R. N. F.; Eady, R. R.; Lowe, D. J. *Nature* **1978**, *272*, 557-558.
91. Davis, L. C. *Arch. Biochem. Biophys.* **1980**, *204*, 270-276.

I and **H**) during hydrazine reduction.[92,93,94] Identical intermediates have also been trapped during reduction of diazene (an equally competent substrate of the wild-type enzyme relative to N_2) by α-70^{Ala}/α-196^{Gln} mutated MoFe protein.[95] Thus, both diazene and hydrazine enter the N_2 reduction pathway and arrive at the same intermediate states.

Advanced EPR, ENDOR, and ESEEM spectroscopic experiments led to the assignment of intermediates **I** and **H** in the LT kinetic model (Figure 1.5, *vide supra*). A combination of X/Q-band EPR and ^{15}N,$^{1,2}H$ pulsed ENDOR measurements showed that **I** represents a late-stage of nitrogen fixation where the N–N bond has been cleaved and one equivalent of ammonia has been released.[96] The metal atom(s) of the FeMoco in intermediate **I** are bound to a single nitrogen atom from a substrate-derived [NH_x] (x = 2 or 3) unit. Q-band CW EPR and ^{95}Mo ESEEM spectroscopy, revealed that intermediate **H** represents an integer-spin ($S \geq 2$) trapped state during reduction of hydrazine or diazene by the α-70^{Ala}/α-196^{Gln} MoFe protein.[94] Intermediate **H** also represents a N–N cleaved product where a [NH_x] (x = 2, based on quadrupole coupling parameters) unit is bound metal atom(s) in the FeMoco. If intermediate **H** represents a [NH_2] bound intermediate (E_7 in the LT kinetic model), intermediate **I** must represent the last E_n state (n = 8), where [NH_3] is bound to the FeMoco (Figure 1.5, *vide supra*).

The site mutagensis studies described above provided the first insight into trapped intermediates that may be involved in N_2 reduction by the MoFe protein. While **H**[NH_2] and **I**[NH_3] intermediates are present in both **A** and **D** mechanisms, the fact that both diazene and

92. Barney, B. M.; Yang, T.-C.; Igarashi, R. Y.; Dos Santos, P. C.; Laryukhin, M.; Lee, H.-I.; Hoffman, B. M.; Dean, D. R.; Seefeldt, L. C. *J. Am. Chem. Soc.* **2005**, *127*, 14960-14961.
93. Barney, B. M.; Laryukhin, M.; Igarashi, R. Y.; Lee, H.-I.; Dos Santos, P. C. D.; Yang, T.-C. *Biochemistry* **2005**, *44*, 8030-8037.
94. Lukoyanov, D.; Yang, Z.-Y.; Barney, B. M.; Dean, D. R.; Seefeldt, L. C.; Hoffman, B. M. *Proc. Natl. Acad. Sci.* **2012**, *109*, 5583-5587.
95. Barney, B. M.; McClead, J.; Lukoyanov, D.; Laryukhin, M.; Yang, T. C.; Hoffman, B. M.; Dean, D. R.; Seefeldt, L. C. *Biochemistry* **2007**, *46*, 6784-6794.
96. Lukoyanov, D.; Dikanov, S. A.; Yang, Z.-Y.; Barney, B. M.; Samoilova, R. I.; Narasimhulu, K. V.; Dean, D. R.; Seefeldt, L. C.; Hoffman, B. M. *J. Am. Chem. Soc.* **2011**, *133*, 11655-11664.

hydrazine can be reduced by the native enzyme[28,90,91,95] suggests that pathway **A** is operative. Therefore, the two intermediates have been assigned as the E_7 and E_8 states, respectively, in the LT kinetic model (Figure 1.5, *vide supra*).[94,97] Additional support of N_2 reduction by the **A** pathway comes from the fact that (1) hydrazine is isolated following acid-quenching of the wild-type MoFe protein during turnover conditions in the presence of N_2[98] and (2) hydrazine is a minor product of N_2 reduction by vanadium-dependent nitrogenase.[99]

1-5. Abiological reduction of N_2 by Fe

1-5-1. Heterogeneous N_2 reduction

In 2004, approximately 130 million tons of ammonia were generated globally through the Haber Bosch process, which uses a Fe-based catalyst to reduce N_2 with H_2 (Eq. 1.3).[23]

$$N_2 + >150 \text{ bar } H_2 \xrightarrow{[Fe]\ \Delta} 2NH_3 \qquad \text{(Eq. 1.3)}$$

The turnover-limiting step of the Haber Bosch process is hypothesized to involve cleavage of the N–N triple bond to generate chemisorbed surface nitrides,[100] which has led to studies aimed at understanding how N_2 and N atoms interact with metal surfaces. Specifically, three single-crystal Fe planes including Fe(100), Fe(111), and Fe(110), have been used to model the adsorption of N_2 on surfaces. Ultraviolet photoelectron spectroscopy, in conjunction with $^{14}N_2$ and $^{15}N_2$ labeling experiments provided the first evidence of surface-bound nitrides to the three Fe planes.[101,102] In the case of chemisorbed N on the Fe(110) surface, it is hypothesized that the surface-bound

97. Hoffman, B. M.; Lukoyanov, D.; Dean, D. R.; Seefeldt, L. C. *Acc. Chem. Res.* **2013**, *46*, 587-595.
98. Thorneley, R. N. F.; Eady, R. R.; Lowe, D. J. *Nature* **1978**, *272*, 557-558.
99. Dilworth, M. J.; Eady, R. R.; *Biochem. J.* **1991**, *277*, 465-468.
100. Ertl, G. *Catalysis Sci. Rev.* **1980**, *21*, 201-223.
101. Bozso, F.; Ertl, G.; Grunze, M.; Weiss, M. *J. Catal.* **1977**, *49*, 18-41.
102. Bozso, F.; Ertl, G.; Weiss, M. *J. Catal.* **1977**, *50*, 519-529.

nitrides coordinate to four Fe centers in a 4-fold symmetric site on the metal surface (Figure 1.8A).[101,103]

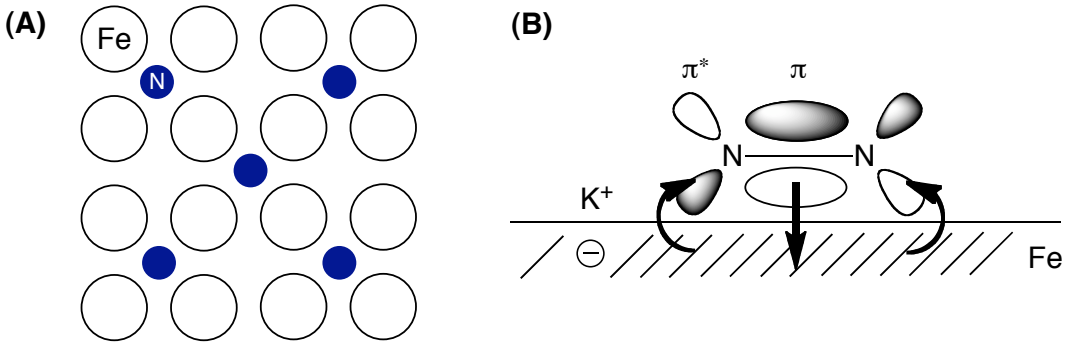

Figure 1.8. (A) Proposed Fe_4N bonding model of chemisorbed nitrides on the Fe(110) surface. White circles represent Fe sites and blue circles represent N atoms. Reprinted from *J. Cataly.* Vol. 49, Bozso, F., Ertl, G., Grunze, M., Weiss, M. "Interaction of nitrogen with iron surfaces: I. Fe(100) and Fe(111)," 519-529, **1977**, with permission from Elsevier. (B) Weakening of the N–N bond by both $\pi \rightarrow d$ and $d \rightarrow \pi^*$ interactions. K atoms enhances $d \rightarrow \pi^*$ back donation by donating valence electrons to the Fe atoms on the surface. Reprinted from *Surface Sci.* Vol. 155, Tsai, M.-C., Ship, U., Bassignana, I. C., Küppers, J., Ertl, G., "A vibrational spectroscopy study on the interaction of N_2 with clean and K-promoted Fe(111) surfaces: π-bonded dinitrogen as precursor for dissociation," 387-399, **1985**, with permission from Elsevier.

In 1977, Ertl and coworkers observed that chemisorption of N_2 decreases with an increase in Fe packing density [relative rates of N_2 activation, Fe(100) < Fe(110) < Fe(111); relative Fe packing density (inverse with respect to number of exposed Fe sites, Fe(100) having the least exposed sites), Fe(100) > Fe(110) > Fe(111)].[101,102] Previously, Ruch had proposed that the empty metal-based orbitals in C_7 sites (locations with 7 adjacent Fe atoms) exposed on the Fe(111) surface could form bonding interactions with the filled π bonds of N_2, thereby weakening the N–N bond and promoting hydrogenation.[101] While no such intermediate has been directly observed spectroscopically, Ertl and coworkers did successfully obtain vibrational spectra of N_2 bound to the Fe(111) plane, which exhibits low N–N stretching frequencies determined by EELS ($^{14}N_2$: 1555 cm^{-1}; $^{15}N_2$: 1490 cm^{-1}; free N_2: 2331 cm^{-1}).[104] The observed N–

103. Jack, K. H. *Proc. Roy. Soc. (London) A* **1948**, *195*, 34-40.
104. Tsai, M.-C.; Seip, U.; Bassignana, I. C.; Küppers, J.; Ertl, G. *Surface Sci.* **1985**, *155*, 387-399.

N stretching frequencies are consistent with vibrational data obtained for crystallographically characterized side-on bound Ti_4– ($^{14}N_2$: 1282 cm^{-1})[105] and Ni_2–N_2 ($^{14}N_2$: <1500 cm^{-1})[106,107] complexes, suggesting that N_2 coordinates to multiple Fe ions on the surface in a side-on bridging fashion.

The most common Fe catalyst used in the Haber Bosch process, developed by Mittasch in 1910,[108] contains K additives, which lowers the activation barrier for N–N dissociation yielding surface bound nitrides.[109] This observation is reflected in surface vibrational data, which demonstrated that the N–N stretching frequency shifts to lower energies ($^{15}N_2$: 1415-1370 cm^{-1}) with increasing K pre-coverage relative to clean Fe(111) surfaces.[104] It was hypothesized that the K atoms on the surface weaken the N–N bond by donating their valence electrons to the Fe surface atoms resulting in increased $d \rightarrow \pi^*$ back-donation (Figure 1.8B).

1-5-2. Homogeneous N_2 reduction

Numerous research programs have been directed to the synthesis of homogeneous Fe containing complexes to study the ability of Fe to mediate N_2 reduction. Monomeric and dimeric Fe compounds with a range of oxidation states (0–II) have been shown to form N_2 adducts.[110,111] However, there are few examples in which these synthetic Fe compounds facilitate N_2 reduction to yield ammonia, [112,113,114,115] none of which have yields or efficiencies comparable to the Haber Bosch process.

---

105. Pez, G. P.; Apgar, P.; Crissey, R. K. *J. Am. Chem. Soc.* **1982**, *104*, 482-490.
106. Jonas, K. *Angew. Chem., Int. Ed.* **1973**, *12*, 997-998.
107. Krüger, C.; Tsay, Y. H. *Angew. Chem., Int. Ed.* **1973**, *12*, 998-999.
108. A. Mittasch, *Geschichte der Ammoniaksynthase.* Verlag Chemie: Weinheim, 1951.
109. Ertl, G.; Lee, S. B.; Weiss, M. *Surface Sci.* **1982**, *114*, 527-545.
110. Hazari, N. *Chem. Soc. Rev.* **2010**, *39*, 4044-4056, and references therein.
111. Crossland, J. L.; Tyler, D. R. *Coord. Chem. Rev.* **2010**, *254*, 1883-1894, and references therein.
112. Schrauzer, G. N.; Guth, T. D. *J. Am. Chem. Soc.* **1976**, *98*, 3508-3513.
113. George, T. A.; Rose, D. J.; Chang, Y.; Chen, Q.; Zubieta, J. *Inorg. Chem.* **1995**, *34*, 1295-1298.
114. Gilbertson, J. D.; Szymczak, N. K.; Tyler, D. R. *J. Am. Chem. Soc.* **2005**, *127*, 10184-10185.

In 2011, Holland and coworkers reported N_2 reduction by a homogeneous Fe system,[115] which was inspired by K-mediated Fe-surface catalyzed reduction of N_2.[104] Holland has targeted the synthesis of low-coordinate Fe(II) β-diketiminate complexes that feature low-valent Fe centers (Figure 1.9). Reduction of Fe(II) complex **1.3** with potassium graphite in a N_2 atmosphere resulted in full N–N bond scission to yield an Fe–potassium system featuring two nitride (N^{3-}) ligands and an overall $Fe_3(N)_2$ core (**1.4**) (Figure 1.9). Isolation of the nitride complex demonstrated that K^+ cations played a role in stabilizing the reduction product. Addition of H_2 to **1.4** liberates ammonia in a 42 ± 2% yield, resulting in formation of a $Fe_2(H)_2$ complex (**1.5**) (Figure 1.9).

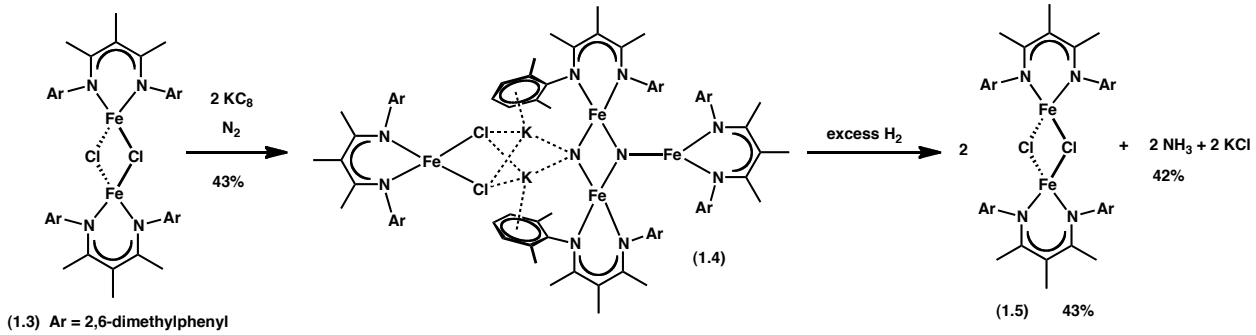

Figure 1.9. $Fe_3(N)_2$ β-diketiminate complex (**1.4**) formed by reductive cleavage of N_2. Addition of excess H_2 results in generation of a $Fe_2(H)_2$ complex (**1.5**) with liberation of ammonia.

The study of N–N bond cleavage in $R_2N–NR_2$ and RN=NR substrates by synthetic Fe compounds has been studied due to the proposed relevance of these reactions to understanding N_2 fixation by nitrogenase. Several groups have explored Fe coordination chemistry with reduced N_2 species including diazenes and hydrazines, proposed intermediates of N_2 reduction by nitrogenase following the **A** pathway.[58] Sellmann, one of the pioneers of Fe stabilized N_xH_y substrates, focused on the development of Fe complexes featuring multidentate organosulfur ligand scaffolds to stabilize and characterize proposed intermediates in the N_2 reduction pathway

115. Rodriguez, M. M.; Bill, E.; Brennessel, W. W.; Holland, P. L. *Science* **2011**, *334*, 780-783.

by nitrogenase enzymes. Bridging diazene complexes bound to Fe–S compounds (**1.7** and **1.9**) were prepared either by oxidation of a monomeric Fe hydrazine complex (**1.6** and **1.8**) with O_2 or by trapping diazene gas generated *in situ* (Figure 1.10).[116,117,118] The work by Sellman demonstrated that Fe–S compounds can stabilize reduced N_2 substrates including diazene, which is extremely unstable and decomposes at temperatures as low as –180 ^{o}C.[95]

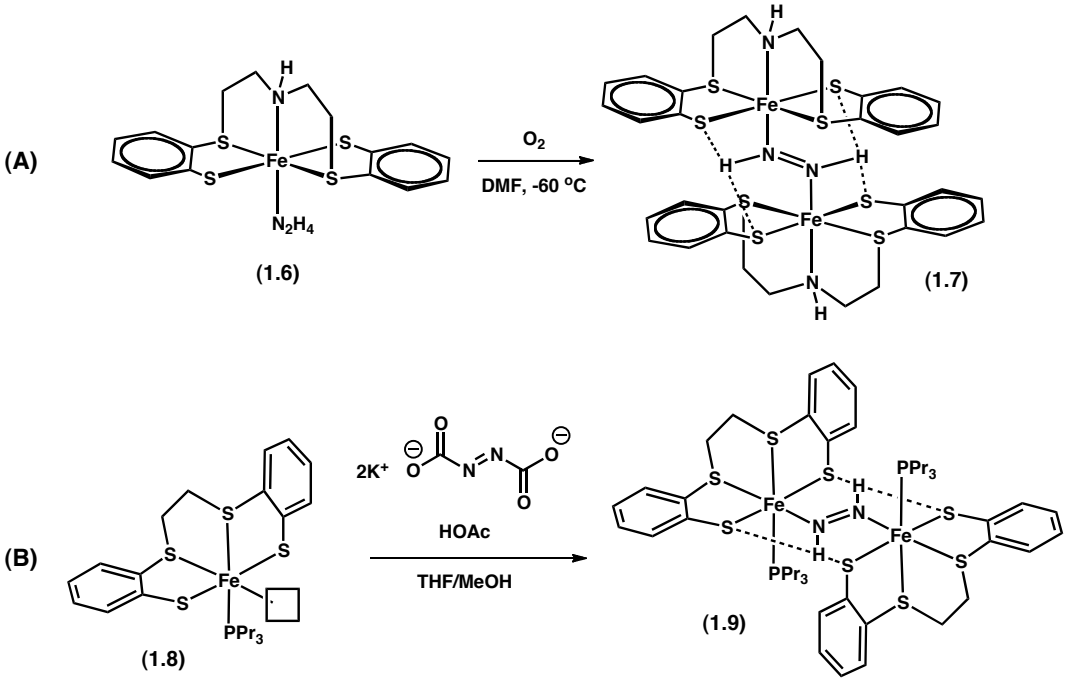

Figure 1.10. Bridging diazene complexes with Fe supported by S–based ligand platforms synthesized by (A) oxidation of Fe–N_2H_4 adduct and (B) *in situ* generation of N_2H_2.

While other groups, including work from Peters,[119,120,121] Tyler,[122,123,124] Field,[125,126] Holland,[127,128,129,130,131] and others,[132,133,134,135] have focused on mononuclear and binuclear Fe

116. Sellmann, D.; Soglowek, W.; Knoch, F.; Moll, M. *Angew. Chem., Int. Ed.* **1989**, *28*, 1271-1272.
117. Sellmann, D.; Soglowek, W.; Knoch, F.; Ritter, G.; Dengler, J. *Inorg. Chem.* **1992**, *31*, 3711-3717.
118. Sellmann, D.; Hennige, A. *Angew. Chem., Int. Ed.* **1997**, *36*, 276-278.
119. Mankad, N. P.; Wited, M. T.; Peters, J. C. *Angew. Chem., Int. Ed.* **2007**, *46*, 5768-5771.
120. Saouma, C. T.; Müller, P.; Peters, J. C. *J. Am. Chem. Soc.* **2009**, *131*, 10358-10359.
121. Lee, Y.; Mankad, N. P.; Peters, J. C. *Nat. Chem.* **2010**, 558-565.
122. Crossland, J. L.; Zakharov, L. N.; Tyler, D. R. *Inorg. Chem.* **2007**, *46*, 10476-10478.
123. Yelle, R. B.; Crossland, J. L.; Szymczak, N. K.; Tyler, D. R. *Inorg. Chem.* **2009**, *48,* 861-871.
124. Crossland, J. L.; Balesdent, C. G.; Tyler, D. R. *Dalton Trans.* **2009**, 4420-4422.
125. Field, L. D.; Li, H.-L.; Dalgarno, S. J.; Turner, P. *Chem. Commun.* **2008**, 1680-1682.
126. Field, L. D.; Li, H.-L.; Magill, A. M. *Inorg. Chem.* **2009**, *48*, 5-7.

systems that stabilize and activate N_xH_y and N_xR_y type-substrates, there are fewer examples that demonstrate polynuclear Fe complexes facilitating N–N cleavage of reduced dinitrogen species. Lee and coworkers recently demonstrated assembly of high-spin Fe(III)-arylimide thiolate cubane clusters (**1.12**) via reductive N–N bond cleavage of 1,2-diarylhydrazines by Fe(II) amide thiolates (**1.10**) (Figure 1.11).[136,137] While the resulting product has a nuclearity >2, N–N bond scission was proposed to go through a μ:η^2,η^2-hydrazide-bridged Fe dimer (**1.11**).

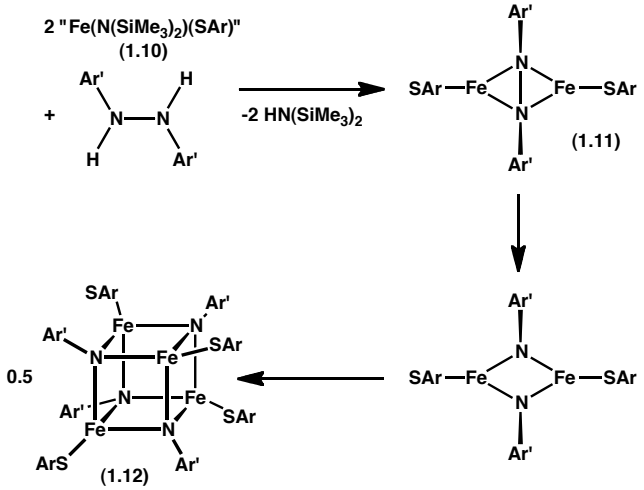

Figure 1.11. Proposed mechanistic pathway during synthesis of high-spin Fe(III)-arylimide thiolate cubane clusters by reductive cleavage of N–N bonds in 1,2-diarylhydrazines.

Low-valent metal carbonyl clusters have been investigated as potential models for M-based heterogeneous catalysts.[138] The N=N bond of azoalkanes can be thermolytically cleaved by low-valent trinuclear Fe carbonyl clusters to yield two imido units $Fe_3(CO)_9(\mu^3\text{-}NR)_2$ (**1.13**)

127. Yu, Y.; Brennessel, W. W.; Holland, P. L. *Organometallics* **2007**, *26*, 3217-3226.
128. Smith, J. M.; Lachicotte, R. J.; Holland, P. L. *J. Am. Chem. Soc.* **2003**, *125*, 15752-15753.
129. Vela, J.; Stoian, S.; Flaschenriem, C. J.; Münck, E.; Holland, P. L. *J. Chem. Soc.* **2004**, *126*, 4522-4523.
130. Yu, Y.; Brennessel, W. W.; Holland, P. L. *Organometallics* **2007**, *26*, 3217-3226.
131. Sadique, A. R.; Gregory, E. A.; Brennessel, W.W.; Holland, P. L. *J. Am. Chem. Soc.* **2007**, *129*, 8112-8121.
132. Kabir, S. E.; Ruf, M.; Vahrenkamp, H. *J. Organomet. Chem.* **1998**, *571*, 91-96.
133. Ohki, Y.; Takikawa, Y.; Hatanaka, T.; Tatsumi, K. *Organometallics* **2006**, *25*, 3111-3113.
134. Chen, Y.; Zhou, Y.; Chen, P.; Tao, Y.; Li, Y.; Qu, J. *J. Am. Chem. Soc.* **2008**, *130*, 15250-15251.
135. Li, Y.; Li, Y.; Wang, B.; Luo, Y.; Yang, D.; Tong, P.; Zhao, J.; Luo, L.; Zhou, Y.; Chen, S.; Cheng, F.; Qu, J. *Nat. Chem.* **2013**, *5*, 320-326.
136. Verma, A. K.; Lee, S. C. *J. Am. Chem. Soc.* **1999**, *121*, 10838-10839.
137. Zdilla, M. J.; Verma, A. K.; Lee, S. C. *Inorg. Chem.* **2011**, *50*, 1551-1562.
138. Muetterties, E. L.; Rhodin, T. N.; Band, E.; Brucker, C. F.; Pretzer, W. R. *Chem. Rev.* **1979**, *79*, 91-137.

(Figure 1.12).[139,140,141] In the presence of a mixture of azoethane ($N_2(CH_2CH_3)_2$) and azopropane ($N_2(CH_2CH_2CH_3)_2$), formation of mixed compounds such as $Fe_3(CO)_9(\mu^3\text{-NEt})(\mu^3\text{-N}^n\text{Pr})$ was not observed, suggesting that the reaction proceeds by intramolecular N=N bond cleavage, which was supported by kinetic analysis.[141]

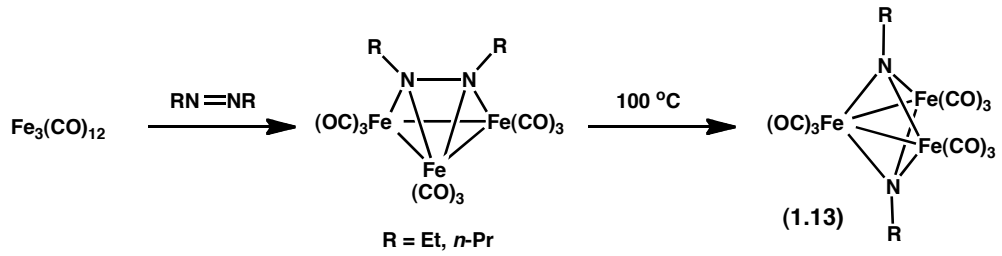

Figure 1.12. N=N bond cleavage of azoalkanes by trinuclear Fe(0) carbonyl cluster.

1-6. Summary and goals

Through this discussion, we have observed that polynuclear reaction sites are common motifs found in metalloenzyme cofactors as well as metal surfaces, both, which catalyze small molecule activation. There is significant interest in exploring the ability of synthetic polynuclear platforms to facilitate small molecule activation in order to gain a better understanding of how such assemblies achieve multi-electron transformations. Many current examples of homogeneous clusters that bind and activate small molecule substrates are comprised of low-valent metal centers (e.g. N=N bond cleavage of azoalkanes by trinuclear Fe(0) carbonyl clusters)[141] or require strong alkali metal reductants such as K^0 (e.g. N_2 bond homolysis to yield $Fe_3(N)_2$ β-diketiminate complex).[115] We are interested in an approach involving the synthesis of polynuclear clusters that possess key design elements common to metalloenzyme cofactors:

139. Albini, A.; Kisch, H. *J. Organomet. Chem.* **1975**, *94*, 75-85.
140. Wucherer, E. J.; Vahrenkamp, H. *Angew. Chem., Int. Ed.* **1987**, *26*, 355-356.
141. Wucherer, E. J.; Tasi, M.; Hansert, B.; Powell, A. K.; Garland, M.-T.; Halet, J.-F.; Saillard, J.-Y.; Vahrenkamp, H. *Inorg. Chem.* **1989**, *28*, 3564-3572.

multiple high-spin, coordinatively unsaturated metal centers that share a common coordination site to facilitate cooperative substrate interaction. Specifically, we aimed to answer the following questions:

1) Can we synthesize a high-spin Fe cluster in the absence of a protein superstructure with coordinatively unsaturated metal sites?
2) Will clusters of this type cooperatively bind substrates?
3) Do these clusters allow small molecule activation?

Herein, the design and synthesis of a polynuclear Fe platform, which is used to probe the polynuclear hypothesis, will be presented.

1-7. Chapter summaries

Chapter 2 discusses the synthesis of a new sterically encumbered hexaamine based ligand platform featuring bulky silyl-amide groups ($^{tbs}LH_6$ = 1,3,5-C_6H_9(NHC_6H_4-*o*-$NHSiMe_2{}^tBu)_3$). Metallation of the resulting ligand scaffold yields a high-spin (S = 6) trinuclear Fe^{II} complex (^{tbs}L)Fe_3(THF). The silyl-amide groups only permit ligation of one solvent molecule to the Fe_3 core, resulting in an molecule with C_1-symmetry wherein each Fe^{II} ion exhibits a distinct local coordination environment. The (^{tbs}L)Fe_3(THF) molecule can cooperatively bind halides yielding pseudo C_3-symmetric clusters of the type (^{tbs}L)$Fe_3(\mu^3$-X) (X = Cl, Br, I). The (^{tbs}L)Fe_3(THF) complex rapidly consumes inorganic azide at ambient temperature to afford an anionic, trinuclear μ^3-nitride complex. The nitride moiety is nucleophilic and can be readily alkylated via reaction with methyl iodide to afford the neutral, trinuclear methylimide complex.

In **Chapter 3**, the $2e^-$ and $4e^-$ reduction of N_xH_y substrates by (^{tbs}L)Fe_3(THF) yielding imido products is presented. Reaction of hydrazine or phenylhydrazine with (^{tbs}L)Fe_3(THF)

yields Fe_3 imido cluster (^{tbs}L)Fe_3(μ^3-NH) and ammonia or aniline, respectively. (^{tbs}L)Fe_3(μ^3-NH) has a similar zero-field ^{57}Fe Mössbauer spectrum comparable to previously reported anionic Fe_3(μ^3-nitride) complex and can be synthesized directly by protonation of the anionic Fe_3 nitride with lutidinium tetraphenylborate. Deprotonation of the Fe_3 imido (^{tbs}L)Fe_3(μ^3-NH) with lithium *bis*-(trimethylsilyl)amide results in regeneration of the Fe_3 nitride capped with a THF-solvated Li cation. A similar $2e^-$ reduction of 1,2-diphenylhydrazine by (^{tbs}L)Fe_3(THF) affords (^{tbs}L)Fe_3(μ^3-NPh) and aniline. Reductive N=N bond cleavage of azobenzene is also achieved in the presence of (^{tbs}L)Fe_3(THF) to yield Fe_3 *bis*-imido complex (^{tbs}L)Fe_3(μ^3-NPh)(μ^2-NPh), which has been structurally characterized. Charge balance indicates that the *bis*-imido cluster has undergone a $4e^-$ metal-based oxidation resulting in a (Fe^{IV})(Fe^{III})$_2$ formulation. Cyclic voltammograms of the series of Fe_3 clusters presented herein suggest that metal oxidation states up to (Fe^{IV})(Fe^{III})$_2$ (in the case of [(^{tbs}L)Fe_3(μ^3-N)]$^-$ are electrochemically accessible. These results highlight the efficacy of high-spin polynuclear reaction sites to cooperatively mediate small molecule activation.

Investigation of metal carbonyl and isonitrile adducts have played a significant role in both the development of transition metal clusters as well as aided in our understanding of how small molecule substrates interact with metal surfaces during chemisorption and catalysis. In **Chapter 4**, the reaction of cluster (^{tbs}L)Fe_3(THF) with a series of unsaturated substrates including tert-butylisocyanide (^{t}BuNC), lithium phenyl acetylide (LiCCPh), tetrabutylammonium thiocyanate ([SCN]NBu_4), and carbon monoxide (CO) is presented. Addition of neutral π-acidic molecules led to the formation of a new series of coordination compounds where binding to a single metal center is favored over cooperative substrate binding. Reduction of unsaturated substrates, including ^{t}BuNC and phenyl acetylide, is also discussed.

Chapter 5 summarizes our efforts to synthesize of a family of mixed Fe–Mn clusters that differ by single metal-site substitutions. Such a series of compounds would provide a template by which metal substitution can be examined in a stepwise fashion. Utilizing the hexaamide ligand varient $^{tbs}L^{6-}$ as a template for bimetallic trinuclear clusters, we are able to access a discrete (^{tbs}L)Fe_2Mn(THF) cluster as a substitutionally homogeneous material. Attempts to access similar Mn_2Fe clusters resulted in isolation of a mixture of heterotrinuclear species. In conjunction with NMR, EPR, Mössbauer, and X-ray fluorescence, spectroscopies, anomalous scattering measurements were critical for the unambiguous assignment of the metal substitution products that were synthesized.

Chapter 2.[142] Oxidative Atom Transfer to a Triiron Complex to Form a Nucleophilic μ^3-nitride, $[Fe_3(\mu^3\text{-}N)]^-$

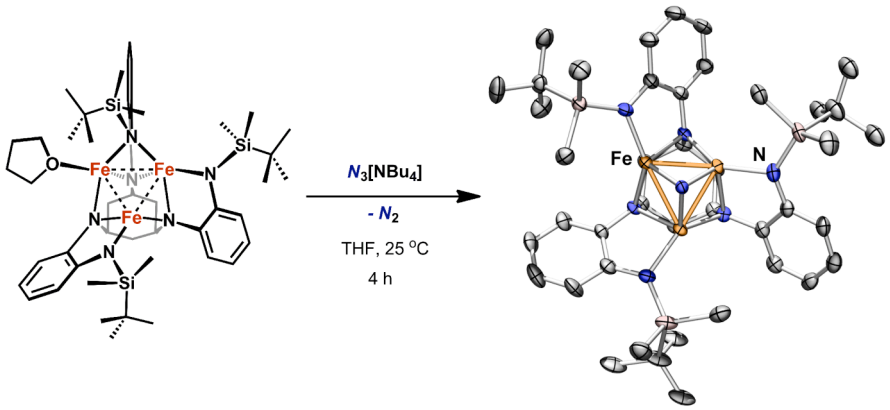

2-1. Introduction: M–M affects on electronic structure

The role M–M interactions play in facilitating redox events in redox reactions with small molecule substrates is often difficult to assess. In order to understand M–M redox synergy, we have targeted the syntheses of metal clusters by developing a family of polynucleating ligand platforms, which provide a method to conduct structure-function analysis through systematic modification of the steric and electronic environment of the cluster. Hexadentate ligands comprised of *o*-phenylenediamine-based subunits have provided a platform for facile construction of trinuclear Fe, Co, and Mn complexes whose intracore interactions and molecular spin states vary as a function of ligand architecture.[143,144,145,146]

Analysis of the series of previously reported Fe_3 clusters including $(^{H}L)Fe_3(PMe_3)_3$ (**2.1**),[143] $(^{Ph}L)Fe_3(PMe_2Ph)_3$ (**2.2**),[145] and $(^{Ph}L)Fe_3(THF)_3$ (**2.3**)[145] (where $^{R}L^{6-}$ = $MeC(CH_2NPh\text{-}o\text{-}NR)_3$; R = H or Ph) demonstrates how the ligand environment may affect molecular spin states.

142. This chapter was adapted with permission from Powers, T. M.; Fout, A. R.; Zhao, S.-L.; Betley, T. A. *J. Am. Chem. Soc.* **2011**, *133*, 3336-3338.
143. Zhao, Q.; Betley, T. A. *Angew. Chem., Int. Ed.* **2011**, *50*, 709-712.
144. Fout, A. R.; Zhao, Q.; Xiao, D. J.; Betley, T. A. *J. Am. Chem. Soc.* **2011**, *133*, 16750-16753.
145. Eames, E. V.; Harris, T. D.; Betley, T. A. *Chem. Sci.* **2012**, *3*, 407-415.
146. Eames, E. V.; Betley, T. A. *Inorg. Chem.* **2012**, *51,* 10274-10278.

All three Fe clusters have been crystallographically characterized (Figure 2.1) and exhibit similar solid-state structures. The Fe centers in all three complexes (**2.1**–**2.3**) exhibit distorted square pyramidal geometries (ignoring Fe–Fe contacts) where four ligand based amide nitrogen atoms make up the basal plane and the trimethyl phosphine occupies the apical position. Each of the *o*-phenylenediamide arms bridge two adjacent metal centers, resulting in pseudo-C_3 symmetric molecules.

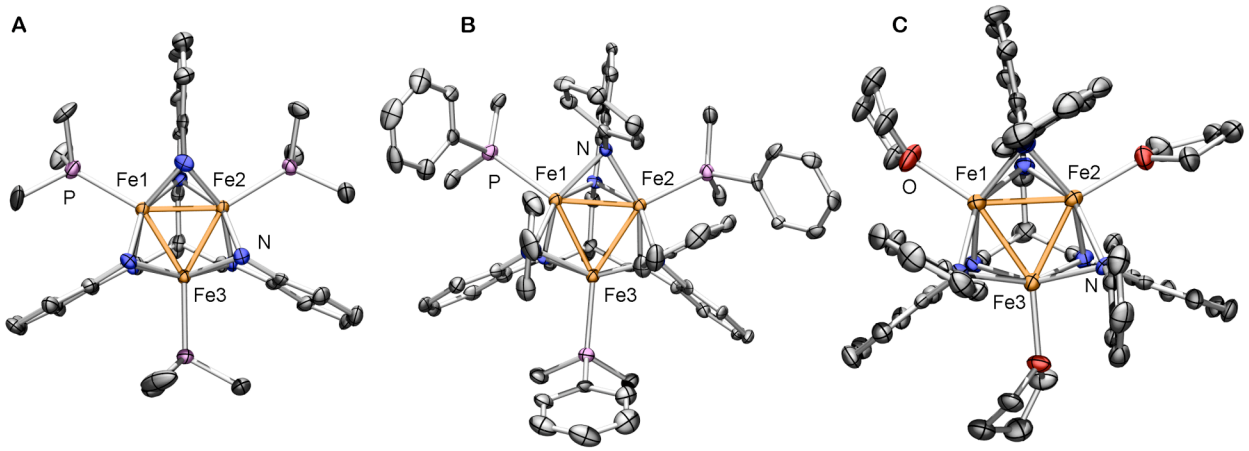

Figure 2.1. Solid-state structures of (A) (^{H}L)Fe$_3$(PMe$_3$)$_3$ (**2.1**), (B) (^{Ph}L)Fe$_3$(PMe$_2$Ph)$_3$ (**2.2**), and (C) (^{Ph}L)Fe$_3$(THF)$_3$ (**2.3**) with the thermal ellipsoids set at the 50% probability level (hydrogen atoms and solvent molecules omitted for clarity; Fe orange, C grey, N blue, O red, P Pink). M–M distances (Å) for **2.1**: Fe1-Fe2, 2.2499(4); Fe1-Fe3, 2.2868(4); Fe2-Fe3, 2.2863(5); for **2.2**: Fe1-Fe2, 2.552(1); Fe1-Fe3, 2.599(1); Fe2-Fe3, 2.606(1); for **2.3**: Fe1-Fe2, 2.438(1); Fe1-Fe3, 2.511(1); Fe2-Fe3, 2.524(1).

The Fe$_3$ cluster supported by the primary anilide ligand ^{H}L^{6-} (**2.1**) exhibits close M–M contacts (Fe–Fe$_{avg}$, 2.229(2) Å) and a low-spin ground state (S = 1) (Figure 2.1A). A molecular orbital diagram, based on Cotton's MO analysis of [Re$_3$Cl$_9$(μ^2-Cl)$_3$]$^{3-}$,[147,148] was proposed for this complex in which the frontier orbitals of the three Fe centers are mixed to generate a single *d*-orbital manifold to describe the M–M bonding within these clusters[143] and has been supported by both magnetic data and Mössbauer spectroscopy.[145] Moving to larger ligand architectures such as ^{Ph}L^{6-} (i.e. compound **2.2**) results in a significant increase in M–M distances (Fe–Fe$_{avg}$,

147. Bertrand, J.; Cotton, F. A.; Dollase, W. A. *J. Am. Chem. Soc.* **1963**, *85*, 1349-1350.
148. Cotton, F. A.; Hass, T. E. *Inorg. Chem.* **1964**, *3*, 10-17.

2.582(2) Å) and an increase in spin ground state to $S = 2$ (Figure 2.1B). Increasing the M–M separations leads to poorer spatial overlap of the metal *d*-orbitals, thereby lowering the energy of anti-bonding orbitals and allowing access of higher spin states. Finally, replacing the strong field exogenous phosphine donors with weaker field THF molecules (**2.3**) compresses the ligand field further, leading to a higher population of anti-bonding orbitals and results in a high-spin $S = 6$ cluster (Figure 2.1C).

Fe_3 clusters **2.1**–**2.3** demonstrate that polynucleating ligand platform $^{R}L^{6-}$ can support Fe_3 cores, with close Fe–Fe contacts, spanning a range of spin states from low-spin $S = 1$ to high-spin $S = 6$ all ferrous clusters. Instead of describing the electronic structure by considering the individual metal centers within the cluster independently, the magnetic and spectral data for these compounds are reflective of a delocalized molecular electronic structure.[145] However, the metal centers within these clusters are coordinatively saturated, which inhibits substrate binding. To probe the cooperative reaction chemistry of trinuclear clusters, we targeted a ligand platform that would restrict exogenous solvent from binding to the metal ions (Figure 2.2). We hypothesized that increasing the steric environment at the peripheral amide groups would serve two purposes: (1) increase the M–M separations leading to higher spin states, and (2) prevent exogenous solvent from binding to the metal ions, thereby compressing the ligand field as well as preserving coordinatively unsaturated metal centers.

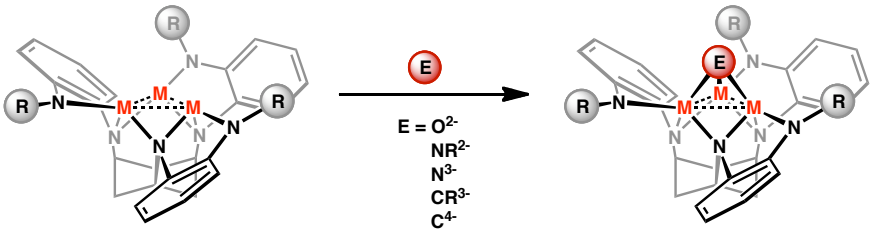

Figure 2.2. Target clusters by which to test the viability of polynuclear assemblies to facilitate small molecule activation.

2-2. Synthesis and metallation of $^{tbs}LH_6$ ligand

Tris-amine α-α-α-1,3,5-*tris*-aminocyclohexane hydrobromic acid (tach·3HBr, **2.4**)[149] was derivatized with *o*-fluoronitrobenzene via nucleophilic aromatic substitution (6 eq. Cs_2CO_3, ACN 120°C for 72 h) yielding a bright orange compound **2.5**. Subsequent reduction of the **2.5** using Zn dust (15 equiv) in a 50:50 mixture of saturated NH_4Cl in H_2O and THF afforded the hexaamine platform 1,3,5-$C_6H_9(NHC_6H_4$-*o*-$NH_2)_3$ (**2.6**) in 80% yield. Deprotonation of **2.6** with three equivalents of *n*-butyl-lithium followed by reaction with *t*-butyldimethylsilyl chloride afforded the target ligand 1,3,5-$C_6H_9(NHC_6H_4$-*o*-$NHSiMe_2{}^tBu)_3$ ($^{tbs}LH_6$) (**2.7**) in 45% yield on a multigram scale (Scheme 2.1).

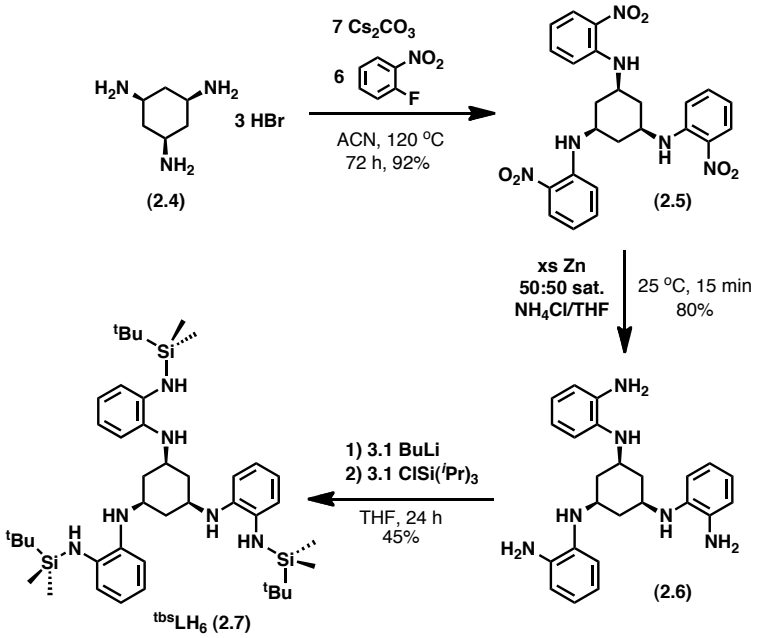

Scheme 2.1. Synthesis of ligand varient $^{tbs}LH_6$ (**2.7**).

Metallation of the ligand platform was effected by treatment of $^{tbs}LH_6$ with $Fe_2(Mes)_4$ (1.5 equivalents) at 75 °C for 12 h in THF. Evolution of mesitylene and consumption of ligand was observed by ^{1}H NMR; the resulting product (compound **2.8**) is ^{1}H NMR silent and was thus not observed. Storing the brown oil in cold hexanes (–33 °C) precipitated the trinuclear complex

149. Bowen, T.; Planalp, R. P.; Brechbiel, M. W. *Bioorg. Med. Chem. Lett.* **1996**, *6*, 807-810.

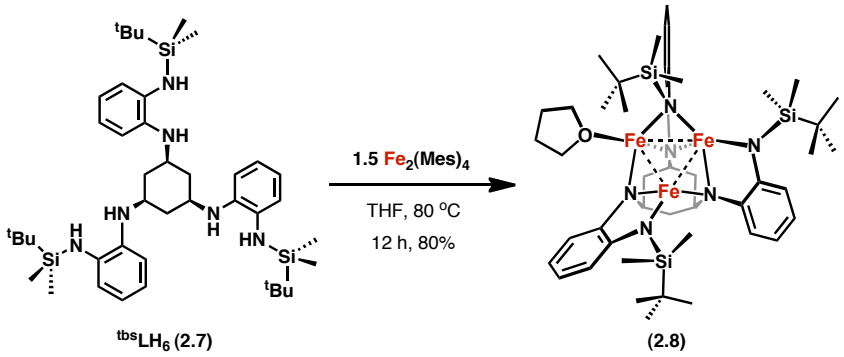

Scheme 2.2. Synthesis of (^{tbs}L)Fe$_3$(THF).

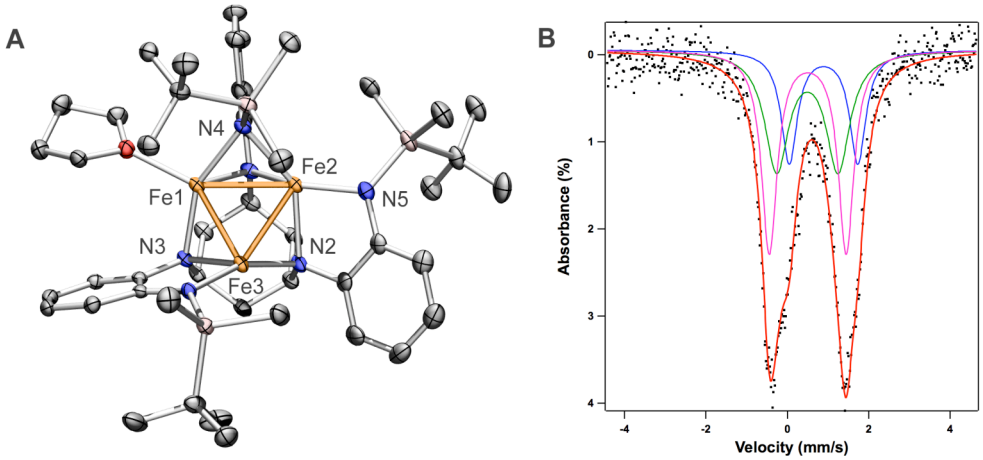

Figure 2.3. (A) Solid-state structure for (^{tbs}L)Fe$_3$(THF) (**2.8**) with the thermal ellipsoids set at the 50% probability level (hydrogen atoms and solvent molecules omitted for clarity; Fe orange, C black, H white, N blue, O red, Si Pink). Bond lengths (Å): Fe1–Fe2, 2.6129(5); Fe1–Fe3, 2.5061(5); Fe2–Fe3, 2.6118(5); Fe–N$_{int}$, (N$_{int}$ = N1, N2, N3), 2.047(2); Fe–N$_{SI}$, (N$_{Si}$ = N4, N5, N6) 1.950(2); Fe-O, 2.1162(18). (B) Zero-field ^{57}Fe Mössbauer spectrum of (^{tbs}L)Fe$_3$(THF) obtained at 110 K. Fitting parameters: δ, $|\Delta E_Q|$ ($^{mm}/_s$) component 1 (blue, 24%): 0.89, *1.69* (Γ = 0.24 $^{mm}/_s$); component 2 (green, 35%): 0.49, *1.51* (Γ = 0.35 $^{mm}/_s$); component 3 (pink, 41%): 0.50, *1.89* (Γ = 0.23 $^{mm}/_s$).

(^{tbs}L)Fe$_3$(THF) (**2.8**) in 80% yield (Scheme 2.2). Crystallographic analysis of single crystals of Fe$_3$ cluster **2.8** provided the structure, consisting of three Fe ions and an asymmetrically bound hexaamide ligand (Figure 2.3A). Unlike the trinuclear complexes we have previously reported (i.e. compounds **2.1**–**2.3**, *vide supra*), the large silyl substituents on the ligand platform prevent two of the three apical amide groups from bridging adjacent metal ions. Only a single silylamide bridges Fe1 and Fe2, while the other two silylamides are terminally bound to Fe2 and Fe3 giving each iron ion a distinct coordination environment. As a result, the molecule is of C_1-symmetry

with two 4-coordinate Fe centers (Fe1 and Fe2) and one 3-coordinate Fe center (Fe3). The average Fe–Fe separation is 2.577(6) Å, which is comparable to previously reported Fe_3 complex **2.2** ($Fe–Fe_{avg}$, 2.582(2) Å).[143,145] The zero-field ^{57}Fe Mössbauer spectrum of (^{tbs}L)Fe_3(THF) reflects its asymmetry, as the 105 K spectrum shows a single broad quadrupole doublet that can be fit using three quadrupole doublets (δ, $|\Delta E_Q|$ ($^{mm}/_s$)): component 1: (24%) 0.89, *1.69*; component 2: (35%) 0.49, *1.51*; component 3: (41%) 0.50, *1.89*) (Figure 2.3B).[150] The ^1H NMR silent material is consistent with the large solution magnetic moment for paramagnetic **2.8** (12.0(2) μ_B) determined by the Evans method. While the measured solution magnetic moment is lower than expected for a high-spin Fe_3 cluster (g = 2, μ_{eff} = 12.96 μ_B), we assign the spin state for this molecule as S = 6.

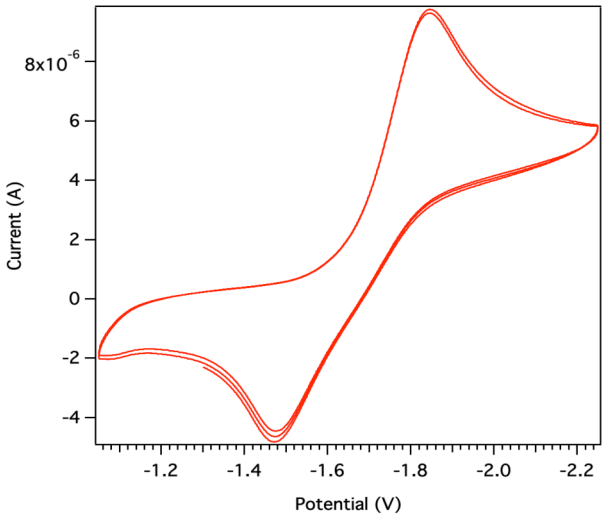

Figure 2.4. Cyclic voltammogram of 3 mM (^{tbs}L)Fe_3(THF) (OCP = –1.29 V, 0.1 M $(Bu_4N)PF_6$, glassy C working electrode, scan rate 0.01 V/s in THF, referenced to $[Cp_2Fe]^{0/+}$).

The cyclic voltammogram of (^{tbs}L)Fe_3(THF) was collected (3 mM analyte, 0.1 M $(Bu_4N)PF_6$, glassy C working electrode, scan rate 0.01 V/s in THF, referenced to $[Cp_2Fe]^{0/+}$). Scanning in the cathodic direction from the open circuit potential at –1.29 V reveals an electrochemically irreversible, but chemically reversible event, with peak cathodic and anodic

150. See **section 2-5** for details on calculating relative percent component values from Mössbauer spectra.

currents at –1.85 V and –1.48 V respectively (peak separation 370 mV) (Figure 2.4). Several additional electrochemically irreversible oxidation events were observed scanning in the anodic direction and attempts at chemical oxidation of Fe_3 cluster **2.8** resulted in decomposition. In contrast, the $1e^-$ reduction of (^{tbs}L)Fe_3(THF) (**2.8**) is chemically accessible. Addition of either KH or KC_8, to a THF solution of **2.8** results in formation of a ^{1}H NMR silent, hexane insoluble material. Storing the product in diethyl ether at –33 ^{o}C deposits black crystals from the solution. The solid-state molecular structure revealed the product as the $1e^-$ reduced Fe_3 cluster [^{tbs}LFe_3]K(THF)(Et_2O)$_2$ (**2.9**) (Scheme 2.3, Figure 2.5).

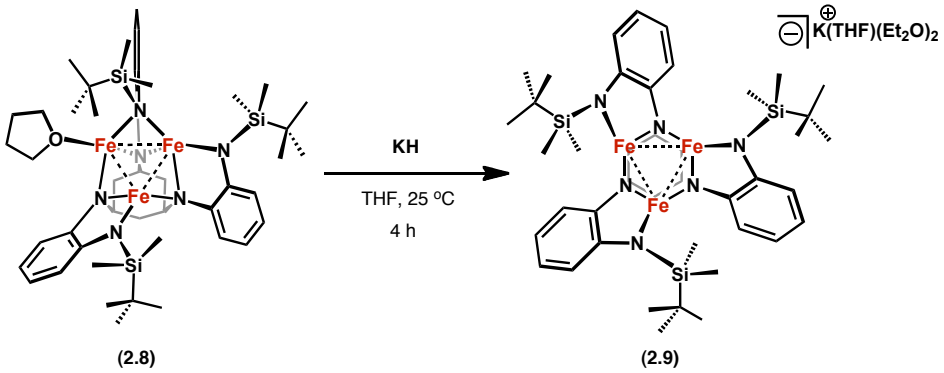

Scheme 2.3. $1e^-$ reduction of (^{tbs}L)Fe_3(THF) by KH.

Reduction of (^{tbs}L)Fe_3(THF) (**2.8**), results in dissociation of THF and ligand rearrangement, where the remaining bridging anilide group becomes terminally bound to a single Fe center. The pseudo-C_3 symmetric molecule features three coordinatively equivalent Fe centers, each of which is bonded to two alkyl aryl amides and one peripheral silyl amide moiety. Ignoring Fe–Fe interactions within the cluster, the coordination environment at each iron center is best described as T-shaped. The average Fe–Fe separation in **2.9** is 2.461(1) Å, shorter than the average Fe–Fe distances in (Fe^{II})$_3$ cluster **2.8** (2.577(6) Å). The K^+ cation coordinates η^3 to one of the aryl rings of the ligand scaffold in the solid-state, breaking the apparent C_3 symmetry of the molecule, which manifests itself in the zero-field ^{57}Fe Mössbauer spectrum containing one

broad, asymmetric quadrupole doublet that can be fit to three quadrupole doublets (δ ($^{mm}/_{s}$), $|\Delta E_Q|$ ($^{mm}/_{s}$) component 1 (24%): 0.41, *1.9*; component 2 (35%) 0.35, *1.32*; component 3 (40%) 0.68, *2.10*, Figure 2.5). Addition of 18-crown-6-ether to **2.9** sequesters the K^+ cation to afford [(^{tbs}L)Fe$_3$]K($C_{12}H_{24}O_6$) in 87% yield.

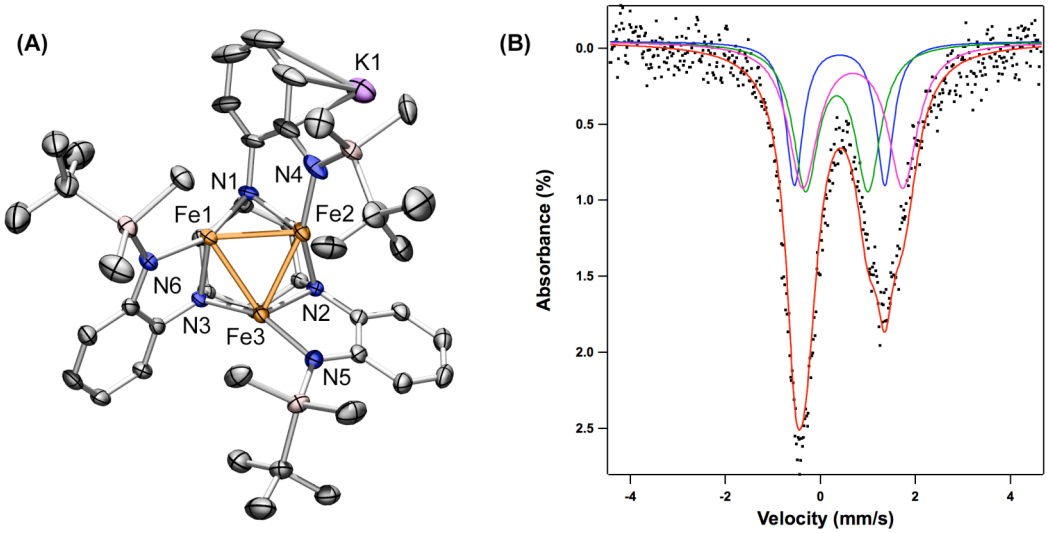

Figure 2.5. (A) Solid-state structure of [(^{tbs}L)Fe$_3$]K(THF)(Et_2O)$_2$ (**2.9**) with the thermal ellipsoids set at the 50% probability level (hydrogen atoms and solvent molecules omitted for clarity; Fe orange, C gray, N blue, Si Pink, K orchid). Bond lengths (Å): Fe1–Fe2, 2.4687(8); Fe1–Fe3, 2.4760(8); Fe2–Fe3, 2.4367(8); Fe–N_{int}, (N_{int} = N1, N2, N3) 2.030(3); Fe–N_{Si}, (N_{Si} = N4, N5, N6) 1.96(1). (B) Zero-field Mössbauer spectrum (110 K) of **2.9**. Simulation yields the following parameters: δ ($^{mm}/_{s}$), $|\Delta E_Q|$ ($^{mm}/_{s}$) component 1 (blue, 24%) 0.41, *1.9* (Γ = 0.22 $^{mm}/_{s}$); component 2 (green, 35%) 0.35, *1.32* (Γ = 0.32 $^{mm}/_{s}$); component 3 (pink, 40%) 0.68, *2.10* (Γ = 0.38 $^{mm}/_{s}$).

2-3. Cooperative substrate binding: formation of halide adducts

With the presence of unsaturated metal centers, we were interested in whether the Fe atoms in (^{tbs}L)Fe$_3$(THF) could cooperatively bind substrate. In the presence of various tetrabutylammonium halide ($XNBu_4$, X = Cl, Br, I) salts, we observe loss of THF and binding of the Fe_3 core to halide, resulting in pseudo-C_3 symmetric all ferrous trinuclear μ^3-halide adducts of the type [(^{tbs}L)Fe$_3$(μ^3-X)]NBu_4 in 80–85% yields (Scheme 2.4). X-ray crystallography of the [(^{tbs}L)Fe$_3$(μ^3-X)]NBu_4 compounds (X = Cl (**2.10**); Br (**2.11**); I (**2.12**) revealed similar structures, which feature three Fe centers binding a central μ^3-halide ligand. The average Fe–Fe separations

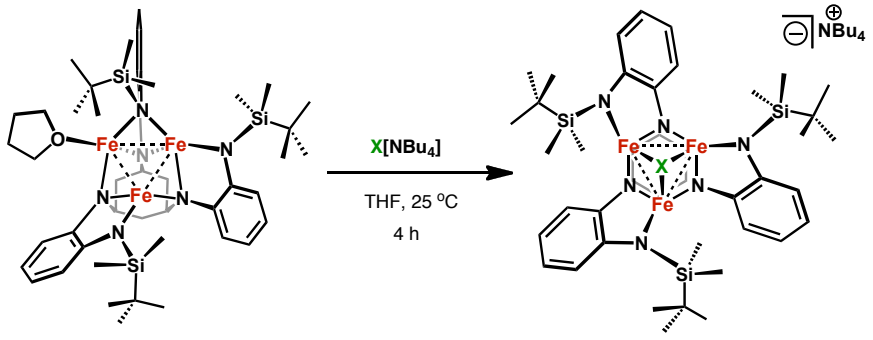

Scheme 2.4. Synthesis of $[(^{tbs}L)Fe_3(\mu^3\text{-}X)]^-$, where X = Cl, Br, or I.

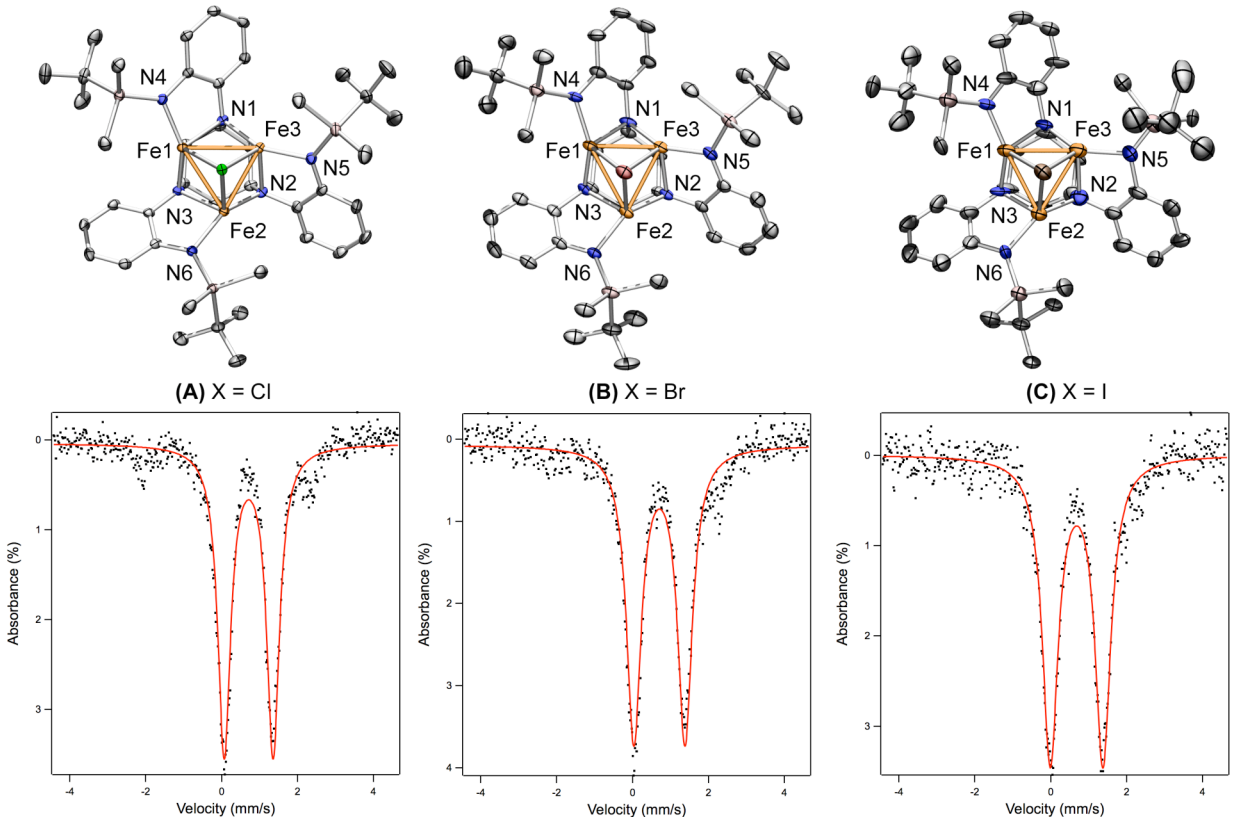

Figure 2.6. Soild-state structures and zero-field Mössbauer spectra of $[(^{tbs}L)Fe_3(\mu^3\text{-}X)]NBu_4$, where (A) X = Cl (**2.10**), (B) X = Br (**2.11**), (C) X = I (**2.12**), with the thermal ellipsoids set at the 50% probability level (hydrogen atoms, NBu_4 counter cations, and solvent molecules omitted for clarity; Fe orange, C gray, N blue, Si Pink, Cl green, Br red, I brown). Bond lengths (Å): (A, X = Cl) Fe1–Fe2, 2.8063(8); Fe1–Fe3, 2.6818(8); Fe2–Fe3, 2.8282(9); Fe–N_{int}, (N_{int} = N1, N2, N3) 2.048(3); Fe–N_{Si}, (N_{Si} = N4, N5, N6) 1.956(3); Fe–Cl_{avg}, 2.518(1); (B, X = Br) Fe1–Fe2, 2.863(1); Fe1–Fe3, 2.657(1); Fe2–Fe3, 2.788(1); Fe–N_{int}, (N_{int} = N1, N2, N3) 2.048(8); Fe–N_{Si}, (N_{Si} = N4, N5, N6) 2.422(5); Fe–Br_{avg}, 2.634(1); (C, X = I) Fe1–Fe2, 2.732(2); Fe1–Fe3, 2.848(2); Fe2–Fe3, 2.727(2); Fe–N_{int}, (N_{int} = N1, N2, N3) 2.04(1); Fe–N_{Si}, (N_{Si} = N4, N5, N6) 1.98(1); Fe–I_{avg}, 2.793(2). Zero-field Mössbauer spectrum obtained at 110 K. Fitting parameters: δ ($^{mm}/_s$), $|\Delta E_Q|$ ($^{mm}/_s$) (A, **2.10**) 0.72, *1.29* (Γ = 0.21 $^{mm}/_s$); (B, **2.11**) 0.71, *1.35* (Γ = 0.24 $^{mm}/_s$); (C, **2.12**) 0.68, *1.25* (Γ = 0.25 $^{mm}/_s$).

found in the Fe_3–Br, –Cl, and –I salts are essentially identical (2.772(1), 2.769(1), and 2.769(1) Å, respectively, Figure 2.6) and the average Fe–X distances increases with increasing size of the halide (Fe–Cl_{avg} 2.518(1) Å; Fe–Br_{avg} 2.634(1) Å; Fe–I_{avg} 2.793(2) Å), as would be expected due to the relative ionic radii of the μ^3-bound halides. Each of the Fe atoms sit in a distorted tetrahedral, nearly cis-divacant octahedral, site, bridged by two ligand internal amide residues (Fe–N_{int}) and capped by one terminal silyl-amide (Fe–N_{Si}). Ligand reorganization, where the remaining bridging anilide group becomes terminally bound to a single Fe center, accommodates binding of the halide ligand (Figure 2.6). All three complexes exhibit nearly identical zero-field ^{57}Fe Mössbauer spectra, which feature a single quadrupole doublet near 0.7 mm/s (Figure 2.6), and exhibit similar solution magnetic moments (X = Cl, 12.1(5) μ_B; X = Br, 12.4(5) μ_B; X = I, 13.4(7) μ_B).

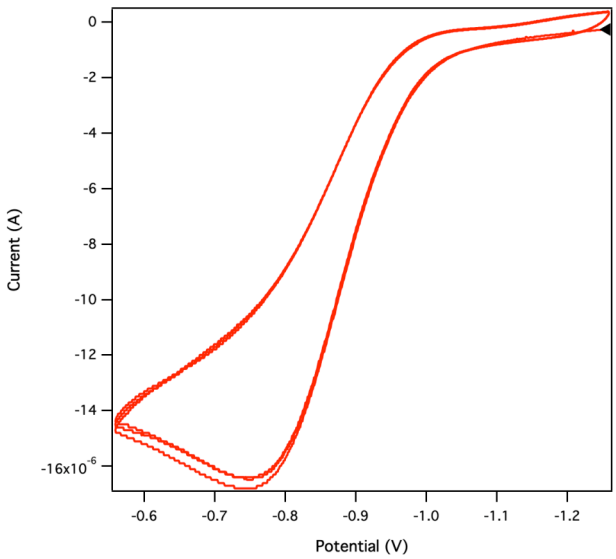

Figure 2.7. Cyclic voltammogram of 2 mM **2.11** at onset of oxidation (OCP = -1.29 V, glassy C working electrode, 0.1 M $(Bu_4N)PF_6$, scan rate 0.01 V/s in THF, referenced to $[Cp_2Fe]^{0/+}$).

The cyclic voltammogram of $[^{tbs}LFe_3(\mu^3\text{-Br})]NBu_4$ (**2.11**) was collected (2 mM analyte, 0.1 M $(Bu_4N)PF_6$, glassy C working electrode, scan rate 0.01 V/s in THF, referenced to $[Cp_2Fe]^{0/+}$) and was found to have an identical open circuit potential compared to the

(^{tbs}L)Fe$_3$(THF) molecule (–1.29 V). While the complex features a single irreversible oxidation with a peak anodic current at –0.74 V (Figure 2.7), as in the case of (^{tbs}L)Fe$_3$(THF) (**2.8**), attempts to chemically access an oxidized product resulted in decomposition yielding uncharacterized products.

2-4. Reaction of (^{tbs}L)Fe$_3$(THF) with inorganic azide to form a nucleophilic μ^3-nitride

We have also observed that Fe$_3$ cluster **2.1** exhibits the ability to mediate multi-electron reduction of small molecule substrates. Reaction of complex (^{tbs}L)Fe$_3$(THF) (**2.8**) with tetrabutylammonium azide at room temperature results in the dissociation of THF and consumption of the azide as judged by the absence of the azide stretch (ν_{N3}) in the IR spectrum. Storing the reaction product in diethyl ether at –33 °C deposited crystals suitable for X-ray diffraction analysis. The solid-state molecular structure for the product, shown in Figure 2.8, confirmed the formation of pseudo C_3-symmetric nitride product [(^{tbs}L)Fe$_3$(μ^3-N)]NBu$_4$ (**2.13**) (Scheme 2.5). Formation of the anionic nitride **2.13** proceeds via the two electron oxidation of (^{tbs}L)Fe$_3$(THF) (**2.8**) where the overall complex geometry is dictated by the trinulceating ligand. While formation of iron-nitride complexes proceeding via thermal or photolytic decomposition of iron azides embedded in tetraazamacrocylic ligand environments is well precedented,[151,152,153] most polynuclear (nuclearity exceeding two) iron-nitride species form via reduction of nitrosyl ligands,[154,155,156] or via metathetical routes using N(SnMe$_3$)$_3$.[157] However, these routes give rise to unpredictable nuclearity and cluster geometries.

151. Summerville, D. A.; Cohen, I. A. *J. Am. Chem. Soc.* **1976**, *98,* 1747-1752.
152. Wagner, W.-D.; Nakamoto, K. *J. Am. Chem. Soc.* **1988**, *110*, 4044-4045.
153. Meyer, K.; Bill, E.; Mienert, B.; Weyhermüller, T.; Wieghardt, K. *J. Am. Chem. Soc.* **1999**, *121*, 4859-4876.
154. Fjare, D. E.; Gladfelter, W. L. *J. Am. Chem. Soc.* **1981**, *103*, 1572-1574.
155. Hourihane, R.; Spalding, T. R.; Ferguson, G.; Deeney, T.; Zanello, P. *J. Chem. Soc., Dalton Trans*. **1993**, 43-46.
156. Della Pergola, R.; Bandini, C.; Demartin, F.; Diana, E.; Garlaschelli, L.; Stanghellini, P. L.; Zanello, P. *J. Chem. Soc., Dalton Trans.* **1996**, 747-754.

Complex [(^{tbs}L)Fe$_3$(μ^3-N)]NBu$_4$ (**2.13**), structurally similar to the [(^{tbs}L)Fe$_3$(μ^3-X)]NBu$_4$ (X = Br, Cl, I) series, features three Fe centers that bind the central μ^3-nitride ligand with average Fe–N and Fe–Fe bond lengths of 1.871(3) and 2.480(1) Å, respectively (Figure 2.8). Each of the Fe atoms is bridged by two ligand internal amide residues (average Fe–N$_{int}$ 2.030(3) Å) and capped by one terminal silyl-amide (average Fe–N$_{Si}$ 1.950(3) Å). Ligand reorganization of the bridging anilide unit in **2.8,** resulting in a terminal anilide bound to a single Fe center,

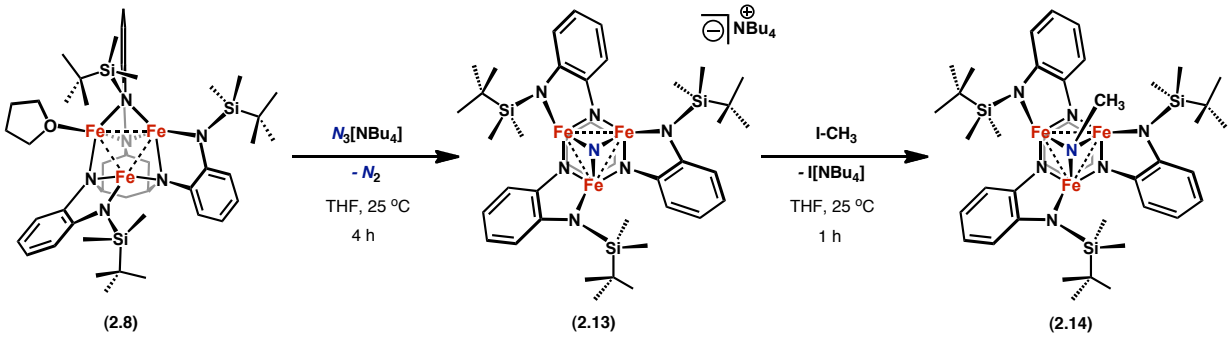

Scheme 2.5. Synthesis of [(^{tbs}L)Fe$_3$(μ^3-N)]NBu$_4$ and (^{tbs}L)Fe$_3$(μ^3-NMe).

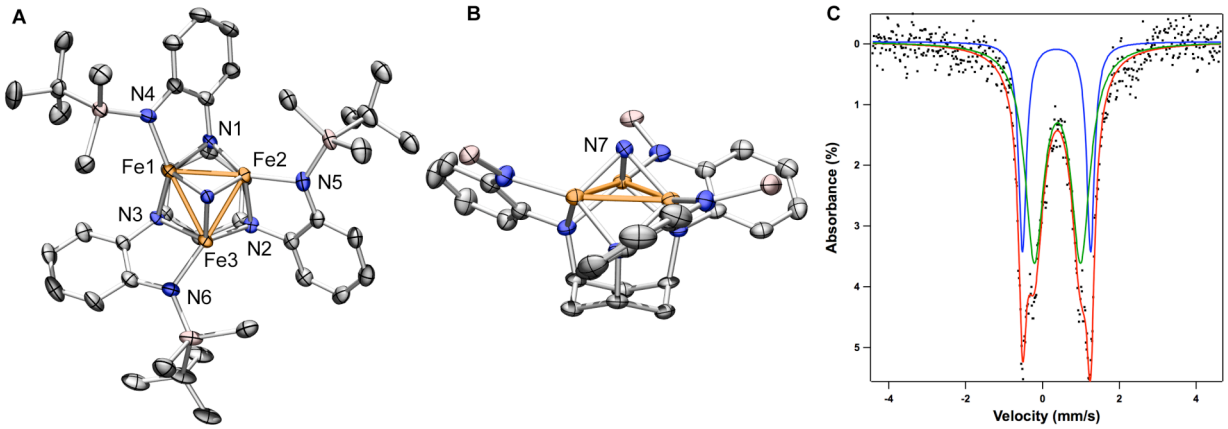

Figure 2.8. Solid-state structure for [(^{tbs}L)Fe$_3$(μ^3-N)]NBu$_4$ (**2.13**) (**A**, side view in **B**) with the thermal ellipsoids set at the 50% probability level (hydrogen atoms, solvent molecules, and Bu$_4$N cation omitted for clarity; Fe orange, C black, H white, N blue, O red, Si Pink). Bond lengths (Å) Fe1–Fe2, 2.4212(7); Fe1–Fe3, 2.5444(7); Fe2–Fe3, 2.4737(7); Fe–N7$_{avg}$, 1.871(3); Fe–N$_{int}$, 2.030(3); Fe–N$_{Si}$, 1.950(3). Zero-field Mössbauer spectrum of **2.13** (C) obtained at 120 K Simulation yields the following parameters δ, $|\Delta E_Q|$ ($^{mm}/_s$): component 1 (blue, 30%): 0.37, *1.78* (Γ = 0.12 $^{mm}/_s$); component 2 (green, 70%): 0.39, *1.23* (Γ = 0.30 $^{mm}/_s$).

157. Bennett, M. V.; Stoian, S.; Bominaar, E. L.; Munck, E.; Holm, R. H. *J. Am. Chem. Soc.* **2005**, *127*, 12378-12386.

accommodates binding of the monoatomic nitride ligand, which is heavily pyramidalized (Σ(Fe–N7–Fe) = 248.9(1)°, NH_3 is 319.8°), sitting 1.205(3) Å above the Fe_3 basal plane. The solution magnetic moment for paramagnetic **2.13** is 7.3(2) μ_B. The zero-field ^{57}Fe Mössbauer spectrum obtained at 120 K shows two quadrupole doublets with nearly identical isomer shifts (δ, $|\Delta E_Q|$ ($^{mm}/_s$)): component 1: (30%) 0.37, *1.72*; component 2: (70%) 0.4, *1.07*) (Figure 2.8C). The isomer shift parameters of **2.13** are lower then that compared to the $(Fe^{II})_3$–halides (Table 2.1), indicating that the $2e^-$ oxidation is metal based, delocalized over all three Fe centers on the Mössbauer timescale (>10^{-9} sec).[158] We hypothesize that the two quadrupole doublets observed in the Mössbauer spectrum of **2.13** are due to deviation from rigorous C_3 symmetry in the solid-state (see bond metrics in crystal structure, Figure 2.8).

Table 2.1. Mössbauer parameters for selected Fe_3 complexes

Complex		Formal oxidation state	δ (mm/s) (% component)	ΔE_Q (mm/s)
$[(^{tbs}L)Fe_3(\mu^3\text{-}Cl)]^-$	**2.10**	$(Fe^{II})_3$	0.72	1.29
$[(^{tbs}L)Fe_3(\mu^3\text{-}Br)]^-$	**2.11**	$(Fe^{II})_3$	0.71	1.35
$[(^{tbs}L)Fe_3(\mu^3\text{-}I)]^-$	**2.12**	$(Fe^{II})_3$	0.68	1.38
$[(^{tbs}L)Fe_3(\mu^3\text{-}N)]^-$	**2.13**	$(Fe^{II})(Fe^{III})_2$	0.37 (30) 0.39 (70)	1.78 1.23
$(^{tbs}L)Fe_3(\mu^3\text{-}NMe)$	**2.14**	$(Fe^{II})(Fe^{III})_2$	0.37 (28) 0.36 (72)	0.94 1.67

In contrast to many terminal Fe-nitride complexes that react as electrophiles,[159,160,161] the nitride in complex **2.13** is nucleophilic at nitrogen, as demonstrated by its rapid reaction with methyl iodide to afford a hexane-soluble methyl imido complex $(^{tbs}L)Fe_3(\mu^3\text{-}NCH_3)$ (**2.14**) with generation of Bu_4NI (Scheme 2.6). Storing complex **2.14** in hexanes at –33 °C deposited crystals

158. Drago, R. S. *Physical Methods for Chemists*, 2nd Ed.; Surfside Scientific Publishers: Gainesville, 1992.
159. Betley, T. A.; Peters, J. C. *J. Am. Chem. Soc.* **2004**, *126*, 6252-6254.
160. Vogel, C.; Heinemann, F. W.; Sutter, J.; Anthon, C.; Meyer, K. *Angew. Chem., Int. Ed.* **2008**, *47*, 2681-2683.
161. Scepaniak, J. J.; Fulton, M. D.; Bontchev, R. P.; Duesler, E. N.; Kirk, M. L.; Smith, J. M. *J. Am. Chem. Soc.* **2008**, *130*, 10515-10517.

suitable for X-ray diffraction analysis. The solid-state molecular structure for (^{tbs}L)Fe$_3$(μ^3-NCH$_3$) is shown in Figure 2.9. Structurally similar to [(^{tbs}L)Fe$_3$(μ^3-N)]NBu$_4$ (**2.13**), complex (^{tbs}L)Fe$_3$(μ^3-NCH$_3$) (**2.14**) features a central μ^3-imide ligand with average Fe–N and Fe–Fe bond lengths of 1.892(3) and 2.483(3) Å, respectively. The imide ligand sits 1.265(9) Å above the Fe$_3$ basal plane, slightly extended from the nitride (core highlights shown in Figure 2.4B). The zero-field ^{57}Fe Mössbauer spectrum of paramagnetic **2.14** (5.3(2) μ_B) obtained at 120 K is similar to that of the Fe$_3$-nitride **2.13**, featuring two quadrupole doublets with nearly identical isomer shifts (δ, $|\Delta E_Q|$ ($^{mm}/_s$)): component 1: (72%) 0.36, *1.69* ; component 2: (28%) 0.37, *0.97*) (Figure 2.9C, Table 2.1). Previous examples of Fe$_3$ imido complexes were synthesized via reaction of iron carbonyl precursors with silylazide,[162] nitroarene,[163,164] or alkyldiazene reagents.[141]

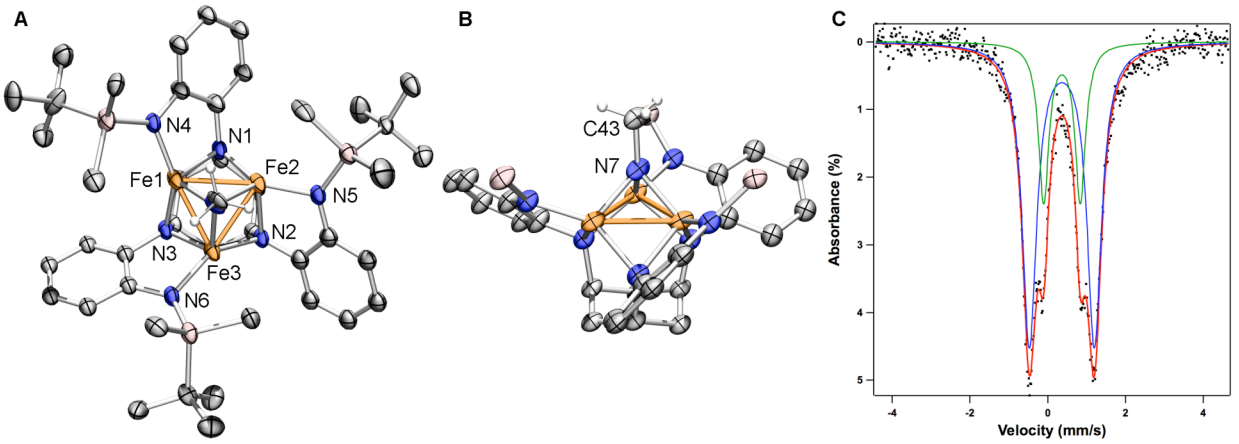

Figure 2.9. Solid-state structure for (^{tbs}L)Fe$_3$(μ^3-NMe) (**2.14**) (A, side view in B) with the thermal ellipsoids set at the 50% probability level (hydrogen atoms omitted for clarity; Fe orange, C black, H white, N blue, O red, Si Pink). Bond lengths (Å): Fe1–Fe2, 2.449(3); Fe1–Fe3, 2.487(2); Fe2–Fe3, 2.513(2); Fe–N7$_{avg}$, 1.892(3); N7-C1, 1.457(14); Fe–N$_{int}$, 1.996(10); Fe–N$_{Si}$, 1.904(10). Zero-field Mössbauer spectrum of **2.14** (C) obtained at 110 K. Simulation yields the following parameters δ, $|\Delta E_Q|$ ($^{mm}/_s$): component 1 (green, 28%): 0.37, *0.94* (Γ = 0.16 $^{mm}/_s$); component 2 (blue, 72%): 0.36, *1.67* (Γ = 0.22 $^{mm}/_s$).

162. Barnett, B. L.; Kruger, C. *Angew. Chem., Int. Ed.* **1971**, *10*, 910-911.
163. Landesberg, J. M.; Katz, L.; Olsen, C. *J. Org. Chem.* **1972**, *37*, 930-936.
164. Ragaini, F.; Song, J.-S.; Ramage, D. L.; Geoffroy, G. L.; Yap, G. A. P.; Rheingold, A. L. *Organometallics* **1995**, *14*, 387-400.

2-4. Conclusions

In summary, the silyl-substituted ligand platform $[^{tbs}L]^{6-}$ supports Fe_3 complex formation with coordinatively unsaturated metal centers. While average Fe–Fe distance in $(^{tbs}L)Fe_3(THF)$ (**2.8**) (2.577(6) Å) is similar to that observed for previously reported $(^{Ph}L)Fe_3(PMe_2Ph)_3$ (**2.2**)[145] (2.582(2) Å, *vide supra*), only a single THF molecule coordinates to the Fe_3 core. As a result, the cluster exhibits a high solution magnetic moment (12.0(2) μ_B) consistent with a high-spin Fe_3 cluster ($S = 6$). While chemical oxidation of $(^{tbs}L)Fe_3(THF)$ (**2.8**) lead to decomposition, the $1e^-$ reduction of the Fe_3 complex with KH leads to the formation of a stable, pseudo C_3-symmetric Fe_3 cluster $[(^{tbs}L)Fe_3]K(THF)(Et_2O)_2$ (**2.9**).

The Fe_3 THF-bound complex **2.8** rapidly reacts with halides and pseudo-halides, resulting in products where the substrate symmetrically binds to the Fe_3 core. Addition of inorganic azide results in metal oxidation to produce a C_3-symmetric, μ^3-nitride complex $[(^{tbs}L)Fe_3(\mu^3\text{-}N)]NBu_4$ (**2.13**). This strategy permits control of the nuclearity of the resultant cluster and elaboration of a cooperatively bound substrate, as demonstrated by alkylation of the nitride to afford a bridging imido complex.

2-5. Experimental methods

Materials and Methods

All manipulations involving metal complexes were carried out using standard Schlenk line or glove-box techniques under a dinitrogen atmosphere. All glassware was oven-dried for a minimum of 10 h and cooled in an evacuated antechamber prior to use in the dry box. Benzene, diethyl ether, hexanes and tetrahydrofuran (THF) were dried and deoxygenated on a Glass Contour System (SG Water USA, Nashua, NH) and stored over 4 Å molecular sieves (Strem)

prior to use. Benzene-d_6 was purchased from Cambridge Isotope Labs and was degassed and stored over 4 Å molecular sieves prior to use. Non-halogenated solvents were typically tested with a standard purple solution of sodium benzophenone ketyl in THF in order to confirm effective oxygen and moisture removal. Fe_2Mes_4 (Mes = 2,4,6-$Me_3C_6H_2$)[165] and α-α-α-1,3,5-$NH_2C_6H_9 \cdot 3HBr$[149] were prepared following published methods. 1-Fluoro-2-nitrobenzene and Cs_2CO_3 were used as received from Aldrich. (1α,3α,5α)-1,3,5-cyclohexane-tricarboxylic acid was purchased from TCI America and used without further purification. Tetrabutylammonium azide was recrystallized from diethyl ether/THF solution at –33 °C prior to use. All other reagents were purchased from commercial vendors and used without further purification unless explicitly stated.

Physical Measurements

All of the measurements for the metal complexes were made under anaerobic conditions. Elemental analyses were performed by Complete Analysis Laboratories, Inc., Parsippany, New Jersey. ^1H and ^{13}C NMR spectra were recorded on a Varian Unity/Inova 500 NMR spectrometer with chemical shifts (δ ppm) referenced to residual NMR solvent. High-resolution mass spectrometry was performed on an Agilent 6210 TOF LC/MS with a dual nebulizer ESI source at the Harvard University FAS Center for Systems Biology Mass Spectrometry and Proteomics Resource Laboratory. UV/Visible spectra were recorded on a Varian Cary 50 UV/Visible spectrometer using quartz cuvettes. Solution magnetic susceptibilities were determined by Evans method using trifluoromethylbenzene as an internal reference.

165. Klose, A.; Solari, E.; Floriani, C.; Chiesi-Villa, A.; Rizzoli, C.; Re, N. *J. Am. Chem. Soc.* **1994,** *116,* 9123-9135.

Mössbauer spectroscopy

Zero-field, ^{57}Fe Mössbauer spectra were measured with a constant acceleration spectrometer (SEE Co, Minneapolis, MN). Isomer shifts are quoted relative to Fe metal at room temperature. Data was processed, fitted, and analyzed using an in-house package for IGOR Pro 6 (Wavemetrics, Lake Oswego, OR). Percent components were determined by integrating the individual component fits and using the areas of those fits to determine the relative area ratios of the quadrupole doublets. The area, A, under a peak in a Mössbauer spectrum is given by Eq. 2.1.[166,167]

$$\boldsymbol{A = {}^{1}/_{2}\,\pi\, n f_a f_s \Gamma\, G(n, f_a, \sigma_0)} \qquad \text{(Eq. 2.1)}$$

n = number of absorbing nuclei

f_a = fraction of atoms that absorb resonantly without recoil

f_s = Mössbauer fraction of the source

σ_0 = maximum resonant absorption cross section

Γ = half height width

$G(n, f_a, \sigma_0)$ = dependant on σ_0, f_a, and the thickness and homogeneity of the absorber

In theory, the relative ratio of unique Mössbauer absorbers in a compound (n_1/n_2) should be determinable from the relative areas (A_1/A_2) of the two absorbers, related by Eq. 2.2.

$$\boldsymbol{A_1/A_2 = C\ (n_1/n_2)} \qquad \text{(Eq. 2.2)}$$

where $C = (f_1 / f_2)(\Gamma_1 / \Gamma_2)\ [G(n_1, f_{a1}, \sigma_0) / G(n_2, f_{a2}, \sigma_0)]$

However, without calculating C, the relative area ratios of the peaks cannot be used to determine the relative ratios of unique Mössbauer absorbers in a sample. Therefore, in this thesis, percent component values determined by Mössbauer spectroscopy do not necessarily represent the ratio

166. Sprenkel-Segel, E. L.; Hanna, S. S. *Geochim. Cosomochim. Acta* **1964**, *28*, 1913-1931.
167. Bancroft, G. M.; Burns, R. G.; Maddock, A. G. *Am. Mineral.* **1967**, *52*, 1009-1026.

of unique Fe centers present in a given compound. The constant C can be approximated as $C = (\Gamma_1 / \Gamma_2)$.[168] While Γ can be calculated from the obtained fit, the value of Γ varies depending on sample preparation. Therefore, assuming $C = (\Gamma_1 / \Gamma_2)$ is not always an accurate approximation and the percent components should be based solely on the areas under the peaks in the Mössbauer spectrum.

Synthesis

$C_6H_9(NHC_6H_4$-*o*-$NO_2)_3$ (2.5). A mixture of α-α-α-1,3,5-$NH_2C_6H_9 \cdot 3HBr$ (10.0 g, 22.9 mmol), 1-fluoro-2-nitrobenzene (19.3 g, 137 mmol) and Cs_2CO_3 (44.6 g, 114 mmol) in 400 mL CH_3CN was stirred and heated in an evacuated, sealed bomb reactor at 120 °C for 72 h. The resulting orange reaction mixture was then cooled to room temperature. The orange suspension was filtered through a fritted glass funnel. The resulting orange solid was washed with water (150 mL) to remove the Cs_2CO_3. The orange solid was then rinsed with a minimal amount of acetone (~50 mL) on a porous glass fritted funnel to remove excess fluoronitrobenzene. The orange solid was dried *in vacuo* overnight. Yield: 10.4 g (92%). HRMS (ESI^+) *m/z* calcd $C_{24}H_{24}N_6NaO_6^+$ $[M+Na]^+$: 515.16549, found 515.1692.

$C_6H_9(NHC_6H_4$-*o*-$NH_2)_3$ (2.6). Solid $C_6H_9(NHC_6H_4$-*o*-$NO_2)_3$ (5.00 g, 10.2 mmol) and Zn dust (9.95g, 152 mmol) were combined in a 500 mL round bottom. A 50:50 mixture of *saturated* NH_4Cl in water and degassed THF (total 300 mL) was added to the reaction vessel. The reaction was stirred vigorously until the orange color was no longer present. The suspension is filtered through Celite and washed with EtOAc (100 mL). The filtrate is extracted with EtOAc and H_2O. The organic layer is collected and dried with Na_2SO_4 and filtered again through Celite. The solvent was removed in vacuo to afford a brown oil. The brown oil, under inert atmosphere and with the use of anhydrous solvents, was purified by dissolving in a benzene (100 mL) and THF (20 mL) mixture. The white solid precipitated upon addition of hexanes (75 mL) to the brown solution.

168. Powers, T. M.; Fout, A. R.; Zhao, S.-L.; Betley, T. A. *J. Am. Chem. Soc.* **2011**, *133*, 3336-3338.

Filtration of the suspension through a fritted glass funnel gave the product as an off-white solid. Isolated yield: 3.29 g (80%). *Note:* More Zn may be added if the orange color is not fading. Also the hexa-amine oxidizes noticeably with exposure to air, thus care must be taken to expedite the work-up until placed under an inert atmosphere. ^{1}H NMR ($CDCl_3$, 500 MHz, δ, ppm): 6.83 (br, 3H, aromatic C–*H*), 6.76–7.71 (m, 9H, aromatic C–*H*), 3.51 (m, 3H, C_6H_9), 3.45 (br s, 9H, N*H*), 2.59 (br d, 3H, C_6H_9), 1.13 (m, 3H, C_6H_9); ^{13}C NMR ($CDCl_3$, 125 MHz, δ, ppm): 136.09, 134.60, 120.69, 118.99, 117.02, 113.06, 49.25, 40.28; HRMS (ESI^+) *m/z* calcd $C_{24}H_{30}N_6Na^+$ $[M+Na]^+$: 425.24242, found: 425.23881.

C_6H_9(NHC_6H_4-*o*-NH(SiMe_2(t-Bu))$_3$ ($^{tbs}LH_6$) (2.7). A 2.5*M* solution of *n*-butyllithium (3.07 g, 11.6 mmol) in hexanes was added cold (–33 °C) to LH_6 (1.50 g, 3.73 mmol) dissolved in 20 mL of THF. The mixture was stirred for 2 h at room temperature. To the reaction, tertbutyldimethylsilyl chloride (1.74 g, 11.6 mmol) in 5 mL of THF was added cold (–33 °C) and allowed to stir at room temperature for 18 h. The volatiles were removed *in vacuo*. Hexanes was added to the resulting green-brown solid and the precipitate was collected on a fritted glass funnel via cold filtration. The solid was then re-dissolved in benzene and filtered through Celite to remove the lithium chloride. The benzene solution was dried to afford $^{tbs}LH_6$ as an off-white solid. Yield: 1.25 g (45%) ^{1}H NMR (benzene-d_6, 500 MHz, δ, ppm): 6.98 (d, 3H, aromatic C–*H*, *J* = 8.00 Hz), 6.93–6.86 (m, 6H, aromatic C–*H*), 6.71 (d, 3H, aromatic C–*H*, *J* = 7.50 Hz), 3.53 (s, 3H, –Si–N*H*–C), 3.03-3.01 (m, 3H, C_6H_9), 2.81 (d, 3H, CH–N*H*–C, *J* = 7.50 Hz), 2.43 (br d, 3H, C_6H_9), 0.97 (s, 9H, –C(CH_3)$_3$), 0.94–0.89 (m, 3H, C_6H_9), 0.18 (s, 6H, –Si(CH_3)$_2$); ^{13}C NMR (benzene-d_6, 125 MHz, δ, ppm): –4.09, 17.82, 26.43, 41.08, 51.04, 118.37, 119.34, 120.10, 121.60, 137.72, 138.46; Anal. Calcd for $C_{42}H_{72}N_6Si_3$: C 67.68, H 9.74, N 11.28. Found: C 67.65, H 9.84, N 11.21.

(^{tbs}L)Fe$_3$(THF) (2.8). ^{tbs}LH$_6$ (0.300 g, 0.403 mmol) was dissolved in 30 mL of THF. The solution was added to solid Fe_2Mes_4 (0.355 g, 1.21 mmol) at room temperature. The reaction was heated in a sealed bomb at 80 °C for 12 h. The reaction was dried *in vacuo* to afford a brown oil. The flask containing the oil was placed in a liquid nitrogen cooled cold well in the dry box. Cold hexanes (40 mL, –33 °C) was added to the oil with stirring in order to remove the mesitylene biproduct. The hexane layer was decanted and the remaining black solid was dried under vacuum. Purity of the compound was established by the absence of (^{tbs}L)Fe$_2$ product in the ^{1}H NMR.[169] Isolated yield: 315 mg, (80%). X-ray quality crystals were grown in hexanes at –33 °C. ^{1}H NMR silent, Anal. Calcd for $C_{46}H_{74}N_6OFe_3Si_3$: C 56.44, H 7.62, N 8.59. Found: C 56.62, H 7.68, N 8.59; Zero-field ^{57}Fe Mössbauer (115 K) δ, $|\Delta E_Q|$ ($^{mm}/_s$)): component 1 (24%): 0.89, *1.69* (Γ = 0.24 $^{mm}/_s$); component 2 (35%): 0.49, *1.51*; component 3: (41%) 0.50, *1.89* (Γ = 0.35 $^{mm}/_s$) component 3: (41%) 0.50, *1.89* (Γ = 0.23 $^{mm}/_s$).

[(^{tbs}L)Fe$_3$]K(THF)(Et$_2$O)$_2$ (2.9). Solid ^{tbs}LH$_6$ (0.100 g, 0.134 mmol) was dissolved in 10 mL of THF. The solution was added to solid Fe_2Mes_4 (0.123 g, 0.416 mmol) at room temperature. The reaction was heated in a sealed bomb at 75 °C for 12 h. The solution was then added to solid KH (0.0059 g, 0.148 mmol) cold (–33 °C). Once the reaction reached room temperature, the solution was stirred for an additional 4 h. The volatiles were removed in vacuum resulting in a brown oil. The oil was washed with 20 mL hexanes and the remaining solid was dried to afford a solid. Zero-field ^{57}Fe Mössbauer (110 K) $|\Delta E_Q|$ ($^{mm}/_s$) component 1 (24%) 0.41,

169. In the absence of coordinating solvent, formation of the diiron cluster (^{tbs}L)Fe$_2$ is favored over formation of the triiron cluster. (^{tbs}L)Fe$_2$ was synthesized from the reaction of Fe_2Mes_4 (41 mg, 0.139 mmol) and ^{tbs}LH$_6$ (50 mg, 0.067 mmol) in benzene at 75 °C for 18 hours. ^{1}H NMR (benzene-d_6, 500 MHz, δ, ppm): 82.9, 52.3, 39.2, 37.7, 32.8, 25.0, 24.4, 23.2, 22.2, 20.1, 19.5, 14.5, 14.2, 12.9, 11.9, –2.31, –5.70, –15.2, –24.7, –32.2, –32.9, –34.0, –40.7. Full characterization of this compound can be found in **Chapter 5**.

1.9 (Γ = 0.22 $^{mm}/_{s}$); component 2 (35%) 0.35, *1.32* (Γ = 0.32 $^{mm}/_{s}$); component 3 (40%) 0.68, *2.10* (Γ = 0.38 $^{mm}/_{s}$). X-ray quality crystals of the potassium salt were grown from cold diethyl ether (–33 ^{o}C). A benzene/THF (3:1) solution (4 mL) of the crude product was added to solid 18-crown-6-ether (0.0389 g, 0.147 mmol). The solution was allowed to stir at room temperature for 1 h. The volatiles were removed in vacuum and the resultant oil was washed with 10 mL of diethyl ether. Benzene (10 mL) was added to the oil and removed in vacuum to yield a solid. Isolated yield: 0.107 g, (87%). Anal. Calcd for $C_{54}H_{90}Fe_3KN_6O_6Si_3$: C 53.59, H 7.50, N 6,94. Found: C 53.49, H 7.47, N 6.88.

[(^{tbs}L)Fe$_3$(μ^3-X)]NBu$_4$, X = Cl (2.10), Br (2.11), I (2.12). The following experimental section describes the synthesis of [(^{tbs}L)Fe$_3$(μ^3-I)]NBu$_4$ (**2.12**). All other μ^3-halide clusters were synthesized by an analogous method. Solid $^{tbs}LH_6$ (0.100 g, 0.134 mmol) was dissolved in 10 mL of THF. The solution was added to solid Fe_2Mes_4 (0.123 g, 0.416 mmol) at room temperature. The reaction was heated in a sealed bomb at 75 °C for 12 h. Solid I[NBu$_4$] (0.055 g, 0.149 mmol) was added to the reaction mixture cold (–33 °C). Once the reaction reached room temperature, the solution was stirred for an additional 4 h. The volatiles were removed in vacuum resulting in a brown oil. The brown oil was stirred in diethyl ether (10 mL) for 15 minutes and subsequently filtered through Celite. The resulting brown solid was dissolved in THF (2 mL), which was then azeotropically distilled with benzene to afford a solid. **[(^{tbs}L)Fe$_3$(μ^3-I)]NBu$_4$** (**2.12**) Isolated yield: 146 mg, (85%). X-ray quality crystals were grown from diethyl ether at –33 °C. ^{1}H NMR (benzene-d_6, 500 MHz, δ, ppm): 41.49, 40.68, 8.16, 6.88, 3.50, 3.00, 2.79, 2.40, 1.20, 0.94, 0.86, 0.65, 0.15, –51.18; Anal. Calcd for $C_{58}H_{102}N_7Fe_3Si_3I$: C 54.59, H 8.06, N 7.68. Found: C 54.74, H 8.15, N 7.66; Zero-field ^{57}Fe Mössbauer (110 K) (δ, $|\Delta E_Q|$ ($^{mm}/_{s}$)): 0.68, *1.39* (Γ = 0.25 $^{mm}/_{s}$).

[(^{tbs}L)Fe$_3$(μ^3-Br)]NBu$_4$ (2.11) Isolated yield: 141 mg, (85%). X-ray quality crystals were grown from diethyl ether at –33 °C. ^{1}H NMR (benzene-d_6, 500 MHz, δ, ppm): 198.1, 44.36, 37.35, 6.31, 1.91, 0.92, 0.15, –40.22; Zero-field ^{57}Fe Mössbauer (110 K) (δ, $|\Delta E_Q|$ ($^{mm}/_s$)): 0.71, *1.35* (Γ = 0.24 $^{mm}/_s$). **[(^{tbs}L)Fe$_3$(μ^3-Cl)]NBu$_4$ (2.10)** Isolated yield: 128 mg, (80%). X-ray quality crystals were grown from diethyl ether at –33 °C. ^{1}H NMR (benzene-d_6, 500 MHz, δ, ppm): 183.01, 44.13, 37.11, 35.18, 5.51, 2.16, 1.90, 0.96, 0.19, –34.91; Zero-field ^{57}Fe Mössbauer (110 K) (δ, $|\Delta E_Q|$ ($^{mm}/_s$)): 0.71, *1.29* (Γ = 0.20 $^{mm}/_s$).

[(^{tbs}L)Fe$_3$(μ^3-N)]NBu$_4$ (2.13). (^{tbs}L)Fe$_3$(THF) (0.100 g, 0.102 mmol) was dissolved in 8 mL of THF. A 2 mL THF solution of [N$_3$]NBu$_4$ (29 mg, 0.102 mmol) was added to the reaction mixture cold (–33 °C). Once the reaction reached room temperature, the solution was stirred for an additional 4 h. The volatiles were removed in vacuum to afford a brown oil. The brown oil was triturated with hexanes (20 mL 2x) and dried. Washing with cold (–33 ^{o}C) hexanes (10 mL) affords a brown solid. Isolated yield: 113 mg, (95%). X-ray quality crystals were grown from diethyl ether at –33 °C. ^{1}H NMR (benzene-d_6, 500 MHz, δ, ppm): 55.9, 16.4, 7.50, 6.38, 3.87, 3.69, 1.96, 1.57, 0.70, –3.20.; Anal. Calcd for C$_{58}$H$_{102}$N$_8$Fe$_3$Si$_3$: C 59.88, H 8.84, N 9.63. Found: C 59.74, H 8.78, N 9.49; Zero-field ^{57}Fe Mössbauer (120 K) (δ, $|\Delta E_Q|$ ($^{mm}/_s$)): component 1 (30%): 0.37, *1.78* (Γ = 0.12 $^{mm}/_s$); component 2 (70%): 0.39, *1.23* (Γ = 0.30 $^{mm}/_s$). UV-vis Spectroscopy (THF): 460 nm (ε = 4.34 × 10^4 M^{-1}cm^{-1}).

(^{tbs}L)Fe$_3$(μ^3-NMe) (2.14) To a THF (3 mL) solution of [(^{tbs}L)Fe$_3$(μ^3-N)]NBu$_4$ (100 mg, 0.09 mmol), 2 mL of a 0.045 mM solution of MeI in THF was added cold (–33 °C). The reaction was stirred at room temperature for 1 h. The volatiles were removed *in vacuo* resulting in a black oil. The product was extracted into hexanes (15 mL) and dried to afford a black solid. X-ray

quality crystals were grown in hexanes at –33 °C. Isolated yield: 30 mg (35%). ^{1}H NMR (benzene-d_6, 500 MHz, δ, ppm): 180.8, 90.23, 76.90, 10.83, 7.46, 4.24, 3.40, 2.74, 1.95, 1.50, 1.27, 1.25, 0.49, –3.40, –4.49; Anal. Calcd for $C_{43}H_{69}N_7Fe_3Si_3$: C 55.19, H 7.43, N 10.48. Found: C 55.13, H 7.39, N 10.42. Zero-field ^{57}Fe Mössbauer (115 K) (δ, $|\Delta E_Q|$ ($^{mm}/_{s}$)): component 1: (72%) 0.36, *1.69* (Γ = 0.22 $^{mm}/_{s}$); component 2 (28%) 0.37, *0.97* (Γ = 0.16 $^{mm}/_{s}$). UV-vis Spectroscopy (THF): 690 nm (ε = 4.07 × 10^4 $M^{-1}cm^{-1}$); 575 nm (ε = 5.18 × 10^4 $M^{-1}cm^{-1}$); 430 nm (ε = 6.73 × 10^4 $M^{-1}cm^{-1}$).

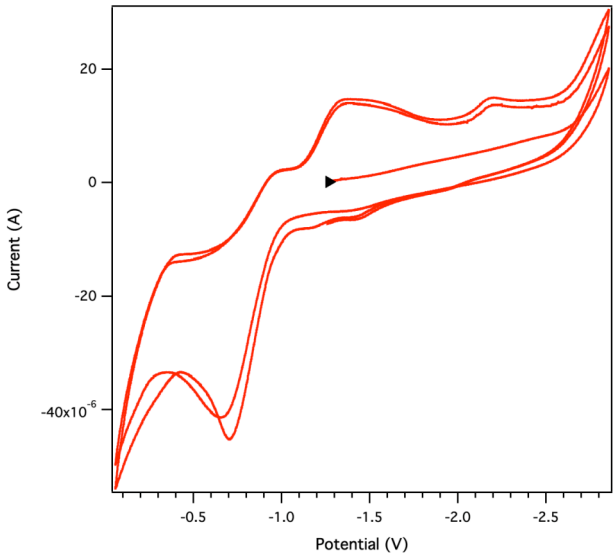

Figure 2.10. Cyclic voltammogram of 2 mM [(^{tbs}L)Fe_3(μ^3-Br)]NBu_4 **2.11** (glassy C working electrode, 0.1 M (Bu_4N)PF_6, scan rate 0.01 V/s in THF, referenced to $[Cp_2Fe]^{0/+}$). The irreversible reduction events do not appear until after scanning past –0.5 V in the anodic direction and therefore likely come from an oxidative byproduct due to some impurity formed during oxidation.

X-Ray Diffraction Techniques

All structures were collected on a Bruker three-circle platform goniometer equipped with an Apex II CCD and an Oxford cryostream cooling device at 100 K radiation for the data collection of **2.8**, **2.9**, **2.10**, **2.11**, **2.12**, **2.13** and **2.14** was from a graphite fine focus sealed tube Mo Kα (0.71073 Å) source. Crystals were mounted on a cryoloop or glass fiber pin using Paratone N oil. Data was collected as a series of φ and/or ω scans. Data was integrated using

SAINT[170] and scaled with either a numerical or multi-scan absorption correction using SADABS.[170] The structures were solved by direct methods or Patterson maps using SHELXS-97 and refined against F^2 on all data by full matrix least squares with SHELXL-97.[171] All non-hydrogen atoms were refined anisotropically. Hydrogen atoms were placed at idealized positions and refined using a riding model. The isotropic displacement parameters of all hydrogen atoms were fixed to 1.2 times the atoms they are linked to (1.5 times for methyl groups). Further details on particular structures are noted below.

(^{tbs}L)Fe$_3$(THF) (2.8). The structure was solved in the triclinic space group $P\ \bar{1}$ with 2 molecules per unit cell. The asymmetric unit was found to contain one molecule of (^{tbs}L)Fe$_3$(THF) and half of a solvent *n*-hexane molecule unit. The solvent *n*-hexane molecule exhibited positional disorder and was refined using similarity restraints.

[(^{tbs}L)Fe$_3$]K(THF)(Et$_2$O)$_2$ (2.9). The structure was solved in the triclinic space group $P\ \bar{1}$ with 2 molecules per unit cell. The asymmetric unit contains one molecule of [(^{tbs}L)Fe$_3$]K(THF)(Et$_2$O)$_2$. One of the ligand arms exhibited positional disorder. Similarity restraints were used to refine the model.

[(^{tbs}L)Fe$_3$(μ^3-Cl)]NBu$_4$ (2.10). The structure was solved in the orthorhombic space group *Pbca* with 8 molecules per unit cell. The asymmetric unit contains one [(^{tbs}L)Fe$_3$(μ^3-Cl)]NBu$_4$ molecule and one THF solvent molecule. Both the NBu$_4$ cation as well as the THF molecule exhibited positional disorder and were refined using similarity restraints

[(^{tbs}L)Fe$_3$(μ^3-Br)]NBu$_4$ (2.11). The structure was solved in the monoclinic space group $P2_1/n$ with 4 molecules per unit cell. The asymmetric unit contains one [(^{tbs}L)Fe$_3$(μ^3-Br)]NBu$_4$

170. Bruker AXS (2009). Apex II. Bruker AXS, Madison, Wisconsin.
171. Sheldrick, G. M. *Acta Cryst.* **2010**, *D66*, 479-485.

and one ether solvent molecule. The solvent molecule exhibited positional disorder and was refined using similarity restraints.

[(^{tbs}L)Fe$_3$(μ^3-I)]NBu$_4$ (2.12). The structure was solved in the orthorhombic space group *Pna*2$_1$ with 4 molecules per unit cell. The asymmetric unit contains one [(^{tbs}L)Fe$_3$(μ^3-I)]NBu$_4$ molecule. The crystal was twinned and exhibited positional disorder at both the NBu$_4$ cation and two of the three (Me)$_2$(^{t}Bu)Si– groups. Similarity restraints were used to refine the model.

[(^{tbs}L)Fe$_3$(μ^3-N)]NBu$_4$ (2.13). The structure was solved in the monoclinic space group *Cc* with 2 molecules per unit cell. The asymmetric unit contains one molecules of [(^{tbs}L)Fe$_3$(μ_3-N)]NBu$_4$ and one diethyl ether solvent molecules. One of the ligand arms exhibited positional disorder and one of the dimethyl-*tert*-butyl silyl groups exhibited positional disorder. Similarity restraints were used to refine the model. No electron density peak could be found above the N, which would suggest the presence of a hydrogen atom bound to the μ^3-N. The reactivity of the molecule indicates that there is no hydrogen on N7.

(^{tbs}L)Fe$_3$(μ^3-NCH$_3$) (2.14). The structure was solved in the triclinic space group $P\ \bar{1}$ with 2 molecules per unit cell. The asymmetric unit contains one (^{tbs}L)Fe$_3$(μ^3-NMe) molecule. The crystal was twinned and weakly diffracting resulting in a higher than usual R-value. However, the high R-value does not seriously affect the chemically significant features of the structures.

Table 2.2. X-ray Crystallographic Data for All Compounds

	2.8	**2.9**	**2.10**	**2.11**	**2.12**	**2.13**	**2.14**
Chemical formula	$C_{46}H_{74}N_6OFe_3Si_3$	$C_{61}H_{108}N_7OFe_3Si_3Cl$	$C_{61}H_{108}N_7OFe_3Si_3Cl$	$C_{62}H_{112}N_7OFe_3Si_3Br$	$C_{58}H_{102}N_7Fe_3Si_3I$	$C_{58}H_{102}N_8Fe_3Si_3$	$C_{43}H_{69}N_7Fe_3Si_3$
fw	1022.02	1166.27	1242.81	1303.32	1276.18	1237.42	935.87
Space group	$P\bar{1}$	$P\bar{1}$	*Pbca*	$P2_1/n$	$Pna2_1$	*Cc*	$P\bar{1}$
a (Å)	10.6174(10)	12.214(2)	26.839(3)	14.992(1)	18.516(4)	26.559(3)	10.057(2)
b (Å)	10.850(1)	13.452(2)	19.359(2)	19.034(2)	14.125(3)	11.667(1)	11.562(3)
c (Å)	23.503(2)	20.082(3)	27.601(4)	24.784(2)	24.427(6)	23.123(2)	20.327(4)
α (deg)	84.540(2)	97.290(2)					82.832(4)
β (deg)	83.122(2)	101.898(2)		93.671(1)		108.849(2)	89.866(4)
γ (deg)	75.734(2)	104.507(2)					89.039(4)
V (Å^3)	2599.1(4)	3067.6(7)	14340(3)	7058(1)	6389(1)	6781(1)	2345.0(9)
Z	2	2	8	4	4	2	2
μ (mm^{-1})	0.94	0.87	0.73	1.27	1.25	0.73	1.03
T (K)	100(1)	100(1)	100(1)	100(1)	100(1)		100(1)
R1[a] (wR2[b])	0.0375 (0.0920)	0.058 (0.158)	0.061 (0.190)	0.072 (0.182)	0.059 (0.135)	0.0489 (0.1042)	0.1196 (0.3115)

[a] $R1 = [\sum w(F_o - F_c)^2/\sum wF_o^2]^{1/2}$

[b] $wR2 = [\sum [w(F_o^2 - F_c^2)^2]/ \sum w(F_o^2)^2]^{1/2}$, $w = 1/[\sigma^2(F_o^2) + (aP)^2 + bP]$, where $P = [\max(F_o^2,0) + 2(F_c^2)]/3$

Chapter 3.[172] Testing the Polynuclear Hypothesis: Multi-electron Reduction of Small Molecules by Triiron Reaction Sites

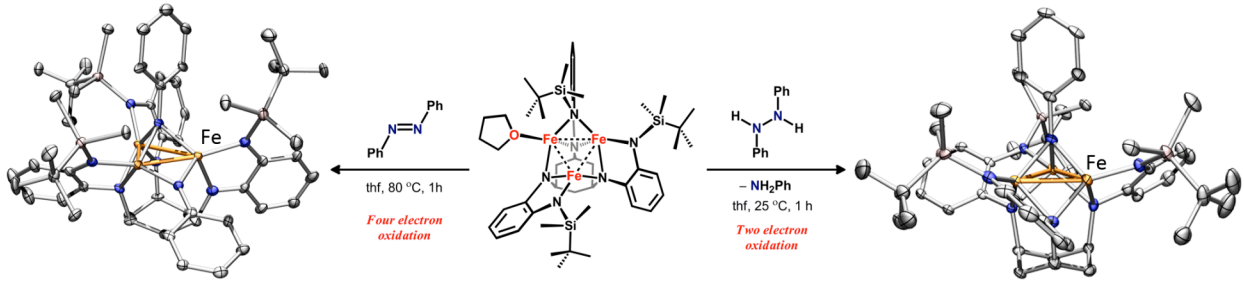

3-1. Introduction: the polynuclear hypothesis

Dinitrogen reduction is mediated biologically by the nitrogenase enzymes[28,29,30] and abiologically by the high temperature, high pressure combination of hydrogen and nitrogen gases in the Haber Bosch process.[173] Despite extensive efforts, the precise sequence of chemical steps in either catalytic system remains elusive.[28,101,173] Biologically, the $6e^{-}/6H^{+}$ reduction of dinitrogen to ammonia is achieved by the metalloenzyme nitrogenase[31] which contain FeMo, FeV, or Fe-only cofactors. Two hypotheses have been proposed regarding how N_2 activation occurs at the FeMoco of nitrogenase: (1) substrate uptake and reduction occur at a single metal center, presumably Mo, by a Chatt-like mechanism;[174,175,176] or (2) a polynuclear Fe face of the cluster mediates all requisite reaction chemistry.[53] The mononuclear hypothesis is predicated on the ability of the Mo atom to access multiple oxidation states. Functional model complexes featuring mononuclear Mo sites have been prepared and have demonstrated that mononuclear Mo complexes are capable of performing N_2 conversion to ammonia and amine-containing

172. This chapter was adapted with permission from Powers, T. M.; Betley, T. A. *J. Am. Chem. Soc.* **2013**, *submitted*. Unpublished work Copyright 2013 American Chemical Society.
173. Ertl, G. *Angew. Chem., Int. Ed.* **2008**, *7*, 3524-3535.
174. Pickett, C. J. *J. Biol. Inorg. Chem.* **1996**, *1*, 601-606.
175. Peters, J. C.; Mehn, M. P. Bio-organometallic Approaches to Nitrogen Fixation Chemistry. In *Activation of Small Molecules*; Tolman, W. B., Ed.; Wiley: Weinheim, 2006; p 81-119.
176. Holland, P. L. Nitrogen Fixation. In *Comprehensive Coordination Chemistry II*; McCleverty, J. A.; Meyer, T. J. eds.; Elsevier: Oxford, 2004; Vol. 8, p 569-599.

products.[174,177,178,179] However, site-mutagenesis at the valine residue α-70^{Val} located above the Fe2, Fe3, Fe6, Fe7 tetrairon face of FeMoco (Section **1-4-1**, Figure 1.4) inhibits substrate binding,[33,89] suggesting the polynuclear Fe face could be the site of substrate uptake and activation.[53,86,88,180] While significant research efforts have focused on structural Fe cluster models of the nitrogenase cofactor,[77,181,182] model complexes that test the viability of polynuclear reaction sites towards effecting multi-electron reduction of small molecule substrates are less well studied.[168]

To test the ability of a polynuclear metal complex to mediate small molecule activation, we have designed flexible, multinucleating ligands to direct the formation of predesigned polynuclear architectures.[143,144,145,168] Using hexadentate ligand platforms comprised of *o*-phenylenediamine-based subunits, we have observed facile construction of polynuclear Fe complexes whose intracore interactions (Fe–Fe: 2.274(1)–2.607(1) Å) and molecular spin states (S = 1–6) vary as a function of ligand architecture.[145,168] Within this family of Fe cluster complexes, core-delocalized[143,145] as well as site-isolated redox events[146] with attendant ligand reorganization have been observed. Preparation of a Fe_3 complex with the sterically restricted ligand variant 1,3,5-$C_6H_9(NHC_6H_4$-*o*-$NHSiMe_2{}^tBu)_3$ ($^{tbs}LH_6$) affords the complex (^{tbs}L)Fe_3(THF) (**3.1**) with a high-spin ground state (S = 6).[168] It was demonstrated in Chapter 2 that complex **3.1** is unique amongst coordination complexes of Fe in that reaction with inorganic azide affords the trinuclear nitrido complex [(^{tbs}L)$Fe_3(\mu^3$-N)]NBu_4 (**3.2a**) at ambient temperature, without requiring photolysis of the azide (Scheme 3.1).[168] Here, we describe the two and four e^-

177. Yandulov, D. V.; Schrock, R. R. *Science* **2003**, *301*, 76-78.
178. Shilov, A. E. *Russ. Chem. Bull. Int. Ed.* **2003**, *52*, 2555-2562.
179. Arashiba, K.; Miyake, Y.; Nishibayashi, Y. *Nature Chem.* **2011**, *3*, 120-125.
180. Christiansen, J.; Cash, V. L.; Seefeldt, L. C.; Dean, D. R. *J. Biol. Chem*. **2000**, *275*, 11459-11464.
181. Han, J.; Beck, K.; Ockwig, N.; Coucouvanis, D. *J. Am. Chem. Soc.* **1999**, *121*, 10448-10449.
182. Coucouvanis, D.; Han, J.; Moon, N. *J. Am. Chem. Soc.* **2002**, *124*, 216-224.

reduction of hydrazine and diazene substrates, respectively, by the high-spin, all-ferrous complex **3.1** to afford imido and nitrido products.

3-2. Results and discussion

Treatment of Fe_3 cluster **3.1** with hydrazine (Scheme 3.1) at room temperature results in the liberation of ammonia, as detected by ^{1}H NMR spectroscopy following vacuum transfer of the reaction volatiles into a HCl/Et_2O solution, as well as a new complex with a paramagnetically shifted ^{1}H NMR spectrum. The zero-field ^{57}Fe Mössbauer spectrum of the crude reaction mixture features a broad quadrupole doublet (δ, $|\Delta E_Q|$ ($^{mm}/_s$): 0.50, *1.4* (Γ = 0.46 mm/s)) with a decreased isomer shift relative to **3.1** and other all ferrous Fe_3 clusters synthesized in our lab (*vide infra*) indicating that the product from complex **3.1** and hydrazine likely features an oxidized trinuclear core. Substituting phenylhydrazine for hydrazine in the reaction with **3.1** results in quantitative formation of Fe_3 imido complex (^{tbs}L)$Fe_3(\mu^3$-NH) (**3.3**) and aniline in 24% isolated yield (identified and quantified by ^{1}H NMR spectroscopy) with no detectable formation of ammonia during the course of the reaction. Complex **3.3**, also observed as a product of the reaction of **3.1** with hydrazine (determined by ^{1}H NMR spectroscopy), has a solution magnetic moment of 5.8(1) μ_B (determined by Evans method) and a zero-field ^{57}Fe Mössbauer spectrum featuring two quadrupole doublets (δ, $|\Delta E_Q|$ ($^{mm}/_s$): component 1: 0.37, *1.94* (78%) component 2: 0.40, *1.17* (22%)). The Mössbauer fitting parameters are very similar to those observed for nitrido anion **3.2a** (see Table 3.1 for comparison of spectroscopic features), which is consistent with a delocalized $2e^-$ oxidation at the Fe_3 core.

Despite the high yield of the paramagnetic product **3.3** during the reaction of **3.1** with phenylhydrazine, the high solubility of **3.3** in all organic solvents prevented isolation of crystals suitable for X-ray crystallographic analysis. In support of our assignment of species **3.3** as the

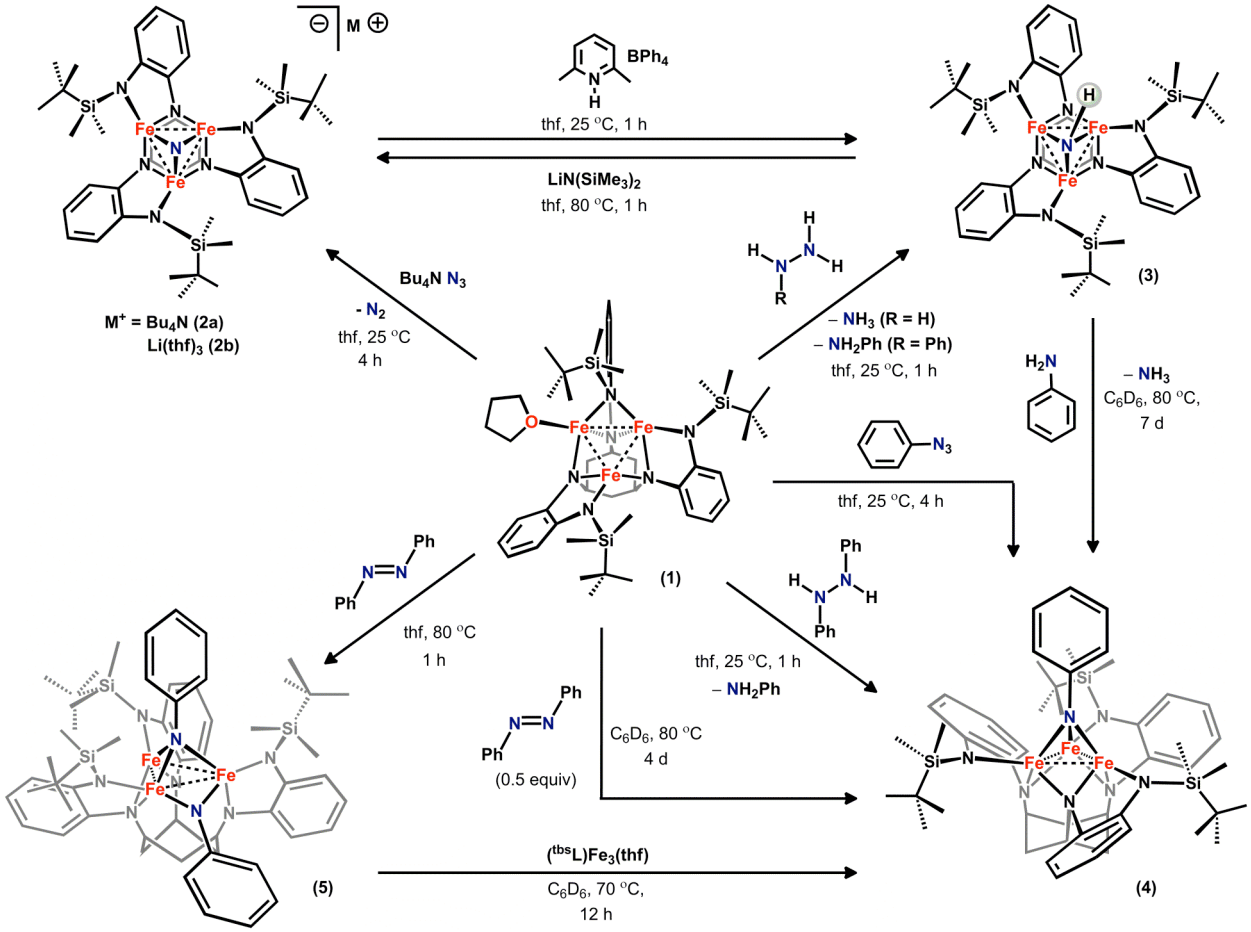

Scheme 3.1. $2e^-$ and $4e^-$ reduction of nitrogenous substrates by (^{tbs}L)Fe$_3$(THF).

Table 3.1. Structural, spectral, and magnetic properties of selected complexes

Complex		$Fe–Fe_{avg}$ (Å)	μ_{eff} (μ_B)	δ ($^{mm}/_{s}$)	$\lvert\Delta E_Q\rvert$ ($^{mm}/_{s}$)	Reference
(^{tbs}L)Fe_3(THF)	**3.1**	2.577(6)	12.0(2)	0.89	1.68	168
				0.49	1.55	
				0.50	1.92	
[(^{tbs}L)Fe_3(μ^3-N)][NBu_4]	**3.2a**	2.480(1)	7.3(2)	0.37	1.78	168
				0.39	1.23	
[(^{tbs}L)Fe_3(μ^3-N)]Li$(THF)_3$	**3.2b**	2.480(1)		0.33	1.34	
(^{tbs}L)Fe_3(μ^3-NH)	**3.3**		5.8(1)	0.37	1.94	
				0.40	1.17	
(^{tbs}L)Fe_3(μ^3-NPh)	**3.4**	2.530(1)	6.6(4)	0.42	1.97	
				0.42	1.09	
(^{tbs}L)Fe_3(μ^3-NPh)(μ^2-NPh)	**3.5**	2.684(1)		0.24	1.46	
				0.45	2.61	
				0.34	1.35	
(^{tbs}L)Fe_3(μ^3-NMe)		2.483(3)	5.3(2)	0.37	0.94	168
				0.36	1.67	
Fe_4(μ^3-N^{t}Bu)$_4Cl_4$				0.35	0.55	183
[Fe_4(μ^3-N^{t}Bu)$_4$(N^{t}Bu)Cl_3]				-0.17	0.38	183
				0.36	0.43	
[(^{tbs}L)Fe_3(μ^3-Br)]NBu_4	**3.6**	2.771(9)	11.9(4)	0.71	1.35	
(^{H}L)Fe_3(PMe_3)$_3$		2.300(2)	3.0	0.38	1.03	143

(^{tbs}L)Fe$_3$(μ^3-NH) cluster, treatment of [(^{tbs}L)Fe$_3$(μ^3-N)]NBu$_4$ (**3.2a**) with lutidinium tetraphenylborate results in formation of a new complex, which displays an identical paramagnetic ^{1}H NMR spectrum to those assigned as **3.3** from the reactions of **3.1** with hydrazine or phenyl hydrazine (Scheme 3.1). Based on the formulation of **3.3** as (^{tbs}L)Fe$_3$(μ^3-NH), protonation of the nitride moiety in **3.2a** with lutidinium tetraphenylborate affords **3.3** in 85% yield. Treatment of complex **3.3** with a suitable H-atom transfer reagent such as TEMPO-H (1-hydroxy-2,2,6,6-tetramethylpiperidine) led to the evolution of ammonia, as identified by ^{1}H NMR spectroscopy following vacuum transfer of the reaction volatiles.

Deprotonation of **3.3** with lithium *bis*-(trimethylsilyl)amide results in regeneration of Fe$_3$ nitride capped with a THF-solvated Li cation [(^{tbs}L)Fe$_3$(μ^3-N)]Li(THF)$_3$ (**3.2b**) in 76% isolated

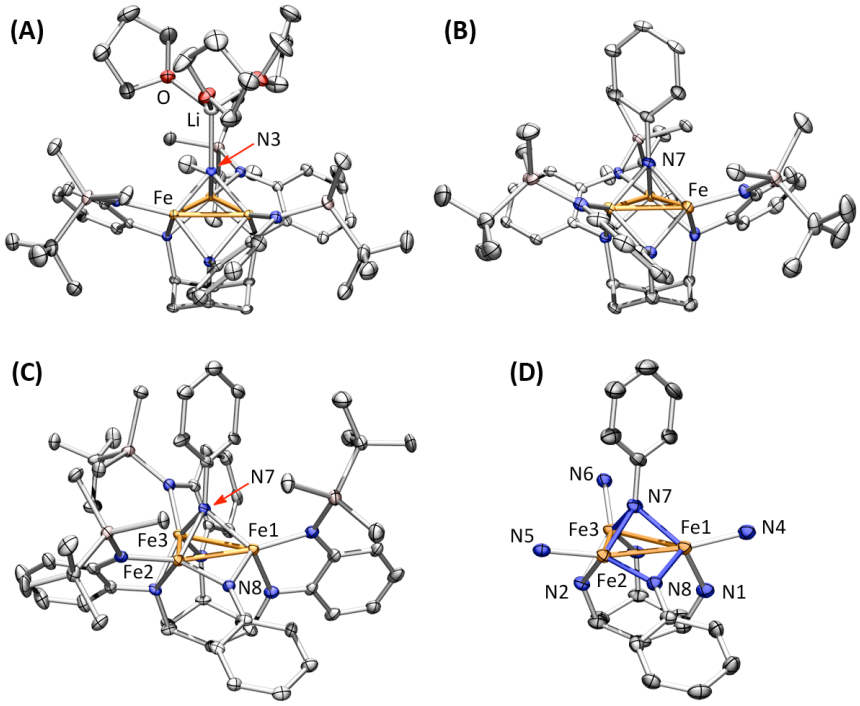

Figure 3.1. Solid-state structures for (A) [(^{tbs}L)Fe$_3$(μ^3-N)]Li(THF)$_3$ (**3.2b**), (B) (^{tbs}L)Fe$_3$(μ^3-NPh) (**3.4**), (C) (^{tbs}L)Fe$_3$(μ^3-NPh)(μ^2-NPh) (**3.5**) (core highlights of **3.5** in D) with the thermal ellipsoids set at the 50% probability level (hydrogen atoms and solvent molecules omitted for clarity; Fe orange, C gray, N blue, O red, Si Pink, Li white). Selected bond lengths (Å) for (**3.2b**): Fe–Fe, 2.4802(5); Fe–N3, 1.877(2); N3–Li, 1.990(6); for (**3.4**): Fe1–Fe2, 2.549(1); Fe1–Fe3, 2.502(1); Fe2–Fe3, 2.539(1); Fe1–N7, 1.935(5); Fe2–N7, 1.944(5); Fe3–N7, 1.944(5); for (**3.5**): Fe1–Fe2, 2.482(1); Fe1–Fe3, 2.966(1); Fe2–Fe3, 2.604(1); Fe1–N7, 1.973(4); Fe2–N7, 1.982(4); Fe3–N7, 1.904(4); Fe1–N8, 1.866(4); Fe2–N8, 1.848(4).

yield (Scheme 1), which has been crystallographically characterized (Figure 3.1A). The crystallographically determined bond metrics for lithium-capped **3.2b** are similar to the previously reported nitride (**3.2a**)[168] but features a rigorously C_3-symmetric complex (space group $Pa\bar{3}$) (Fe–Fe, 2.4802(5) Å; Fe–N3, 1.877(2) Å; N3–Li, 1.990(6) Å Figure 3.1A). The C_3-symmetry is also manifested as a single quadrupole doublet in the Mössbauer spectrum (δ, $|\Delta E_Q|$ ($^{mm}/_s$): 0.33, *1.34*) (Figure 2.1A).

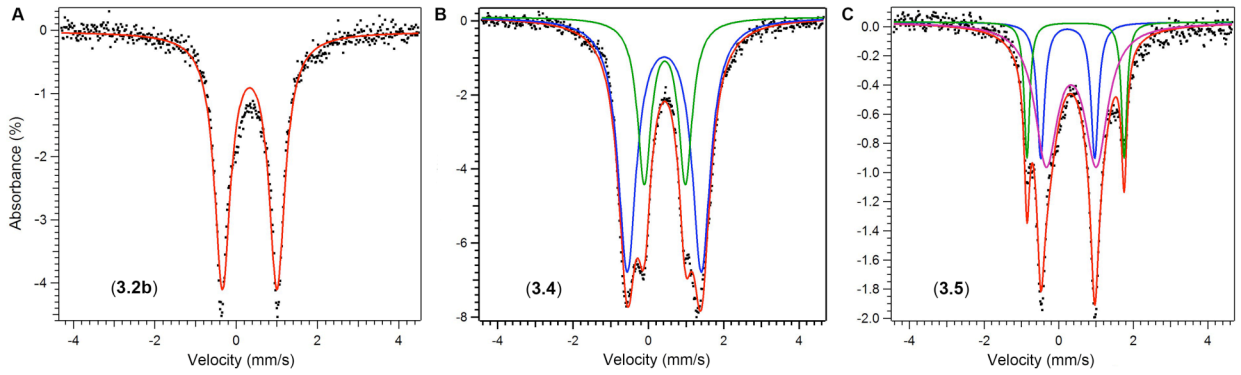

Figure 3.2. Zero-field ^{57}Fe Mössbauer spectrum of (A) [(^{tbs}L)Fe$_3$(μ^3-N)]Li(THF)$_3$ (**3.2b**), (B) (^{tbs}L)Fe$_3$(μ^3-NPh) (**3.4**), and (C) (^{tbs}L)Fe$_3$(μ^3-NPh)(μ^2-NPh) (**3.5**) obtained at 90 K. Fitting parameters [δ, $|\Delta E_Q|$ ($^{mm}/_s$)] for **3.2b**: 0.33, *1.34* (Γ = 0.24 $^{mm}/_s$); for **3.4**: component 1 (blue, 67%) 0.42, *1.97* (Γ = 0.29 $^{mm}/_s$); component 2 (green, 33%) 0.42, *1.09* (Γ = 0.22 $^{mm}/_s$); and for **3.5**: component 1 (blue, 21%) 0.24, *1.46* (Γ = 0.12 $^{mm}/_s$); component 2 (green, 18%) 0.45, *2.61* (Γ = 0.10 $^{mm}/_s$); component 3 (magenta, 60%) 0.34, *1.33* (Γ = 0.36 $^{mm}/_s$).

No ammonia was detected following the formation of imido complex **3.3** by treatment of **3.1** with phenylhydrazine (1h, 25 ^{o}C). However, heating the crude reaction mixture at 80 ^{o}C for 7 days produced a new compound that displayed a paramagnetically shifted ^{1}H NMR spectrum distinct from **3.3**, along with formation of ammonia (identified via ^{1}H NMR following vacuum transfer of the reaction volatiles). The similarities between the ^{1}H NMR spectra of this new species and the ^{1}H NMR spectrum of **3.3** suggest that a transamination has occurred between (^{tbs}L)Fe$_3$(μ^3-NH) and aniline remaining from phenylhydrazine reduction to yield phenylimido complex (^{tbs}L)Fe$_3$(μ^3-NPh) (**3.4**) (Scheme 3.1). Addition of a THF solution of 1,2-diphenylhydrazine to **3.1** in THF also produces **3.4** (determined by ^{1}H NMR spectroscopy) (83%

isolated yield) and free aniline (identified and quantified by ^{1}H NMR). Complex **3.4** can also be synthesized by treatment of Fe_3 cluster **3.1** with phenyl azide in a 98% yield (Scheme 3.1). Zero-field ^{57}Fe Mössbauer analysis of Fe_3 imido **3.4** features two quadrupole doublets (δ, $|\Delta E_Q|$ ($^{mm}/_s$): component 1: 0.42, *1.97* (67%) component 2: 0.42, *1.09* (33%)) (Figure 3.2B), which have similar parameters to **3.2** and **3.3** (Table 3.1). Single crystals from the reaction of **3.1** with phenyl azide were grown from cold hexanes (–33 ^{o}C) and contained the μ^3-phenylimido species (^{tbs}L)Fe$_3$(μ^3-NPh) (**3.4**) (6.6(4) μ_B; Figure 3.1B). Complex **3.4** is structurally similar to methyl imido complex (^{tbs}L)Fe$_3$(μ^3-NMe),[168] featuring a central μ^3-imido ligand with average Fe–N$_{imido}$ and Fe–Fe bond lengths of 1.941(6) Å and 2.530(1) Å, respectively (Table 3.1).

With the knowledge that complex **3.1** could readily activate the N–N bonds in hydrazine and inorganic and organic azides, we investigated the reaction of **3.1** with azobenzene. Addition of 0.5–1 equivalents of azobenzene to compound **3.1** followed by heating at 80 ^{o}C for 4 days leads to the formation of phenylimido complex **3.4** as the major paramagnetic product as identified by both ^{1}H NMR and Mössbauer spectroscopies (Scheme 3.1). This reaction also proceeds at room temperature, albeit over longer time spans. Monitoring the reaction by ^{1}H NMR, we find that complex **3.4** is not the first observable species detected upon addition of azobenzene to **3.1**. The initial product formed showed paramagnetically shifted resonances, which diminish over time give rise to resonances corresponding to **3.4**. Addition of 1 equivalent of azobenzene to **3.1** followed by heating at 80 ^{o}C for 1 h generated this intermediate prior to the appearance of compound **3.4** as ascertained by ^{1}H NMR. Storage of this product at –33 ^{o}C in a mixture of hexanes and heptane precipitated crystalline material suitable for isolation and analysis (17% crystalline yield). Treatment of this intermediate with one equivalent of **3.1** (70 $^\circ$C, 12h) produces the phenylimido product **3.4** (as identified by ^{1}H NMR). Crystallization from a

concentrated heptane solution at –33 °C produced crystals suitable for X-ray diffraction analysis. The solid-state structure revealed the intermediate as the Fe_3 *bis*-imido cluster (^{tbs}L)Fe_3(μ^3-NPh)(μ^2-NPh) (**3.5**) (Scheme 3.1, Figure 3.1C) in which the molecule has been oxidized by 4e^- and the N=N double bond of azobenzene has been cleaved. The crystal structure of complex **3.5** features two molecules in the asymmetric unit with several structural features similar to **3.4**, most notably a central μ^3-imido ligand. While the average μ^3-N_{imido}–Fe bond lengths in **3.4** and **3.5** are nearly identical (1.941(6) Å and 1.953(5) Å, respectively), the Fe–Fe separations in **3.5** are significantly elongated from **3.4** (molecule A: Fe1–Fe2, 2.482(1) Å; Fe1–Fe3, 2.966(1) Å; Fe2–Fe3, 2.604(1) Å; molecule B: Fe4–Fe5, 2.481(1) Å; Fe4–Fe6, 3.244(1) Å; Fe5–Fe6, 2.594(1) Å) (Table 3.1). The average Fe–N distance to the μ^2-imido ligand is shorter than that found to the μ^3-imido ligand (1.857(5) Å and 1.953(5) Å respectively). In order to accommodate the second imido unit bound to Fe centers Fe1 and Fe2 (Figure 3.1C), the (^{tbs}L)$^{6-}$ ligand based amide groups reorganize to optimize the bonding interaction with the two imido moieties. Such ligand reorganization has been previously reported upon oxidation of Fe clusters with open-shell electron configurations.[146] Each of the (^{tbs}L)$^{6-}$ ligand peripheral amide groups remain terminally bound to a single Fe center and only one of the three internal alkyl aryl amide moieties (N2) bridge adjacent metal centers.

Charge balance would indicate that *bis*-imido cluster **3.5** has undergone a four-electron oxidation, suggestive of a (Fe^{IV})(Fe^{III})$_2$ formulation. The N–C and C–C bond metrics in the *o*-phenylenediamide subunits of the (^{tbs}L)$^{6-}$ ligand in **3.1**, **3.2a**, **3.4**, and **3.5** are similar, alluding to the lack of substantial ligand redox participation during the oxidation event leading to formation of **3.5** (Table 3.2). Comparison of the Fe–ligand amide bond distances within cluster **3.5** does not reveal which metal center bears the 4+ charge (see **Section 3-4**, *vide infra*).

Table 3.2. Selected ligand bond distances (Å) **3.1**, **3.2a**, **3.4**, and **3.5**.

Compound	3.1	3.2a	3.4	3.5
C7—C8	1.391(4)	1.386(5)	1.386 (8)	1.417 (7)
C7—N1	1.410(3)	1.434(5)	1.421 (7)	1.340 (6)
C7—C12	1.428(4)	1.430(6)	1.425 (8)	1.453 (7)
C8—C9	1.392(4)	1.389(6)	1.396 (8)	1.377 (8)
C9—C10	1.378(4)	1.387(7)	1.391 (8)	1.415 (8)
C10—C11	1.396(4)	1.390(6)	1.379 (8)	1.369 (7)
C11—C12	1.388(4)	1.415(6)	1.419 (8)	1.407 (7)
C12—N4	1.443(3)	1.393(5)	1.386 (7)	1.369 (6)
C13—C14	1.397(4)	1.386(6)	1.393 (8)	1.394 (7)
C13—C18	1.420(4)	1.431(5)	1.408 (8)	1.408 (7)
C13—N2	1.430(3)	1.448(5)	1.432 (7)	1.444 (6)
C14—C15	1.390(4)	1.390(6)	1.368 (9)	1.385 (8)
C15—C16	1.388(4)	1.390(6)	1.38 (1)	1.380 (8)
C16—C17	1.384(4)	1.385(6)	1.402 (9)	1.387 (8)
C17—C18	1.405(4)	1.395(6)	1.409 (8)	1.399 (7)
C18—N5	1.402(3)	1.376(5)	1.411 (7)	1.403 (6)
C19—C24	1.428(4)	1.432(5)	1.402 (8)	1.428 (7)
C19—C20	1.395(3)	1.383(5)	1.400 (8)	1.418 (7)
C19—N3	1.426(3)	1.431(4)	1.432 (7)	1.351 (6)
C20—C21	1.392(4)	1.398(6)	1.380 (9)	1.374 (7)
C21—C22	1.383(4)	1.382(7)	1.38 (1)	1.407 (8)
C22—C23	1.389(4)	1.374(6)	1.382 (9)	1.367 (7)
C23—C24	1.402(3)	1.408(5)	1.411 (8)	1.423 (7)
C24—N6	1.410(3)	1.387(5)	1.399 (8)	1.358 (6)

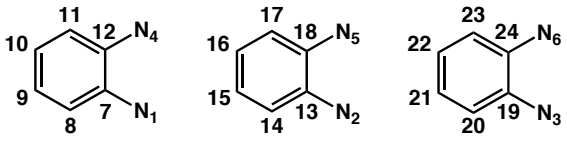

The zero-field ^{57}Fe Mössbauer spectrum of bis-imido complex **3.5** (Figure 3.3c) was fit with three quadrupole doublets (δ, $|\Delta E_Q|$ ($^{mm}/_s$): component 1: 0.24, *1.46* (21%) component 2: 0.45, *2.61* (18%) component 3: 0.34, *1.35* (60%); Table 1). The isomer shifts observed for **3.5** are lower relative to those observed in the $2e^-$ oxidized clusters in **3.2**–**3.4**, though a rigorous comparison between species cannot be made given the dramatic changes observed for the local iron coordination environments. Lee and coworkers have observed isomer shifts at ~0.35 mm/s for high-spin imidoiron(III) cubanes $Fe_4(\mu^3\text{-}N^tBu)_4Cl_4$ and $[Fe_4(\mu^3\text{-}N^tBu)_4(N^tBu)Cl_3]$ and an isomer shift of –0.17 $^{mm}/_s$ for the Fe^{IV} center bound to a terminal imide group in complex $[Fe_4(\mu^3\text{-}N^tBu)_4(N^tBu)Cl_3]$ (Table 3.1).[183] We hypothesize that the overall higher isomer shifts of 0.24, 0.34, and 0.45 $^{mm}/_s$ for compound **3.5** relative to Lee's iron imido cubanes could be due to cooperative binding of the imido moieties to multiple metal centers. Imido ligand binding to multiple metal centers may result in an overall decrease in e^- donation thereby deshielding the 1*s* orbital less at each metal center relative to that if the substrate was bound to a single metal center.

The presence of a formally tetra-valent Fe center in **3.5** prompted us to investigate the redox limits of clusters **3.2a**, **3.3**, **3.4**, and an isostructural, all-ferrous Fe_3 cluster $[(^{tbs}L)Fe_3(\mu^3\text{-}Br)]NBu_4$ (**3.6**) (Chapter 2, *vide supra*). The cyclic voltammograms for both imido Fe_3 clusters **3.3** and **3.4** feature three well-separated redox events and possess nearly identical open circuit potentials (–1.14 V and –1.13 V respectively) (Figure 3.3). Each imido complex exhibits two quasi-reversible one-electron reduction processes [$E_{1/2}$ (V) for **3.3**: –1.36, –2.54; for **3.4**: –1.25, –2.48] as well as a single irreversible one-electron oxidation event [peak anodic current (V) for

183. Verma, A. K.; Nazif, T. N.; Achim, C.; Lee, S. C. *J. Am. Chem. Soc.* **2000**, *122*, 11013-11014.

3.3: –0.20, **3.4:** –0.12] (Table 3.3). These electrochemical events suggest that the imido complexes can traverse three molecular redox states, which we formulate as $(Fe^{II})_3 \rightarrow (Fe^{III})_3$.

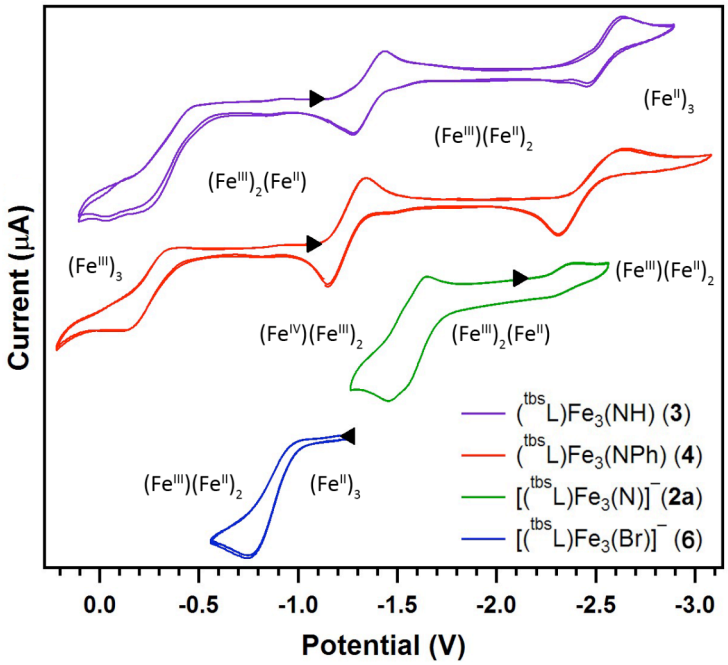

Figure 3.3. Cyclic voltammograms of **3.2a** (green, 2 mM), **3.3** (purple, 3 mM), **3.4** (red, 3 mM), **3.6** (blue, 2 mM) using standard conditions (glassy C working electrode, 0.1 M $(Bu_4N)PF_6$, scan rate 0.01 V/s in THF, referenced to $[Cp_2Fe]^{+/0}$).

Table 3.3. Redox potentials of selected compounds

Compound	Open circuit potential (V)[a]	Redox Potential (V)[a]	Oxidation Event
3.2a	–2.25	–1.48	$(Fe^{III})_3 \rightarrow (Fe^{III})_2(Fe^{IV})$
		–1.60	$(Fe^{II})(Fe^{III})_2 \rightarrow (Fe^{III})_2$
		–2.41[c]	$(Fe^{II})_2(Fe^{III}) \rightarrow (Fe^{II})(Fe^{III})_2$
3.3	–1.14	–0.20[b]	$(Fe^{II})(Fe^{III})_2 \rightarrow (Fe^{III})_3$
		–1.36	$(Fe^{II})_2(Fe^{III}) \rightarrow (Fe^{II})(Fe^{III})_2$
		–2.54	$(Fe^{II})_3 \rightarrow (Fe^{II})_2(Fe^{III})$
3.4	–1.13	–0.12[b]	$(Fe^{II})(Fe^{III})_2 \rightarrow (Fe^{III})_3$
		–1.25	$(Fe^{II})_2(Fe^{III}) \rightarrow (Fe^{II})(Fe^{III})_2$
		–2.48	$(Fe^{II})_3 \rightarrow (Fe^{II})_2(Fe^{III})$
3.6	–1.29	–0.74[b]	$(Fe^{II})_3 \rightarrow (Fe^{II})_2(Fe^{III})$

[a]Referenced to $[Cp_2Fe]^{+/0}$; [b]Peak anodic current; [c]Peak cathodic current.

Based on the observed electrochemical behavior of **3.3** and **3.4**, we sought to isolate the $1e^-$ oxidation and reduction products of (^{tbs}L)Fe$_3$(μ^3-NR) type complexes. One-electron reduction of the analogous Fe$_3$-adamantylimido cluster (^{tbs}L)Fe$_3$(μ^3-NAd) (**3.7**), synthesized via reaction of (^{tbs}L)Fe$_3$(THF) (**3.1**) with adamantyl azide (N_3Ad), was achieved with KC_8 and resulted in formation of the formally (Fe^{III})(Fe^{II})$_2$ cluster [(^{tbs}L)Fe$_3$(μ^3-NAd)]K(THF)$_4$ (**3.8**) (Scheme 3.2). X-ray crystallographic analysis of **3.7** and **3.8** revealed that the [(^{tbs}L)Fe$_3$(μ^3-NAd)]$^-$ anion is structurally similar to its neutral counterpart and exhibits an overall elongation of the Fe–Fe separations relative to the formally (Fe^{III})$_2$(Fe^{II}) cluster (Fe–Fe$_{avg}$ for **3.7**: 2.5297(8) and for **3.8**: 2.561(1) Å, Figure 3.4A). Unlike the Mössbauer spectrum of the neutral cluster (^{tbs}L)Fe$_3$(μ^3-NAd) (**3.7**), which features a single quadrupole doublet, a result of rigorous C_3 symmetry in the solid-state ($R\bar{3}c$), [(^{tbs}L)Fe$_3$(μ^3-NAd)]K($C_{12}H_{24}O_6$) (**3.8**), in which the K^+ ion is sequestered with 18-crown-6, features two quadrupole doublets with nearly identical isomer shifts and slightly different quadrupole splittings (δ ($^{mm}/_s$), $|\Delta E_Q|$ ($^{mm}/_s$) component 1 (blue, 65%) 0.49, *1.13* (Γ = 0.13 $^{mm}/_s$); component 2 (green, 35%) 0.46, *1.50* (Γ = 0.10 $^{mm}/_s$)) (Figure 3.4B). The increase in

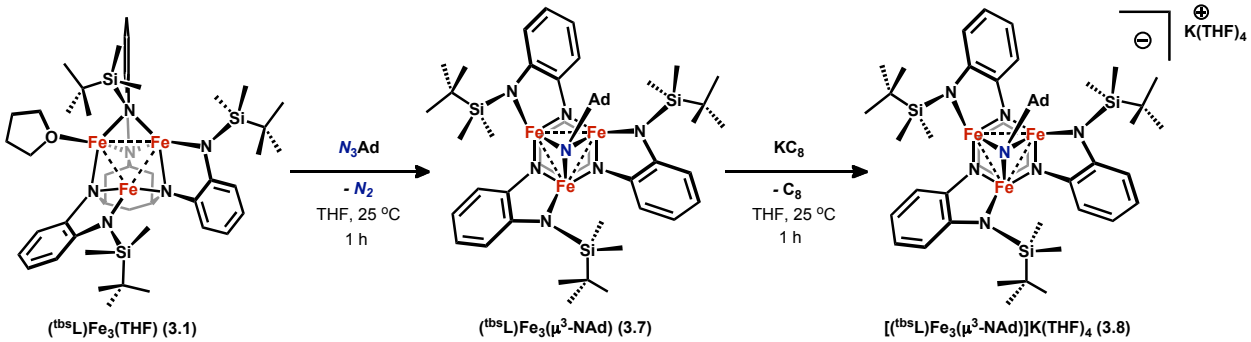

Scheme 3.2. Chemical reduction of (^{tbs}L)Fe$_3$(μ^3-NAd) with KC_8.

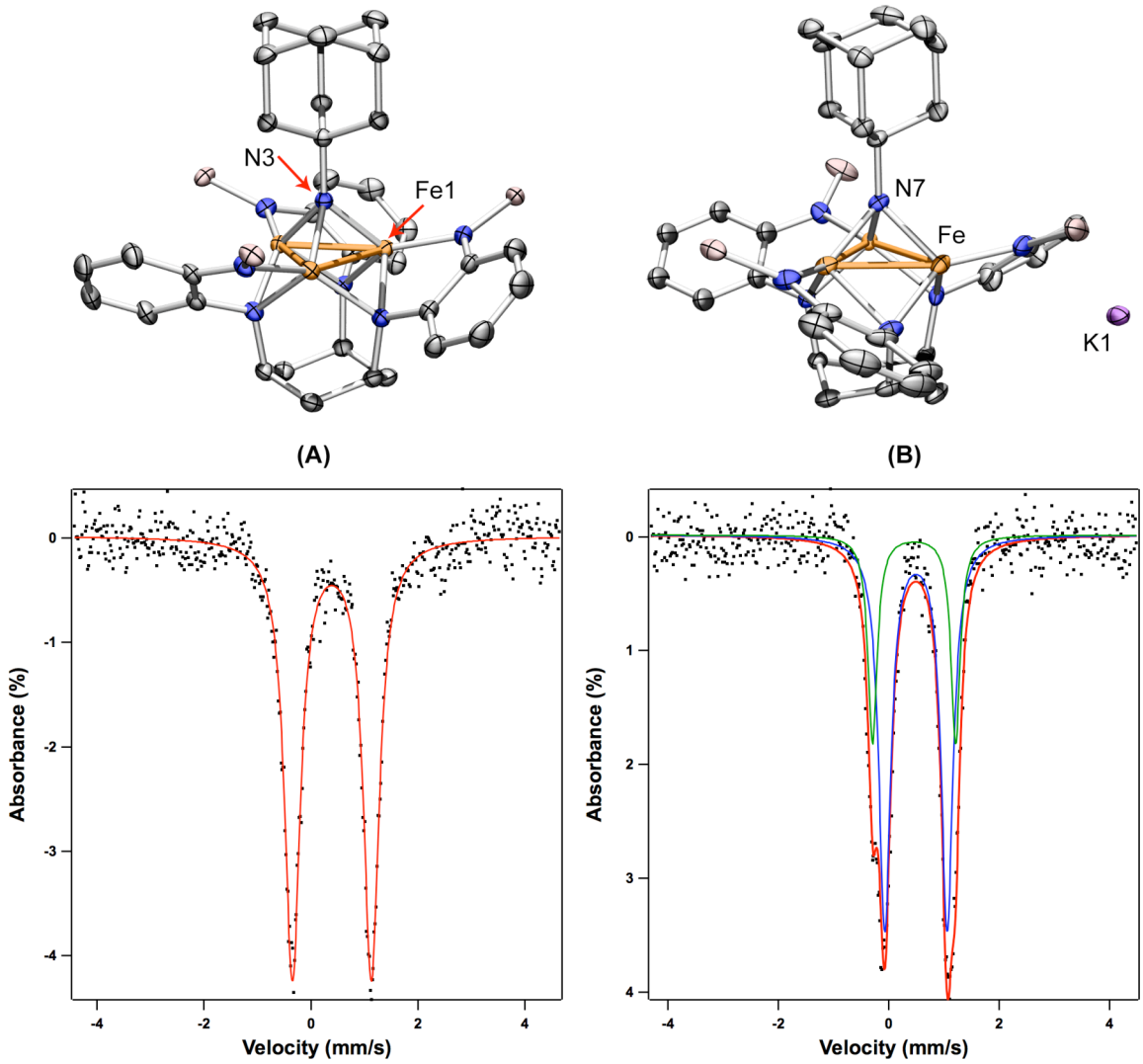

Figure 3.4. Solid-state structures of (A) (^{tbs}L)Fe$_3$(μ^3-NAd) (**3.7**) and (B) [(^{tbs}L)Fe$_3$(μ^3-NAd)]K(THF)$_4$ (**3.8**) with the thermal ellipsoids set at the 50% probability level (hydrogen atoms, solvent molecules, and alkyl groups on Si omitted for clarity; Fe orange, C gray, N blue, Si Pink, K orchid). Selected bond lengths (Å) for **3.7**: Fe–Fe, 2.5297(8); Fe–N3, 1.934(3); for **3.8**: Fe–Fe$_{avg}$, 2.561(1); Fe–N7$_{avg}$, 1.955(4). Zero-field Mössbauer spectrum of (A) (**3.7**) obtained at 110 K and (B) [(^{tbs}L)Fe$_3$(μ^3-NAd)]K($C_{12}H_{24}O_6$) obtained at 105 K. Fitting parameters: (A) δ ($^{mm}/_s$), $|\Delta E_Q|$ ($^{mm}/_s$) 0.39, *1.48* (Γ = 0.18 $^{mm}/_s$) and (B) component 1 (blue, 65%) 0.49, *1.13* (Γ = 0.13 $^{mm}/_s$); component 2 (green, 35%) 0.46, *1.50* (Γ = 0.10 $^{mm}/_s$).

isomer shift upon reduction is consistent with a decrease in electron density at the Fe nucleus, which is a result of increased shielding effects on core *s* electrons upon addition of an electron to the 3*d* manifold.[184]

184. Gütlich, P.; Ensling, J. Mössbauer Spectroscopy. In *Inorganic Electronic Structure and Spectroscopy*; Solomon, E. I.; Liver, A. B. P., Eds.; Wiley: Hoboken, 1999; Vol. 1, p 161-211.

While the cyclic voltammogram of (^{tbs}L)Fe$_3$(μ^3-NR) type complexes indicates that the 1e^- oxidized all-ferric cluster (^{tbs}L)Fe$_3$(μ^3-NR)$^+$ is accessible, all attempts to observe chemical oxidation of **3.7** proved unsuccessful. Upon treatment of **3.7** with [NO]SbF$_6$ in THF, we did not observe oxidation, as evidenced by isolation of unreacted complex **3.7** by both ^{1}H NMR and zero-field ^{57}Fe Mössbauer spectroscopies. Treatment of Fe$_3$ cluster **3.7** with stronger oxidizing agents, including [(NH$_4$)$_2$]Ce(NO$_3$)$_6$, resulted only in the decomposition of complex **3.7**.

The cyclic voltammogram of nitrido complex **3.2a** exhibits an open circuit potential of –2.25 V and features two nearly coincident quasi-reversible one-electron oxidation events ($E_{1/2}$ (V): –1.48, –1.60; Table 3.3, Figure 3.3). The electrochemical data of nitrido **3.2a** is suggestive of a (Fe^{II})(Fe^{III})$_2$ → (Fe^{III})$_2$(Fe^{IV}) redox change, indicating that tetravalent states may be accessible in Fe$_3$ clusters featuring a single functionality (e.g. N^{3-}). This observation should be compared to terminal Fe nitride complexes wherein the nitrides are typically redox endpoints.[159,160,161,185]

Comparing the first oxidation [(Fe^{II})$_3$ → (Fe^{III})(Fe^{II})$_2$] for the series of complexes of the type (^{tbs}L)Fe$_3$(μ^3-E) (where E = N$^-$ in **3.2a**, NH in **3.3**, NPh in **3.4**, Br in **3.6**) reveals a considerable shift in redox potentials. For imido complexes **3.3** and **3.4** this redox event occurs near –2.5 V, whereas for the Br adduct **6**, this redox couple is observed at –0.74 V. For the nitride **3.2a** this redox couple is not observed, but the [(Fe^{III})(Fe^{II})$_2$ → (Fe^{III})$_2$(Fe^{II})] redox event occurs at –2.35 V. A substantial cathodic shifting is observed upon exchange of the μ^3-ligand from the Br adduct (**3.6**), to imido ligands (**3.3**, **3.4**), to the nitrido ligand (**3.2a**). This cathodic shift on going from Br anion (**3.6**) to the neutral imidos (**3.3**, **3.4**) results from the enhanced Fe–Fe interactions found in the imidos (average Fe–Fe: 2.530(1) Å in **3.4**) that is not present in the

185. Scepaniak, J. J., Vogel, C. S.; Khusniyarov, M. M.; Heinemann, F. W.; Meyer, K.; Smith, J. M. *Science* **2011**, *331*, 1049-1052.

Br anion (average Fe–Fe: 2.769(1) Å in **3.6**). Although the nitride **3.2a** is isoelectronic with the imidos, the Fe–Fe separation shortens further (average Fe–Fe: 2.483(1) Å in **3.2a**) and the negative charge for the complex cathodically shifts the redox potentials even further as observed. The charge of the complex, close Fe–Fe interactions, and the hexa-anionic ($^{tbs}L^{6-}$) ligand platform all contribute to the highly cathodically shifted materials reported herein.

3-3. Conclusions

The results herein highlight the advantages that polynuclear reaction sites can offer as a design strategy for small molecule activation. (1) The polynuclear reaction site allows small molecule binding and activation. Upon exposure of cluster (^{tbs}L)Fe$_3$(THF) to hydrazine or phenylhydrazine, typically employed as reducing agents, the core is oxidized to yield Fe$_3$ μ^3-imido complexes with liberation of ammonia (or aniline). Furthermore, complex **3.1** also facilitates the 4e^- reduction of azobenzene to yield Fe$_3$ *bis*-imido cluster (^{tbs}L)Fe$_3$(μ^3-NPh)(μ^2-NPh). While Fe compounds have been shown to reduce hydrazines,[128,129,130,133,134,136,137] there are fewer examples in which Fe facilitates the N=N bond cleavage.[131,141] (2) Our system demonstrates that low oxidation state clusters are not required to achieve multi-electron reduction of substrate. The open-shell Fe$_3$ clusters reported herein are strong reductants, as evidenced by the observed reactivity and electrochemical behavior, and are stable across multiple oxidation states (Fe^{II})$_3$ – (Fe^{III})$_2$(Fe^{IV}). (3) The open-shell electronic configuration of the all-ferrous starting material allows for facile ligand reorganization. As substrate is engaged, facile ligand rearrangement occurs and the resulting products maintain an open-shell electronic configuration, which renders the imido and nitrido moieties reactive towards further elaboration. For example, the Fe$_3$ *bis*-imido cluster (^{tbs}L)Fe$_3$(μ^3-NPh)(μ^2-NPh) is capable of transferring an

imido unit to another Fe_3–THF cluster (**3.1**). Additionally, we have observed transamination of aniline with Fe_3 cluster (^{tbs}L)$Fe_3(\mu^3$-NH) (**3.3**) to generate (^{tbs}L)$Fe_3(\mu^3$-NPh) (**3.4**) and ammonia.

Through our investigation, we have demonstrated that in the absence of a protein superstructure, a high-spin, all-ferrous polynuclear cluster is capable of multi-electron reduction of small molecule substrates. The Fe cluster presented herein stabilizes potential chemical species along the dinitrogen activation pathway, including imido and nitrido moieties. Even upon oxidation, the clusters maintain an open-shell configuration and the increased covalency between substrate and the Fe_3 core results in a more reducing compound that can potentially participate in further redox chemistry, as would be necessary in an N_2 reduction scheme. The breadth of accessible oxidation states of the the polynuclear complexes reported herein make them compelling platforms on which small molecule activation processes can be pursued. By demonstrating the ability of polynuclear reaction sites to effect multi-electron reduction of substrates, we have begun to collect evidence in support of the polynuclear hypothesis.

3-4. Experimental methods

Materials and Methods

All manipulations involving metal complexes were carried out using standard Schlenk line or glove-box techniques under a dinitrogen atmosphere. All glassware was oven-dried for a minimum of 10 h and cooled in an evacuated antechamber prior to use in the dry box. Benzene, diethyl ether, hexanes and tetrahydrofuran (THF) were dried and deoxygenated on a Glass Contour System (SG Water USA, Nashua, NH) and stored over 4 Å molecular sieves (Strem) prior to use. Benzene-d_6 was purchased from Cambridge Isotope Labs and was degassed and stored over 4 Å molecular sieves prior to use. Non-halogenated solvents were typically tested with a standard purple solution of sodium benzophenone ketyl in THF in order to confirm

effective oxygen and moisture removal. Fe_2Mes_4[165] and TEMPOH (1-hydroxy-2,2,6,6-tetramethylpiperidine)[186] were prepared following published methods. All other reagents were purchased from commercial vendors and used without further purification unless explicitly stated.

Physical Measurements

All of the measurements for the metal complexes were made under anaerobic conditions. Elemental analyses were performed by Complete Analysis Laboratories, Inc., Parsippany, New Jersey. ^{1}H NMR spectra were recorded on Varian Unity/Inova 500B/600 NMR spectrometers with chemical shifts (δ ppm) referenced to residual NMR solvent. Zero-field, ^{57}Fe Mössbauer spectra were measured with a constant acceleration spectrometer (SEE Co, Minneapolis, MN). Solid or crystalline samples were prepared as Paratone-N mulls in a drybox and frozen in liquid nitrogen prior to handling in air. Isomer shifts are quoted relative to Fe metal at room temperature. Data was processed, simulated, and analyzed using an in-house package for IGOR Pro 6 (Wavemetrics, Lake Oswego, OR). Solution magnetic susceptibilities were determined by Evans method using trifluoromethylbenzene as an internal reference. Gas chromatography–mass spectrometry (GC-MS) data was collected on a Shimadzu Gas-chromatograph (GCMS-QP2010S).

Synthesis.

(^{tbs}L)Fe$_3$(μ^3-N)Li(THF)$_3$ (3.2b). Solid (^{tbs}L)Fe$_3$(μ^3-NH) (**3.3**) (0.100 g, 0.108 mmol) (prepared as described below) was dissolved in 15 mL of cold THF (–33 ^{o}C). A cold solution of LiN(SiMe$_3$)$_2$ in 2 mL of THF was added dropwise to the solution of (^{tbs}L)Fe$_3$(μ^3-NH). The resulting mixture was allowed to stir at room temperature for 30 min. The volatiles were

186. Mader, E. A.; Davidson, E. R.; Mayer, J. M. *J. Am. Chem. Soc.* **2007**, *129*, 5153-5166.

removed in vacuum, resulting in an oil. The oil was washed with hexanes (20 mL) and the resulting solid was dried. Isolated yield: 0.094 g (76 %). ^{1}H NMR (benzene-d_6, 500 MHz, δ, ppm): 56.6, 16.7, 7.53, 6.70, 5.77, 4.88, 4.12, 3.85, 3.21, 1.24, –2.70; Anal. Calcd for $C_{54}H_{90}Fe_3LiN_7O_3Si_3$: C 56.69, H 7.93, N 8.57. Found: C 56.55, H 7.88, N 8.31; Zero-field ^{57}Fe Mössbauer (90 K) (δ, $|\Delta E_Q|$ ($^{mm}/_{s}$)): 0.33, *1.34.*

(^{tbs}L)Fe$_3$(μ^3-NH) (3.3). Method 1. Solid (^{tbs}L)Fe$_3$(THF) (0.069 g, 0.070 mmol) was dissolved in 15 mL of THF. A THF solution (2 mL) of phenylhydrazine (0.0076 g, 0.070 mmol) was added dropwise to the solution of (^{tbs}L)Fe$_3$(THF) (Note: It is important to run this reaction at high dilution to prevent observation of free ligand). The reaction was then allowed to stir at room temperature for 1 h at which point the volatiles were removed in vacuum. In addition to (^{tbs}L)Fe$_3$(μ^3-NH), the crude product mixture contained aniline (1.6 mg, 0.017 mmol determined by ^{1}H NMR). [The formation of aniline was confirmed by ^{1}H NMR and GCMS. Aniline was isolated from the crude reaction mixture via column chromatography using 10% methanol in dichloromethane as the eluent and was quantified by ^{1}H NMR using ferrocene as an internal standard. Due to solubility, the aniline could not be separated from the complex without the use of column chromatography.] The resulting oil was lyophilized from benzene affording a solid. The product was dissolved in 5–10 mL of hexanes and filtered through a Celite plug. The hexanes were removed under reduced pressure and the resulting product was lyophilized again from benzene to afford pure (^{tbs}L)Fe$_3$(μ^3-NH) (**3.3**) in quantitative yield. Isolated yield: 61 mg (100%).

Method 2. Solid (^{tbs}L)Fe$_3$(THF) (**3.1**) (0.065 g, 0.067 mmol) was dissolved in 15 mL of THF. A syringe was used to add 0.065 mL of a 1 M THF solution of hydrazine to 1 mL of THF. The resulting hydrazine solution was added dropwise to the solution of (^{tbs}L)Fe$_3$(THF). Upon

stirring for 1 h at room temperature, the volatiles were removed in vacuum resulting in an oil. Lyophilization from benzene resulted in a brown solid. In the crude ^{1}H NMR, resonances that match that of (^{tbs}L)Fe$_3$(μ^3-NH) were identified. Due to the solubility of the product and the impurities formed during the reaction, an isolated yield could not be obtained. A crude zero-field ^{57}Fe Mössbauer was obtained at 90 K. Fitting the known parameters of the product, (^{tbs}L)Fe$_3$(μ^3-NH), produced a 40% yield of the reaction. However, the actual yield is most likely less than 40% due to formation of free ligand during the course of the reaction. Vacuum transfer of the volatiles into a solution of 1M HCl in diethylether resulted in trapping the NH_3 as the ammonium chloride salt (quantified by ^{1}H NMR using ferrocene as an internal standard, ranging from 14–70% isolated yield).

Method 3. Solid [(^{tbs}L)Fe$_3$(μ^3-N)]NBu$_4$ (**3.2a**) (0.040 g, 0.034 mmol) was dissolved in 9 mL of THF. A THF solution (1 mL) of lutidinium tetraphenylborate (0.015 g, 0.034 mmol) was added dropwise to the solution of [(^{tbs}L)Fe$_3$(μ^3-N)]NBu$_4$ at room temperature. The reaction was then allowed to stir at room temperature for 1 h at which point the volatiles were removed in vacuum. The resulting oil was lyophilized from benzene prior to the product being extracted into hexanes (~10 mL). The hexane solution was dried and lyophilized from benzene, resulting in an oil. Isolated yield: 0.027 mg, (85%).

Spectroscopic details for (^{tbs}L)Fe$_3$(μ^3-NH) (3.3). ^{1}H NMR (benzene-d_6, 500 MHz, δ, ppm): 170.0, 56.3, 16.7, 8.36, 5.22, 3.38, 3.03, 2.86, 2.22, 1.94, –6.04; Anal. Calcd for $C_{42}H_{67}Fe_3N_7Si_3$: C 54.72, H 7.33, N 10.64. Found: C 54.66, H 7.41, N 10.55; Zero-field ^{57}Fe Mössbauer (115 K) (δ, $|\Delta E_Q|$ ($^{mm}/_{s}$)): component 1: 0.37, *1.94* (78%) component 2: 0.40, *1.17* (22%).

(^{tbs}L)Fe$_3$(μ^3-NPh) (3.4). Method 1. Solid (^{tbs}L)Fe$_3$(THF) (**3.1**) (0.060 g, 0.061 mmol) was dissolved in 15 mL of THF. A THF (1 mL) solution of 1,2-diphenylhydrazine (0.011 g, 0.061 mmol) was added dropwise to the solution of (^{tbs}L)Fe$_3$(THF) at room temperature (NOTE: It is important to run this reaction at high dilution to prevent observation of free ligand). The reaction was then allowed to stir at room temperature for 1 h at which point the volatiles were removed in vacuum, resulting in an oil. In addition to (^{tbs}L)Fe$_3$(μ^3-NPh), the crude product mixture contained aniline (3.3 mg, 0.035 mmol) and azobenzene (1.6 mg. 0.0086 mmol) determined by ^{1}H NMR. [The formation of aniline and azobenzene was confirmed by ^{1}H NMR and GCMS. Both the aniline and azobenzene were isolated by column chromatography using 10% methanol in dicholromethane as the eluent and was quantified by ^{1}H NMR using ferrocene as an internal standard. Due to solubility, both the aniline and azobenzene could not be separated from the complex without the use of column chromatography. Aniline was also isolated upon column chromatography of (^{tbs}L)Fe$_3$(μ^3-NPh) synthesized by method 3 suggesting that H_2O results in protonation of the phenyl imido moiety.] The oil was lyophilized from benzene to afford a solid, which was then dissolved in 5–10 mL of hexanes and filtered through a Celite plug. The hexanes were removed under reduced pressure at which point the resulting oil was lyophilized again from benzene to afford clean (^{tbs}L)Fe$_3$(μ^3-NPh) as a solid. Isolated yield: 55 mg (83%).

Method 2. Solid (^{tbs}L)Fe$_3$(THF) (0.060 g, 0.061 mmol) was dissolved in 5 mL of benzene. A benzene solution of azobenzene (0.11 mL of a 50 mg/mL stock solution, 0.031 mmol) was added to the solution at room temperature. The reaction was subsequently heated to 80 ^{o}C for 4 days. The reaction also proceeds at room temperature, albeit with longer reaction times. In the crude ^{1}H NMR, resonances that match (^{tbs}L)Fe$_3$(μ^3-NPh) (**3.4**) were identified.

Due to the solubility of the product and the impurities formed during the reaction, an isolated/crystalline yield could not be obtained. A zero-field ^{57}Fe Mössbauer of unpurified reaction products obtained at 90 K.

Method 3. Solid (^{tbs}L)Fe$_3$(THF) (**3.1**) (0.130 g, 0.134 mmol) was dissolved in 5 mL of cold THF (–33 ^{o}C). Phenylazide (0.0160 g, 0.134 mmol) in approximately 1 mL of THF was added to the solution of (^{tbs}L)Fe$_3$(THF) (**3.1**). The reaction was allowed to stir at room temperature for 4 h at which point the volatiles were removed in vacuum. The resulting oil was lyophilized from benzene. Subsequently, the solid was dissolved in approximately 5 mL of cold (–33 ^{o}C) hexanes and filtered. The hexanes were removed in vacuum and the resulting oil was lyophilized from benzene again, resulting in a brown solid. Isolated yield: 0.130 g (98 %).

Method 4. Solid (^{tbs}L)Fe$_3$(THF) (**3.1**) (0.014 g, 0.015 mmol) was dissolved in 0.5 mL of C_6D_6. A C_6D_6 solution (0.5 mL) of phenylhydrazine (0.0016 g, 0.015 mmol) was added dropwise to the solution of (^{tbs}L)Fe$_3$(THF) at room temperature in a J-young tube. The reaction was allowed to sit at room temperature for 30 min, prior to heating at 80 ^{o}C for approximately 7 days. [The length of heating depended on the concentration and size of reaction vessel. Additional heating after full conversion to (^{tbs}L)Fe$_3$(μ^3-NPh) resulted in decomposition.] Vacuum transfer of the volatiles into a solution of 1M HCl in diethylether resulted in trapping the NH_3 as the ammonium chloride salt (quantified by ^{1}H NMR using ferrocene as an internal standard, 7.9% isolated yield). The resulting solid was dissolved in hexanes and filtered through Celite. Removal of the solvent in vacuum resulted in isolation of (^{tbs}L)Fe$_3$(μ^3-NPh) (**3.4**). Isolated yield: 7.8 mg (54%).

Spectroscopic details for (^{tbs}L)Fe$_3$(μ^3-NPh) (3.4). ^{1}H NMR (benzene-d_6, 500 MHz, δ, ppm): 199.9, 62.2, 21.6, 9.17, 8.92, 4.26, 2.59, 2.47, –3.15, –3.85, –7.61, –13.3; Anal. Calcd for

$C_{48}H_{71}Fe_3N_7Si_3$: C 57.77, H 7.17, N 9.83. Found: C 57.76, H 6.98, N 9.74; Zero-field ^{57}Fe Mössbauer (95 K) (δ, $|\Delta E_Q|$ ($^{mm}/_s$)): component 1: 0.42, *1.97* (67%) component 2: 0.42, *1.09* (33%).

(^{tbs}L)Fe$_3$(μ^3-NPh)(μ^2-NPh) (3.5). Solid (^{tbs}L)Fe$_3$(THF) (**3.1**) (0.060 g, 0.061 mmol) was dissolved in 5 mL of C_6D_6. Azobenzene (0.011 g, 0.061 mmol) dissolved in 1 mL of C_6D_6 was added to the solution of (^{tbs}L)Fe$_3$(THF) (**3.1**) and allowed to stir at room temperature for 24 h or at 80 ^{o}C for 1 h. The volatiles were removed in vacuum. X-ray quality crystals were grown from cold (–33 ^{o}C) heptane. Clean material for spectroscopic analysis was obtained by storing a concentrated hexanes or heptane solutions at –33 ^{o}C for several weeks, at which point polycrystalline material precipitated from solution. Crystalline yield: 0.011 g (17%). ^{1}H NMR (benzene-d_6, 500 MHz, δ, ppm): 45.1, 34.1, 27.9, 24.2, 22.1, 19.9, 17.2, 14.3, 9.16, 9.92, 6.73, 5.40, 2.47, 2.22, 2.16, 1.93, 0.18, –0.99, –1.21, –2.46, –3.56, –9.29, –13.0, –16.4, –20.1, –27.2, –38.0; Anal. Calcd for $C_{54}H_{76}Fe_3N_8Si_3$: C 59.56, H 7.03, N 10.29. Found: C 59.52, H 6.96, N 10.37; Zero-field ^{57}Fe Mössbauer (90 K) (δ, $|\Delta E_Q|$ ($^{mm}/_s$)): component 1: 0.24, *1.46* (21%) component 2: 0.45, *2.61* (18%) component 3: 0.34, *1.33* (60%).

(^{tbs}L)Fe$_3$(μ^3-NAd) (3.7). Solid ^{tbs}LH$_6$ (0.200 g, 0.268 mmol) was dissolved in 15 mL of THF. The solution was added to solid Fe_2Mes_4 (0.244 g, 0.823 mmol) at room temperature. The reaction was heated in a sealed bomb at 75 °C for 12 h. Solid [N$_3$]Ad (52.3 mg, 0.295 mmol) was added to the reaction mixture cold (–33 °C). Once the reaction reached room temperature, the solution was stirred for an additional 4 h. The volatiles were removed in vacuum resulting in a brown oil. The brown oil was washed with cold hexanes (20 mL) and dried resulting in a brown solid. Isolated yield: 287 mg, (97%). X-ray quality crystals were grown from diethyl ether at –33 °C. ^{1}H NMR (benzene-d_6, 500 MHz, δ, ppm): 193.3, 46.37, 6.69, 5.43, 4.12, 3.52, 2.12,

1.91, 1.70, 0.72, –0.89, –1.99, –10.13; Anal. Calcd for $C_{52}H_{81}N_7Fe_3Si_3$: C 59.14, H 7.73, N 9.28. Found: C 59.17, H 7.67, N 9.14; Zero-field ^{57}Fe Mössbauer (110 K) (δ, $|\Delta E_Q|$ ($^{mm}/_s$)): 0.39, *1.48* ($\gamma = 0.18$ $^{mm}/_s$).

[(^{tbs}L)Fe$_3$(μ^3-NAd)]K(THF)$_4$ (3.8). A solution of (^{tbs}L)Fe$_3$(μ^3-NAd) (**3.7**) (0.100 g, 0.134 mmol) in THF was added cold (–33 °C) to solid KC_8 (0.0200 g, 0.148 mmol). Once the reaction reached room temperature, it was allowed to stir for an additional 4 h. The solution was filtered through Celite to remove excess KC_8 and the volatiles were removed in vacuum resulting in a brown oil. The brown oil was washed with hexanes (20 mL) and dried resulting in a brown solid. X-ray quality crystals of the THF-ligated potassium salt were grown from vapor diffusion of hexanes into a solution of THF at room temperature. A benzene/THF (3:1) solution (4 mL) of the [(^{tbs}L)Fe$_3$(μ^3-NAd)]K·(THF)$_4$ (**3.8**) salt was added to solid 18-crown-6-ether (0.0363 g, 0.148 mmol). The solution was allowed to stir at room temperature for 1 h. The reaction mixture was then dried and the solvent was removed in vacuum resulting in a brown oil. The oil was washed with diethyl ether (10 mL) and subsequently dried. Benzene (10 mL) was added to the oil and removed in vacuum to yield a solid. Isolated yield: 0.092 g, (95%). ^{1}H NMR (benzene-d_6, 500 MHz, δ, ppm): 54.81, 18.90, 5.78, 0.18, –0.84, –10.93, –12.49, –26.56; Anal. Calcd for $C_{64}H_{105}N_7O_6KFe_3Si_3$: C 56.54, H 7.79, N 7.21. Found: C 56.47, H 7.66, N 7.17; Zero-field ^{57}Fe Mössbauer (110 K) (δ, $|\Delta E_Q|$ ($^{mm}/_s$)): component 1 (65%) 0.49, *1.13* ($\Gamma = 0.13$ $^{mm}/_s$); component 2 (35%) 0.46, *1.50* ($\Gamma = 0.10$ $^{mm}/_s$).

Reaction of (^{tbs}L)Fe$_3$(μ^3-NH) (3.3) with TEMPOH. A THF (0.5 mL) solution of TEMPOH (1-hydroxy-2,2,6,6-tetramethylpiperidine) (0.013 g, 0.083 mmol) is added to a frozen THF solution of (^{tbs}L)Fe$_3$(μ^3-NH) (**3.3**) (0.025 g, 0.027 mmol) and Bu_4NBr (0.0097 g, 0.030

mmol) in a J-Young NMR tube. The mixture is allowed to thaw and sit at room temperature for 3 h at which point all of the paramagnetic features in the ^{1}H NMR associated with **2** are no longer present. Vacuum transfer of the volatiles into a solution of 1M HCl in diethylether resulted in trapping the NH_3 as the ammonium chloride salt (quantified by ^{1}H NMR using ferrocene as an internal standard, 13% isolated yield).

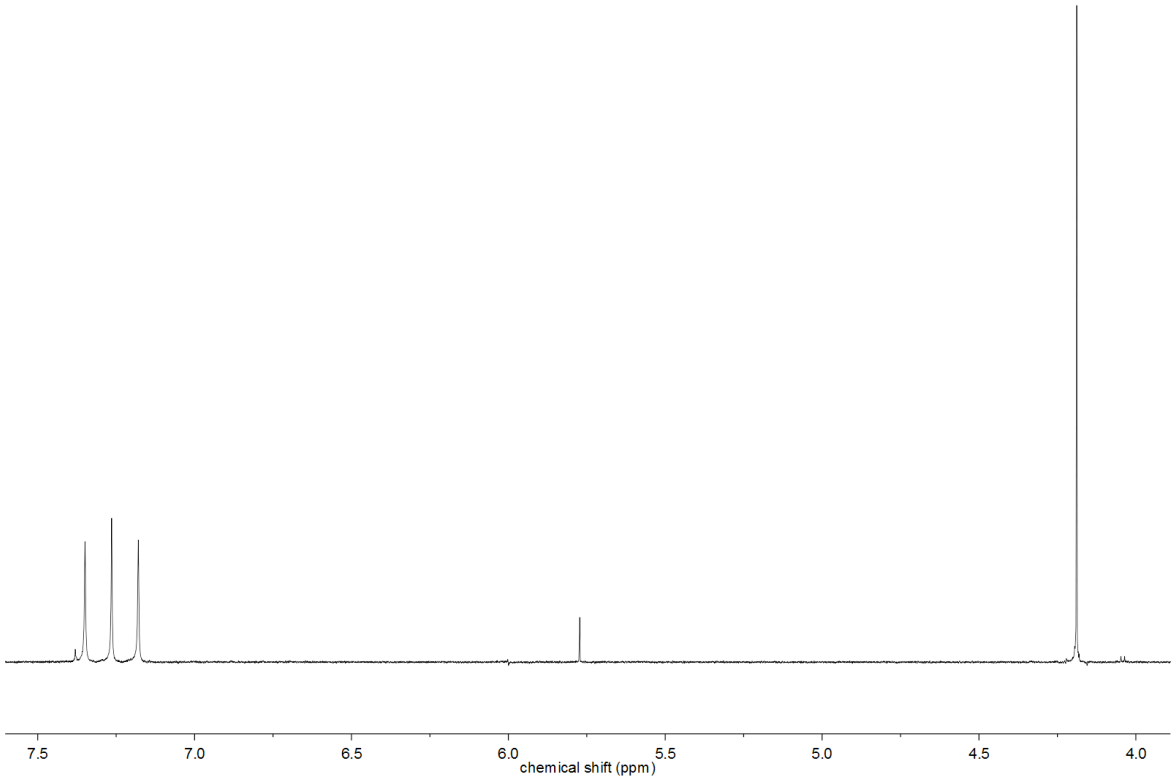

Figure 3.5. Generation of NH_3 during synthesis of (**3.3**) with H_2NNH_2 (ferrocene used as internal standard, 4.2 ppm) ^{1}H NMR (DMSO-d_6, 600 MHz, δ, ppm): 7.26 (t, J = 50.9 Hz, 4H, NH_4Cl).

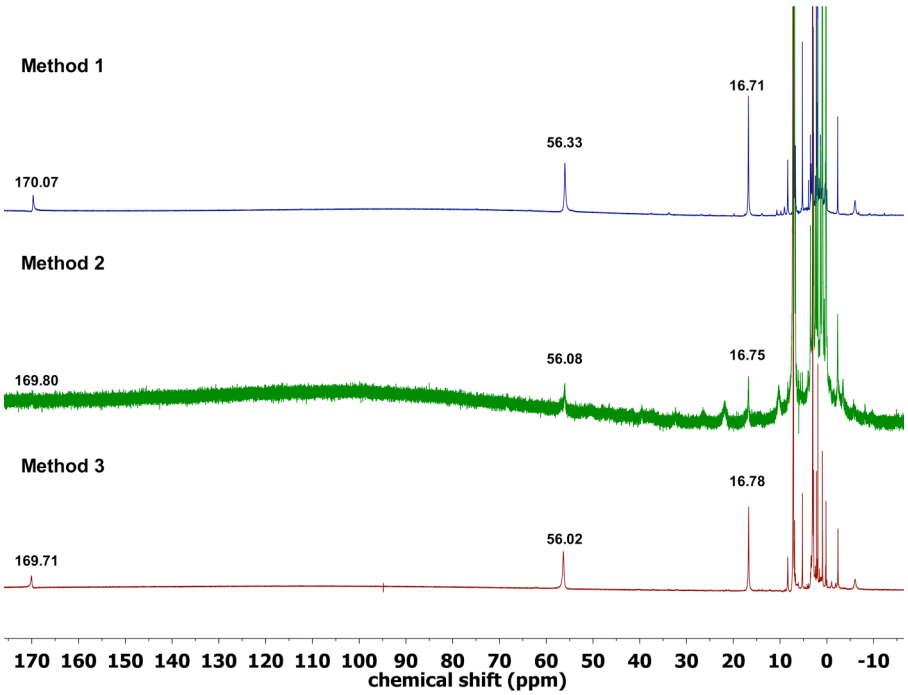

Figure 3.6. ^{1}H NMR overlays of the three methods used to synthesize (^{tbs}L)Fe$_3$(μ^3-NH) (**3.3**). Method 1: **3.1** + PhHNNH$_2$; Method 2: **3.1** + H$_2$NNH$_2$; Method 3: **3.2a** + lutidinium tetraphenylborate.

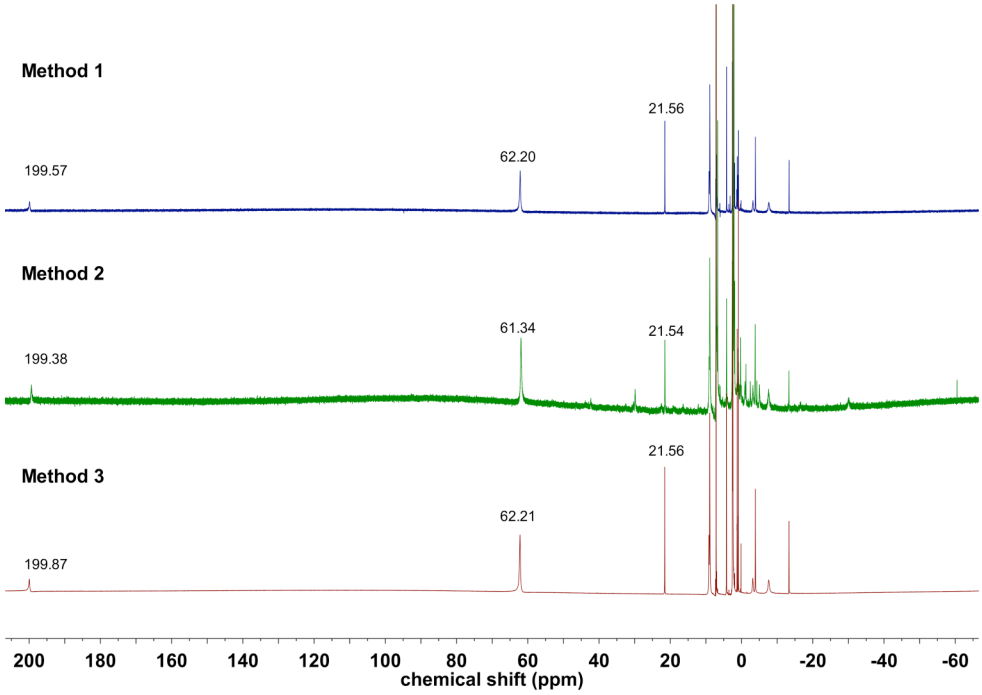

Figure 3.7. ^{1}H NMR overlays of methods 1, 2, and 3 to synthesize (^{tbs}L)Fe$_3$(μ^3-NPh) (**3.4**). Method 1: **3.1** + PhHNNHPh; Method 2: **3.1** + PhNNPh; Method 3: **3.1** + N$_3$Ph.

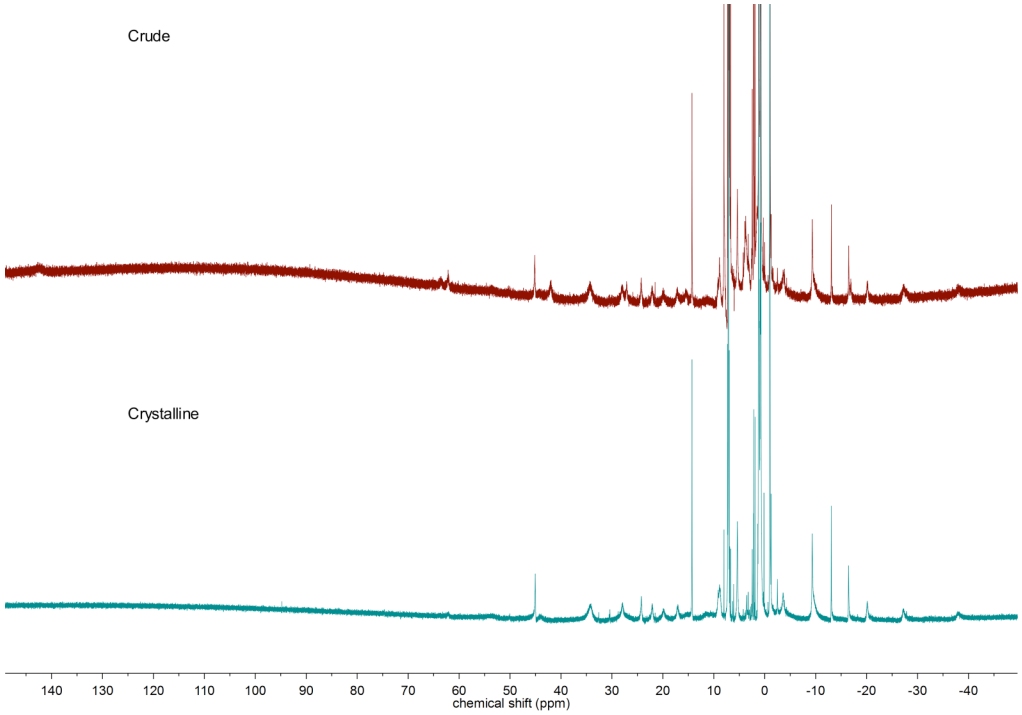

Figure 3.8. ^{1}H NMR of (^{tbs}L)Fe$_3$(μ^3-NPh)(μ^2-NPh) (**3.5**) crude and crystalline material.

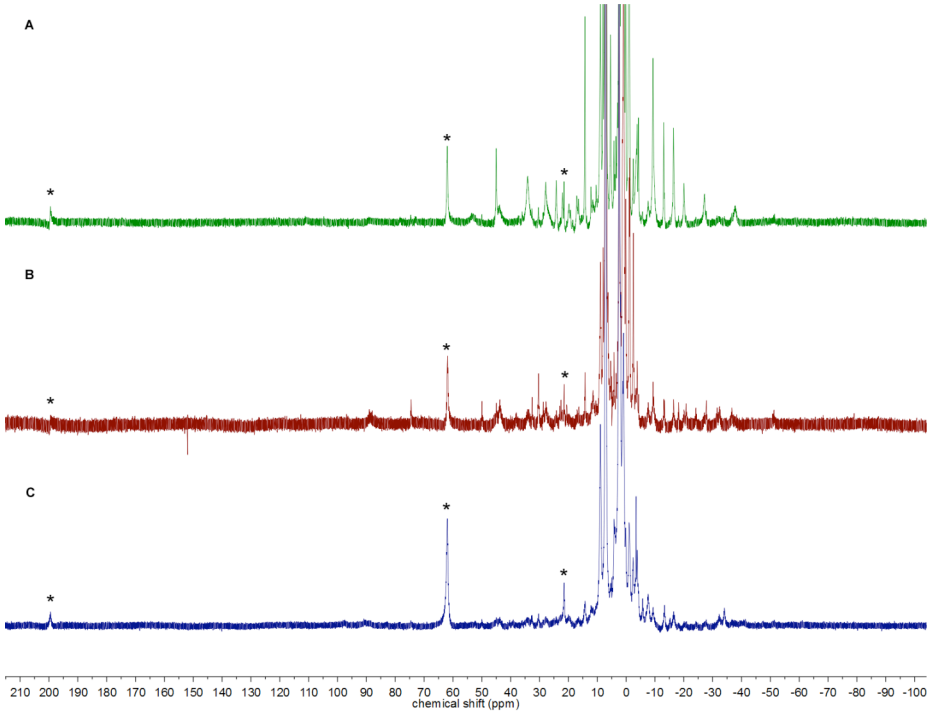

Figure 3.9. (A) ^{1}H NMR (green) of crystalline (^{tbs}L)Fe$_3$(μ^3-NPh)(μ^2-NPh) (**3.5**) prior to heating. A small amount of (^{tbs}L)Fe$_3$(μ^3-NPh) (**3.4**) co-crystallized with **3.5** (resonances associated with **3.4** indicated with a star). (B) ^{1}H NMR (red) of crystalline **3.5** (same sample as A) heated overnight at 70 ^{o}C. Heating the sample overnight did not lead to a significant increase in the resonance peaks associated with **3.4**. (C) ^{1}H NMR (blue) of crystalline **3.5** (same sample as A) heated overnight at 70 ^{o}C in the presence of 1 equivalent of (^{tbs}L)Fe$_2$(THF) (**3.1**). The major product of this reaction is **3.4** suggesting that it is formed during the reaction of **3.1** with **3.5**.

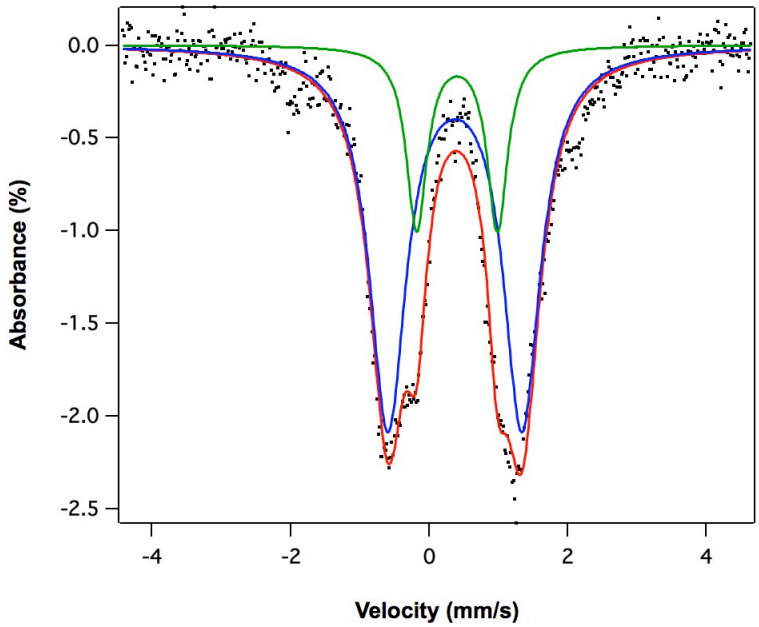

Figure 3.10. Zero-field Mössbauer spectrum of (^{tbs}L)Fe$_3$(μ^3-NH) (**3.3**) obtained at 115 K. Fitting parameters: δ, $|\Delta E_Q|$ ($^{mm}/_s$) component 1 (blue, 78%) 0.37, *1.94* (Γ = 0.32 $^{mm}/_s$); component 2 (green, 22%) 0.40, *1.17* (Γ = 0.18 $^{mm}/_s$).

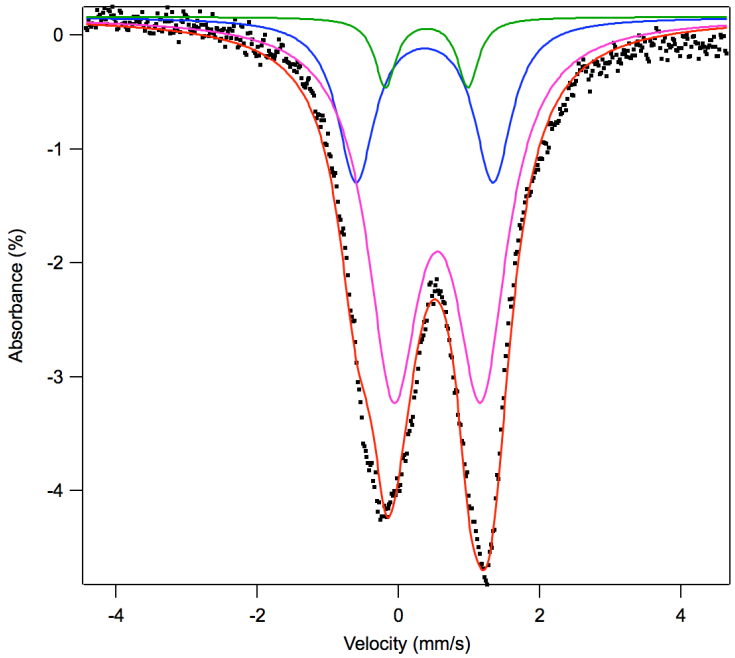

Figure 3.11. Crude zero-field Mössbauer spectrum of (^{tbs}L)Fe$_3$(μ^3-NH) (**3.3**) obtained at 90 K prepared by method 2. Fitting parameters: δ, $|\Delta E_Q|$ ($^{mm}/_s$) component 1 (blue, 28%) 0.37, *1.94* (Γ = 0.32 $^{mm}/_s$); component 2 (green, 12%) 0.40, *1.17* (Γ = 0.18 $^{mm}/_s$); component 3 (pink, 60%) 0.55, *1.24* (Γ = 0.45 $^{mm}/_s$). To obtain the fit, the parameters of components 1 and 2 representing **3.3** were fixed while component 3 was allowed to vary to obtain an approximate crude yield based on Fe content. Fitting the spectrum to a single quadrupole doublet yields the following parameters: δ, $|\Delta E_Q|$ ($^{mm}/_s$) 0.50, *1.4* (Γ = 0.46 $^{mm}/_s$).

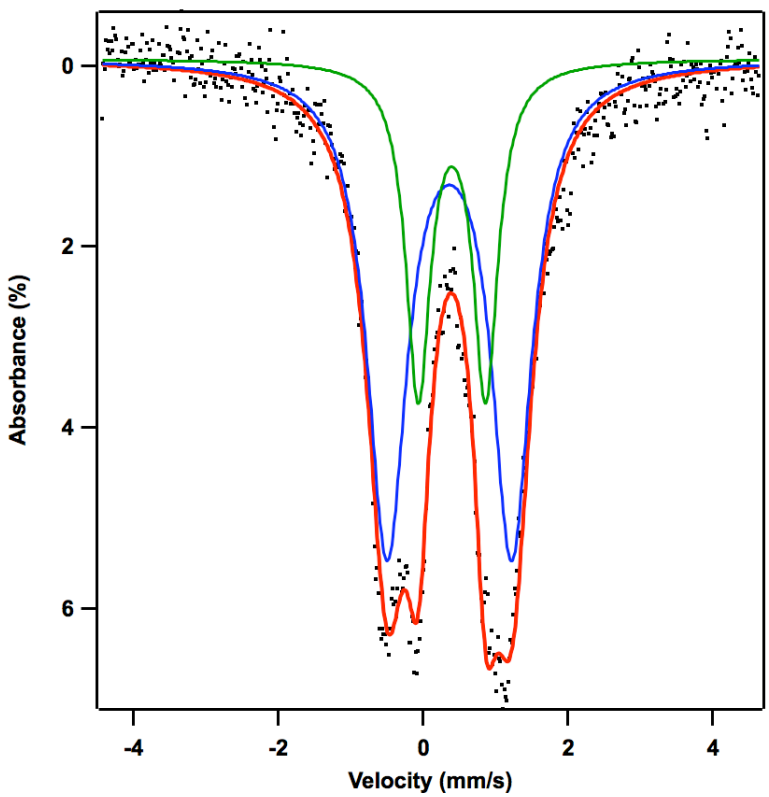

Figure 3.12. Crude zero-field Mössbauer spectrum of (^{tbs}L)Fe$_3$(μ^3-NPh) (**3.4**) obtained at 90 K prepared by method 2. Fitting parameters: δ, $|\Delta E_Q|$ ($^{mm}/_s$) component 1 (blue, 69%) 0.37, *1.72* (Γ = 0.33 $^{mm}/_s$); component 2 (green, 31%) 0.41, *0.93* (Γ = 0.21 $^{mm}/_s$).

X-Ray Diffraction Techniques

All structures were collected on a Bruker three-circle platform goniometer equipped with an Apex II CCD and an Oxford cryostream cooling device. Radiation was from a graphite fine focus sealed tube Mo Kα (0.71073 Å) source. Crystals were mounted on a cryoloop or glass fiber pin using Paratone N oil. Structures were collected at 100 K. Data was collected as a series of φ and/or ω scans. Data was integrated using SAINT and scaled with either a numerical or multi-scan absorption correction using SADABS.[170] The structures were solved by direct methods or Patterson maps using SHELXS-97 and refined against F^2 on all data by full matrix least squares with SHELXL-97.[171] All non-hydrogen atoms were refined anisotropically. Hydrogen atoms were placed at idealized positions and refined using a riding model. The isotropic displacement

parameters of all hydrogen atoms were fixed to 1.2 times the atoms they are linked to (1.5 times for methyl groups). Further details on particular structures are noted below.

[(^{tbs}L)Fe$_3$(μ^3-N)]Li(THF)$_3$ (3.2b). The structure was solved in the cubic space group $Pa\bar{3}$ with 24 molecules per unit cell. The asymmetric unit was found to contain 1/3 of the molecule [(^{tbs}L)Fe$_3$(μ^3-N)]Li(THF)$_3$. The solvent located on a special position could not be resolved in the Fourier map and therefore was squeezed out using the Olex2 masking function.

(^{tbs}L)Fe$_3$(μ^3-NPh) (3.4). The structure was solved in the monoclinic space group *C2/c* with 8 molecules per unit cell. The asymmetric unit was found to contain one molecule of (^{tbs}L)Fe$_3$(μ^3-NPh) and two hexane molecules. Both hexane molecules were located on special positions. Similarity restraints were used to obtain a model for the solvent molecules.

(^{tbs}L)Fe$_3$(μ^3-NPh)(μ^2-NPh) (3.5). The structure was solved in the triclinic space group $P\bar{1}$ with 2 molecules per unit cell. The asymmetric unit contains two molecules of (^{tbs}L)Fe$_3$(μ^3-NPh)(μ^2-NPh), two *n*-hexane solvent molecules and two *n*-heptane solvent molecues. One of the ^{tbs}LFe$_3$(μ^3-NPh)(μ^2-NPh) molecules exhibited positional disorder within the ortho-phenylene diamine unit as well as in the *tert*-butyl dimethyl silyl unit and were refined using similarity restraints. Three of the four solvent molecules exhibited positional disorder and were also refined using similarity restraints.

(^{tbs}L)Fe$_3$(μ^3-NAd) (3.7). The structure was solved in the hexagonal space group $R\bar{3}c$ with 12 molecules per unit cell. The asymmetric unit contains 1/3 of a (^{tbs}L)Fe$_3$(μ^3-NAd) molecule and an diethyl ether solvent molecule located on a special position.

[(^{tbs}L)Fe$_3$(μ^3-NAd)]K(THF)$_4$ (3.8). The structure was solved in the monoclinic space group $P2_1/n$ with 4 molecules per unit cell. The asymmetric unit contains one molecule of

$[(^{tbs}L)Fe_3(\mu^3\text{-NAd})]K(THF)_4$. The solvent THF molecules exhibited positional disorder and was refined using similarity restraints.

Table 3.4. Selected Core Bond Distances (Å) and Angles (degrees) for **3.5**.

N1—Fe1	1.993 (4)	N9—Fe4	1.978 (4)
N2—Fe3	2.016 (4)	N10—Fe6	2.020 (4)
N2—Fe2	2.081 (4)	N10—Fe5	2.072 (4)
N3—Fe3	1.916 (4)	N11—Fe6	1.932 (4)
N4—Fe1	1.952 (4)	N12—Fe4	1.951 (5)
N5—Fe2	1.911 (4)	N13—Fe5	1.905 (4)
N6—Fe3	1.951 (4)	N14—Fe6	1.939 (4)
N7—Fe3	1.904 (4)	N15—Fe6	1.947 (4)
N7—Fe1	1.973 (4)	N15—Fe5	1.964 (4)
N7—Fe2	1.982 (4)	N15—Fe4	1.973 (4)
N8—Fe2	1.848 (4)	N16—Fe5	1.849 (4)
N8—Fe1	1.866 (4)	N16—Fe4	1.852 (4)
Fe1—Fe2	2.4819 (10)	Fe4—Fe5	2.4899 (11)
Fe1—Fe3	2.9662 (11)	Fe5—Fe6	2.5938 (11)
Fe2—Fe3	2.6038 (10)		

Table 3.5. X-ray Crystallographic Data for All Compounds

	$[(^{tbs}L)Fe_3(\mu^3\text{-}N)]Li(THF)_3$	$(^{tbs}L)Fe_3(\mu^3\text{-}NPh)$	$(^{tbs}L)Fe_3(\mu^3\text{-}NPh)(\mu^2\text{-}NPh)$	$(^{tbs}L)Fe_3(\mu^3\text{-}NAd)$	$[(^{tbs}L)Fe_3(\mu^3\text{-}NAd)]Li(THF)_4$
Chemical formula	$C_{18}H_{30}FeLi_{0.33}N_{2.33}OSi$	$C_{54}H_{85}Fe_3N_7Si_3$	$C_{131}H_{205}Fe_6N_{16}Si_6$	$C_{18.33}H_{29.50}FeN_{2.33}O_{0.25}Si$	$C_{72}H_{105}Fe_3KN_7O_5Si_3$
fw	381.36	1084.11	2507.75	370.55	1439.55
Space group	$Pa\bar{3}$	$C2/c$	$P\bar{1}$	$R\bar{3}c$	$P2_1/n$
a (Å)	23.057(1)	30.620(3)	15.281(1)	15.433(2)	15.723(2)
b (Å)		25.011(2)	21.682(2)	15.433(2)	30.243(4)
c (Å)		18.039(1)	22.529(2)	89.93(1)	17.449(2)
α (deg)			96.398(2)		
β (deg)		109.703(2)	108.873(2)		112.980(2)
γ (deg)			100.447(2)	120	
V (Å^3)	12258(1)	13006(2)	6829(1)	18550(4)	7639(2)
Z	24	8	2	12	4
μ (mm^{-1})	0.8	0.75	0.73	0.79	1.17
T (K)	100(1)	100(1)	100(1)	100(1)	100(1)
R1[a] (wR2[b])	0.030 (0.081)	0.051 (0.146)	0.064 (0.178)	0.047 (0.162)	0.065 (0.208)

[a] $R1 = [\sum w(F_o - F_c)^2/\sum wF_o^2]^{1/2}$

[b] $wR2 = [\sum [w(F_o^2 - F_c^2)^2]/\sum w(F_o^2)^2]^{1/2}$, $w = 1/[\sigma^2(F_o^2) + (aP)^2 + bP]$, where $P = [\max(F_o^2,0) + 2(F_c^2)]/3$

Chapter 4.[187] Triiron Adducts with Unsaturated Ligands: 1-, 2-, and 4e^- Reduction of Substrates

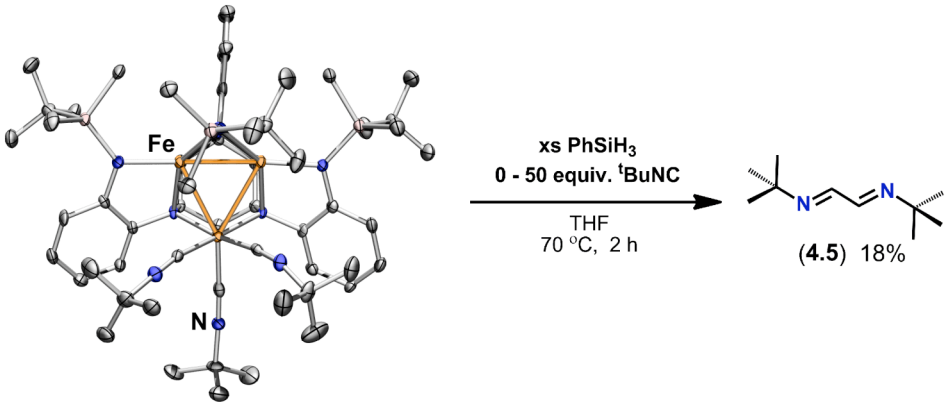

4-1. Introduction: molecular carbonyl compounds

Metal surfaces used in heterogeneous catalysis mediate multi-electron transformations to achieve small molecule activation. For example, the Fischer-Tropsch process catalyzes the production of petroleum substitutes by combination of CO and H_2 over a metal surface catalyst (Equation 4.1).[1]

$$(2n + 1)\,H_2 + n\,CO \xrightarrow{[M]} C_nH_{(2n+2)} + n\,H_2O \qquad \text{(Eq. 4.1)}$$

The role that polynuclear metal sites play during binding and chemical breakdown of substrates on metal surfaces is still debated due to the complexity of these systems.[188,189,190,191] As such, synthetic metal clusters have been viewed as potential simplified models for the polynuclear binding sites in heterogenous catalysts.[138,192,193] Attempts to distill the surface to its smallest molecular reactive unit enables the use of a wide range of spectroscopic techniques to probe the

187. This chapter was adapted with permission from Powers, T. M.; Betley, T. A. *J. Am. Chem. Soc.* **2013**, *submitted*. Unpublished work Copyright 2013 American Chemical Society.
188. Zhang, Y.; Hou, L.; Tierney, J. W.; Wender, I. *Top. Catal.* **2005**, *32*, 125-133.
189. Inderwildi, O. R.; Jenkins, S. J.; King, D. A. *J. Phys. Chem. C* **2008**, *112*, 1305-1307.
190. Shetty, S.; Jansen, A. P. J.; van Santen, R. A. *J. Am. Chem. Soc.* **2009**, *131*, 12874-12875.
191. Mirwald, J. W.; Inderwildi, O. R. *Phys. Chem. Chem. Phys.* **2012**, *14*, 7028-7031.
192. Muetterties, E. L. *Science* **1977**, *196*, 839-848.
193. Mingos, D. M. P. *J. Clust. Sci.* **1992**, *3*, 397-409.

mechanism of the transformations of interest. Specifically, the investigation of molecular metal carbonyl (CO) and isonitrile (CNR) compounds, which are isoelectronic with CO and therefore considered to be CO surrogates, has played a significant role in both the development of transition metal clusters as well as aided in our understanding of how small molecule substrates interact with metal surfaces during chemisorption in reactions such as the Fischer-Tropsch process.[188,189,190,191]

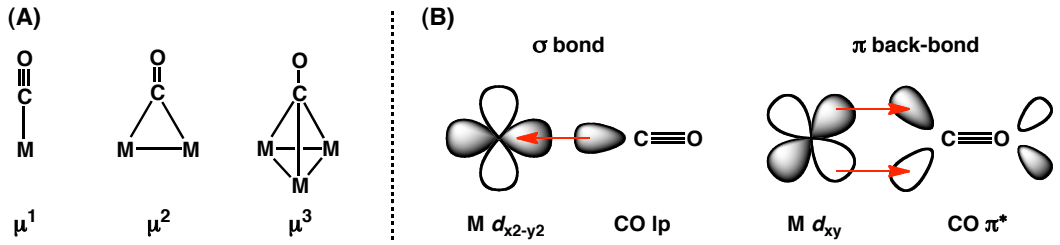

Figure 4.1. (A) Common coordination modes of CO and CNR molecules to metal centers. (B) Orbital interactions that make up a metal carbonyl bond. The σ-bond is formed between a metal *d* orbital of σ-symmetry and the lone pair (lp) on C (a *sp* hybridized orbital). The π back-bond is formed between a filled metal *d* orbital of π-symmetry with an empty π* anti-bonding CO based orbital.

Table 4.1. Vibrational stretching frequencies of select bonding modes of CO and CNR

	Free	**M(μ^1)**	**M_2(μ^2)**	**M_3(μ^3)**
CO, ν(CO), cm^{-1}	2143	2120 – 1850	1850 – 1750	1750 – 1600
CNR, ν(CN), cm^{-1}	2165 – 2110	>1900	1700 – 1870	

Molecular coordination complexes with CO and CNR substrates have shed light on the binding modes available on surfaces. While several binding modes of CO and isonitriles to metal clusters have been demonstrated, including terminal (μ^1), bridging (μ^2), and face-capping (μ^3), terminal coordination is the most common bonding motif, typically resulting in low-spin metal centers (Figure 4.1A).[194,195,196,197] Both CO and CNR molecules are weak σ donors [Ligand(lp)

194. C. E. Housecroft *Metal-metal Bonded Carbonyl Dimers and Clusters*, Oxford Science Publications: Oxford, **1996**, and references therein.
195. Dyson, P. J.; McIndoe, J. S. *Transition Metal Carbonyl Cluster Chemistry*, Gordon and Breach Science Publishers: Amsterdam, 2000.
196. Dyson, P. J. *Coord. Chem. Rev.* **2004**, *248*, 2443-2458, and references therein.

→ M(*d*)] and strong π acceptors [M(*d*) → Ligand(π*)] (Figure 4.1B).[195] The π back-bond between filled metal *d* orbitals to empty π* ligand based orbitals weakens the C–O or C–N bond, which results in a decrease in stretching frequency upon coordination to a metal center (Table 4.1). The π back-bonding effect is enhanced for bridging and face-capping ligands, leading to weaker C–O or C–N bonds in those cases (Table 4.1).[195,198,199,200]

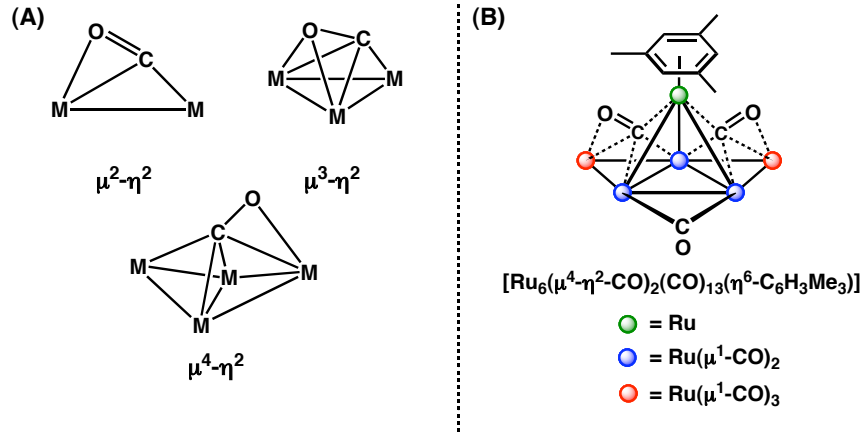

Figure 4.2. (A) Less common coordination modes of C–O to bi- and polynuclear metal complexes. η^2-coordination results in significant C–O bond elongation. For example (B) shows the Ru carbonyl complex $[Ru_6(\mu^4\text{-}\eta^2\text{-}CO)_2(CO)_{13}(\eta^6\text{-}C_6H_3Me_3)]$, which features two $\mu^4\text{-}\eta^2$-carbonyl groups with an average C–O bond length of 1.26(1) Å (terminally (μ^1) coordinated CO ligands ca. 1.14 Å).

Several alternative carbonyl bonding modes to metal clusters are available and have been observed in particular cases (Figure 4.2).[195,201] Side-on (η^2) coordination of a carbonyl ligand is accessible for both bi- and polynuclear assemblies and results in significant C–O bond elongation.[201,202] For example, ruthenium carbonyl cluster $[Ru_6(\mu^4\text{-}\eta^2\text{-}CO)_2(CO)_{13}(\eta^6\text{-}C_6H_3Me_3)]$

197. Ratliff, K. S.; Broeker, G. K.; Fanwick, P. E.; Kubiak, C. P. *Angew. Chem., Int. Ed.* **1990**, *29*, 395-396.
198. Yamamoto, Y. *Coord. Chem. Rev.* **1980**, *32*, 193-233.
199. Lazar, M.; Angelici, R. J. Isocyanide Binding Modes on Metal Surfaces and Metal Complexes. In *Modern Surface Organometallic Chemistry*; Basset, J.-M.; Psaro, R.; Roberto, D.; Ugo, R.; Ed. Wiley-VCH: Germany, 2009, p 513-556.
200. Stephany, R. W.; de Bie, J. A.; Drenth, W. *Org. Magn. Resonance* **1974**, *6*, 45-47.
201. Horowitz, C. P.; Shriver, D. F. *Adv. Organomet. Chem.* **1984**, *23*, 219-305, and references therein.
202. Bailey, P. J.; Duer, M. J.; Johnson, B. F. G.; Lewis, J.; Conole, G.; McParlin, M.; Powell, H. R.; Anson, C. E. *J. Organomet. Chem.* **1990**, *383*, 441-461.

features two μ^4-η^2-CO units and has been crystallographically characterized (Figure 4.2B).[202,203] The solid-state structure reveals that the average C–O bond length of the μ^4-η^2-coordinated carbonyl groups to be 1.26(1) Å, which is considerably elongated relative to terminally (μ^1) coordinated ligands (ca. 1.14 Å). The μ^4-η^2-coordinated carbonyl groups in the mentioned Ru_6 carbonyl cluster also exhibit lower frequency stretching bands at 1423 and 1392 cm^{-1} corresponding to the anti-symmetric and symmetric stretches, respectively.

Metal carbonyl complexes have been targeted to study reductive coupling of CO to generate C–C bonds, one of the key steps in the FT process. There are several homogeneous systems capable of CO reductive coupling. For example, hydride or alkyl insertion into Zr carbonyls, followed by carbene coupling, results in C–C bond formation between CO molecules (Figure 4.3).[204,205] Other examples rely on highly reducing alkali metals such as Na^0 to achieve carbonyl reduction.[206] Despite the diversity of carbonyl clusters in the literature, there are few examples of carbonyl coupling by polynuclear assemblies.[207]

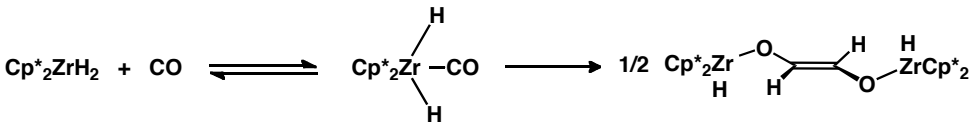

Figure 4.3. Reductive coupling of CO by $Cp^*_2ZrH_2$ occurs via hydride insertion into a Zr carbonyl intermediate, followed by carbene coupling.

Given the multitude of available substrate bonding modes accessible with polynuclear assemblies, we viewed small, synthetic clusters as an attractive target to template the activation of small molecules. We hypothesized that M–M interactions in synthetic polynuclear clusters would facilitate activation of unsaturated substrates and have pursued the synthesis of metal

203. Anson, C. E.; Bailey, P. J.; Conole, G.; Johnson, B. F. G.; Lewis, J.; McPartlin, M.; Powell, H. R. *J. Chem. Soc., Chem. Commun.* **1989**, 442-444.
204. Wolczanski, P. T.; Bercaw, J. E. *Acc.Chem. Res.* **1980**, *13*, 121-127, and references therein.
205. Erker, G. *Acc. Chem. Res.* **1984**, *17*, 103-109, and references therein.
206. Carnahan, E. M.; Protasiewicz, J. D.; Lippard, S. J. *Acc. Chem. Res.* **1993**, *26*, 90-97, and references therein.
207. West, N. M.; Miller, A. J. M.; Labinger, J. A.; Bercaw, J. E. *Coord. Chem. Rev.* **2011**, *255*, 881-898, and references therein.

clusters with electronically unsaturated metal sites.[143,144,145,146,168] The results discussed in Chapters 2 and 3 demonstrated the ability of (^{tbs}L)Fe$_3$(THF) (**4.1**) to mediate 2- and 4e^- reduction of nitrogenous substrates to yield imido and nitrido products. In this Chapter, the reaction of Fe$_3$ cluster **4.1** with a series of unsaturated substrates including *tert*-butylisocyanide (^{t}BuNC), lithium phenyl acetylide (LiCCPh), tetra-*n*-butylammonium thiocyanate ([SCN]NBu$_4$), and carbon monoxide (CO) will be discussed.

4-2. Synthesis of (^{tbs}L)Fe$_3$(μ^1-CNR)$_3$, (^{tbs}L)Fe$_3$(μ^3-η^2-CCPh)$^-$, and (^{tbs}L)Fe$_3$(μ^3-S)$^-$

Addition of 3 equivalents of *tert*-butylisonitrile (^{t}BuNC) to (^{tbs}L)Fe$_3$(THF) (**4.1**) resulted in a green compound featuring an ^{1}H NMR with 20 resonances, suggesting that the resulting product exhibits C_s symmetry in solution. The IR spectrum features three C–N stretches at 2137, 2103, 2070 cm^{-1} consistent with multiple μ^1 coordinated isonitrile ligands. Single crystal analysis corroborated the ^{1}H NMR and IR spectra and revealed the identity of the product to be (^{tbs}L)Fe$_3$(μ^1-CN^{t}Bu)$_3$ (**4.2**, 89% isolated yield) where three ^{t}BuNC moieties are bound in a μ^1 fashion to a single metal center (Scheme 4.1, Figure 4.4A).

Coordination of ^{t}BuNC results in ligand rearrangement to accommodate the three strong field ligands bound to Fe3. Metal centers Fe1 and Fe2 in **4.2** are bridged by one of the *ortho*-phenylenediamide ligand units. In the solid-state, the molecule exhibits C_1 symmetry, whereas in solution the *tert*-butyldimethylsilyl substitutent that sits above the trinuclear face could rotate, giving rise to the 20 line pattern in the ^{1}H NMR. Ignoring Fe–Fe interactions, both Fe1 and Fe2 have pseudo-tetrahedral geometries while Fe3 exhibits a square pyramid local geometry where two of the three R-groups (R = ^{t}BuNC) and the two internal amide ligand groups (N2 and N3) make up the basal plane and the third R-group occupies the apical position. The Fe–amide bond distances of **4.2** are consistent with Fe3 adopting a low-spin electron configuration; when

comparing the Fe–amide (alkyl aryl amides: N2, N3) bond distances of the three Fe centers in **4.2**, we see that the Fe3–amide distances (Fe3–N2, 2.032(3) Å and Fe3–N3, 2.002(3) Å) are shorter relative to the Fe1 and Fe2–amide distances (Fe1–N3, 2.071(3) Å and Fe2–N2, 2.080(3) Å) (Figure 4.4A).

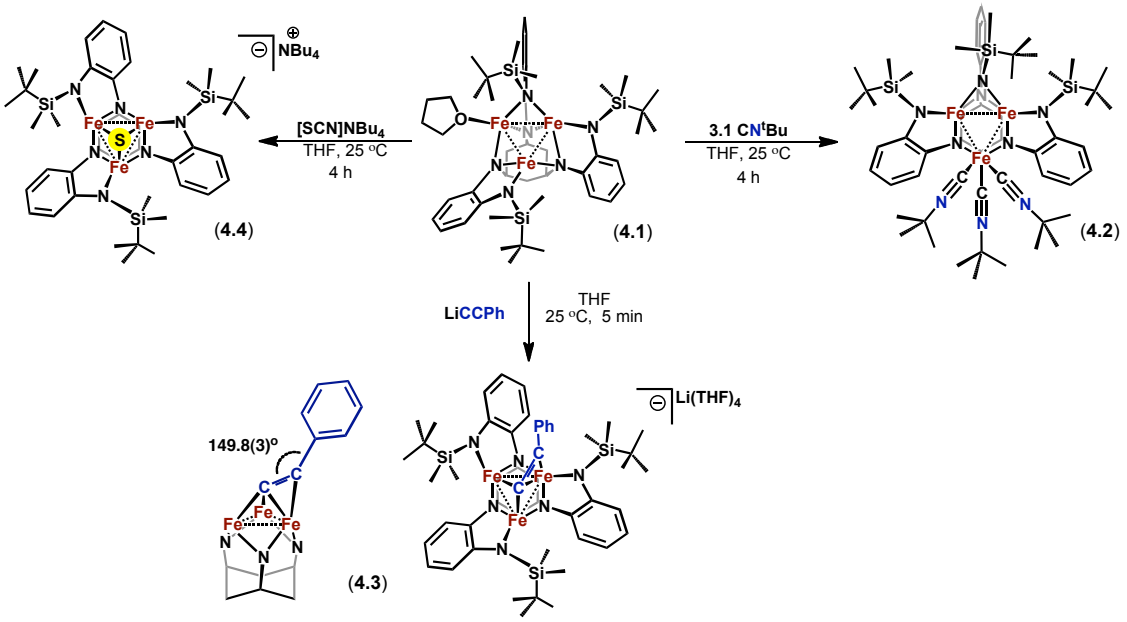

Scheme 4.1. Synthesis of (^{tbs}L)Fe$_3$(μ^1–CN^{t}Bu)$_3$ (**4.2**), [(^{tbs}L)Fe$_3$(μ^3-η^2-CCPh)]Li(THF)$_4$ (**4.3**), and [(^{tbs}L)Fe$_3$(μ^3-S)]NBu$_4$ (**4.4**).

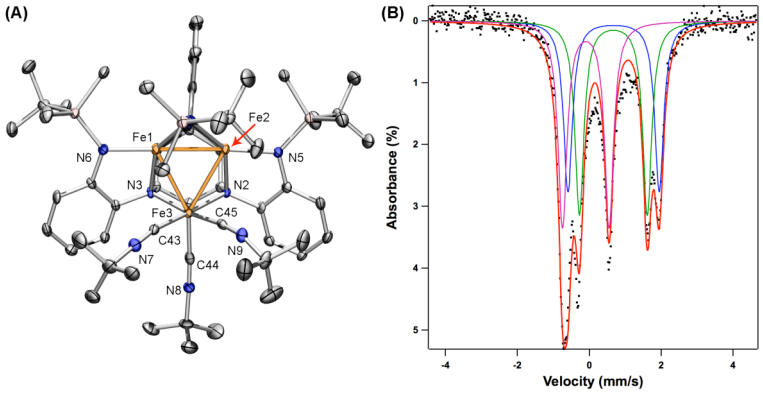

Figure 4.4. Solid-state structure for (^{tbs}L)Fe$_3$(μ^1-CN^{t}Bu)$_3$ (**4.2**) with the thermal ellipsoids set at the 50% probability level (hydrogen atoms and solvent molecules omitted for clarity; Fe orange, C black, N blue, Si pink). Bond lengths (Å) Fe1–Fe2, 2.6003(9); Fe1–Fe3, 2.6835(9); Fe2–Fe3, 2.7585(11); Fe1–N3, 2.071(3); Fe1–N6, 1.966(3); Fe2–N2, 2.080(3); Fe2–N5, 1.982(3); Fe3–N2, 2.032(3); Fe3–N3, 2.002(3). Zero field ^{57}Fe Mössbauer spectrum of **4.2** at (130 K). Fitting parameters: δ, $|\Delta E_Q|$ ($^{mm}/_s$): component 1 blue (30%) 0.68, *2.54* (Γ = 0.15 mm/s); component 2 green (34%) 0.67, *1.89* (Γ = 0.15 mm/s); component 3 pink (36%) -0.10, *1.30* (Γ = 0.15 mm/s).

The zero field ^{57}Fe Mössbauer spectrum of **4.2** (μ_{eff} = 5.8(1) μ_B) corroborates the bond metrics obtained by X-ray crystallography and is consistent with two open-shell Fe^{2+} centers and one isolated low-spin Fe^{2+} center. The Mössbauer spectrum was fit with three quadrupole doublets (Table 4.2, Figure 4.3B) where two of the quadrupole doublets are comparable to high-spin all ferrous complex [(^{tbs}L)Fe$_3$(μ^3-Br)]NBu$_4$ (Chapter 2, *vide supra*) (Table 4.2). The third quadrupole doublet (δ, $|\Delta E_Q|$ ($^{mm}/_s$): -0.10, *1.30*) has an isomer shift that is significantly lower relative to high-spin Fe^{2+} ions (Table 4.2). The isomer shift for the low-spin Fe center is lower then that of previously reported iron-sulfur clusters that feature a single low-spin Fe^{2+} center bound to three isonitriles ([Fe$_4$S$_4$(LS$_3$)(^{t}BuNC)$_3$]$^{1-}$ (LS$_3$ = tris[(4,6-dimethyl-3-mercaptophenyl)thio]-2,4,6-tris(ρ-tolylthio)benzene(3-)) and Fe$_4$S$_4$Cl$_2$(^{t}BuNC)$_6$ (Table 4.2).[208,209]

Table 4.2. Zero-field ^{57}Fe Mössbauer Parameters for compounds **4.2**, **4.3**, [Fe$_4$S$_4$(LS$_3$)(^{t}BuNC)$_3$]$^{1-}$, Fe$_4$S$_4$Cl$_2$(^{t}BuNC)$_6$, and [(^{tbs}L)Fe$_3$(μ^3-Br)]NBu$_4$

Compound		*δ (mm/s)*	*$\|\Delta E_Q\|$ (mm/s)*	*Spin state*
(^{tbs}L)Fe$_3$(μ^1-CN^{t}Bu)$_3$	(**4.2**)	0.67	2.58	Fe^{2+} hs
		0.67	1.92	Fe^{2+} hs
		–0.10	**1.32**	**Fe^{2+} ls**
[Fe$_4$S$_4$(LS$_3$)(^{t}BuNC)$_3$]$^{1-}$	ref 208	**0.20**	**0.50**	**Fe^{2+} ls**
		0.46	1.21	$Fe^{2.5+}$ hs
		0.47	1.49	$Fe^{2.5+}$ hs
		0.34	0.59	Fe^{3+} hs
Fe$_4$S$_4$Cl$_2$(^{t}BuNC)$_6$	ref 209	**0.19**	**0.45**	**Fe^{2+} ls**
		0.41	0.60	Fe^{2+} hs
[(^{tbs}L)Fe$_3$(μ^3-Br)]NBu$_4$		0.71	1.35	Fe^{2+} hs
[(^{tbs}L)Fe$_3$(μ^3-η^2-CCPh)]Li	(**4.3**)	0.66	1.58	Fe^{2+} hs
		0.47	1.94	Fe^{2+} hs
		0.57	1.30	Fe^{2+} hs

208. Weigel, J. A.; Holm, R. H. *J. Am. Chem. Soc.* **1989**, *111*, 9246-9247.
209. Weigel, J. A.; Srivastava, K. K. P.; Day, E. P.; Münck, E.; Holm, R. H. *J. Am. Chem. Soc.* **1990**, *112*, 8015-8023.

Like isonitrile and carbonyl complexes, alkynyl metal clusters have also been investigated to understand chemisorption of unsaturated small molecules to metal surfaces.[213,214] Specifically, functionalization of the α-carbon to form C–C bonds[214] and hydrogenation to alkenes[210] has been investigated. Addition of the linear anionic donor lithium phenyl acetylide to **4.1** results in immediate formation of a new Fe_3 cluster [(^{tbs}L)Fe_3(μ^3-η^2-CCPh)]Li(THF)$_4$ (**4.3**) in quantitative yield (Scheme 4.1). The paramagnetic ^{1}H NMR exhibits only 5 broad resonances, likely a result of the high solution magnetic moment for **4.3** (μ_{eff} = 11.9(4) μ_B) determined by the Evans method. X-ray quality crystals of **4.3** were grown from concentrated diethyl ether solutions stored at –33 °C. The solid-state structure shows that each Fe center is bound to two internal alkyl-aryl amide centers and is capped by one terminal silyl amide residue of the hexadentate ligand scaffold (Figure 4.5).

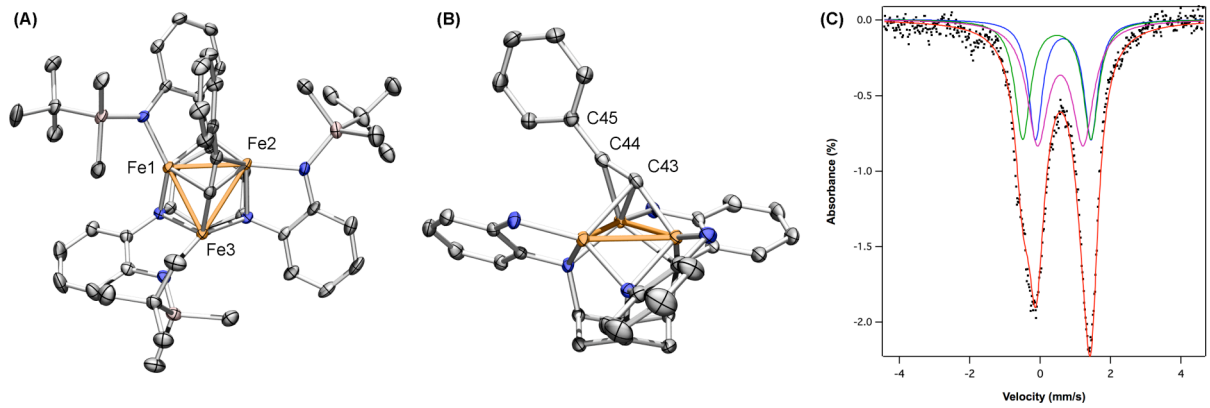

Figure 4.5. (A) Solid-state structure for [(^{tbs}L)Fe_3(μ^3-η^2-CCPh)]Li(THF)$_4$ (**4.3**) with the thermal ellipsoids set at the 50% probability level (hydrogens, lithium cation, and solvent molecules omitted for clarity; side view in B ^{t}BuMe$_2$Si– groups omitted for clarity; Fe orange, C black, N blue, Si pink). Bond lengths (Å) and bond angles (degrees): Fe1–Fe2, 2.6577(7); Fe1–Fe3, 2.5557(8); Fe2–Fe3, 2.8063(9); Fe1–C43, 2.264(3); Fe2–C43, 2.144(3); Fe3-C43, 1.984(3); Fe3–C44, 2.170(3); C43–C44, 1.244(4); C43–C44–C45, 149.8(3). (B) Zero-field Mössbauer spectrum of **4.3** obtained at 115 K. Fitting parameters: δ, $|\Delta E_Q|$ ($^{mm}/_s$) component 1 (green, 28%) 0.66, *1.58* (Γ = 0.24 $^{mm}/_s$); component 2 (blue, 31%) 0.47, *1.94* (Γ = 0.26 $^{mm}/_s$); component 3 (pink, 41%) 0.57, *1.30* (Γ = 0.36 $^{mm}/_s$).

210. Enthaler, S.; Haberberger, M.; Irran, E. *Chem. Asian J.* **2011**, *6*, 1613-1623.

Complex **4.3** features a highly desymmeterized Fe core with Fe–Fe distances ranging from 2.5557(8) to 2.8063(9) Å (Figure 4.5). The acetylide group is bound μ^3-η^2- to the Fe_3 core of the molecule (see core highlights in Figure 4.5B), with an average Fe–C43 bond length 2.131(3) Å and a Fe3–C44 bond length of 2.170(3) Å. The acetylenic moiety is substantially bent (C43–C44–C45 bond angle of 149.8(3)^o) and the C43–C44 bond distance of 1.255(4) Å is elongated relative to phenylacetylene (C–C 1.193 Å).[211] The observed decrease in bond length and bond angle in **4.3** is consistent with previously reported trinuclear μ^3-η^2-acetylide complexes,[212,213] and suggests C–C bond "activation," or elongation of an unsaturated bond upon coordination to multiple metal centers.[214] The zero-field ^{57}Fe Mössbauer spectrum of **4.3** was fit to three quadrupole doublets whose isomer shifts are lower than that observed for high-spin Fe_3 complex [(^{tbs}L)Fe_3(μ^3-Br)]NBu_4, a result of decreased shielding effects on core *s* electrons (Figure 4.5C, Table 4.2).

Finally, we investigated the reaction of **4.1** with (SCN)NBu_4. A THF solution of (SCN)NBu_4 was added to **4.1** at –33 ^{o}C resulting in a yellow-brown compound with a new ^{1}H NMR featuring 13 paramagnetic resonances, consistent with a C_3-symmetric molecule. The solution IR spectrum of the isolated product did not contain C–N or S–N stretching frequencies, suggesting the resulting compound is not a $(SCN)^-$ adduct. Storing the resulting material in diethyl ether at –33 ^{o}C deposited crystals suitable for single crystal X-ray analysis. The solid-state structure revealed that the S–C bond had been cleaved to afford a 1e^- oxidized Fe_3 cluster featuring a μ^3-sulfido moiety, [(^{tbs}L)Fe_3(μ^3-S)]NBu_4 (**4.4**) (Scheme 4.1, Figure 4.6).

211. Weiss, H.-C., Bläser, Boese, R.; Doughan, B. M.; Haley, M. M. *Chem. Comm.* **1997**, 1703-1704.
212. Hriljac, J.; Shirver, D. F. *Organometallics* **1985**, *4*, 2225-2226.
213. Hoke, J. B.; Seyferth, D. *Organometallics* **1988**, *7*, 2163-2172.
214. Sappa, E.; Tiripicchio, A.; Braunstein, P. *Chem. Rev.* **1983**, *83*, 203-239.

The structure of $[\mu^3\text{-S}]^-$ cluster **4.4** is reminiscent of the $[\mu^3\text{-X}]^-$ series, where X = Cl^-, Br^-, I^-, or N^{3-}, discussed in Chapter 2 (*vide supra*). The average Fe–Fe bond length in sulfido complex **4.4** is 2.602(1) Å, which is between that observed for the $[\mu^3\text{-N}]^-$ (Fe–Fe 2.480(1) Å) and the $[\mu^3\text{-X}]^-$ series (Fe–Fe ca. 2.77 Å). The μ^3-S ligand is heavily pyramidalized [Σ(Fe–S1–Fe) = 207.66(5)°], sitting 1.741(2) Å above the Fe_3 basal plane. Charge balance of cluster **4.4** is consistent with a $1e^-$ reduction of the Fe_3 core giving rise to a $(Fe^{III})(Fe^{II})_2$ formulation. Therefore, the $(SCN)^-$ unit formally undergoes a homolytic S–C bond cleavage, liberating CN radical upon formation of **4.4**. We hypothesize that one of the resulting byproducts could be cyanogen $(CN)_2$, however we were unable to identify any C–N stretching modes in the IR spectrum consistent with this molecule.

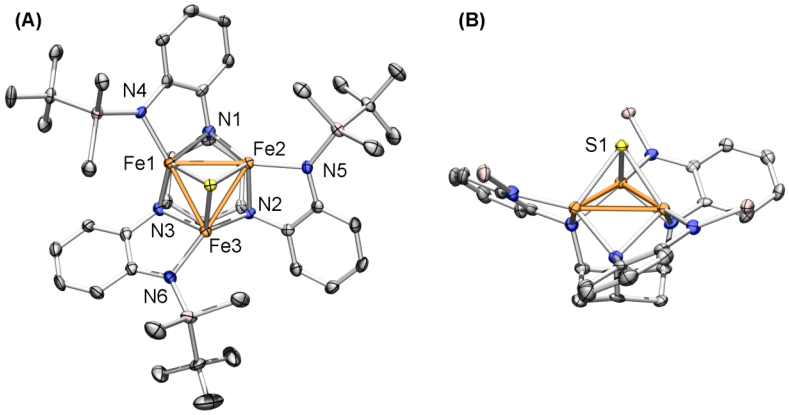

Figure 4.6. (A) Solid-state structure for $[(^{tbs}L)Fe_3(\mu^3\text{-S})]NBu_4$ (**4.4**) with the thermal ellipsoids set at the 50% probability level (hydrogens, NBu_4 cation, and solvent molecules omitted for clarity; side view in B alkyl groups on Si omitted for clarity; Fe orange, C black, N blue, Si pink, S yellow). Bond lengths (Å): Fe1–Fe2, 2.5967(9); Fe1–Fe3, 2.5508(9); Fe2–Fe3, 2.6584(9); Fe1–S1, 2.295(1); Fe2–S2, 2.276(1); Fe3–S1, 2.343(1); Fe–N_{int}, (N_{int} = N1, N2, N3) 2.031(3); Fe–N_{Si}, (N_{Si} = N4, N5, N6) 1.947(4).

Based on the coordination mode observed upon addition of phenyl acetylide to Fe_3 cluster **4.1**, it is tempting to hypothesize that sulfide formation goes through a μ^3-η^2-SCN bound intermediate. However, alternate coordination modes cannot be ruled out, including μ^3-η^1-SCN, which has been observed upon coordination of azide to Mn_3 cluster $(^{tbs}L)Mn_3(THF)$ resulting in

$[(^{tbs}L)Mn_3(\mu^3\text{-}N_3)]^-$,[215] μ^1-η^1-SCN, or an alternate binding mode not yet observed for complex **4.1**.

4-3. Substrate reduction by $(^{tbs}L)Fe_3(\mu^1\text{-}CNR)_3$ and $[(^{tbs}L)Fe_3(\mu^3\text{-}\eta^2\text{-}CCPh)]^-$

The reduction of isonitriles, which are isoelectronic with CO, at a metal cluster could provide valuable insight into the requirements to reductively couple carbonyl groups.[206] We therefore were interested in investigating the ability of **4.2** to reduce the coordinated ^{t}BuNC molecules. Heating Fe_3 cluster **4.2** in the presence of weak Si–H bonds found in phenylsilane (6–300 equiv) and varying equivalents of ^{t}BuNC (0–50 equiv) in benzene results in consumption of **4.2**, indicated by a color change from green to brown, yielding a ^{1}H NMR silent material. Analysis of the organic byproducts by gas chromatography–mass spectrometry (GC-MS) reveals formation of diimine **4.5** in 18% yield (based on moles of Fe_3 complex, quantified by GC-MS) (Scheme 4.2).

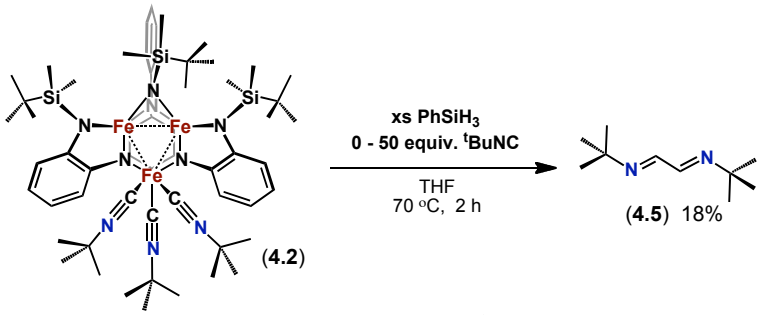

Scheme 4.2. Reductive C–C bond coupling of isonitriles by $(^{tbs}L)Fe_3(\mu^1\text{-}CNR)_3$

In this case, we not only observe reduction of ^{t}BuNC, but also C–C bond formation, an overall $2e^-$ reduction of substrate. Tetranuclear nickel clusters,[216] as well as common reducing agents such as $LiAlH_4$,[217] effect reduction of isonitriles, but do not promote C–C bond formation.

215. Unpublished work by Alison Fout, $[(^{tbs}L)Mn_3(\mu^3\text{-}N_3)]NBu_4$ has been crystallographically characterized
216. Band, E.; Pretzer, W. R.; Thomas, M. G.; Muetterties, E. L. *J. Am. Chem. Soc.* **1977**, *99*, 7380-7381.
217. Saegusa, T.; Ito, Y. Simple α-Additions. In *Isonitrile Chemistry*; Ugi, I. Ed.; Academic Press: New York, 1971, p 65-92.

Nickel salts including $NiCl_2(H_2O)_6$ and $Ni(acac)_2$ (HAcac = acetylacetone)[218] as well as heterogeneous catalysts such as Raney nickel, and Raney cobalt[219] have been shown as competent catalysts towards polymerization of both aliphatic and aromatic isonitriles. Reduction of isonitriles to form C–C bonds using homogeneous catalysts face similar challenges to CO reductive coupling, generally requiring the use of alkali metal reductants.[206,220,221,222,223]

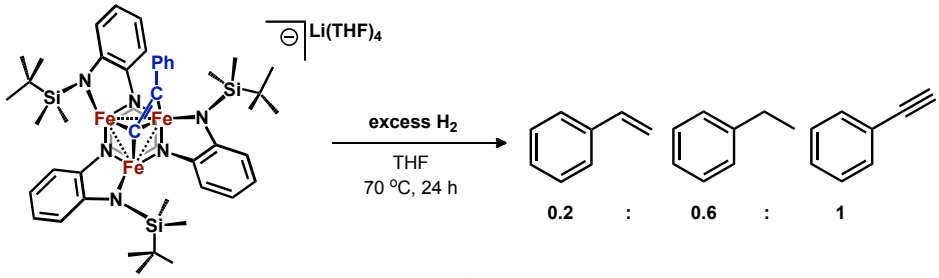

Scheme 4.3. Hydrogenation of acetylide moiety in $(^{tbs}L)Fe_3(\mu^3\text{-}\eta^2\text{-}CCPh)^-$

The C–C bond length in Fe_3–CCPh cluster **4.4** is elongated relative to free phenyl acetylene, which is consistent with an activated acetylide unit. Therefore, we were interested in investigating hydrogenation of the activated acetylene moiety in cluster **4.4**. Heating **4.4** in the presence of excess H_2 results in consumption of **4.4**, as indicated by formation of a ^{1}H NMR silent material. Analysis of the organic byproducts by GC-MS reveals formation of a mixture of hydrogenated organic products including styrene and ethylbenzene, in addition to phenyl acetylene in a 0.2:0.6:1 ratio (determined by GC-MS) (Scheme 4.3). Addition of weak acids such as lutidinium tetraphenylborate does not result in reduction and instead liberates phenyl acetylene as the only organic byproduct.

218. Nolte, R. J. M. *Chem. Soc. Rev.* **1994**, *23*, 11-19.
219. Ionkin, A.; Solek, S.; Bryndza, H.; Koch, T. *Catal. Lett.* **1999**, *61*, 139-141.
220. Lam, C. T.; Corfield, P. W. R.; Lippard, S. J. *J. Am. Chem. Soc.* **1977**, *99*, 617-618.
221. Lippard, S. J. Seven and Eight Coordinate Molybdeum Complexes and Related Molybdenum (IV) Oxo Complexes with Cyanide and Isocyanide Ligands. In *Prog. Inorg. Chem.*; Lippard, S. J., Ed.; Wiley: Malden, 1976; Vol. 21, p 91-103.
222. Hoffmann, R.; Wilker, C. N.; Lippard, S. J.; Templeton, J. L.; Bower, D. C. *J. Am. Chem. Soc.* **1983**, *105*, 146-147.
223. Okazaki, M.; Suto, K.; Kudo, N.; Takano, M.; Ozawa, F. *Organometallics* **2012**, *31*, 4110-4113.

4-4. Evidence for (^{tbs}L)Fe$_3$(μ^1-CO)$_3$

Ultimately, we would like to be able to expand this type of chemistry to CO. Preliminary results indicate that a similar Fe_3 cluster can be accessed with CO. Addition of excess CO to complex **4.1** resulted in formation of a purple paramagnetic species with a new ^{1}H NMR similar to that observed for tris-isonitrile complex **4.2**. While free ligand is formed during the reaction (identified by ^{1}H NMR) and the crude IR features numerous C–O stretches, we were able to obtain crystals that contained a compound with three C–O stretches in the IR (1973, 2034, 2069 cm^{-1}) consistent with μ^1 Fe carbonyl complexes previously reported in the literature.[224,225,226] X-ray crystallography revealed the identity of the product as tris-carbonyl cluster (^{tbs}L)Fe$_3$(μ^1-CO)$_3$ (**4.6**) (Scheme 4.4, Figure 4.7). The coordination environment at each metal center of **4.6** is identical to that of tris-isonitrile cluster **4.2** and the average C–O distance (1.144(3) Å) of the carbonyl groups in **4.6** is consistent with the μ^1 carbonyl groups found in Fe_3 dodecacarbonyl.[227,228] Fe_3 complex **4.6** is an appealing compound by which to study the reductive coupling of carbonyl groups and should be pursued in future studies.

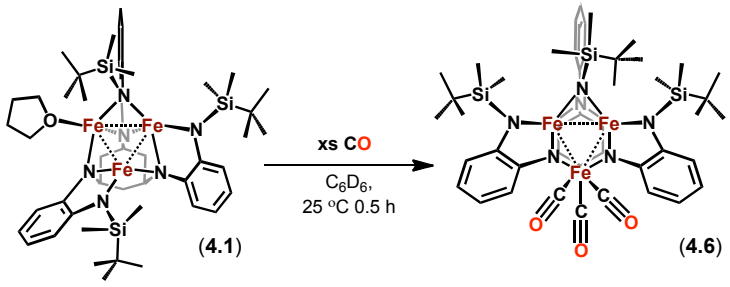

Scheme 4.4. Synthesis of (^{tbs}L)Fe(μ^1-CO)$_3$

224. Box, J. W.; Gray, G. M. *Inorg. Chem.* **1987**, *26*, 2774-2778.
225. Darensbourg, D. J.; Nelson, III, H. H.; Hyde, C. L. *Inorg. Chem.* **1974**, *13*, 2135-2145.
226. Chong, T. S.; Tan, S. T.; Fan, W. Y. *Chem. Eur. J.* **2006**, *12*, 5128-5133.
227. C.H. Wei, Dahl, L. F. *J. Am. Chem. Soc.* **1969**, *91*, 1351-1361.
228. Cotton, F. A.; Troup, J. M. *J. Am. Chem. Soc.* **1974**, *26*, 4155-4159.

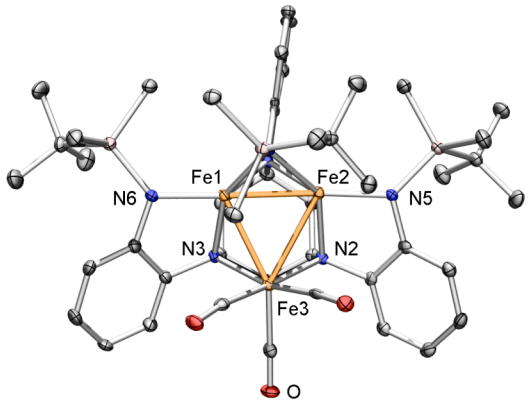

Figure 4.7. Solid-state structure for (^{tbs}L)Fe$_3$(μ^1-CO)$_3$ (**4.6**) with the thermal ellipsoids set at the 50% probability level (hydrogens and solvent molecules omitted for clarity; Fe orange, C black, N blue, Si pink, O red). Bond lengths (Å) Fe1–Fe2, 2.5074(6); Fe1–Fe3, 2.6229(6); Fe2–Fe3, 2.7589(6); Fe1–N3, 1.966(2); Fe1–N6, 1.942(2); Fe2–N2, 2.053(2); Fe2–N5, 1.936(2); Fe3–N2, 2.035(2); Fe3–N3, 2.020(2); C–O$_{avg}$, 1.144(3).

4-5. Conclusions

With the precedent that (^{tbs}L)Fe$_3$(THF) is capable of reducing unsaturated nitrogenous substrates, we were interested in exploring the ability of **4.1** to activate other unsaturated small molecules. We used both ^{1}H NMR and IR spectroscopies as well as X-ray crystallography to determine the coordination mode of a variety of linear substrates bound to Fe$_3$ cluster **4.1**. Fe$_3$ cluster **4.1** binds both neutral and anionic donors and supports several different binding motifs. While anionic ligand donors including X$^-$ (X = halide), N^{3-}, PhCC$^-$, and S$^-$ moieties bind symmetrically to all three metal centers, yielding clusters with open-shell electron configurations, neutral π-acidic molecules including ^{t}BuNC and CO preferentially bind μ^1 to a single metal center within the assembly. The filled anti-bonding orbitals in high-spin cluster **4.1** (S = 6) makes the barrier for ligand rearrangement low, providing a pathway by which coordination of three strong field ligands to a single metal center is favored over cooperative substrate binding. On the other hand, the charge buildup incurred upon coordination of an

anionic substrate likely precludes multiple molecules from binding to the Fe_3 core and as a result cooperative binding modes are preferred.

Anionic donor phenyl acetylene forms a μ^3-η^2 adduct with Fe_3 cluster **4.1**, resulting in an elongation of the C–C bond in the acetylene unit and a deviation from linearity. The bond metrics and geometry of the phenyl acetylide unit suggest substrate "activation" has taken place. Hydrogenation of phenyl acetylide Fe_3 adduct **4.3** yields both styrene and ethyl benzene as the resulting 2 and 4e^- reduced products. Fe_3 cluster **4.1** also activates the anionic donor $(SCN)^-$, resulting in S–C bond homolysis to yield the 1e^- oxidized cluster $[(^{tbs}L)Fe_3(\mu^3\text{-}S)]NBu_4$.

The structural and spectroscopic data of tris-isonitrile adduct **4.2** is consistent with metal center Fe3 (bound to three strong field ligands) adopting a low-spin configuration, while the remaining two metal centers maintain an open-shell electron configuration. Complex **4.2** undergoes C–C reductive coupling in the presence of phenylsilane to yield *bis*-imine product **4.5**. Preliminary results indicate that a similar cluster with CO can be synthesized and we are interested in exploring its reactivity with weak H-bond donors. The results herein substantiate that cooperative substrate binding to all three metal centers is not required in order to observe reduction chemistry by $(^{tbs}L)Fe_3(THF)$.

4-6. Experimental methods

Materials and Methods

All manipulations involving metal complexes were carried out using standard Schlenk line or glove-box techniques under a dinitrogen atmosphere. All glassware was oven-dried for a minimum of 10 h and cooled in an evacuated antechamber prior to use in the dry box. Benzene, diethyl ether, hexanes and tetrahydrofuran (THF) were dried and deoxygenated on a Glass Contour System (SG Water USA, Nashua, NH) and stored over 4 Å molecular sieves (Strem)

prior to use. Benzene-d_6 was purchased from Cambridge Isotope Labs and was degassed and stored over 4 Å molecular sieves prior to use. Non-halogenated solvents were typically tested with a standard purple solution of sodium benzophenone ketyl in THF in order to confirm effective oxygen and moisture removal. Lithium phenyl acetylide[229] and $FeMes_4$[165] were prepared following published methods. All other reagents were purchased from commercial vendors and used without further purification unless explicitly stated.

Physical Measurements

All of the measurements for the metal complexes were made under anaerobic conditions. Elemental analyses were performed by Complete Analysis Laboratories, Inc., Parsippany, New Jersey. ^{1}H NMR spectra were recorded on a Varian Unity/Inova 500 NMR spectrometer with chemical shifts (δ ppm) referenced to residual NMR solvent. UV-visible spectra were recorded on a Varian Cary 50 UV-visible spectrometer using quartz cuvettes. Zero-field, ^{57}Fe Mössbauer spectra were measured with a constant acceleration spectrometer (SEE Co, Minneapolis, MN). Solid or crystalline samples were prepared as Paratone-N mulls in a drybox and frozen in liquid nitrogen prior to handling in air. Isomer shifts are quoted relative to Fe metal at room temperature. Data was processed, simulated, and analyzed using an in-house package for IGOR Pro 6 (Wavemetrics, Lake Oswego, OR). Solution magnetic susceptibilities were determined by Evans′ method using trifluoromethylbenzene as an internal reference. Gas chromatography–mass spectrometry (GC-MS) data was collected on a Shimadzu Gas-chromatograph (GCMS-QP2010S).

Synthesis

(^{tbs}L)Fe$_3$(μ^1-CN^{t}Bu)$_3$ (4.2). A THF (10 mL) solution of (^{tbs}L)Fe$_3$(THF) (0.130 g, 0.133

229. Carrera, N.; Gutiérrez, E.; Benavente, R.; Villavieja, M. M.; Albéniz, A. C.; Espinet, P. *Chem. Eur. J.* **2008**, *14*, 10141-10148.

mmol) was added to liquid *t*-butylisocyanide (^{t}BuNC) (0.0342 g, 0.412 mmol) cold (–33 °C). Once the reaction reached room temperature, the solution was stirred for an additional 4 h. The volatiles were removed in vacuum, resulting in a dark green solid. The solid was stirred in cold hexanes (2 × 7 mL at –40 °C) and filtered to remove excess ^{t}BuNC. The resulting solid was then re-dissolved in benzene (10 mL) and removed in vacuum to yield pure product. Isolated yield: 0.135 g, (89%). ^{1}H NMR (benzene-d_6, 500 MHz, δ, ppm): 103.4, 30.37, 22.67, 20.31, 19.62, 13.32, 12.70, 12.49, 6.26, 1.75, 1.20, –0.30, –0.39, –0.84, –3.48, –5.52, –12.67, –26.11, –57.75, –67.74; Anal. Calcd for $C_{57}H_{93}Fe_3N_9Si_3$: C 59.21, H 8.11, N 10.90. Found: C 59.10, H 8.07, N 10.79; Zero-field ^{57}Fe Mössbauer (130 K) (δ, $|\Delta E_Q|$ ($^{mm}/_s$)): component 1: 0.67, *2.58* (32%) component 2: -0.10, *1.32* (32%) component 3: 0.67, *1.92* (35%); IR Spectroscopy (Solution Cell, THF, ν_{CN}, cm^{-1}): 2137, 2103, 2070; UV-vis Spectroscopy (THF): 254 nm ($\varepsilon = 3.58 \times 10^5$ $M^{-1}cm^{-1}$); 589 nm ($\varepsilon = 4.12 \times 10^4$ $M^{-1}cm^{-1}$).

[(^{tbs}L)Fe$_3$(μ^3-η^2-CCPh)]Li(THF)$_4$ (4.3) A THF solution of (^{tbs}L)Fe$_3$(THF) (0.080 g, 0.082 mmol) was added to solid lithium phenyl acetylide (0.0084 g, 0.078 mmol) cold (–33 °C). Once the reaction reached room temperature, the solution was stirred for an additional 3 h. The volatiles were removed in vacuum resulting in a brown oil. The oil was washed with 10 mL of hexanes and filtered through Celite to remove excess (^{tbs}L)Fe$_3$(THF). The product was then re-dissolved into THF (2 mL) and lyophilized from benzene (2 mL) to afford a solid in quantitative yield. ^{1}H NMR (benzene-d_6, 500 MHz, δ, ppm): 45.57, 16.13, 11.56, 3.25, 1.13; Anal. Calcd for $C_{50}H_{71}Fe_3LiN_6Si_3$: C 59.17, H 7.05, N 8.82. Found: C 59.08, H 7.05, N 8.23; Zero-field ^{57}Fe Mössbauer (115 K) (δ, $|\Delta E_Q|$ ($^{mm}/_s$)): component 1: 0.66, *1.58* (33%) component 2: 0.47, *1.94* (33%) component 3: 0.57, *1.30* (33%); UV-vis Spectroscopy (THF): 300 nm ($\varepsilon = 2.63 \times 10^4$ $M^{-1}cm^{-1}$); 247 nm ($\varepsilon = 8.71 \times 10^4$ $M^{-1}cm^{-1}$).

[(^{tbs}L)Fe$_3$(μ^3-S)]NBu$_4$ (4.4). A THF solution (5 mL) of ^{tbs}LH$_6$ (0.045 g, 0.060 mmol) was added to solid FeMes$_4$ (0.0056 g, 0.19 mmol). The reaction was heated in a sealed bomb at 75 °C for 12 h. The solution was then added to solid [SCN]NBu$_4$ (0.020 g, 0.067 mmol) cold (–33 ^{o}C). Once the reaction reached room temperature, the solution was stirred for an additional 4 h. The volatiles were removed in vacuum resulting in a yellow-brown oil. X-ray quality crystals were grown from a cold (–33 ^{o}C) hexanes/diethyl ether solution. ^{1}H NMR (benzene-d_6, 500 MHz, δ, ppm): 53.69, 14.02, 12.85, 12.23, 2.70, 0.94, 0.60, -0.93, –1.05, –3.80, –4.71, –9.98, –32.22; Anal. Calcd for $C_{58}H_{102}Fe_3N_7SSi_3$: C 58.97, H 8.70, N 8.30. Found: C 58.92, H 8.66, N 8.18.

(^{tbs}L)Fe$_3$(μ^1-CO)$_3$ (4.6). A benzene solution (0.5 mL) of (^{tbs}L)Fe$_3$(THF) (0.035 g, 0.036 mmol) was sealed in a j-young tube. The solution was frozen at 77 K and the headspace was evacuated (3×). To the frozen sample, 1 atmosphere of CO gas (passed through a drying tube filled with anhydrous calcium sulfate) was added to the reaction and allowed to sit for 3 h at room temperature. X-ray quality crystals were grown from benzene (0.5 mL). The reaction was not amenable to scale-up and frequently resulted in formation of free-ligand along with product (determined by ^{1}H NMR). Anal. Calcd for $C_{45}H_{69}Fe_3N_6O_3Si_3$: C 54.39, H 7.00, N 8.46. Found: C 54.38, H 7.08, N 8.32; Zero-field ^{57}Fe Mössbauer (115 K) (δ, $|\Delta E_Q|$ ($^{mm}/_s$)): component 1 (22%) 0.75, *2.65*; component 2 (22%) 0.71, *1.30*; component 3 (55%) 0.16, *0.75*; IR Spectroscopy (Solution Cell, C_6D_6, ν_{CO}, cm^{-1}): 1973, 2034, 2069.

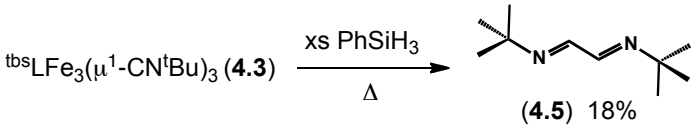

Reduction of (4.2) by phenylsilane. Solid **4.2** (0.020 g, 0.017 mmol) was dissolved in 0.5 mL of C_6D_6 and was added to a 0.5 mL C_6D_6 solution of phenylsilane (0.011 g, 0.102 mmol). The mixture was heated to 70 ^{o}C for 2 h, resulting in a ^{1}H NMR silent material. A series of

similar experiments were run in the presence of excess ^{t}BuNC (up to 50 equivalents ^{t}BuNC and 600 equivalents of phenylsilane). In the presence of excess ^{t}BuNC, the reaction was heated for longer periods of time, until all of the starting material (**4.2**) was consumed. The mixtures were filtered through Celite and a sample of the solution was prepared for yield determination. An aliquot of the solution was diluted with diethyl ether and analyzed by GC-MS (method: hold at 50 ^{o}C for 1 minute, heat from 50–200 ^{o}C at a rate of 15^{o}/minute, hold at 200 ^{o}C for 3 minutes). A series of standard samples of **4.5** were run prior to each set of experiments to establish a calibration curve. Peak areas of the formed products were compared to the calibration curve and resulted in yields ranging from <1% – 18% (yield dependant on the amount of excess ^{t}BuNC added to the reaction). GC-MS (EI) t_R = 5.56 min; m/z: 41, 57, 70, 97, 111, 126, 141. In addition to **7**, diphenylsilane was identified by GC-MS as one of the organic byproducts. GC-MS (EI) t_R = 9.41 min; m/z: 40, 53, 66, 79, 91, 106, 115, 129, 153, 184. Several other fractions were observed by GC-MS during analysis but were not identified.

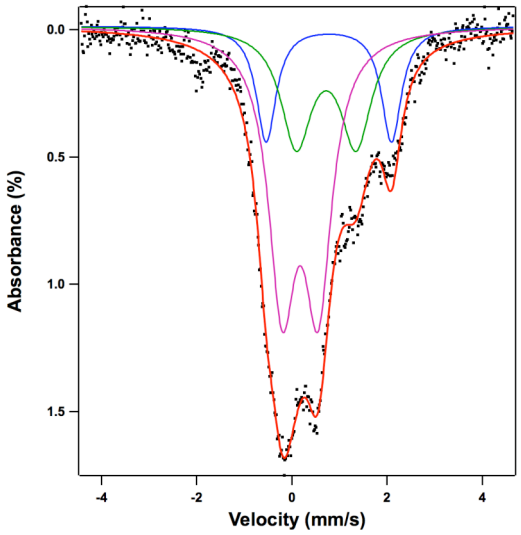

Figure 4.8. Zero-field Mössbauer spectrum of non-crystalline (^{tbs}L)Fe$_3$(CO)$_3$ (**4.6**) obtained at 115 K. Simulation yields the following parameters: δ, $|\Delta E_Q|$ ($^{mm}/_{s}$) component 1 (18%) 0.78, *2.63* (Γ = 0.25 $^{mm}/_{s}$); component 2 (27%) 0.72, *1.26* (Γ = 0.39 $^{mm}/_{s}$); component 3 (55%) 0.17, *0.76* (Γ = 0.35 $^{mm}/_{s}$). The reported parameters represent the best fit obtained with respect to the isomer shifts (compared to the parameters obtained for isoelectronic **4.2**).

X-Ray Diffraction Techniques

All structures were collected on a Bruker three-circle platform goniometer equipped with an Apex II CCD and an Oxford cryostream cooling device. Radiation was from a graphite fine focus sealed tube Mo Kα (0.71073 Å) source. Crystals were mounted on a cryoloop or glass fiber pin using Paratone N oil. Structures were collected at 100 K. Data was collected as a series of φ and/or ω scans. Data was integrated using SAINT and scaled with either a numerical or multi-scan absorption correction using SADABS.[170] The structures were solved by direct methods or Patterson maps using SHELXS-97 and refined against F^2 on all data by full matrix least squares with SHELXL-97.[171] All non-hydrogen atoms were refined anisotropically. Hydrogen atoms were placed at idealized positions and refined using a riding model. The isotropic displacement parameters of all hydrogen atoms were fixed to 1.2 times the atoms they are linked to (1.5 times for methyl groups). Further details on particular structures are noted below.

(^{tbs}L)Fe$_3$(CN^{t}Bu)$_3$ (4.2). The structure was solved in the triclinic space group $P\ \bar{1}$ with 2 molecules per unit cell. The asymmetric unit contains one molecule of (^{tbs}L)Fe$_3$(CN^{t}Bu)$_3$ and one diethyl ether solvent molecule. The solvent diethyl ether molecule exhibited positional disorder and was refined using similarity restraints.

[(^{tbs}L)Fe$_3$(CCPh)]Li(THF)$_4$ (4.3). The structure was solved in the triclinic space group $P\ \bar{1}$ with 2 molecules per unit cell. The asymmetric unit contains one [(^{tbs}L)Fe$_3$(CCPh)]Li with four diethyl ether/THF solvent molecules coordinated to the lithium center. The solvent molecules exhibited positional disorder and were refined using similarity restraints.

[(^{tbs}L)Fe$_3$(μ^3-S)]NBu$_4$ (4.4). The structure was solved in the orthorhombic space group *Pbca* with 8 molecules per unit cell. The asymmetric unit contains two [(^{tbs}L)Fe$_3$(μ^3-S)]NBu$_4$ and two diethyl ether solvent molecules. One of the diethyl ether molecules exhibited positional

disorder and was refined using similarity restraints.

(^{tbs}L)Fe$_3$(CO)$_3$ (4.6). The structure was solved in the triclinic space group $P\ \bar{1}$ with 2 molecules per unit cell. The asymmetric unit contains one (^{tbs}L)Fe$_3$(CO)$_3$ molecule and two benzene solvent molecules.

Table 4.3. X-ray Crystallographic Data for All Compounds

	4.2	4.3	4.4	4.6
Chemical formula	$C_{61}H_{103}Fe_3N_9OSi_3$	$C_{66}H_{107}Fe_3LiN_6O_4Si_3$	$C_{124}H_{224}Fe_6N_{14}Si_6O_2S_2$	$C_{57}H_{78}Fe_3N_6O_3Si_3$
fw	1230.34	1307.35	2510.93	1147.07
Space group	$P\bar{1}$	$P\bar{1}$	*Pbca*	$P\bar{1}$
a (Å)	11.755(4)	12.306(3)	19.174(3)	10.1242(7)
b (Å)	14.424(5)	16.315(4)	27.457(5)	13.978(1)
c (Å)	21.029(7)	18.872(5)	53.284(9)	20.711(1)
α (deg)	92.724(6)	104.108(4)		83.932(1)
β (deg)	105.643(5)	103.336(4)		80.715(1)
γ (deg)	98.835(6)	99.373(4)		76.953(1)
V (Å^3)	3378(2)	3477(2)	28053(8)	2810.5(3)
Z	2	2	8	2
μ (mm^{-1})	0.73	0.72	0.74	0.88
T (K)	100(1)	100(1)	100(1)	100(1)
R1[a] (wR2[b])	0.052 (0.120)	0.045 (0.112)	0.059 (0.126)	0.040 (0.093)

[a] $R1 = [\sum w(F_o - F_c)^2/\sum wF_o^2]^{1/2}$

[b] $wR2 = [\sum [w(F_o^2 - F_c^2)^2]/ \sum w(F_o^2)^2]^{1/2}$, $w = 1/[\sigma^2(F_o^2) + (aP)^2 + bP]$, where $P = [\max(F_o^2,0) + 2(F_c^2)]/3$

Chapter 5.[230] Towards the Synthesis of Bimetallic Trinuclear Clusters

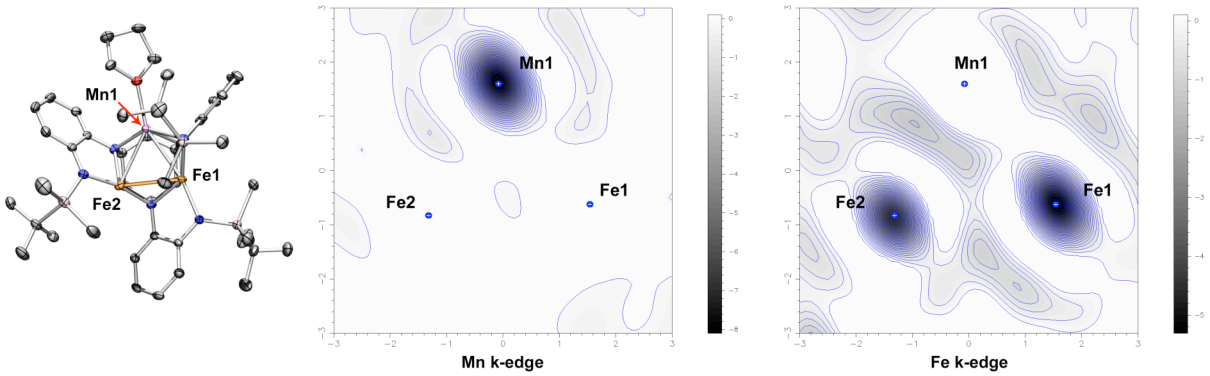

5-1. Introduction: effects of metal substitution

Metal substitution in Fe-only nitrogenase – Nature's nitrogen fixation machinery – to FeMo- and FeV-based nitrogenase results in significant changes in enzymatic activity and chemoselectivity (Figure 5.1A).[28,30,33,34] For example, at ambient temperature and pressure, FeMoco has a higher activity toward dinitrogen relative to FeVco and Fe-only nitrogenase[32] and mixed-metal FeMo and FeV cofactors engage alternative substrates including CO and ethylene,[231] while Fe-only nitrogenase does not. Analogously, substitution of a single Fe center in ribonucleotide reductase (RNR) with Mn changes the mechanism by which the enzyme generates 2' deoxyribonucleotides for DNA synthesis; while Class I Fe-only RNRs operate by generating a stable tyrosyl radical initiator, bimetallic Mn/Fe RNRs feature a Mn(IV)/Fe(III) unit which acts as the radical initiator during catalysis (Figure 5.1B).[232,233,234]

---

230. This chapter was adapted with permission from Powers, T. M.; Gu, N.; Fout, A. R.; Hernández Sánchez, R.; Alfonso, D.; Chen, Y.-S.; Zheng, S.-L.; Betley, T. A. *J. Am. Chem. Soc.* **2013**, *submitted*. Unpublished work Copyright 2013 American Chemical Society.
231. Hu, Y.; Lee, C. C.; Ribbe, M. W. *Dalton Trans.* **2012**, *41*, 1118-1127.
232. Jiang, W.; Yun, D.; Saleh, L.; Barr, E. W.; Xing, G.; Hoffart, L. M.; Maslak, M.-A.; Krebs, C.; Bollinger Jr., M. *Science* **2007**, *316*, 1188-1191.
233. Younker, J. M.; Krest, C. M.; Jiang, W.; Krebs, C.; Bollinger Jr., J. M.; Green, M. T. *J. Am. Chem. Soc.* **2008**, *130*, 15022-1527.
234. Bollinger Jr., J. M.; Jiang, W.; Green, M. T.; Krebs, C. *Curr. Opinion Struct. Biol.* **2008**, *18*, 650-657.

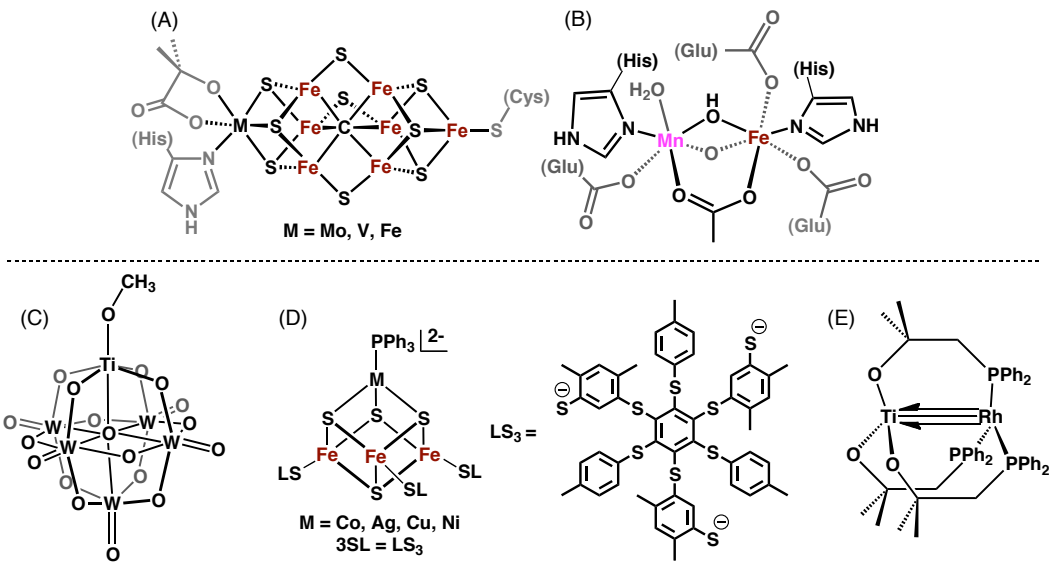

Figure 5.1. Examples of metalloenzymes featuring bimetallic cofactors: (A) FeMoco of nitrogenase and (B) proposed Fe(III)Mn(IV) cofactor of ribonucleotide reductase (note: site-placement of metal ions unknown).[233] Examples of previously synthesized bimetallic compounds accessed by (C) self-assembly methods (e.g. polyoxometalates),[235,236] (D) reaction of incomplete clusters (e.g. cubodal Fe_3S_4 clusters)[3,237,238] with divalent transition metal or alkaline ions, and (E) polynucleating ligands that have different elemental binding affinities (heterobimetallic Ti/Rh cluster).[239]

The observed changes in reactivity upon metal substitution are not limited to biological systems. Alloys are frequently utilized for heterogeneous catalysis in industrial processes, and in some cases demonstrate vastly different catalytic properties as well as higher catalytic reactivity relative to the pure metal surface counterparts.[240,241,242,243,244,245] For example, long chain hydrocarbons are generated industrially by the Fischer-Tropsch process, which utilizes bimetallic surfaces including Fe/Co, Co/Ni and Ni/Fe alloys.[246] When alloys are replaced with pure metal

235. Clegg, W.; Elsegood, M. R. J.; Errington, J.; Havelock, J. *J. Chem. Soc., Dalton Trans.* **1996**, 681-690.
236. Wei, Y.; Lu, M.; Cheung, C. F.-c.; Barnes, C. L.; Peng, Z. *Inorg. Chem.* **2001**, *40*, 5489-5490.
237. Ciurli, S.; Ross, P. K.; Scott, M. J.; Yu, S.-B.; Holm, R. H. *J. Am. Chem. Soc.* **1992**, *114*, 5415-5423.
238. Zhou, J.; Scott, M. J.; Hu, Z.; Peng, G.; Münck, E.; Holm, R. H. *J. Am. Chem. Soc.* **1992**, *114*, 10843-10854.
239. Slaughter, L. M.; Wolczanski, P. T.; *Chem. Commun.* **1997**, 2109-2110.
240. Sinfelt, J. H. *Bimetallic Catalysts. Discoveries, Concepts, and Applications*; Wiley: New York, 1983.
241. Sinfelt, J. H. *Acc. Chem. Res.* **1977**, *10*, 15-20.
242. Ponec, V. *Appl. Catal., A* **2001**, *222*, 31-45.
243. Thomas, J. M.; Raja, R.; Johnson, B. F. G.; Hermans, S.; Jones, M. D.; Khimyak, T. *Ind. Eng. Chem. Res.* **2003**, *42*, 1563-1570.
244. Gladys, M. J.; Inderwildi, O. R.; Karakatsani, S.; Fiorin, V.; Held, G. *J. Phys. Chem. C* **2008**, *112*, 6422-6429.
245. Santo, V. D.; Gallo, A.; Naldoni, A.; Guidotti, M.; Psaro, R. *Catal. Today* **2012**, *197*, 190-205.
246. Calderone, V. R.; Shiju, N. R.; Ferré, D. C.; Rothenberg, G. *Green Chem.* **2011**, *13*, 1950-2216.

materials under catalytic conditions, lower activity towards substrate as well as decreased selectivity towards higher molecular weight hydrocarbons is observed.[246,247]

Metalloenzymes and synthetic heterogeneous catalysts demonstrate that metal substitution is a powerful synthetic tool that can be used to tune reactivity without ligand modification. However, the exact role that metal substitution plays in enzymatic systems like nitrogenase and bimetallic solid-state catalysts is difficult to assess. Synthetic heterometallic clusters have been studied to understand the effect of metal substitution on reactivity, as well as gain a better understanding of the stability, reactivity, and coordination environment of the individual metal reaction sites.[248,249] Three general strategies have been pursued for the synthesis of mixed-metal clusters: 1) self-assembly processes[235,236,250] (Figure 5.1C); 2) reaction of incomplete clusters (e.g. partially formed cubanes) with divalent transition metal or alkaline ions[3,21,251,252,253,254,255] (Figure 5.1D); and, 3) utilization of polynucleating ligand scaffolds that possess different elemental binding affinities to selectively interact with one metal ion in preference to another[239,256,257,258,259,260,261] (Figure 5.1E).

247. Arai, H.; Mitsuishi, K.; Seiyama, T. *Chem. Lett.* **1984**, 1291-1294.
248. Hung, S. Y.-W.; Wong, W.-T. *Chem. Commun.* **1997**, 2099-2100.
249. Adams, R. D.; Barnard, T. S.; Li, Z.; Wu, W.; Yamamoto, J. H. *J. Am. Chem. Soc.* **1994**, *116*, 9103-9113.
250. Tulsky, E. G.; Long, J. R. *Inorg. Chem.* **2001**, *40*, 6990-7002.
251. Johnson, M. K.; Duderstadt, R. E.; Duin, E. C. *Adv. Inorg. Chem.* **1999**, *47*, 1-82.
252. Holm, R. H. *Adv. Inorg. Chem.* **1992**, *38*, 1-71.
253. Hernandex-Molina, R.; Sokolov, M. N.; Sykes, A. G. *Acc. Chem. Res.* **2001**, *34*, 223-230.
254. Clerác, R.; Cotton, F. A.; Dunbar, K. R.; Murillo, C. A.; Wang, X. *Inorg. Chem.* **2001**, *40*, 420-426.
255. Nippe, M.; Berry, J. F. *J. Am. Chem. Soc.* **2007**, *129*, 12684-12685.
256. Pilkington, N. H.; Robson, R. *Aust. J. Chem.* **1970**, *23*, 2225-2236.
257. Beissel, T.; Birkelback, F.; Bill, E.; Glaser, T.; Kesting, F.; Krebs, C.; Weyhermüller, T.; Wieghardt, K.; Butzlaff, C.; Trautwein, A. X. *J. Am. Chem. Soc.* **1996**, *118*, 12376-12390.
258. Glaser, T.; Kesting, F.; Beissel, T.; Bill, E.; Weyhermüller, T.; Klaucke, W.; Wieghardt, K. *Inorg. Chem.* **1999**, *38,* 722.
259. Akilne, S.; Taniguchi, T.; Nabeshima, T. *Inorg. Chem.* **2008**, *47*, 3255-3264.
260. Greenwood, B. P.; Forman, S. I.; Rowe, G. T.; Chen, C.-H.; Foxman, B. M.; Thomas, C. M. *Inorg. Chem.* **2009**, *48*, 6251-6260.
261. Rudd, P. A.; Liu, S.; Gagliardi, L.; Young, V. G. Jr.; Lu, C. C. *J. Am. Chem. Soc.* **2011**, *133*, 20724-20727.

Our lab has approached the synthesis of metal clusters through the development of a family of hexadentate ligand platforms, which provide a method of structure-function analysis through systematic modification of the steric and electronic environment of the cluster. We have previously reported the synthesis of several homotrinuclear clusters of Co, Mn, and Fe, supported by hexadentate ligand platforms comprised of *o*-phenylenediamine-based subunits, whose intracore interactions and molecular spin states vary as a function of ligand architecture.[143,144,145,146] Adapting our synthetic protocol to yield bimetallic trinuclear clusters supported by hexaamide ligand platforms would provide an alternative avenue by which we can investigate the role M–M interactions play in both electronic structure and reactivity. The synthesis of heteronuclear clusters supported by polynucleating ligand scaffolds that feature unbiased metal-binding sites has not yet been realized, potentially due to the challenge of controlling the metal incorporation. In the absence of coordinating solvent, we access binuclear metal complexes ($^{tbs}LH_2)M_2$, providing a platform by which we can explore the stepwise synthesis of a family of mixed-metal clusters that differ by single metal-site substitutions (Scheme 5.1). Through this investigation we have sought to address the following questions:

1) Can the hexaamide ligand ($^{tbs}L^{6-}$) support all metal substitution combinations from Mn_3 to Fe_3 in single metal-substitution steps?
2) Is the metal insertion site isolated, or does the unique metal center exchange with the other metals within the cluster?
3) Can ancillary ligands, such as coordinated solvent molecules (THF in Scheme 5.1), be used to tune the selectivity of metal substitution reaction?

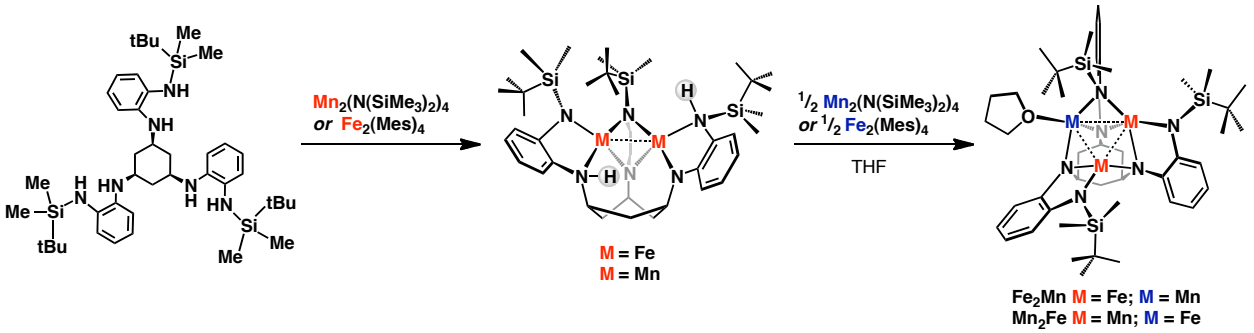

Scheme 5.1. Synthetic strategy for the synthesis of bimetallic trinuclear clusters.

5-2. Synthesis and bulk spectroscopic characterization

Herein, we present the synthesis of trinuclear Fe_3 (**5.1**), Mn_3 (**5.2**), and Fe_2Mn (**5.5**) complexes supported by hexaamide ligand ($^{tbs}L^{6-}$). Spectroscopic and structural characterization establishes that these compounds are substitutionally homogenous materials. Synthetic attempts to prepare analogous Mn_2Fe complexes (**5.6** and **5.7**, which differ by the coordinated solvent molecule, THF or py, respectively, Scheme 5.1) resulted in the preparation and isolation of mixtures of metal species. In **Section 5-2**, we describe the spectral and structural data of the materials as bulk crystalline compounds, which was used to assign the metal substitution patterns in complex Fe_2Mn **5.5** and THF ligated mixed-metal complex **5.6**. In **Section 5-3** we present anomalous scattering measurements of all three mixed-metal species (**5.5**, **5.6**, and **5.7**[262]), providing single-site elemental analysis of the metal positions.

Metallation of the hexaamine ligand scaffold 1,3,5-C_6H_9-(NHC_6H_4-*o*-$NHSi^tBuMe_2$)$_3$ ($^{tbs}LH_6$) was effected using 1.5 equivalents of $Fe_2(Mes)_4$ or 1 equivalent of $Mn_3(Mes)_6$; Mes = 2,4,6-$Me_3C_6H_2$, in the presence of tetrahydrofuran (THF) to yield Fe_3 complex (^{tbs}L)Fe_3(THF) (**5.1**)[168] and Mn_3 complex (^{tbs}L)Mn_3(THF) (**5.2**, 49%), respectively. Crystallographic analysis of single crystals of Mn_3 cluster **5.2** shows that the three Mn ions each possess unique coordination

262. While mixed-metal py ligated cluster **5.7** is not discussed in **Section 5-2**, it has been fully characterized by the spectroscopic methods described herein and exhibits similar spectroscopic features compared to THF ligated mixed-metal cluster **5.6** (see **Section 5-6**).

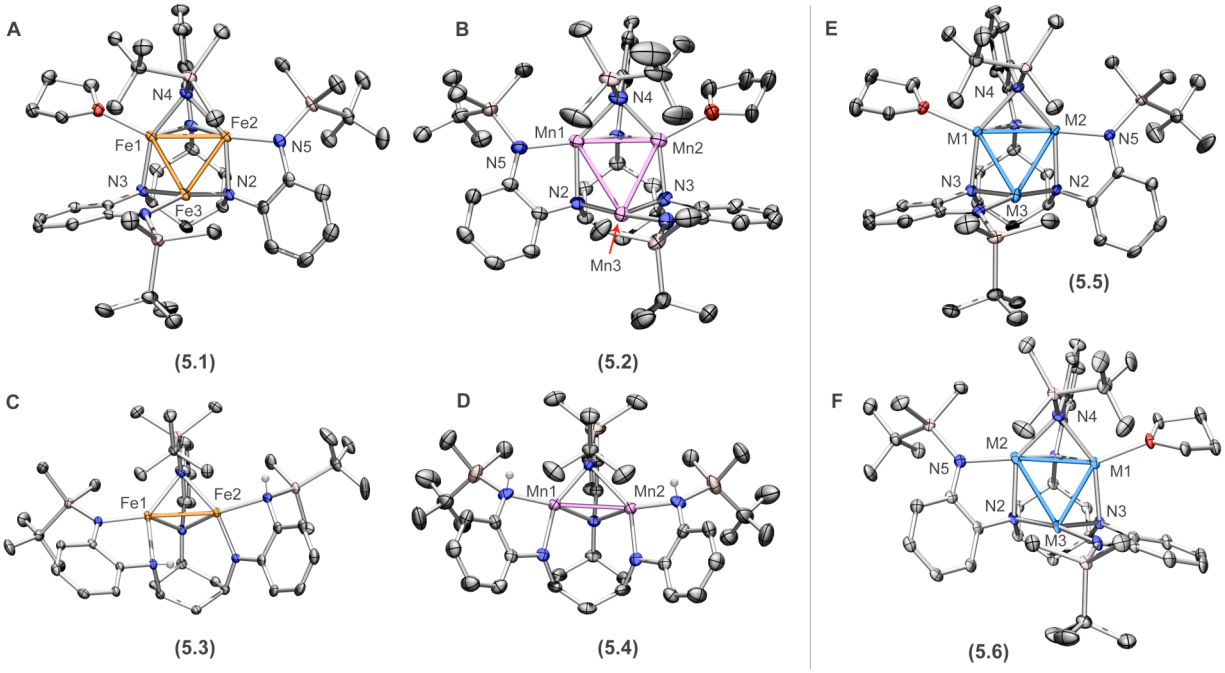

Figure 5.2. Solid-state structures for (A) (^{tbs}L)Fe$_3$(THF) (**5.1**), (B) (^{tbs}L)Mn$_3$(THF) (**5.2**), (C) (^{tbs}LH$_2$)Fe$_2$ (**5.3**), (D) (^{tbs}LH$_2$)Mn$_2$ (**5.4**) with the thermal ellipsoids set at 50% probability level (hydrogen atoms and solvent molecules omitted for clarity; Fe orange, Mn orchid, N blue, O red, C grey, H white, Si pink). Solid-state structures for bimetallic trinuclear compounds (E) (^{tbs}L)M$_3$(THF) (**5.5**), and (F) (^{tbs}L)M$_3$(THF) (**5.6**) with the thermal ellipsoids set at 50% probability level. The identity of the metal centers could not be determined using traditional X-ray crystallographic methods and therefore all metal centers are depicted as light blue.

Table 5.1. Select metal–metal and metal–ligand bond lengths for compounds **5.1**, **5.2**, **5.5**, and **5.6**

Bond	5.1	5.2	5.5	5.6
M1–M2	2.6129(5)	2.8785(7)	2.7247(5)	2.7681(6)
M2–M3	2.6118(5)	3.2213(7)	2.8687(5)	3.0176(6)
M1–M3	2.5061(5)	3.1191(7)	2.7485(5)	2.8030(6)
M1–N1	2.126(2)	2.116(3)	2.148(2)	2.123(2)
M1–N3	2.016(2)	2.077(3)	2.121(2)	2.126(2)
M1–N4	2.081(2)	2.148(3)	2.170(2)	2.158(2)
M2–N1	2.047(2)	2.109(3)	2.047(2)	2.079(2)
M2–N2	2.091(2)	2.162(2)	2.108(2)	2.123(2)
M2–N4	2.149(2)	2.202(3)	2.121(2)	2.171(2)
M2–N5	1.950(2)	2.098(3)	1.956(2)	1.985(2)
M3–N2	1.955(2)	2.000(3)	1.945(2)	1.935(2)
M3–N3	2.053(2)	2.098(3)	2.018(2)	2.019(2)
M3–N6	1.938(2)	1.976(3)	1.920(2)	1.920(2)

environments (Figure 5.2). The coordination environments of the Mn centers in **5.2** are identical to those found in previously reported Fe_3 cluster **5.1** (Figure 5.2). While all three internal alkyl aryl amides bridge two adjacent metal centers, only one of the silylamide ligands bridges Mn1 and Mn2. The remaining two silylamides are terminally bound to Mn2 and Mn3. The average Mn–Mn distance (3.0730(9) Å) as well as the average Mn–N_{Si} (2.042(2) Å) and Mn–N_{int} (2.0645(2) Å) distances in **2** are longer than the average Fe–Fe (2.577(6) Å), Fe–N_{Si} (1.950(2) Å) and Fe–N_{Int} (2.047(2) Å) distances in **5.1** (Table 5.1).

In the absence of coordinating solvent, metallation of ($^{tbs}LH_6$) with $Fe_2(Mes)_4$ or $Mn_2(N(SiMe_3)_2)_4$ occurs at 75 ^oC and results in the formation of binuclear compounds ($^{tbs}LH_2$)Fe_2 (**5.3**, 62%) and ($^{tbs}LH_2$)Mn_2 (**5.4**, 70%), respectively. Single crystal analysis of complexes **5.3** and **5.4** showed that the two metal centers are bridged by one of the three *o*-phenylene diamide units of the ligand (Figure 5.2). The remaining two *o*-($C_6H_4N_2$) units contain one amide and one amine based nitrogen and are each bound to one of the two metal centers, creating a pocket for a third divalent metal center to occupy (protons located in the electron density map). In the case of **5.3**, one of the alkyl aryl nitrogen amines remains protonated, while the second amine is located in the basal position. The structure of compound **5.4** was solved with a disorder model, one of which is shown in Figure 5.2 and features both of the peripheral amines available for deprotonation. While the M–M separation in Fe_2 complex **5.3** (2.7086(6) Å) is longer than the M–M distances observed in the homotrinuclear Fe_3 counterpart **5.2** (Table 5.1), the Mn–Mn distance increases upon insertion of a third metal center (Mn_2 complex **5.4**: 2.8560(8) Å; Mn_3 complex **5.2** (avg): 3.0730(9) Å).

The ability to access binuclear species **5.3** and **5.4** is imperative for accessing bimetallic trinuclear species supported by the ligand variant $^{tbs}LH_6$. Importantly, even upon addition of

excess divalent Fe or Mn metallating reagent, we never observe formation of a trinuclear species without the presence of coordinating solvent (L = THF or py; see Scheme 5.1). The role solvent L plays in metallation and/or stabilization of the product is currently unknown. The coordinating solvent could either facilitate the monomerization of the dimeric metallating agent, which is ultimately necessary to generate a trinuclear species, or simply stabilize the resulting trinuclear complex that cannot be supported solely by $^{tbs}L^{6-}$ in the present oxidation state. If solvent coordination plays a role in stabilizing the trinuclear product, the identity of the coordinating solvent may have an effect on the selectivity of the resulting bimetallic trinuclear clusters.

The synthesis of bimetallic trinuclear cluster (^{tbs}L)Fe$_2$Mn(THF) (**5.5**) was achieved by treatment of the binuclear Fe complex (^{tbs}LH$_2$)Fe$_2$ (**5.3**) with 0.5 equivalent of Mn$_2$(N(SiMe$_3$)$_2$)$_4$ in THF at 75 ^{o}C (62% isolated yield). Single crystals were obtained from concentrated diethyl ether solutions at –33 ^{o}C (33% crystalline yield). The resulting crystalline product has a paramagentic ^{1}H NMR spectra with 32 resonances, consistent with a C_1 complex in solution (Figure 5.3). C_1-symmetry is also observed in the solid-state where the metal coordination environments in **5.5** are identical to that of the homonuclear counterparts **5.1** and **5.2** (Figure 5.2). The average M–M distance in bimetallic trinuclear cluster **5.5** (2.7806(6) Å) lies between the average distances of the homotrinuclear Fe and Mn complexes (**5.1**: 2.577(6) Å; **5.2**: 3.0730(9) Å) (Table 5.1). While traditional X-ray crystallography allowed us to establish connectivity, it cannot be used to discern between Mn and Fe centers; anomalous scattering measurements were carried out to assign the identity of metal sites (*vide infra*). However, examining the metal–ligand bond lengths can provide some insight into the identity of the metal centers in **5.5**. The metal–ligand bond distances for metal centers M2 and M3 are all shorter then or nearly equal to the respective M–N distances found in Fe$_3$ cluster **5.1** and the M1–N bond

distances are longer than the metal–ligand bond distances in Mn_3 cluster **5.2** (Table 5.1). These bond metrics suggest that for compound **5.5**, M1 = Mn and M2 = M3 = Fe, which is consistent with site isolated insertion of a single Mn ion into Fe_2 cluster **5.3** to yield (^{tbs}L)Fe_2Mn(THF).

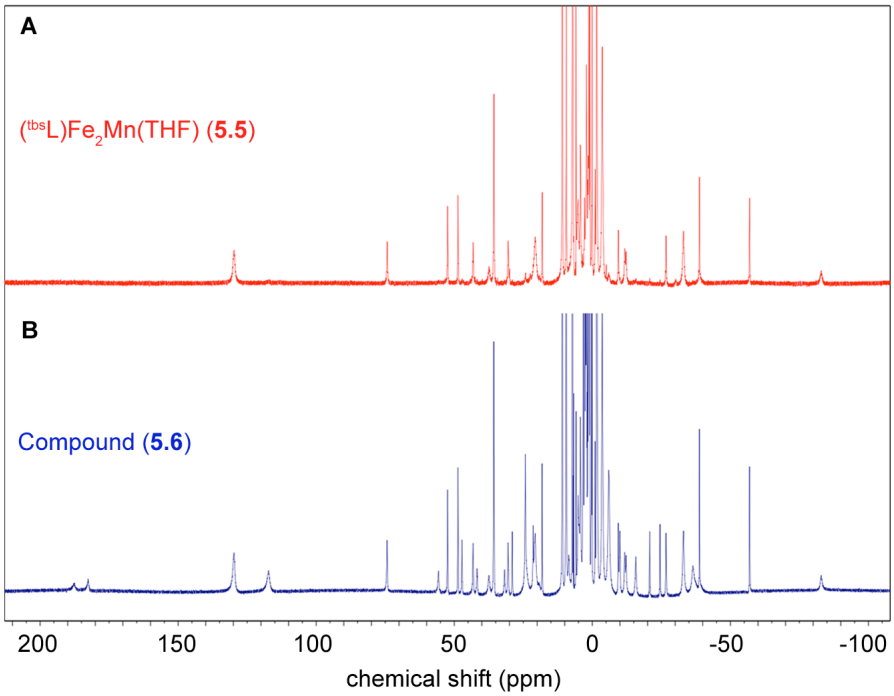

Figure 5.3. Paramagnetic ^{1}H NMR of crystalline (A) (^{tbs}L)Fe_2Mn(THF) (**5.5**) (red) and (B) bimetallic trinuclear compound (**5.6**) (blue). Complex **5.6** has nearly twice the number of resonances observed in the spectrum of **5.5**, consistent with a mixture of bimetallic trinuclear products (^{tbs}L)Fe_2Mn(THF) and (^{tbs}L)Mn_2Fe(THF) (*vide infra*).

We approached the synthesis of a Mn_2Fe cluster in a similar fashion to **5.5**. ^{1}H NMR analysis of a solution generated by treatment of binuclear Mn complex (^{tbs}LH_2)Mn_2 (**5.4**) in the presence of 0.5 equivalent of Fe_2Mes_4 at 75 ^{o}C displayed more than twice the number of resonances as were observed for **5.5** (Figure 5.3). While resonances for **5.5** appeared in the spectrum, they could be a result of either: (1) the two compounds exhibit similar solid-state structures which could result in overlapping ^{1}H NMR signals; (2) non-site isolated insertion of the third metal center may lead to unique ^{1}H NMR signatures depending on the location of the third metal center in the cluster; or (3) the resulting NMR could also represent a mixture of

species, one of which was Fe_2Mn cluster **5.5**. For simplicity, the resulting material from the reaction of Mn_2 **5.4** with 0.5 equivalent Fe_2Mes_4 will be referred to as compound **5.6**.

Crystallization of **5.6** from cold diethyl ether (–33 ^{o}C) afforded single crystals that contained a trinuclear species with the same connectivity as observed for homotrinuclear complexes **5.1** and **5.2** and bimetallic trinuclear complex **5.5**, with an average M–M distance of 2.8629(7) Å (Figure 5.2, Table 5.1). Based on metal–ligand bond metrics in **5.6**, it is not clear whether one or two metal types occupy the metal positions. As in the case of Fe_2Mn complex **5.5**, the M1–N bond distances in trinuclear cluster **5.6** are consistent with those distances observed in homotrinuclear Mn_3 cluster **5.2** (Table 5.1). Likewise, M3–N bond metrics of **5.6** suggest that metal position 3 is occupied by Fe (Table 5.1). However, the M2–N bond lengths for compound **5.6** do not appear to follow a similar trend and fall between the metal–ligand bond lengths found in the homotrinuclear clusters **5.1** and **5.2** (Table 5.1), making it difficult to assign M2. We tentatively assigned M2 as Mn based on the fact that the material was synthesized from binuclear Mn_2 complex **5.4** (Figure 5.2). However, additional bulk spectroscopic techniques would be necessary to corroborate this hypothesis.

EPR spectroscopy was utilized as an additional fingerprint for both the homo and heteronuclear species reported herein. The perpendicular X-band EPR spectra at 4 K for homotrinuclear Mn_3 cluster **5.2** and binuclear Mn_2 cluster **5.4** exhibit substantial hyperfine coupling at g = 2.01, due to the I = 5/2 ^{55}Mn nuclei (Figure 5.4). Both **5.2** and **5.4** show spectra exceeding the 16-line pattern expected for hyperfine coupling to three equivalent Mn nuclei ($2nI$ + 1; $A\|$ = 29–59 G for **5.2** at 4 K; $A\|$ = 35–64 G for **5.4** at 4 K). The twenty line pattern is therefore attributed to overlapping 6-line hyperfine patterns, a result of non-equivalent Mn environments in both **5.2** and **5.4**. The transition centered at g = 4.43 (compound **5.2**) likely

corresponds to a spin-allowed transition associated with the $m_s = \pm 3/2$ excited state of Mn (S = 5/2) and has been observed in X-band EPR spectrum of previously reported Mn_3 clusters.[144] A similar transition can be observed for **5.4** at g = 4.04 and features hyperfine coupling to the I = 5/2 ^{55}Mn nucleus ($A\|$ = 29–35 G at 4 K).

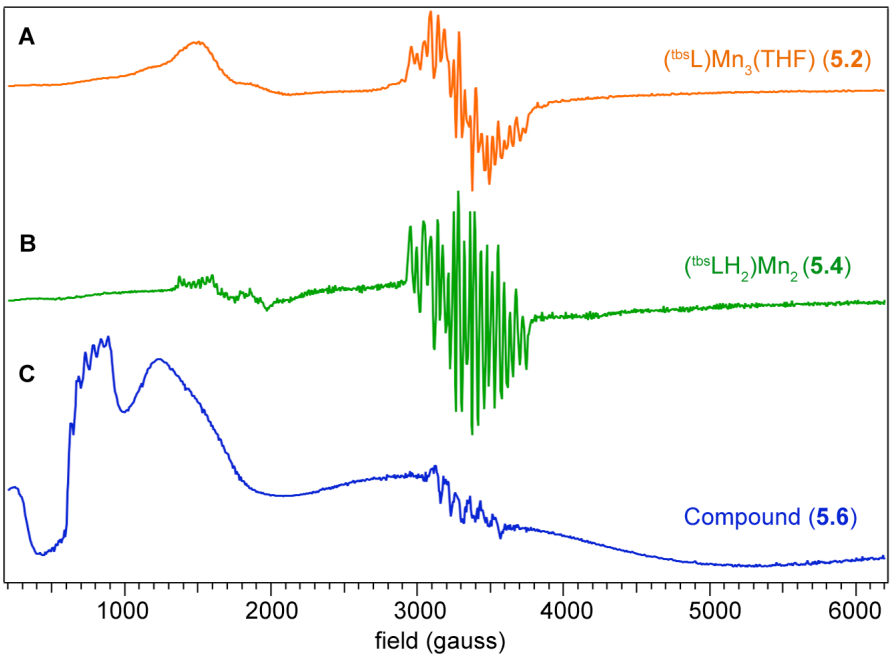

Figure 5.4. EPR spectra of (A) (^{tbs}L)Mn_3(THF) (**5.2**) (orange), (B) (^{tbs}LH_2)Mn_2 (**5.4**) (green), and (C) crystalline bimetallic trinuclear compound (**5.6**) (blue) at 4 K.

Like the Mn_3 (**5.2**) and Mn_2 (**5.4**) species, compound **5.6** also exhibits a X-band EPR spectrum at 4 K with hyperfine coupling near g = 2 ($A\|$ = 64–88 G at 4 K) (Figure 5.4). Compound **5.6** has two additional features at g = 8.91 ($A\|$ = 53 G at 4 K), likely corresponding to spin-allowed transitions associated with the $m_s = \pm 1/2$ excited state of S = 5/2 Mn ion, as well as a spin forbidden transition at g = 15.43. While the hyperfine coupling observed in the EPR spectrum of **5.6** confirms the presence of a [Mn_2] unit in the resulting crystalline material, it is

difficult to ascertain the amount of material that is responsible for the signatures attributed to that unit.[263]

Zero-field ^{57}Fe Mössbauer was used to determine the number of non-equivalent Fe centers in bimetallic trinuclear clusters **5.5** and **5.6**. Table 5.2 summarizes the Mössbauer parameters after fitting the spectra of the Fe containing compounds **5.1**, **5.3**, **5.5**, and **5.6**. Mixed-metal compounds **5.5** and **5.6** have nearly identical Mössbauer spectra featuring two quadrupole doublets with isomer shifts lower then that of Fe_2 complex **5.3** (Table 5.2). In the case of Fe_2Mn cluster **5.5**, the Mössbauer spectrum (parameters δ, $|\Delta E_Q|$ ($^{mm}/_s$): component 1 (52%) 0.58, 1.30; component 2 (48%) 0.35, 1.77) (Figure 5.5) is consistent with the presence of two non-equivalent Fe centers and is demonstrative of a site isolated insertion of a single Mn center into the Fe_2 complex **5.3**. One would expect that site-isolated insertion of a single Fe center into Mn_2 compound **5.4** would result in a Mössbauer spectrum containing a single quadrupole doublet; however, the spectrum of crystalline **5.6**, in fact, features two quadrupole doublets (parameters δ, $|\Delta E_Q|$ ($^{mm}/_s$): component 1 (52%) 0.57, 1.31; component 2 (48%) 0.33, 1.85) (Figure 5.5). While the Mössbauer spectra of cluster **5.6** could be indicative of a mixture of clusters (e.g. Mn_2Fe and Fe_2Mn), the two quadrupole doublets could also arise from a single species where the Fe atom is occupied at more than one site.

263. Murphy, D. M. EPR (Electron Paramagnetic Resonance) Spectroscopy of Polycrystalline Oxide Systems. In *Metal Oxide Catalysis*; Jackson, S. D.; Hargreaves, J. S. J.; Eds.; Wiley-VCH: Weinheim, 2009.

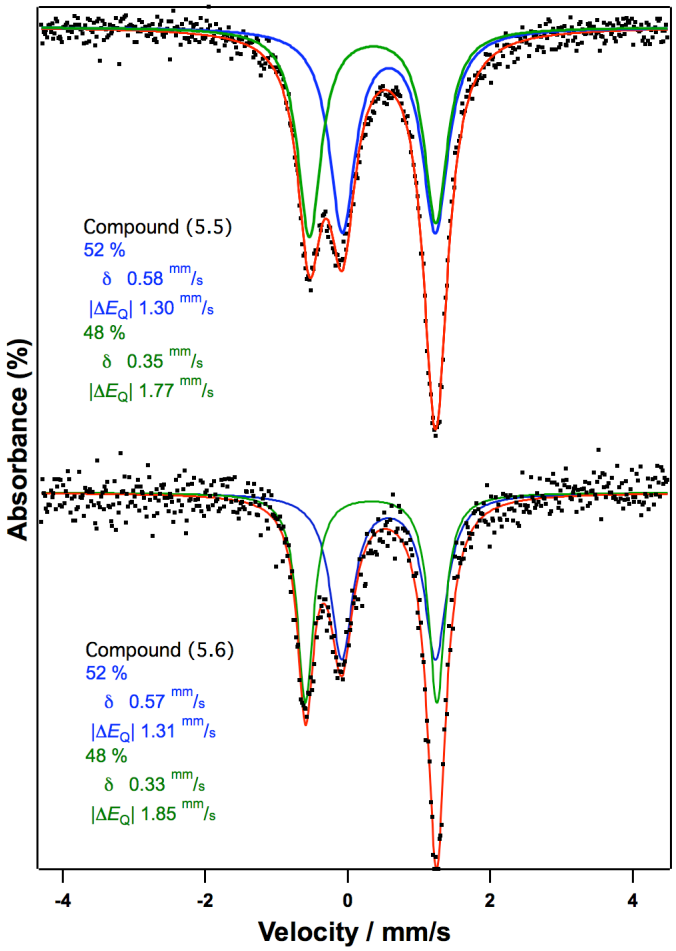

Figure 5.5. Zero-field ^{57}Fe Mössbauer spectra of compounds **5.5** and **5.6** with fitting parameters.

Table 5.2. Zero-field ^{57}Fe Mössbauer Parameters for Fe containing compounds

Compound		δ (mm/s)	$\|\Delta E_Q\|$ (mm/s)	% component
(^{tbs}L)Fe$_3$(THF)	(**5.1**)	0.89	1.69	24
		0.49	1.51	35
		0.50	1.89	41
(^{tbs}L)Fe$_2$	(**5.3**)	0.67	2.18	39
		0.68	1.57	61
(^{tbs}L)Fe$_2$Mn(THF)	(**5.5**)	0.35	1.77	48
		0.58	1.30	52
(^{tbs}L)Mn$_2$Fe(THF)	(**5.6**)	0.33	1.85	48
		0.57	1.31	52

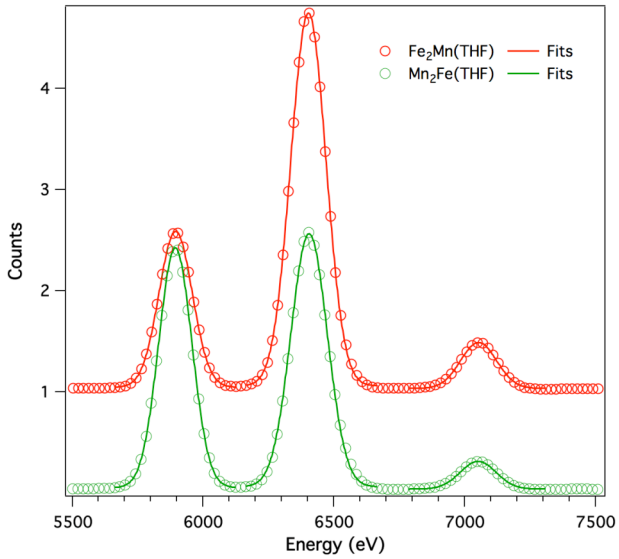

Figure 5.6. X-ray fluorescence spectra of $Fe_2Mn(THF)$ complex **5.5** (red trace) and $Mn_2Fe(THF)$ complex **5.6** (green trace).

The spectroscopic data discussed thus far for Fe_2Mn cluster **5.5** is consistent with isolation of a substitutionally homogenous material (^{tbs}L)$Fe_2Mn(THF)$. However, the data associated with compound **5.6** is less clear and could either be attributed to a mixture of species or a homogeneous material where the Fe is located in multiple metal positions. While crystalline **5.6** passed C, H, N combustion analysis as a discrete homogeneous (^{tbs}L)$Mn_2Fe(THF)$ compound, the molecular weights of the Mn_2Fe and Fe_2Mn compounds are too similar to distinguish by C, H, N elemental analyses and the technique does not provide evidence for the metal composition of the samples. Therefore, X-ray fluorescence spectroscopy was used as a means of bulk elemental analysis of the metal composition in the crystalline material. X-ray fluorescence spectra of mixed-metal compounds **5.5** and **5.6** exhibited both Fe and Mn Kα and Kβ emission lines, where the Fe Kα and the Mn Kβ overlap (Figure 5.6). A calibration curve of solution samples in H_2O of $FeCl_3$ and $MnCl_2(H_2O)_4$ at various ratios was generated to determine the composition of the samples.[264] X-ray fluorescence measurements were conducted in

264. See Section **5-6** for XRF calibration curve.

duplicate for both Fe_2Mn cluster **5.5** and Mn_2Fe cluster **5.6**. The superposition of the Fe Kα and Mn Kβ emission lines for clusters **5.5** resulted in Fe:Mn ratios of 2.3:1 (70% Fe content) and 1.8:1 (64% Fe content) (Figure 5.6), which are consistent with what would be expected for a substitutionally homogeneous Fe_2Mn cluster. However, this is not the case for putative Mn_2Fe compound **5.6**, which was found to have a Fe:Mn ratio lower than expected (1:1.3 and 1:1.2 from the two samples collected, 45% and 47% Fe content respectively) (Figure 5.6). X-ray fluorescence spectroscopy of compound **5.6** indicates that we have isolated a species containing >33% Fe.

Therefore, we used anomalous scattering to determine the relative metal occupancies at the three unique sites within the reported mixed-metal clusters. In **Section 5-3**, we present anomalous scattering data on Fe_2Mn cluster **5.5** and mixed-metal complex **5.6**. To better understand the role ancillary ligands (coordinated solvent molecule, Scheme 5.1 *vide supra*) play in the selectivity of the metal substitution reaction, we conducted the synthesis of Mn_2Fe cluster in the presence of pyridine (py) (**5.7**, *vide supra*)[262] and grew crystals of the material for anomalous scattering experiments.

5-3. Anomalous X-ray scattering

While conventional single-crystal X-ray diffraction provides information regarding identity and connectivity of the atoms, it is not capable of discerning between two metals of nearly the same atomic number in the periodic table. Anomalous X-ray scattering is a technique that allows for differentiation between metal centers with similar atomic weights.[265] At an incident radiation wavelength close to the absorption edge of a metal center, the atomic

265. Waseda, Y. *Anomalous X-ray Scattering for Materials Characterization: Atomic-Scale Structure Determination*; Springer: Berlin, 2002.

scattering factors for elements with similar atomic numbers becomes more distinct. The atomic scattering factor for a given element is expressed by Eq. 5.1:

$$f = f^o + f' + if'' \qquad \text{(Eq. 5.1)}$$

where f^o is the scattering factor of the unperturbed atom (proportional to the atomic number of the element) and f' and f'' are the real and imaginary components of the anomalous scattering term, which vary as a function of the X-ray wavelength energy.[265] Normal single crystal X-ray diffraction data is collected at a wavelength of incident X-rays away from the absorption edges of the constituent elements, where $f \approx f^o$. At energies close to the absorption edge of an atom M, the anomalous dispersion terms become more significant in the overall atomic scattering factor (f) of that atom, which affects the diffraction intensity associated with M. This method has been used to differentiate metal centers in solid-state materials by both powder[266,267,268] and single-crystal diffraction[269,270,271,272] and is also utilized in protein crystallography.[273] We have employed anomalous X-ray scattering as a method for site-specific elemental analysis to elucidate the elemental composition at each of the three metal-binding sites in our trinuclear complexes. Table 5.3 summarizes the synchrotron datasets measured at different wavelengths. The real (f') and imaginary (f'') components of anomalous scattering are theoretical values for

266. Battle, P. D.; Blundell, S. J.; Coldea, A. I.; Cussen, E. J.; Rosseinsky, M. J.; Singleton, J.; Spring, L. E.; Vente, J. F. *J. Mater. Chem*. **2001**, *11*, 160-167.
267. Zhang, Y.; Wilkinson, A. P.; Nolas, G. S.; Lee, P. L.; Hodges, J. P. *J. Appl. Cryst.* **2003**, *36*, 1182-1189.
268. Zhang, Y.; Wilkinson, A. P.; Lee, P. L.; Shastri, S. D.; Shu, D.; Chung, D.-Y.; Kanatzidis, M. G. *J. Appl. Cryst.* **2005**, *38*, 433-441.
269. Helliwell, M.; Helliwell, J. R.; Kaucic, V.; Logar, N. Z.; Teat, S. J.; Warren, J. E.; Dodson, E. J. *Acta Cryst.* **2010**, *B66*, 345-357.
270. Wulf, R. *Acta Cryst.* **1990**, *A46*, 681-688.
271. Freedman, D. E.; Han, T. H.; Prodi, A.; Müller, P.; Huang, Q.-Z.; Chen, Y.-S.; Webb, S. M.; Lee, Y. S.; McQueen, T. M.; Nocera, D. G. J. Am. Chem. Soc. **2010**, *132*, 16185-16190.
272. Zhang, X.; Huang, D.; Chen, Y.-S.; Holm, R. H. Inorg. Chem. **2012**, *51*, 11017-11029.
273. Dauter, M.; Dauter, Z. Phase Determination Using Halide Ions. In *Macromolecular Crystallography Protocols: Volume 2: Structure Determination*; Doublié, S., Ed.; Humana Press: New Jersey, 2007; Vol. 364; p 149.

pure Fe and Mn metal.[274] While the anomalous scattering terms will vary with charge and coordination environment, theoretical values of pure metals have been used in the past with success at accurately determining metal occupancies at mixed-metal sites.[269,275] In all cases, a reference dataset was collected away from any metal absorption edges (dataset 1a or 1b). Compound **5.5** was measured at the absorption edge of Mn and Fe (dataset 3 and 6 respectively). Additional datasets were collected above and/or below the absorption edge for compounds **5.6** and **5.7**.

Table 5.3. Synchrotron datasets measured at different wavelengths: anomalous dispersion terms f' and f'' are for pure Fe^0 and Mn^0 metal

Dataset	Wavelength (Å)	Energy (KeV)	Fe f', f'' (e^-)	Mn f', f'' (e^-)
1a	0.44280	28.000	0.255, 0.434	0.234, 0.373
1b	0.49594	25.000	0.255, 0.434	0.234, 0.373
2	1.91068	6.489	-2.166, 0.552	-4.594, 0.469
3	1.89607	6.539	-2.241, 0.544	-9.901, 0.462
4	1.88169	6.589	-2.324, 0.537	-4.486, 3.904
5a	1.75565	7.062	-4.646, 0.474	-1.731, 3.452
5b	1.75070	7.082	-5.183, 0.471	-1.686, 3.437
6	1.74331	7.112	-9.812, 0.468	-1.622, 3.414
7	1.73114	7.162	-4.547, 3.896	-1.522, 3.377

Electron density difference maps provide a means to visualize the anomalous scattering data obtained at the absorption edges. Dispersive difference Fourier 2D maps of the tri-metal plane were generated for compounds **5.5**, **5.6**, and **5.7** at both the Mn and Fe absorption edges (Figure 5.7). Dispersive difference maps at the Mn absorption edge were generated using the coefficients $F_{\mathrm{Mn}f''} - F_{\mathrm{ref}}$, where $F_{\mathrm{Mn}f''}$ is dataset 3 and F_{ref} is one of the two reference datasets 1a or 1b, which was previously refined with all Fe metal centers. Likewise, the coefficients $F_{\mathrm{Fe}f''} - F_{\mathrm{ref}}$

274. Real (f') and imaginary (f'') components were obtained from Kissel, L.; Pratt, R. H. *Acta Cryst.* **1990**, *A46*, 170-175, unless otherwise noted.
275. While Argonne National Lab has the ability to determine anomalous scattering terms of samples, a mechanical issue prevented us from doing so while at Argonne.

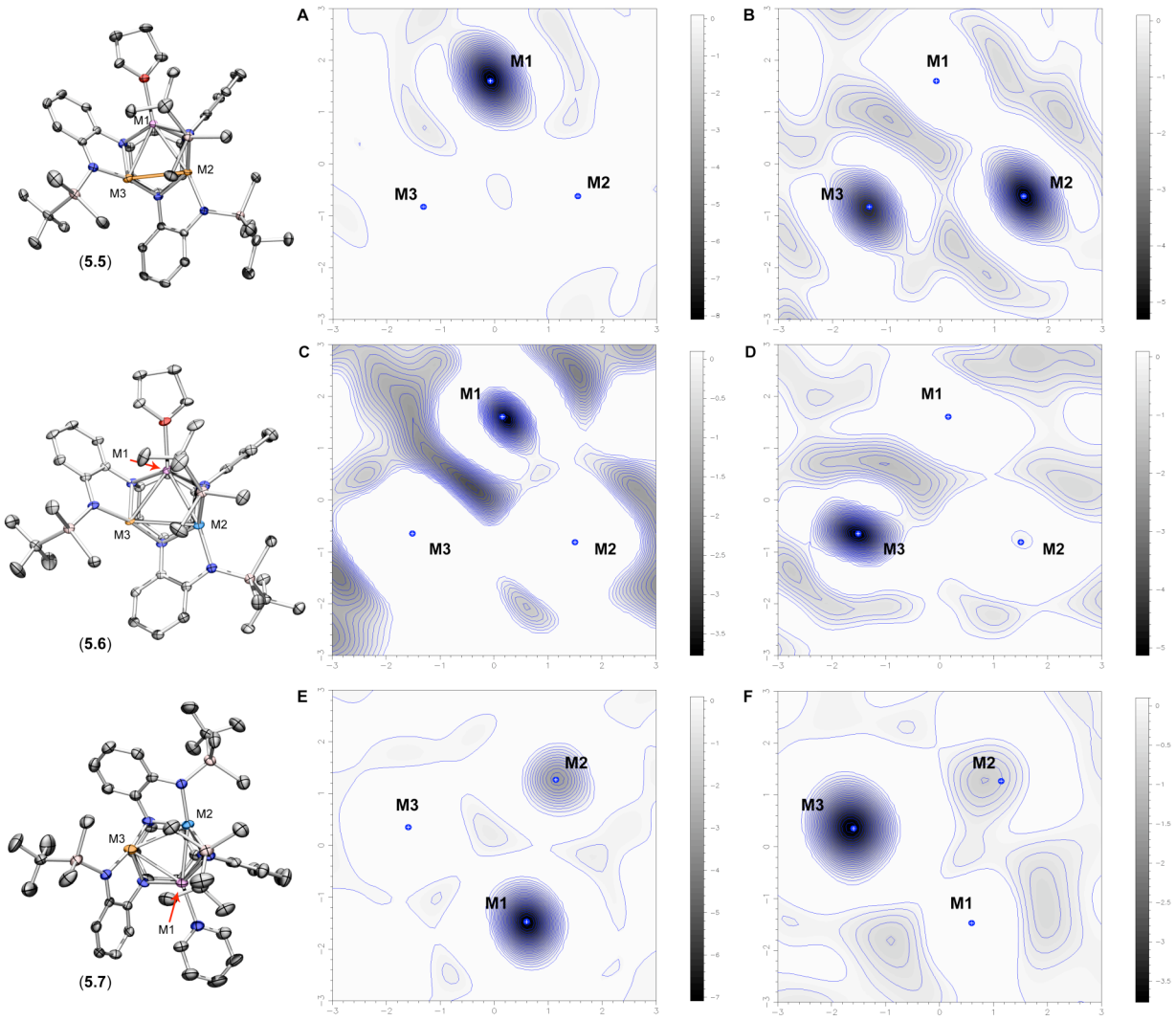

Figure 5.7. Anomalous difference Fourier maps at the Mn and Fe absorption edges of compounds (^{tbs}L)Fe$_2$Mn(THF) (**5.5**) (A and B), (^{tbs}L)Mn$_2$Fe(THF) (**5.6**) (C and D), and (^{tbs}L)Mn$_2$Fe(pyr) (**5.7**) (E and F). Maps A, C, and E were calculated with dataset 3 (at the Mn absorption edge) and maps B, D, and F were calculated with dataset 6 (at the Fe absorption edge).

(F_{Fef} = dataset 6, reference structure previously refined with all Mn metal centers) where used to create the difference maps at the Fe absorption edge.

The difference map at the Mn absorption edge (dataset 3) of (^{tbs}L)Fe$_2$Mn(THF) **5.5** (Figure 5.7A) features an electron density hole at M1 (–3.78 e^-/Å^3), indicating incorporation of Mn into that binding site. At the Fe absorption edge (dataset 6) of compound **5.5** the difference map shows deep electron density holes at M2 and M3 with energies –5.31 e^-/Å^3 and –4.58 e^-/Å^3

respectively, indicative of Fe incorporation into those metal sites (Figure 5.7B). The difference in electron density at M2 and M3 could either be a result of slight atomic movements/changes in unit cell size upon irradiation of X-rays at different wavelengths (the 2D plane at the Fe absorption edge may not contain the absolute centers, location of lowest electron density, of all three metal ions) or the difference may indicate that the two metal positions are not equivalently occupied with Fe.[269] Free refinement of the data at the Mn absorption edge results in statistically equivalent percent occupancies at metal sites 2 and 3 (M2, 95.9(5)%; M3, 96.2(6)%), which supports equivalent Fe occupancy at M2 and M3. The anomalous difference Fourier 2D maps of the tri-metal plane of compound **5.5** in conjunction with the free-refinement of the metal centers at the metal absorption edges is demonstrative of site isolated insertion of a single divalent Mn center into the cluster (M1) which is bound to the solvent molecule THF.

Electron density difference maps of **5.6** and **5.7** (Figure 5.7) are consistent with M1 fully occupied by Mn and M3 fully occupied by Fe, showing deep electron density holes at the Mn and Fe absorption edges, respectively, at those metal sites (at Mn absorption edge of **5.6**: M1 = –3.62 e^{-}/Å^3; **5.7**: M1 = –6.99 e^{-}/Å^3; at Fe absorption edge of **5.6**: M3 = –5.03 e^{-}/Å^3; **5.7**: M3 = –3.71 e^{-}/Å^3). M2 of both **5.6** and **5.7** is a mixed-metal site, occupied by both Fe and Mn, as indicated by the observation of weaker negative electron density at both absorption edges (at Mn absorption edge of **5.7**: –3.08 e^{-}/Å^3; at Fe absorption edge of **5.6**: M2 = –0.07 e^{-}/Å^3; **5.7**: –0.71 e^{-}/Å^3).

Anomalous structure refinements of **5.5**, **5.6**, and **5.7** were conducted using the SHELX program package.[171] A disorder model was utilized to determine the extent of mixing at position M2 in **5.6** and **5.7**. The results of the disorder refinements at various wavelengths for compounds **5.6** and **5.7** are summarized in Table 5.4. While the disorder refinement indicates that both Fe

and Mn occupy position M2 in **5.6** and **5.7** in nearly a 1:1 ratio, the disorder model did not produce consistent results at the different wavelengths, due to variability associated with the anomalous dispersion terms (*vide supra*).[269,270]

Table 5.4. Refined Fe occupancies (%) with *SHELXL* for **5.6** and **5.7**.

Metal site	Dataset 2	Dataset 3	Dataset 4	Dataset 5	Dataset 6	Dataset 7
Compound **5.6**				5a		
M1	0*	6(2)	0*	10(3)	5(2)	29(7)
M2	53(3)	59(1)	54(3)	58(3)	44(2)	84(7)
M3	100**	100(1)	100**	100**	66(2)	100**
Compound **5.7**				5b		
M1		15(2)		0*	12(3)	
M2		41(3)		41(3)	36(3)	
M3		100**		100**	81(3)	

* Disorder model results in >100% occupancy Mn at M1, therefore refined as 100% Mn
** Disorder model results in >100% occupancy Fe at M3, therefore refined as 100% Fe

To assess the relative errors in percent occupancy associated with the anomalous dispersion terms, the values of f' and f'' were varied for compound **5.6** and the percent occupancies at the different metal sites were calculated.[267,268] We found that datasets 3, 4, 6, and 7 showed high errors associated with varying f' and f'' values (Table 5.5). The f' and f'' values at the absorption edges (datasets 3 and 6) are most sensitive to variation in energy and are therefore difficult to approximate at the absorption edge.[270] The dataset after the highest absorption edge (Fe, dataset 7) is less accurate because the f'' values for the two metal centers are closest at this energy, lowering the Δf value and making it more difficult to discern between the two metal centers.[269] Similarly, the dataset following the Mn absorption edge (dataset 4) is less accurate because the Mn f'' is highest at this energy, also lowering the Δf value. Therefore, only datasets 2 and 5 were utilized to determine the percent occupancies of the metal positions in **5.6**, while dataset 5 was used to determine the percent occupancies of the metal positions in **5.7** (we were

Table 5.5. Refined Fe occupancies (%) with *SHELXL* for compound **5.6**

Metal site	Dataset 2	Dataset 3	Dataset 4	Dataset 5a	Dataset 6	Dataset 7
with EXYZ[a]						
M1	3(3)	23(2)	22(2)	11(4)	2(2)	19(4)
M2	61(3)	66(1)	67(2)	57(4)	33(2)	45(4)
M3	100**	100**	100**	99(4)	48(2)	64(4)
without EXYZ[a]						
M1	0(2)	24(1)	22(2)	11(4)	2(2)	0*
M2	61(2)	66(2)	66(2)	57(4)	33(2)	40(4)
M3	100**	100**	100**	100**	48(2)	59(4)
with EXYZ						
M1	0*	6(2)	0*	10(3)	5(2)	29(7)
M2	53(3)	59(1)	54(3)	58(3)	44(2)	84(7)
M3	100**	100(1)	100**	100**	66(2)	100**
$f' + 1e^-; f'' + 0.25e^-$						
M1	0*	0*	0*	7(4)	5(2)	
M2	53(3)	55(1)	53(3)	62(4)	51(2)	
M3	100**	100**	100**	100**	76(2)	
$f' - 1e^-; f'' - 0.25e^-$						
M1	0*	16(2)	0*	12(3)	5(2)	29(5)
M2	61(2)	64(1)	57(2)	46(3)	39(2)	66(5)
M3	100**	100(1)	100**	82(3)	58(2)	100**

[a] Real (f') and imaginary (f'') components were obtained from "International Tables Vol C Tables 4.2.6.8 and 6.1.1.4" (see **section 5-6** for table of values from this reference).
* Disorder model results in >100% occupancy Mn at M1, therefore refined as 100% Mn
** Disorder model results in >100% occupancy Fe at M3, therefore refined as 100% Fe
EXYZ A restraint used in crystallography, which forces the named atoms to possess the same coordinates as the first atom of the list (in this case, the disordered metal atoms)

unable to collect at dataset 2 for compound **5.7**). Based on this analysis, we would recommend that when collecting anomalous scattering data to determine the relative ratio of two metals occupying the same atomic position, one should collect at wavelengths above, below, and at the absorption edges of the metal centers to ensure that an accurate dataset is obtained at each absorption edge. Using the results of the disorder model at datasets 2 and 5, we found the average percent occupancies of Fe for compound **5.6** to be: M1 = 5(3), M2 = 56(4), and M3 = 100 (Table 5.4). While the disorder model predicts that a small amount of inclusion of Mn has occurred at M1, based on the fact that no negative electron density hole was observed at that

position in the electron density map at the Fe absorption edge and that the zero-field ^{57}Fe Mössbauer spectrum contains only two quadrupole doublets, we have assigned M1 as a fully occupied Mn site, resulting in a 1.3:1 mixture of (^{tbs}L)Fe$_2$Mn(THF):(^{tbs}L)Mn$_2$Fe(THF) based on crystal structure analysis. Compound **5.7** has a similar composition to **5.6**, with Fe percent occupancies of M1 = 0, M2 = 41(3), and M3 = 100 (dataset 5) resulting in a 1:1.4 mixture of (^{tbs}L)Fe$_2$Mn(py):(^{tbs}L)Mn$_2$Fe(py) based on anomalous crystal structure analysis.

5-4. Discussion

Substitution of metal centers to generate heteronuclear species has been used as a method of accomplishing changes in both reactivity and electronic structure of polynuclear clusters. Through this study we aimed to adapt our synthetic approach to include bimetallic trinuclear species, which would allow us to investigate changes in M–M interactions upon metal substitution in a stepwise fashion. Utilizing homo binuclear compounds as our building block, we targeted the synthesis of mixed Fe/Mn clusters supported by a C_3 symmetric hexaamide based ligand platform (Scheme 5.1, *vide supra*). Our strategy resulted in the synthesis of a discrete Fe$_2$Mn complex (^{tbs}L)Fe$_2$Mn(THF) (**5.5**) (Scheme 5.2). Spectroscopic techniques including ^{1}H NMR, Mössbauer, and X-ray crystallography were all consistent with isolation of a substitutionally homogeneous material, while X-ray fluorescence spectroscopy of the bulk crystalline material established that the Fe:Mn content was ~2:1. Based on these data, we predicted that we would be able to access a similar Mn$_2$Fe cluster in an analogous fashion. However, X-ray fluorescence spectroscopy of compound **5.6** indicated more Fe incorporation into the crystalline material than expected (46±1% Fe content, based on the average of two measurements). Both Mössbauer spectroscopy as well as ^{1}H NMR of **5.6** was also consistent with a mixture of Fe$_2$Mn and Mn$_2$Fe species, containing two quadrupole doublets in the

Mössbauer and more than double the number of resonances in the ^{1}H NMR compared to Fe_2Mn cluster **5.5**.

Traditional X-ray crystallography only established connectivity within the bimetallic trinuclear clusters – Fe and Mn sites could not be differentiated. Therefore, we turned to anomalous X-ray scattering as a method of site-specific elemental analysis of the metal centers within the clusters. Anomalous X-ray scattering corroborates both bond metrics obtained by single crystal X-ray analysis of Fe_2Mn cluster (**5.5**) as well as the Mössbauer spectrum, which is all consistent with site isolated metal insertion in the solid-state, with the more oxophilic Mn[276] center bound to the THF molecule (Scheme 5.2).

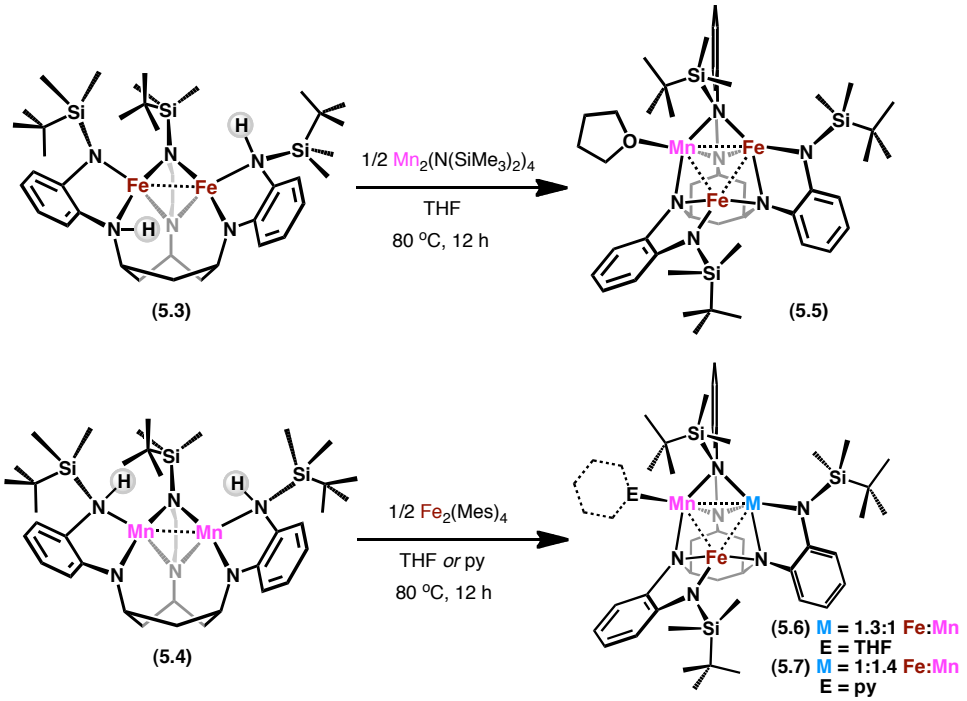

Scheme 5.2. Metal composition of **5.5**, **5.6**, and **5.7**, based on anomalous scattering refinements.

Both electron density difference maps and data refinement obtained from anomalous scattering measurements confirmed the presence of a mixture of the two species (^{tbs}L)Fe_2Mn(E) and (^{tbs}L)Mn_2Fe(E) (where E = THF or py) in the crystal structure of **5.6** and **5.7**. In both **5.6** and

276. Klabunde, K. J. *Free Atoms, Clusters, and Nanoscale Particles*; Academic Press, Inc: San Diego, 1994.

5.7, M1 is fully occupied by Mn and M3 is fully occupied by Fe, while the only mixed-metal site in the solid-state was determined to be M2 (**5.6**: 56(4)% Fe; **5.7**: 41(3)% Fe) (Scheme 5.2).

Ligand or metal lability allows for the Mn atoms to be displaced by divalent Fe centers. Monitoring the reaction of Mn_2 **5.4** with 0.5 equivalent Fe_2Mes_4 by ^{1}H NMR spectroscopy, we see immediate formation of the resonances associated with Fe_2Mn and Mn_2Fe. By ^{1}H NMR, we observe that upon addition of 1-2 equivalents of Fe_2Mes_4 to Mn_2 complex **5.4**, we see the disappearance of the peaks associated with Mn_2Fe cluster to yield a paramagnetic ^{1}H NMR that predominantly contains the resonances associated with Fe_2Mn cluster **5.5** (Figure 5.8). The ability to isolate Fe_2Mn complex **5.5** is likely because this is the thermodynamic product under the reaction conditions employed. Metal atom exchange has been previously observed in trinuclear clusters supported by hexaamide based ligand platforms to generate mixed Fe/Co systems at room temperature.[277]

Although we present the Fe and Mn ions with an unbiased ligand scaffold comprised of three ortho-phenylenediamine pockets, crystallographically each metal site has a unique coordination environment in the solid-state. The results herein demonstrate that the differences in coordination sphere at each metal position of these clusters have an effect on whether Fe or Mn preferentially binds in each unique pocket. In all three mixed-metal complexes, Fe (d^6) fully occupies the M3 position, which is 3-coordinate, bound to two internal alkyl aryl amides and one peripheral amide ligand moiety. Mn has a lower *d*-electron count (d^5) relative to Fe and prefers the 4-coordinate positions M1 and M2.

While Fe_2Mn cluster **5.5** was demonstrated to be the thermodynamic product, we were interested to see if the composition of the cluster could be affected by changing the ancillary ligand (E) bound to the trinuclear core. However, ligated solvent appears to have little to no

277. Eames, E.V.; Hernández Sánchez, R.; Betley, T.A. *Inorg. Chem*, **2013**, *52*, 5006-5012.

effect on the ratio of metal clusters. While the Fe_2Mn cluster was slightly favored in the presence of THF relative to py, in both cases solvent is bound to the fully occupied Mn site (M1) (Scheme 5.2) and therefore we do not attribute the difference in Fe_2Mn:Mn_2Fe ratio for **5.6** and **5.7** to solvent effects. Instead, we hypothesize that the coordinating solvent facilitates the third metallation event by breaking up the dimeric M(II) precursor into its monomeric form.

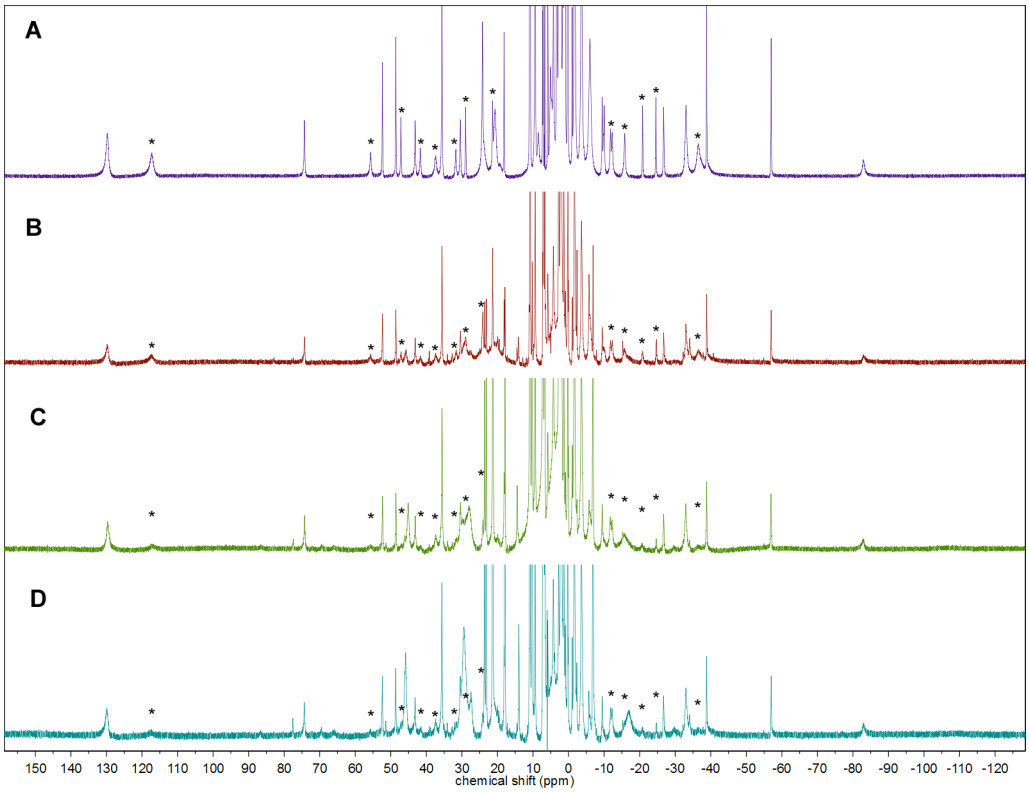

Figure 5.8. ^{1}H NMR overlays of (A) (^{tbs}LH$_2$)Mn$_2$ + 0.5 equivalent Fe_2Mes_4 (crystalline material, purple), (B) (^{tbs}LH$_2$)Mn$_2$ + 1 equivalent Fe_2Mes_4 (red), (C) (^{tbs}LH$_2$)Mn$_2$ + 1.5 equivalents Fe_2Mes_4 (green), and (D) (^{tbs}LH$_2$)Mn$_2$ + 2 equivalents Fe_2Mes_4 in C_6D_6. (*) represents resonances assigned to (^{tbs}L)Mn$_2$Fe(THF). Upon addition of excess Fe_2Mes_4, the resonances for (^{tbs}L)Mn$_2$Fe(THF) diminish giving rise to (^{tbs}L)Fe$_2$Mn(THF) as the major paramagnetic product.

5-5. Conclusions and outlook

Polynucleating ligand platform $^{tbs}LH_6$ was selected as the template for the synthesis of bimetallic trinuclear clusters. By accessing the binuclear metal species (^{tbs}LH$_2$)M$_2$ (M = Fe, Mn), we envisioned the synthesis of discrete metal platforms from Mn_3 to Fe_3 in single metal-

substitution steps. While the C_3 symmetric ligand $^{tbs}LH_6$ presents each metal center with an identical binding pocket, the resulting trinuclear clusters are C_1 in the solid-state, where each metal possesses a unique coordination environment. The thermodynamic bimetallic trinuclear product (^{tbs}L)Fe_2Mn(THF) (**5.5**) was accessed cleanly as a substitutionally homogenous material, where the Mn insertion is site isolated. During attempts at the synthesis of Mn_2Fe clusters (**5.6** and **5.7**), we observe formation of the thermodynamic product, (^{tbs}L)Fe_2Mn(THF), immediately upon reaction of ($^{tbs}LH_2$)Mn_2 with Fe_2Mes_4, along with the kinetic product (^{tbs}L)Mn_2Fe(THF).

The work in this thesis demonstrates that high-spin trinuclear $(Fe^{2+})_3$ cluster (^{tbs}L)Fe_3(THF) is capable of cooperatively binding anionic substrates and allows small molecule activation to yield oxidized clusters ranging from $(Fe^{II})_2(Fe^{III})$ – $(Fe^{III})_2(Fe^{IV})$. Future studies could be targeted at both understanding the electronic structure of homo- and heterometallic trinuclear clusters as well as investigating small molecule activation by substitutionally homogeneous bimetallic trinuclear clusters reported herein. Mixed-metal clusters such as (^{tbs}L)Fe_2Mn(THF) (**5.5**) would be interesting platforms to investigate how metal substitution affects reactivity.

While the results herein highlight the advantages that high-spin polynuclear reaction sites can offer as a design strategy for small molecule activation, we have yet to determine the role of the individual metal centers during activation. The synthetic protocol outlined in Chapter 5 for the synthesis of mixed-metal clusters could be a valuable tool for building clusters featuring redox inactive metal centers (Scheme 5.3). Comparing the electronic structure and reactivity of the series of clusters shown in Scheme 5.3 would allow us to begin to both understand the requirements of small molecule activation by metal clusters as well as assess the role of individual metal centers during substrate binding and activation. Similar synthetic challenges

seen in Chapter 5 will likely be encountered and therefore should be considered when designing systems that will further test the ability of polynuclear assemblies towards effecting multi-electron activation of small molecule substrates.

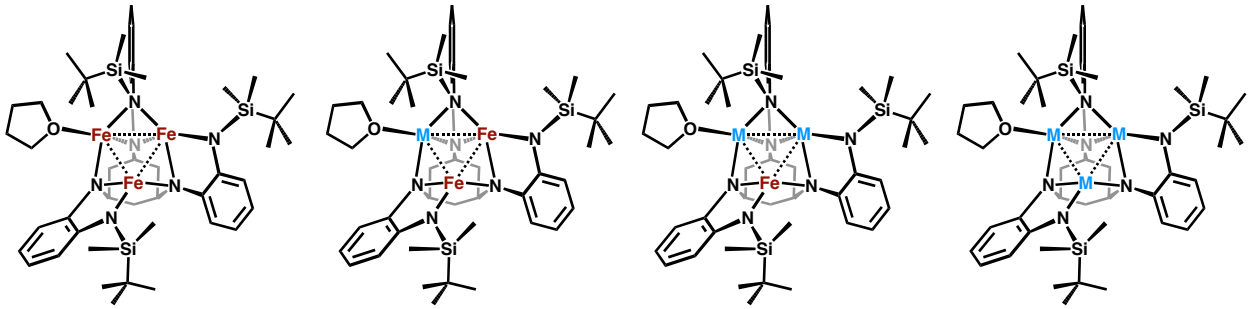

Scheme 5.3. Proposed mixed-metal clusters to assess the role of individual metal centers during substrate binding and activation.

5-6. Experimental methods

Materials and Methods

All manipulations involving metal complexes were carried out using standard Schlenk line or glove-box techniques under a dinitrogen atmosphere. All glassware was oven-dried for a minimum of 10 h and cooled in an evacuated antechamber prior to use in the dry box. Benzene, diethyl ether, hexanes and tetrahydrofuran (THF) were dried and deoxygenated on a Glass Contour System (SG Water USA, Nashua, NH) and stored over 4 Å molecular sieves (Strem) prior to use. Benzene-d_6 was purchased from Cambridge Isotope Labs and was degassed and stored over 4 Å molecular sieves prior to use. Non-halogenated solvents were typically tested with a purple solution of sodium benzophenone ketyl in THF in order to confirm effective oxygen and moisture removal. Fe_2Mes_4 (Mes = 2,4,6-$Me_3C_6H_2$),[165] $Mn_3(Mes)_6$,[278] and

278. Solari, E.; Musso, F.; Gallo, E.; Floriani, C.; Re, N.; Chiesi-Villa, A.; Rizzoli, C. *Organometallics* **1995**, *14*, 2265-2276.

$Mn_2(NSi(CH_3)_3)_4$[279] and were prepared following published methods. All other reagents were purchased from commercial vendors and used without further purification.

All of the measurements for the metal complexes, except for X-ray fluorescence spectroscopy, were made under anaerobic conditions. Elemental analyses were performed by Complete Analysis Laboratories, Inc., Parsippany, New Jersey. ^{1}H NMR spectra were recorded on Varian Unity/Inova 500/600 NMR spectrometers with chemical shifts (δ ppm) referenced to residual NMR solvent (C_6D_6, 7.16 ppm). Prependicular and parallel mode X-band EPR spectra were recorded on Bruker ElexSys E500 EPR (fitted with a cryostat for measurements at 4.3 K). The EPR spectra were referenced to diphenylpicrylhydrazyl (DPPH; g = 2.0037).

Synthesis

(^{tbs}L)Mn$_3$(THF) (5.2). $^{tbs}LH_6$ (0.300 g, 0.403 mmol) and Mn_3Mes_6 (0.366 g, 0.416 mmol) were each dissolved in 1 mL of benzene. The Mn_3Mes_6 solution was then added to the $^{tbs}LH_6$ solution at 23 ^{o}C followed by the addition of THF (5 mL) to the reaction mixture. The reaction was heated in a sealed bomb at 80 °C for 3 h. The volatiles were removed by lyophilization to afford a brown solid. The resulting material was dissolved in hexanes (20 mL) and filtered through Celite on a medium porosity fritted funnel. The filtrate was dried in vacuo to afford the title complex as a reddish-brown solid. Complex **5.2** is NMR silent; no ^{1}H NMR signals were observed for this complex. X-ray quality crystals were grown from cold hexanes (–33 ^{o}C). Isolated yield: 0.188, (49%). Anal. Calcd for $C_{46}H_{74}Mn_3N_6OSi_3$: C 56.60, H 7.64, N 8.61. Found: C 56.47, H 7.65, N 8.53.

(^{tbs}LH$_2$)Fe$_2$ (5.3). Solid $^{tbs}LH_6$ (0.130 g, 0.174 mmol) was dissolved in 10 mL of benzene. The solution was added to solid Fe_2Mes_4 (0.129 g, 0.435 mmol) at 23 ^{o}C. The reaction was heated in a sealed reaction vessel at 75 °C for 12 h. The volatiles were removed by

279. Bradley, D. C.; Hursthouse, M. B.; Malik, K. M. A.; Moseler, R. *Transition Met. Chem.* **1978**, *3*, 253.

lyophilization and the residue was washed with 5 mL of cold hexanes (–33 ^{o}C) to afford the title complex as a brown solid. Compound **5.3** is stable as a solid at –33 ^{o}C for at least 2 weeks. X-ray quality crystals were grown from cold hexanes (–33 ^{o}C). Isolated yield: 0.092 g, (62%). ^{1}H NMR (benzene-d_6, 500 MHz, δ, ppm): 82.9, 52.3, 39.2, 37.7, 32.8, 25.0, 24.4, 23.2, 22.2, 20.1, 19.5, 14.5, 14.2, 12.9, 11.9, –2.31, –5.70, –15.2, –24.7, –32.2, –32.9, –34.0, –40.7; Anal. Calcd for $C_{50}H_{71}Fe_3LiN_6Si_3$: C 59.14, H 8.04, N 9.85. Found: C 59.07, H 7.98, N 9.74; Zero-field ^{57}Fe Mössbauer (90 K) (δ, $|\Delta E_Q|$ ($^{mm}/_{s}$)): component 1 (39%): 0.67, *2.19* (Γ = 0.17 mm/s); component 2 (61%): 0.68, *1.60* (Γ = 0.28 mm/s); UV-vis Spectroscopy (THF): 262 nm (ε = 1.98 × 10^5 M^{-1}cm^{-1}); 290 nm (ε = 1.40 × 10^5 M^{-1}cm^{-1}); 334 nm (ε = 7.45 × 10^4 M^{-1}cm^{-1}); 455 nm (ε = 1.49 × 10^5 M^{-1}cm^{-1}).

(^{tbs}LH$_2$)Mn$_2$ (5.4). Solid ^{tbs}LH$_6$ (0.160 g, 0.215 mmol) was dissolved in 10 mL of benzene. The solution was added to solid $Mn_2(N(SiMe_3)_2)$ (0.192 g, 0.512 mmol) at room temperature. The reaction was heated in a sealed bomb at 75 °C for 12 h. The volatiles were removed by lyophilization and the residue was dissolved in 10 mL of hexanes. The hexane solution was filtered through Celite and the volatiles were removed in vacuo to afford the title complex as a tan solid. Complex **5.4** is NMR silent. X-ray quality crystals were grown from cold hexanes (–33 ^{o}C). Isolated yield: 0.128 g, (70%). Anal. Calcd for $C_{42}H_{68}Mn_2N_6Si_3$: C 59.27, H 8.05, N 9.87. Found: C 59.13, H 7.95, N 9.79.

(^{tbs}L)Fe$_2$Mn(THF) (5.5). Solid (^{tbs}LH$_2$)Fe$_2$ (**5.3**) (0.060 g, 0.070 mmol) was dissolved in 5 mL of THF. The solution was added to solid $Mn_2(N(SiMe_3)_2)$ (0.026 g, 0.070 mmol) at 23 ^{o}C and the resulting mixture was heated at 75 ^{o}C for 12 h. The volatiles were removed in vacuo and dissolved in approximately 3 mL of hexanes. The hexanes were removed in vacuo to afford a brown solid. Isolated yield: 0.043 g, (62%). Crystalline material was isolated from a diethyl

ether solution at –33 °C. Crystalline yield: 0.023 g, (33%). ^{1}H NMR (benzene-d_6, 500 MHz, δ, ppm): 285.4, 262.3, 129.8, 74.27, 52.38, 48.60, 43.15, 37.38, 35.62, 30.43, 24.20, 20.61, 18.13, 10.83, 9.38, 5.82, 5.09, 2.78, 2.07, 1.20, 0.06, –1.07, –1.66, –3.63, –9.47, –12.28, –12.31, –26.74, –33.05, –38.83, –56.99, –82.97; Anal. Calcd for $C_{46}H_{74}Fe_2MnN_6OSi_3$: C 56.49, H 7.63, N 8.59. Found: C 56.37, H 7.61, N 8.47; Zero-field ^{57}Fe Mössbauer (90 K) (δ, $|\Delta E_Q|$ ($^{mm}/_s$)): component 1 (48%): 0.35, *1.77* (Γ = 0.20 mm/s); component 2 (52%): 0.58, *1.30* (Γ = 0.22 mm/s).

(^{tbs}L)Mn$_2$Fe(THF) (5.6). Solid (^{tbs}LH$_2$)Mn$_2$ (**5.4**) (0.060 g, 0.070 mmol) was dissolved in 5 mL of THF. The solution was added to solid Fe_2Mes_4 (0.023 g, 0.078 mmol) at 23 °C. The reaction was heated at 75 °C for 12 h. The volatiles were removed in vacuo and the residue was washed with approximately 1 mL of hexanes. The remaining brown solid was dissolved in diethyl ether (~2 mL). Crystalline material was isolated from the diethyl ether solution at –33 °C. Crystalline yield: 0.010 g, (14%). ^{1}H NMR (benzene-d_6, 500 MHz, δ, ppm): 187.6, 182.6, 129.8, 117.3, 74.33, 55.73, 52.4, 48.62, 47.19, 43.19, 41.73, 37.44, 35.66, 31.75, 30.47, 28.99, 24.26, 21.41, 20.73, 18.17, 10.87, 9.42, 6.73, 5.86, 5.14, 4.30, 3.31, 2.81, 2.40, 2.16, 0.30, 0.10, –1.00, –1.63, –3.61, –5.96, –9.44, –10.03, –11.76, –12.24, –15.79, –20.79, –24.52, –26.72, –32.95, –36.53, –38.80, –56.94, –82.98; Anal. Calcd for $C_{46}H_{74}FeMn_2N_6Si_3O$: C 56.54, H 7.63, N 8.60. Found: C 56.48, H 7.67, N 8.54; Zero-field ^{57}Fe Mössbauer (90 K) (δ, $|\Delta E_Q|$ ($^{mm}/_s$)): component 1 (48%): 0.33, *1.85* (Γ = 0.14 mm/s); component 2 (52%): 0.57, *1.31* (Γ = 0.19 mm/s).

(^{tbs}L)Mn$_2$Fe(py) (5.7). Solid Fe_2Mes_4 (0.023 g, 0.078 mmol) was dissolved in 3 mL of benzene at 23 °C. Pyridine (py; ~15 μL) was added to the Fe_2Mes_4 solution followed by addition of a solution of (^{tbs}LH$_2$)Mn$_2$ (**5.4**) (0.060 g, 0.070 mmol) in benzene (2 mL). The resulting mixture was heated at 75 °C for 12 h. The volatiles were removed in vacuo and the residue was washed with approximately 1 mL of hexanes. The remaining brown solid was dissolved in

diethyl ether (1–2 mL). Crystalline material was isolated from the diethyl ether solution at –33 °C. Crystalline yield: 0.022 g, (31%). ^{1}H NMR (benzene-d_6, 500 MHz, δ, ppm): 185.5, 172.5, 128.4, 116.0, 72.41, 54.02, 53.20, 48.10, 47.28, 46.54, 42.62, 39.73, 34.18, 31.94, 28.74, 25.63, 23.44, 22.18, 19.90, 18.51, 11.10, 11.10, 9.77, 6.69, 3.23, 2.92, 2.18, 2.12, 0.93, 0.14, –0.27, –1.45, –2.19, –3.87, –6.34, –7.60, –9.99, –11.23, –12.01, –14.10, –17.32, –20.98, –22.31, –23.92, –25.90, –30.86, –35.48, –37.87, –55.08, –81.72; Anal. Calcd for $C_{47}H_{71}FeMn_2N_7Si_3$: C 57.36, H 7.27, N 9.96. Found: C 57.43, H 7.20, N 9.78; Zero-field ^{57}Fe Mössbauer (90 K) (δ, $|\Delta E_Q|$ ($^{mm}/_{s}$)): component 1 (54%): 0.33, *1.85* (Γ = 0.17 mm/s); component 2 (46%): 0.57, *1.24* (Γ = 0.19 mm/s).

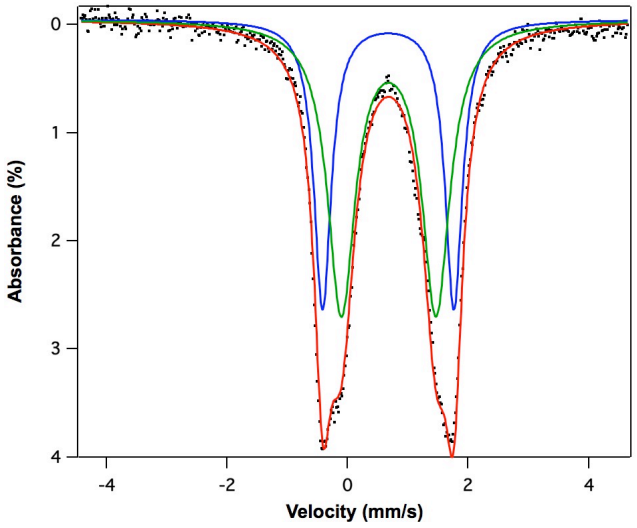

Figure 5.9. Zero-field Mössbauer spectrum of (^{tbs}LH$_2$)Fe$_2$ (**3**) obtained at 90 K. Simulation yields the following parameters: δ, $|\Delta E_Q|$ ($^{mm}/_{s}$) component 1 (39%) 0.67, *2.18* (Γ = 0.17 $^{mm}/_{s}$); component 2 (61%) 0.68, *1.57* (Γ = 0.28 $^{mm}/_{s}$).

X-Ray Diffraction Techniques

All structures were collected on a Bruker three-circle platform goniometer equipped with an Apex II CCD and an Oxford cryostream cooling device at 100 K Radiation for the data collection of **5.2**, **5.3**, and **5.4** was from a graphite fine focus sealed tube Mo Kα (0.71073 Å)

source. All other structures were obtained using radiation from a synchrotron source (0.4428 Å or 0.49594 Å). Crystals were mounted on a cryoloop or glass fiber pin using Paratone N oil. Data was collected as a series of φ and/or ω scans. Data was integrated using SAINT and scaled with either a numerical or multi-scan absorption correction using SADABS.[170] The structures were solved by direct methods or Patterson maps using SHELXS-97 and refined against F^2 on all data by full matrix least squares with SHELXL-97.[171] All non-hydrogen atoms were refined anisotropically. Hydrogen atoms were placed at idealized positions and refined using a riding model. The isotropic displacement parameters of all hydrogen atoms were fixed to 1.2 times the atoms they are linked to (1.5 times for methyl groups).

X-ray diffraction details.

(^{tbs}L)Mn$_3$(THF) (5.2). The structure was solved in the monoclinic space group C2/c with 8 molecules per unit cell. The asymmetric unit was found to contain 1 molecule of (^{tbs}L)Mn$_3$(THF). The THF molecule as well as one of the *tert*-butyl groups exhibited positional disorder and were refined with similarity restraints.

(^{tbs}LH$_2$)Fe$_2$ (5.3). The structure was solved in the triclinic space group $P\ \bar{1}$ with 2 molecules per unit cell. The asymmetric unit was found to contain one molecule of (^{tbs}LH$_2$)Fe$_2$ and one solvent *n*-hexane molecule unit. The solvent *n*-hexane molecule exhibited positional disorder and was refined using similarity restraints.

(^{tbs}LH$_2$)Mn$_2$ (5.4). The structure was solved in the monoclinic space group P2$_1$/m with 4 molecules in the asymmetric unit. The asymmetric unit was found to contain ½ of the (^{tbs}LH$_2$)Mn$_2$ molecule which exhibited positional disorder. The disorder was refined with similarity restraints.

(^{tbs}L)Fe$_2$Mn(THF) (5.5). The structure was solved in the monoclinic space group $P2_1/c$ with 4 molecules per unit cell. The asymmetric unit was found to contain the molecule (^{tbs}L)Fe$_2$Mn(THF) and two diethyl ether molecules. One of the diethyl ether molecules was located on a special position.

(^{tbs}L)Mn$_2$Fe(THF) (5.6). The structure was solved in the triclinic space group $P\bar{1}$ with 2 molecules per unit cell. The asymmetric unit was found to contain one molecule of (^{tbs}L)Mn$_2$Fe(THF) and two diethyl ether molecules. One of the diethyl ether molecules was located on a special position.

(^{tbs}L)Mn$_2$Fe(py) (5.7). The structure was solved in the monoclinic space group $P2_1/n$ with 4 molecules per unit cell. The asymmetric unit contains one molecule of (^{tbs}L)Mn$_2$Fe(py).

Table 5.6. X-ray Crystallographic Data for All Compounds

	5.2	5.3	5.4	5.5	5.6	5.7
Chemical formula	$C_{46}H_{72}Mn_3N_6Si_3$	$C_{48}H_{82}Fe_2N_6Si_3$	$C_{21}H_{32}MnN_3Si_{1.5}$	$C_{51.5}H_{87.5}Fe_2MnN_6Si_3O_{2.5}$	$C_{52}H_{89}Mn_2FeN_6Si_3O_{2.5}$	$C_{47}H_{71}MnFe_2N_7Si_3$
fw	976.2	939.17	423.57	1081.69	1088.29	984.11
Space group	*C*2/*c*	*P*-1	$P2_1/m$	$P2_1$/c	*P*-1	$P2_1/n$
a (Å)	25.172(1)	12.814(2)	10.7074(9)	10.4595(3)	10.5159(9)	15.0027(9)
b (Å)	20.141(1)	14.009(2)	17.260(2)	26.4759(9)	14.112(1)	21.471(1)
c (Å)	21.771(1)	15.800(3)	11.904(1)	21.6466(8)	20.413(2)	15.931(1)
α (deg)		79.054(2)			89.350(2)	
β (deg)	116.579(1)	76.144(2)	92.046(2)	102.319(1)	80.618(2)	103.347(2)
γ (deg)		70.450(1)			71.678(2)	
V (Å^3)	9871.3(9)	2576.3(6)	2198.1(3)	5856.5	2834.7(4)	4993.1(6)
Z	8	2	4	4	2	4
μ (mm^{-1})	0.87	0.67	0.69	0.42	0.42	0.47
T (K)	100(1)	100(1)	100(1)	100(1)	100(1)	100(1)
R1[a] (wR2[b])	0.043 (0.111)	0.047 (0.101)	0.043 (0.099)	0.035 (0.126)	0.048 (0.147)	0.045 (0.091)
Wavelength (Å)	0.71073	0.71073	0.71073	0.49590	0.49590	0.49590

[a] $R1 = [\sum w(F_o - F_c)^2/\sum wF_o^2]^{1/2}$

[b] $wR2 = [\sum [w(F_o^2 - F_c^2)^2]/ \sum w(F_o^2)^2]^{1/2}$, $w = 1/[\sigma^2(F_o^2) + (aP)^2 + bP]$, \
where $P = [\max(F_o^2,0) + 2(F_c^2)]/3$

Mössbauer Spectroscopy

Zero-field, ^{57}Fe Mössbauer spectra were measured with a constant acceleration spectrometer (SEE Co, Minneapolis, MN). Crystalline samples were prepared as Paratone-N mulls in a drybox and frozen in liquid nitrogen prior to handling in air. Isomer shifts are quoted relative to Fe metal at room temperature. Data was processed, simulated, and analyzed using an in-house package for IGOR Pro 6 (Wavemetrics, Lake Oswego, OR).

X-ray fluorescence

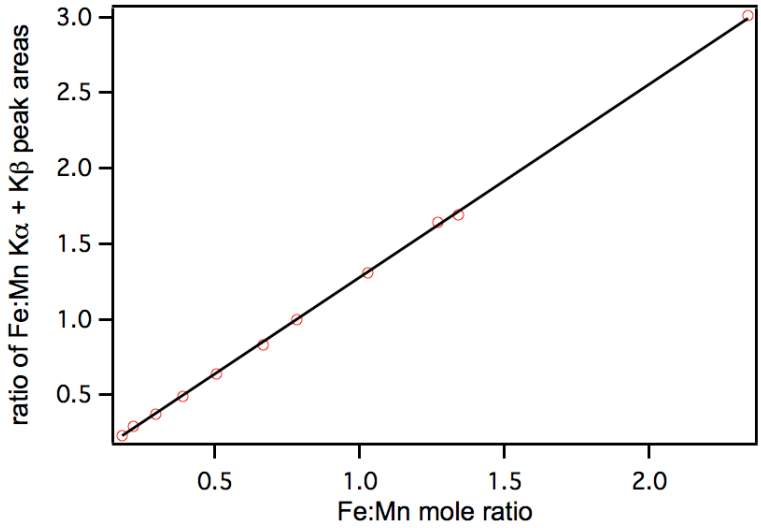

Figure 5.10. Calibration curve for X-ray fluorescence analysis. Solution samples of $FeCl_3$ and $MnCl_2(H_2O)_4$ in water. Linear fit shown (y = 1.22x).

X-ray fluorescence analyses were recorded on a Bruker Tracer III-SD XRF analyzer with no additional filter and data was collected on each sample for at least 10 min. Samples for the calibration curve were prepared by dissolving iron(III) chloride and manganese(II) chloride tetrahydrate in water. The Kα and Kβ of pure Fe and Mn were each fit to a Gaussian lineshape. The calibration samples were fit to three Gaussian lineshapes representing the Mn Kα emission, the overlapping Mn Kβ and Fe Kα emissions, and the Fe Kβ emission. The area of the Mn Kβ emission was calculated using the area of the Gaussian fit of the Mn Kα emission and the Mn

Kα and Kβ ratio of the areas of a pure sample manganese(II)chloride tetrahydrate. Quantification was performed using the sum of the Kα and Kβ areas. Fe:Mn ratios in samples were determined from the peak area ratios using the linear fit to the calibration curve (Figure 5.9).

Anomalous X-ray Diffraction Techniques

All anomalous x-ray diffraction data were collected at ChemMatCARS at the Advanced Photon Source at Argonne National Laboratory (CARS Center for Advanced Radiation Sources). The data sets were collected on a Bruker three-circle platform goniometer equipped with an Apex II CCD and an Oxford cryostream cooling device at 100 K. Anomalous X-ray diffraction data was collected at wavelengths at the elemental absorption edges of Mn (6.539 keV) and Fe (7.112 keV). In some cases, data was collected between 30–50 eV above and/or below the Mn and Fe K-edges. Data was integrated using SAINT and scaled with either a numerical or multi-scan absorption correction using SADABS.[170] Structure factors f' and f'' were determined for a given wavelength based on theoretical values[274] from the XDISP function in the WINGX program[280] unless otherwise noted. Anomalous difference Fourier electron density maps at the absorption edges were also generated using SHELXL-97[171] and WINGX,[280] by fixed refinement of the atomic model generated by the reference dataset (1a or 1b) with the reflection data obtained at the metal absorption edge. The electron density holes measured in $e^-/Å^3$ were determined by looking at the 2D electron density maps in MCE.[281] The percent occupancies of Fe and Mn at each metal position were refined using SHELXL-97[171] as described by Helliwell *et al*.[269] When refining the metal occupancies near and at the metal absorption edges, the metal positions were fixed using the EXYZ restraint unless otherwise noted.

280. Farrugia, L. J. *J. Appl. Cryst.* **1999**, *32*, 837-838.
281. Rohlicek, J.; Husak, M. *J. Appl. Cryst.* **2007**, *40*, 600-601.

Table 5.7. Summary of the synchrotron datasets measured at different wavelengths. Anomalous scattering terms from two sources were used to assess the sensitivity of the refinement method to the possible errors associated with the calculated *f″* and *f ″* values for pure Fe and Mn metal (oxidation state 0).

			OLEX[a]		*WINGX*[b]	
	Wavelength (Å)	**Energy (KeV)**	**Fe f′, f ″ (e^-)**	**Mn f′, f ″ (e^-)**	**Fe f′, f ″ (e^-)**	**Mn f′, f ″ (e^-)**
1a	0.4428	28	0.222, 0.347	0.203, 0.297	0.220, 0.350	0.200, 0.300
1b	0.49594	25	0.258, 0.432	0.238, 0.370	0.255, 0.434	0.234, 0.373
2	1.91068	6.489	-2.17, 0.565	-5.57, 0.487	-2.166, 0.552	-4.594, 0.469
3	1.89607	6.539	-2.24, 0.557	-11.24, 2.38	-2.241, 0.544	-9.901, 0.462
4	1.88169	6.589	-2.33, 0.550	-7.48, 3.83	-2.324, 0.537	-4.486, 3.904
5a	1.75565	7.062	-4.83, 0.488	-1.75, 3.46	-4.646, 0.474	-1.731, 3.452
5b	1.7507	7.082	-5.59, 0.485	-1.70, 3.45	-5.183, 0.471	-1.686, 3.437
6	1.74331	7.112	-9.81, 0.468	-1.62, 3.41	-9.812, 0.468	-1.622, 3.414
7	1.73114	7.162	-4.83, 0.488	-1.75, 3.46	-4.547, 3.896	-1.522, 3.377

a real (*f′*) and imaginary (*f″*) components obtained from "International Tables Vol C Tables 4.2.6.8 and 6.1.1.4"

b real (*f′*) and imaginary (*f″*) components obtained from Kissel, L.; Pratt, R. H. *Acta Cryst.* **1990**, *A46*, 170-175.

Table 5.8. Free refinement of metal centers at absorption edges of Fe and Mn

Metal site	**Compound 5.5**	**Compound 5.6**	**Compound 5.7**
Dataset 3 (6.539 keV)			
Fe1	69.0(9)	64.3(7)	67.3(4)
Fe2	95.9(5)	83.6(6)	78.7(4)
Fe3	96.2(6)	99.9(7)	96.9(4)
Dataset 6 (7.112 keV)			
Mn1	93.0(6)	97.4(7)	95.7(8)
Mn2	75.3(6)	84.5(7)	87.2(9)
Mn3	70.4(6)	77.0(9)	73(1)

Table 5.9. Refined Fe occupancies (%) with *SHELXL* for **5.5**

Metal site	Dataset 3	Dataset 6
	with EXYZ[a]	
M1	31(1)	12(2)
M2	91(3)	55(2)
M3	92(1)	66(2)
	without EXYZ[a]	
M1	32(1)	11(2)
M2	92(1)	55(2)
M3	92(2)	66(2)
	with EXYZ	
M1	18(2)	16(2)
M2	90(1)	75(2)
M3	90(1)	88(2)
	$f' + 1e^-; f'' + 0.25e^-$	
M1	7(2)	18(2)
M2	88(2)	86(2)
M3	89(2)	100*
	$f' - 1e^-; f'' - 0.25e^-$	
M1	27(2)	15(2)
M2	90(1)	66(2)
M3	91(1)	78(2)

[a] Real (f') and imaginary (f'') components obtained from "International Tables Vol C Tables 4.2.6.8 and 6.1.1.4"